UCLA
UCLA Electronic Theses and Dissertations

Title

Study of Device Physics and Active Layer Morphology in Polymer-Fullerene Based Solar Cells: The Role of Vertical Phase Segregation and Organic/Metal Interface

Permalink

https://escholarship.org/uc/item/4gr4v15g

Author

Zhang, Guangye

Publication Date

2015

Peer reviewed|Thesis/dissertation

eScholarship.org Powered by the California Digital Library
University of California

UNIVERSITY OF CALIFORNIA

Los Angeles

Study of Device Physics and Active Layer Morphology in Polymer-Fullerene Based Solar Cells: The Role of Vertical Phase Segregation and Organic/Metal Interface

A dissertation submitted in partial satisfaction of the requirements

for the degree of Doctor of Philosophy

in Chemistry

By

Guangye Zhang

2015

© Copyright by

Guangye Zhang

2015

ABSTRACT OF THE DISSERTATION

Study of Device Physics and Active Layer Morphology in Polymer:Fullerene Based Solar Cells: The Role of Vertical Phase Segregation and Organic/Metal Interface

by

Guangye Zhang

Doctor of Philosophy in Chemistry

University of California, Los Angeles, 2015

Professor Benjamin J. Schwartz, Chair

Organic photovoltaics (OPVs) are flexible, low cost and easily processable, which provides them with a very short energy payback time compared to most PV technologies and makes them strong candidates for industrial mass production. The richness of organic synthesis has afforded a large library of molecular semiconductors, among which the combination of conjugated polymers as electron donors and fullerenes as electron acceptors has been demonstrated to be the best sellers as building blocks of OPV devices. In the past few years, the majority of research focus on OPVs has been devoted to improving their power conversion efficiencies by using new combinations of polymer and fullerene materials. Most devices are based on blend-cast bulk heterojunctions (BHJs), in which a polymer and fullerene are mixed together in a solution that is then used to cast the active layer of the organic solar cell. Because the nm-scale morphology of the film depends on so many of the details of how it is cast, the device performance of blend-cast

BHJ solar cells is hypersensitive to the processing kinetics of the active layer. Thus, for any new set of OPV materials, an Edisonian approach involving the fabrication of hundreds of blend-cast devices is needed to find the processing conditions that lead to the optimal morphology and best device performance. In this thesis, I will focus on two main contributions that I have made to help rationally design OPVs.

First, our group recently has gone beyond the traditional method of simply blending the donor and acceptor material by developing a new technique to process the active layer of OPVs called sequential processing. This method takes advantage of a pair of quasi-orthogonal solvents to process the two components used in the active layer separately. By studying a series of crystalline polymers with controlled regioregularities and polydispersities, I have found that increasing polymer crystallinity produces the opposite behavior in BHJ solar cells fabricated by sequentially-processing and blend-casting. This suggests that the two processing techniques are complementary and provides guidance on selecting the appropriate processing technique for a given polymer.

Second, I have studied the performance and device physics of a new series of controllably tuned fullerene derivatives applied in traditional blend-cast active layers. We obtained a series of carefully designed 1,4-dibenzyl fullerene bisadducts synthesized by our collaborators in Prof. Yves Rubin's group. The fullerenes have methoxy substituents selectively positioned on pendant phenyl rings, which allows us to examine the effect of the subtle molecular changes on both macroscopic solar cell performance and the underlying device physics. Through carrier recombination studies, I have learned that solar cell performance often depends on the material's surface energy and the vertical phase segregation caused by this surface energy in the active

layer. The results will allow us to offer new directions on how to select the best device structure with a given new fullerene material.

Finally, I have helped to make an interesting discovery during my study of the device physics of as-cast sequentially processed solar cells. I found that the specific type of vertical phase segregation in the as-cast devices gives rise to dark carriers, whose presence can be measured using the charge extraction by linear increasing voltage (CELIV) technique. The dark carriers directly clearly are created by the evaporation of metal electrodes because I found no such carriers when non-metal interfacial layers were inserted between the metal and the organic layer. Through capacitance analysis and transmission electron microscopy studies, we found this n-type doping is caused by metal penetration into the fullerene domain. These findings could have significant impact on determining device performance, explaining device physics and guiding future research directions.

The dissertation of Guangye Zhang is approved.

Yves F. Rubin

Yuanxun Ethan Wang

Benjamin J. Schwartz, Committee Chair

University of California, Los Angeles

2015

DEDICATION

To my wife and my parents.

TABLE OF CONTENTS

Chapter 1 Introduction..... 2

1.1 Need for Solar Energy 2

1.2 Working Principles of OPVs..... 4

1.3 Study the Polymer-Fullerene BHJ Morphology Formed through a Novel Technique: Sequential Processing (SqP)..... 8

1.4 Synthesis Novel Fullerene Derivatives for Efficient OPVs 10

1.5 Using 1,4-fullerene Bisadducts to Study the Vertical Phase Segregation in BHJ Solar Cells..... 11

1.6 Apparent Fullerene Layer Doping Caused by Evaporation of Metal Electrodes..... 13

1.7 References..... 13

Chapter 2 Crystallinity Effects in Sequentially-processed and Blend-cast Bulk-heterojunction Polymer/Fullerene Photovoltaics..... 17

2.1 Background 17

2.2 Introduction..... 18

2.3 Experimental 20

2.4 Results and discussions..... 23

2.4.1 The Device Physics of BC and SqP Solar Cells Made from Different P3HTs..... 24

2.4.2 Understanding How P3HT Crystallinity Affects the BHJ Architecture for SqP and BC OPVs:..... 32

2.5 Experimental Details and Additional Morphological Characterization..... 44

2.5.1 Detailed Parameters for the Different Batches of P3HT Used in This Work..... 44

2.5.2 Experimental Details 45

2.5.3 Injected Current Characteristics of Pure P3HT Diodes 48

2.5.4 SqP Solar Cells with Different P3HT/PCBM Compositions 50

2.5.5 Performance Properties of As-Cast SqP Solar Cells 53

2.5.6 Performance and Properties of BC BHJ Solar Cells with 50k HR P3HT 54

2.5.7 Composition Effect in BC-BHJ Solar Cells 55

2.6 Conclusions 60

2.7 References 61

Chapter 3 Novel 1,4-[60]Fullerene Bisadducts for Efficient Polymer Solar Cells 78

3.1 Introduction 78

3.2 Results and discussion 80

3.3 References 91

Chapter 4. Vertical Phase Segregation and Surface Recombination in Polymer:Fullerene BHJ Solar Cells: The Role of Surface Energy 96

4.1 Background 96

4.2 Experimental Methods 100

4.3 Results and Discussion 102

4.3.1 Structural Characterization of the Polymer:Fullerene Active Layer 102

4.3.2 Interfacial States Measured by Photocurrent Spectral Response 105

4.3.3 Ideality Factor and Bulk Recombination 107

4.4.4 Vertical Phase Segregation and Surface Recombination 111

4.4.5 The Role of Surface Recombination in Charge Carrier Density and Lifetime 113

4.4.6 Using the VPS Model to Explain Device Physics: Dark Carriers Measured by CELIV 116

4.4.6 Using Vertical Phase Separation to Understand the Difference Between V_{oc} and E_{ct} 118

4.4.7 Understanding Vertical Phase Segregation by Measuring Surface Energies via Contact Angle 120

4.4.8 Using Surface Energies to Understand the Operation of Normal vs. Inverted Device 124

4.4 Conclusions 127

4.5 Experimental Details 128

4.5.1 Device Fabrication 128

4.5.2 GIWAXS 130

4.5.3 Optoelectronic Measurements and CELIV 130

4.5.4 Contact Angle and Surface Energy Analysis 130

4.6 References 131

Chapter 5 Investigation of the Dark Carriers in Fullerene Based Diodes Measured by CELIV: the Role of Metal Penetration into the Fullerene-layer Induced by Metal Evaporation 143

5.1 Introduction 143

5.2 Results and Discussion 145

5.2.1 Studying Doping with the CELIV Technique 145

5.2.2 Investigating Fullerene Doping in Different Device Structures 150

5.2.3 The Distribution of Dark Carriers: Surface or Bulk? 154

5.2.4 Changes in C_g with VPS Indicate Metal Penetration 157

5.2.5 Number of Dark Carriers Governed by Metal Penetration Depth 161

5.2.6 Direct Evidence for Metal Penetration: Imaging the Device's Cross-section by TEM 162

5.2.7 Exploring the Possible Origin of Doping: C_g Analysis for Different Metals and Temperature Dependence of the Carrier Concentration and Mobility 164

5.3 Conclusion 169

5.4 CELIV Transients and Experimental Methods 170

5.4.1 Equivilant Circuit Modeling of Depleted Devices 170

5.4.2 CELIV Transients for Devices with Various Organic Layers 171

5.4.3 Devices with Different Metal Cathodes 172

5.4.4 Discussion on Polymer Effect on Measured Dark Carriers 174

5.4.5 XPS Analysis: Calculating Volume Fraction from C/S Ratio 175

5.4.6 Device Fabrication Procedure 176

5.5 References 178

LIST OF FIGURES

Chapter 1

Figure 1.1 World energy consumption between 1988 – 2013. The unit for the consumption is million tonnes oil equivalent. Adapted from Ref. 1..... 2

Figure 1.2 An typical structure for polymer:fullerene based solar cells (Top right) and a scheme illustrating the four-step light-to-current conversion process..... 5

Figure 1.3 Chemical structures of three widely used conjugated polymers (left) and fullerene derivatives (right) in OPVs. 6

Figure 1.4 The basic steps for fabricating a P3HT:PCBM based SqP device. Instead of simply blending the polymer and fullerene derivative in one solution, we prepare the polymer layer first by spin-coating the polymer solution onto the substrate. Then a solution containing the fullerene derivatives in a quasi-orthogonal solvent is spin-coated onto the polymer underlayer. Through thermal annealing (not for all polymers) and cathode deposition, a SqP device is made..... 9

Figure 1.3 Chemical structure of the 1,2-fullerene bisadduct (PCBM) on the left and the 1,4-fullerene bisadduct used in Chapter 3 on the right. 11

Chapter 2

Figure 2.1 Current density versus applied bias for (a) ITO/poly(ethylene-dioxythiophene):poly(styrenesulfonic acid)(PEDOT:PSS)/P3HT/PCBM/Ca/Al sequentially-processed solar cells and (b) ITO/PEDOT:PSS/P3HT:PCBM/Ca/Al BC-BHJ solar cells under AM-1.5 illumination. The SqP active layer was made by spinning 5 mg/mL PCBM solution onto a 110 nm P3HT underlayer (see SI). All of the SqP and BC films were thermally annealed at 150 °C for 20 min prior to deposition of the cathode. The error bars show 1 standard

deviation in measurements over at least 12 independent devices. Although error bars can be clearly seen in panel (b), they are comparable to or smaller than the symbols used to plot the data in panel (a), indicating that SqP devices are more reproducible than BC devices. 22

Figure 2.2 Effect of molecular weight, regioregularity and film composition on the *J–V* characteristics of P3HT/PCBM devices made via SqP. LR P3HT (blue up-triangles) and two HR P3HTs with different molecular weights, e.g. 37k Da (violet squares) and 16 kDa (green left triangles) are used as underlayer. All P3HT underlayers were kept at ~110 nm. Three different concentrations of PCBM (5 mg/mL, 10 mg/mL and 15 mg/mL) were spun on top of the P3HT underlayers from DCM and the corresponding *J–V* curves are shown in panels (a), (b) and (c), respectively. The total thicknesses of the active layers are 155 nm, 169 nm and 185 nm with increasing PCBM solution concentratio, respectively. All samples were annealed at 150° C for 20 min before deposition of the Ca/Al cathode. The error bars show 1 standard deviation for measurements over at least 12 independent devices. 27

Figure 2.3 Dark *J-V* characteristics of the same SqP devices in Figure 2.2 and the same BC devices in Figure 2.1. 29

Figure 2.4 UV-visible absorption spectra of thin films made from different batches of pure P3HT (solid dashed and dash-dotted lines) and SqP P3HT/PCBM films (symbols) made from the same P3HTs with (a) 5 mg/mL PCBM, (b) 10 mg/mL PCBM and (c) 15 mg/mL PCBM spun on top; and (d) BC P3HT:PCBM films made from the same P3HTs. The pure P3HT films were 110 nm thick in all cases. All films were thermally annealed at 150 °C for 20 minutes and the spectra in both panels are normalized to the highest polymer optical density (i.e. highest OD red of 490 nm) for ease of comparison. 33

Figure 2.5 Photoluminescence (PL) spectra of thin films made from: pure P3HTs (same as Figure 2.4a), SqP P3HT/PCBM films (same as Figure 2.4a) and P3HT:PCBM BC films (same as Figure 2.4d). The measured PL intensities were divided by each film's optical density at 530 nm, the excitation wavelength used in this experiment. and then normalized to the highest PL value (that of the pure 16k HR P3HT film) to best illustrate the extent of PL quenching in the different samples. 36

Figure 2.6 (a) Radially-integrated 2-D GIWAXS intensities for P3HT/PCBM sequentially processed active layers cast on a silicon substrate for LR and HR P3HT. In each case, the P3HT film thickness was 110 nm, and the PCBM over-layer was spun from a 5mg/mL solution. (b) Integrated peak area for the (200) polymer peak for SqP. (c) Integrated GIWAXS intensity for P3HT/PCBM BC films. (d) Integrated peak area for the (200) polymer peak for BC-BHJ films. Dashed lines indicate as-cast films and solid lines are after 20 min of thermal annealing at 150 °C for both (a) and (c). 38

Figure 2.7 2-D GIWAXS of a thermally-annealed LR P3HT/PCBM SqP active layer (left) and corresponding P3HT packing structures (right). The (100), (200), and (300) peaks correspond to the distance *a* and the (010) peak corresponds to the distance *b*. 48

Figure 2.8 Current density vs. applied voltage square and the space charge limited current (SCLC) model fits in the high bias region for ITO/PEDOT:PSS/P3HT/Au hole only diodes. The thickness of the LR P3HT (blue upward triangle), 16k HR P3HT (green left triangle), and 37k HR P3HT (purple square) polymers were 112 nm, 137 nm and 107 nm, respectively. 49

Figure 2.9 Optical microscopy images of thermally annealed films with three batches of P3HTs and three different PCBM concentrations spun on top of each batch of them. The scale bar is 100 μm. 51

Figure 2.10 Integrated GIWAXS intensity for LR P3HT/PCBM SqP films with (a) 5 mg/mL PCBM, (b) 10 mg/mL PCBM and (c) 15 mg/mL PCBM spun on top of the P3HT underlayers. Dashed lines indicate as-cast films and solid lines are for films annealed at 150 °C for 20 min. 52

Figure 2.11 *J-V* characteristics of the as-cast P3HT/PCBM devices corresponding to the annealed device *J-V* curves used in Figure 2.1. The error bars show 1 standard deviation in measurements over at least 12 independent devices. 53

Figure 2.12 Dark *J-V* curves of the as-cast SqP P3HT/PCBM devices shown in Figure 2.11. 54

Figure 2.13 *J-V* characteristics of P3HT:PCBM 1:0.9 BC-BHJ with three batches of P3HTs. The device performance increase from LR P3HT to HR P3HT is observed in both 16k and 50k HR P3HT batches. The similarity of the molecular weights between 50k HR P3HT and LR P3HT supports the conclusion that the increase of device performance in the BC-BHJ devices is mainly due to the increase of polymer regioregularity. 54

Figure 2.14 Optical microscopy images of P3HT:PCBM 1:0.9 BC-BHJ with LR P3HT (left) and 16k HR P3HT (Right). No significant phase separation is observed at this length scale for both films. 55

Figure 2.15 *J-V* characteristics of BC-BHJ solar cells made from 16k HR P3HT (orange) and LR P3HT (black) with two polymer:fullerene weight ratios. 56

Figure 2.16 UV-Visible absorption spectra of thin BC-BHJ P3HT:PCBM films made from the same P3HTs as in Figure 2.15. All of the BC-BHJ films were thermally annealed at 150 °C for 20 minutes. The spectra were normalized to their highest polymer optical densities (OD) for ease of comparison. 57

Figure 2.17 PL spectra of thin films made from: pure P3HTs (same as those in Figure 2.16) and P3HT:PCBM BC-BHJ films (same as those in Figure 2.16). The measured PL intensities were

all divided by their optical densities at 530 nm, the excitation wavelength used in this experiment, and further normalized to the highest value of the pure HR P3HT film to best illustrate the extent of PL quenching in different samples. 58

Figure 2.18 (a) Integrated GIWAXS intensity for P3HT:PCBM BC-BHJ films. Dashed lines indicate as-cast films and solid lines are after 20 min of thermal annealing at 150 °C. (b) Full width at the half maximum (FWHM) for the polymer (200) peaks. 59

Chapter 3

Figure 3.1 X-ray structures and packing modes of fullerene 2c ((a) and (b)) and fullerene 2g ((c) and (d)). For clarity, protons are omitted. Red: oxygen; Grey: carbon; Yellow: Sulfur. 81

Figure 3.2 Synthesis of symmetric and asymmetric 1,4-dibenzyl [60]fullerene bisadducts. 83

Figure 3.3 (a) and (b): Current density versus applied bias for photovoltaic devices based on P3HT:DBCBA where each of the benzyl rings in the DBCBA are substituted with one side group (a) and two methoxy groups (b). The standard P3HT:PCBM based devices is plotted in (b) as a control. The error bars show 1 standard deviation for measurements over at least 6 independent devices. (c): Example of radially integrated 2-D GIWAXS intensities for three P3HT:fullerene active layers processed on silicon substrates. 85

Figure 3.4 (a): Current density versus applied bias for photovoltaic devices based on PTB7:PCBM (open black square) and PTB7:**2g** (red circle). The error bars show 1 standard deviation for measurements over at least 6 independent devices; (b): UV-visible absorption spectra for the same active layers used in (a). 90

Chapter 4

Figure 4.1 (a): *J-V* characteristics for solar cells with a structure of ITO/PEDOT:PSS/P3HT:Fullerene/Ca/Al under AM-1.5 solar illumination. All active layers were annealed at 150 ºC for 20 min prior to the deposition of the cathode material. (b): *J-V* characteristics of PTB7:PCBM (black square) and PTB7:2g (red circle) photovoltaic devices under 1-sun with the same device structure as in (a). Below the *J-V* curves are the chemical structures for the polymers and fullerene derivatives used. 99

Figure 4.2 Radially integrated 2-D GIWAXS intensities for pure P3HT and three P3HT:fullerene BHJs (a) and two PTB7:fullerene BHJs (b) processed on silicon substrates. The polymer:fullerene active layers were prepared with the same method as used in device fabrication. 102

Figure 4.3 PSR spectra for the same P3HT:fullerene (a) and PTB7:fullerene (b) photovoltaic devices used in Figure 4.1. The horizontal difference (green arrow) between the spectra of devices with PCBM and 2g (or 2h) in the photon energy range of ~1.3 – 1.6 eV in (a) or ~1.2 – 1.4 eV in (b) is mainly ascribed as the LUMO level difference between PCBM and 2g (or 2h). The sub-gap EQE (<~1.3 eV) contains information on the interfacial transitions involving localized states within the CT bandgap. The device with 2h clearly shows more localized density of states than those with 2g or PCBM. 106

Figure 4.4 (a) and (b): Dark *J-V* curves for the same devices used in Figure 4.1. The dashed lines show the fitting region used to obtain the dark ideality factors. (c) and (d): The measured V_{oc} as a function of illumination intensity for the same devices. The insets show the corresponding differential ideality factors calculated using Eq. (1). 109

Figure 4.5 A cartoon illustrating the idea of surface recombination. The red solid lines represent the polymer and the purple circles represent the fullerene derivatives. 112

Figure 4.6 Total carrier lifetime versus average excess carrier density for the same P3HT:fullerene (a) and PTB7:fullerene (b) devices used in Figure 4.1. The total carrier lifetime and average excess charge carrier density are obtained from TPV and TPC measurements, respectively. Each data set represents the average of at least two devices. 114

Figure 4.7 Dark CELIV current transients on diodes with P3HT:fullerene (a) and PTB7:fullerene (b). All curves were divided by the product of their geometric capacitance (C_g) and CELIV ramp rate (U_R). 117

Figure 4.8 Plot of V_{oc}*q versus charge transfer state energy for the five polymer:fullerene BHJ systems. The solid line in the left plot represents the typical difference between V_{oc} and E_{ct} for OPVs, which is about 0.6 eV. All of our devices are above the line except for the P3HT:2h device due to its non-ideal bulk recombination. The arrows in the left plot show the difference between the V_{oc} when different fullerenes are used and the arrows in the band diagrams on the right side show the LUMO difference between the fullerene derivatives. 118

Figure 4.9 Top: Contact angle images taken on liquid water/thin films (<100 nm) consisted of pure organic material. Bottom: Bar graphs for the calculated surface energies for pure polymers or fullerene derivatives from water contact angle measurements. 123

Figure 4.10 Cartoons illustrating different vertical phase segregation in different polymer:fullerene systems, based on the relative surface energies of the different polymers and fullerenes summarized in Table 4.1. 124

Figure 4.11 “Normal” versus “Inverted” devices using the same polymer:fullerene active layers where (a) is P3HT:fullerene and (b) is PTB7:fullerene. The “normal” devices’ *J-V* curves are reprinted results from Figure 4.1 for ease of comparison. The “normal” device has a structure of ITO/PEDOT:PSS/Polymer:Fullerene/Ca/Al while the “inverted” device has a structure of

ITO/ZnO/Polymer:Fullerene/MoO_3/Ag. The error bars are omitted in the figure for clarity but the standard deviations are included in Table 4.2. 125

Chapter 5

Figure 5.1 (a.) Sample simulated CELIV transients based on three commonly observed regimes. The "Doped" curve (red squares) was calculated using the Juska *et al*.[14] CELIV formalism with the addition of a finite series resistance. The "No Doping, Capacitor" curve (blue spheres) is the response of a series RC circuit to a CELIV pulse, and the "Leaky Capacitor" data (yellow triangles) corresponds to the response of a parallel RC circuit with a series resistance to the same CELIV pulse (see Section 5.4.1 for model details). All curves were divided by the product of their geometric capacitance (C_g) and the CELIV ramp rate (U_R). (b.) Experimentally measured dark CELIV current transients on diodes with different organic semiconducting materials in the configuration ITO/PEDOT:PSS/Organic Semiconductor/Ca/Al. 146

Figure 5.2 (a.) Measured (symbols) CELIV transients and fitted (lines) curves using circuit model (inset) on pure PCBM diodes with structures of ITO/PEDOT:PSS/PCBM/Ca/Al (black circle) and ITO/ZnO/PCBM/MoO_3/Ag (open blue square). The equations used for fitting are presented in Section 5.4.1. (b.) CELIV transients on diodes with a structure of ITO/LiF/C_{60}/Ca/Al. LiF (50 nm) and C_{60} (105 nm) were thermally evaporated sequentially onto ITO substrates. Both a non-leaky device and leaky devices were plotted to illustrate the effect of leakage current on CELIV transients. (c.) CELIV transients on diodes with structures of ITO/P3HT/C_{60} (105 nm)/Ag (green up triangles) and ITO/P3HT/C_{60} (105 nm)/LiF (15 nm)/Ag (purple circles). 152

Figure 5.3 (a.) Sheet doping density versus fullerene volume fraction near the organic/cathode interface (derived from XPS analysis, see SI) for diodes made with various organic semiconductors. All devices have the structure: ITO/PEDOT:PSS/Organic Semiconductor/Ca(10 nm)/Al(70 nm); (b.) Simulation of sheet charge density versus fullerene layer thickness for diodes with a P3HT/fullerene bilayer configuration, using "A Solar Cell Capacitance Simulator" (SCAPS) simulation;[41] (c.) experimental data of measured sheet charge density versus fullerene layer thickness obtained by subtracting the P3HT layer thickness (115 nm) from the total organic layer thickness measured from profilometry. The PCBM overlayer thickness is controlled by adjusting the concentration of PCBM solution[6] while the C_{60} layer thickness controlled by the evaporation time and rate. 155

Figure 5.4 (a.) Actual organic layer thickness measured by profilometry (solid bars) and calculated thickness from C_g (dashed bars) for diodes with different organic semiconductors. (b.) Metal penetration depth (shaded bars) and sheet charge density (red circles) for the same diodes in (a.). The metal penetration depth is calculated by subtracting the d_g thickness from actual thickness. The sheet charge density is obtained from the dark CELIV measurement using the method mentioned in 5.2.1. All diodes have a structure of ITO/PEDOT:PSS/Organic Semiconductor/Ca/Al. For the annealed samples, annealing was performed prior to the evaporation of the Ca/Al electrode. The P3HT/PCBM organic layers were prepared by SqP and the P3HT/C_{60} ones by evaporation of C_{60} onto the P3HT underlayer. The error bars show 1 standard deviation over at least three separate measurements. 158

Figure 5.5 The metal penetration cartoon. Left: SqP P3HT/PCBM active layer before metal evaporation. Middle: SqP P3HT/PCBM/Evaporated Metal. Right: P3HT/C_{60} (evaporate)/Evaporated Metal. 162

Figure 5.6 Bright field cross-sectional images of glass/ITO/PEDOT/P3HT:PCBM/PCBM:Au/Au as-cast SqP devices. A) Zoomed out image of the entire device, showing the various layers and their persistence in the in-plane direction. B) Zoomed in image of the P3HT:PCBM/PCBM:Au/Au interface, showing the remarkable nanoparticle formation resulting from thermal evaporation of Au onto a PCBM-rich layer. C) Further zoomed in image on the belt of ~3.5 nm nanoparticle at the P3HT-rich interface. The elemental composition in each portion of the image was identified by EDX analysis)..... 163

Figure 5.7 Metal penetration depth (shaded bars) and sheet charge density (red circles) for SqP ITO/PEDOT:PSS/P3HT/PCBM/Metal diodes with different top metal electrodes. The first shaded bar is the same 150 ºC annealed SqP P3HT/PCBM sample used in Figure 5.4. The rest of the bars summarize the results for as-cast SqP P3HT/PCBM active layers prepared under the same conditions with 10 mg/mL PCBM spun on top of the P3HT underlayer. The total organic layer thickness measured by profilometry is ~180 nm for all samples. The metal penetration depths are obtained by subtracting the C_g thicknesses from the actual thicknesses. 165

Figure 5.8 (a): CELIV transients for as-cast SqP ITO/P3HT/PCBM/Ca/Al diode at different temperatures. The device area is small enough (~4 mm^2) to ensure the transient is not RC time constant limited and that the mobility calculated is meaningful. (b): Calculated mobility of the dark carriers versus temperature. E_A is the activation energy obtained from fitting. The inset shows the sheet charge density versus temperature for the same device..... 167

Figure 5.9 The equivalent circuit for modeling depleted (no doping) CELIV curves. The current for this circuit/voltage-ramp combination are given by Eqns. (2-4)..... 171

Figure 5.10 The effect of annealing on the measured CELIV transients of SqP P3HT/PCBM devices, compared with a BC device. Annealing at higher temperature causes more PCBM to

mix into the P3HT underlayer, leading to less apparent doping upon metal cathode evaporation. 172

Figure 5.11 CELIV transients for as-cast SqP P3HT/PCBM and as-cast SqP P3HT/ICBA devices with different metal electrodes. The devices with ICBA show much less dark carriers. The SqP P3HT/ICBA/Ag result (Table 5.1) is not shown here due to the high leakage current. 172

Figure 5.12 The effect of metal penetration on device dark *J-V* characteristics..... 173

Figure 5.13 CELIV transients for as-cast P3HT/PCBM SqP devices with different metal electrodes. 174

LIST OF TABLES

Chapter 1

Table 1.1 A comparison on different renewable energy technologies. GWP stands for global warming potential. Adapted from Krebs, F. C. *et al*.[5] 3

Chapter 2

Table 2.1 Characteristics of P3HT used in this work. 20

Table 2.2 Summary of Device Parameters 29

Table 2.3 Summary of Parameters from GIWAXS 39

Table 2.4 Characteristics of P3HT used in this work[a] 44

Table 2.5 Solar cell parameters summary for the devices in Figure 2.11 and 2.12 54

Table 2.6 Solar Cell Parameters Summary for the Devices in Figure 2.15 56

Chapter 3

Table 3.1 Summary of Photovoltaic Device Parameters 86

Chapter 4

Table 4.1 Summary of measured contact angles and the calculated surface energies 123
Table 4.2 Summary of photovoltaic device parameters[a] 126

Chapter 5
Table 5.1 Measured Sheet Charge Densities for Various Organic Semiconductor Diodes……..147

ACKNOLEDGEMENTS

There are so many people who helped me finish the journey of pursuing my PhD. I could not obtain my degree without their assistance, support and comfort:

First and foremost I would like to express my sincere gratitude to my PhD advisor, Professor Benjamin J. Schwartz who accepted me as an undergraduate research assistant in 2008 and a graduate student in 2009. He helped me throughout the years of my Ph.D. study in the United States, which was an unfamiliar continent to me at the beginning, and supported me with his brilliant ideas for my research and of course his guidance as an advisor. I could not express all my gratitude for his continuous advice on my research directions, my presentation skills, and my career path and so on. He has taught me to be a model scientist with a style that combines both carefulness and creativity.

I would like to thank Professor Sarah Tolbert for her help with my research. I have learned numerous knowledge from the joint solar cell group meetings in which Professor Tolbert is a co-PI. A significant amount of my work is through the collaboration with her and her group. I have learned so many useful skills and gained insightful ideas from my conversations with her as well as the paper writing process.

I thank Dr. Alexander Ayzner and Dr. Bertrand Tremolet de Villers for their guidance on my undergrad research and my early PhD work. They taught me how to make organic solar cells in a research lab and provided me with ideas and detailed instructions for my early work.

Steven Hawks and Jordan Aguirre are the closest lab mates I had. A huge amount of my work was through collaborations with them. We spent hours working alongside with each other in the lab. We talked about research and life all the time throughout these years. They are both

talented and hard-working researchers with an appreciation for science. They are both coworkers and friends to me.

Matthew Fontana spent more than three years with me in the same office. He helped me many times with different types of lab work in his first year when he joint Schwartz group. I appreciated the everyday conversation with him on both research and life as a friend.

Tyler Scholes and Benjamin Finck are my labmates who also gave me help on some of the projects I have been working with. I thank them for their conversations and/or help with lab work.

Professor Yves Rubin and his group, especially Dr. Shaohua Huang, provided me with beautiful fullerene derivatives. A significant part of my research is based on either studying the performance of these molecules in solar cells or using them to investigate interesting solar cell physics. I thank them for their excellent synthesizing skills.

Professor Christine Luscombe and her group are collaborators from University of Washington. My first first-author paper was published through the collaboration with her group. I am grateful to her and her group members who provided me with the polymers that had great properties.

Professor Samson Jenekhe and Dr. Selvam Subramaniyan are also collaborators from University of Washington. I thank them for synthesizing novel conjugated polymers for our group.

Professor Daniel Neuhauser and Dr. Chris Arntsen are collaborators who helped me with theoretical calculations done on some fullerene derivative molecules I studied.

I thank my wife Yang Cao for her continuous support and love. We landed on this continent together to pursue knowledge and start a new life as a family. We have accompanied each other

throughout these years ever since the first quantum mechanics class. She is my best friend, partner and my source of energy.

I thank all Schwartz group members, both previous and current, for the wonderful research environment they created.

Last but not least, I would like to thank my committee and UCLA chemistry department.

Chapter 2 is published work reprinted with permission from a version of Zhang, G.; Huber, R. A.; Ferreira, A. S.; Boyd, S. D.; Luscombe, C. K.; Tolbert, S. H. and Schwartz, B. J. *The Journal of Physical Chemistry C*; **2014**, *118*, 18424-18435.

Chapter 3 represents work that is soon to be published.

Chapter 4 represents work that is in preparation for publication.

Chapter 5 represents work that is in preparation for publication.

VITA

2008-2009	Research Fellow
	Cross-disciplinary Scholars in Science and Technology program
	University of California, Los Angeles
	Los Angeles, California
2009	B. S. Chemistry
	University of Science and Technology of China
	Hefei, China
2009-present	Graduate Student
	Department of Chemistry and Biochemistry
	University of California, Los Angeles
	Los Angeles, California
2010-2012	Laboratory Safety Manager, Benjamin J. Schwartz Research Group
2009-2014	Teaching Assistant
	Department of Chemistry and Biochemistry
	University of California, Los Angeles
	Los Angeles, California

PUBLICATIONS AND PRESENTATIONS

Zhang, G.; Huber, R. C.; Ferreira, A. S.; Boyd, S. D.; Luscombe, C. K.; Tolbert, S. H.; Schwartz, B. J. Crystallinity Effects in Sequentially Processed and Blend-Cast Bulk-Heterojunction Polymer/Fullerene Photovoltaics. *J. Phys. Chem. C* **2014**, *118*, 18424–18435.

Hawks, S. A.; Aguirre, J. C.; Schelhas, L. T.; Thompson, R. J.; Huber, R. C.; Ferreira, A. S.; Zhang, G.; Herzing, A. A.; Tolbert, S. H.; Schwartz, B. J. Comparing Matched Polymer:Fullerene Solar Cells Made by Solution-Sequential Processing and Traditional Blend Casting: Nanoscale Structure and Device Performance. *J. Phys. Chem. C* **2014**, *118*, 17413–17425.

Zhang, G.; Huang, S.; Fontana, M. T.; Knutson, N.; Hawks, S. A.; Huber, R. C.; Ferreira, A. S.; Yee, P.; Tolbert, S. H.; Schwartz, B. J. and Rubin, Y. F. High Performance Organic Solar Cells with New 1,4-Bis-Benzyl Fullerene Derivatives: Vertical Phase Segregation and Surface Recombination. Excited State Processes in Electronic and Bio Nanomaterials, Santa Fe, NM. **2014**. Poster Presentation.

Zhang, G.; Luscombe, C. K. and Schwartz, B. J. Impact of Poly(3-hexylthiophene) Regioregularity and Monodispersity on the Performance of Organic Photovoltaic Devices. 243rd ACS National Meeting, San Diego, CA. **2012**. Poster Presentation.

Chapter 1 Introduction

1.1 Need for Solar Energy

According to the Office of Science, U.S. Department of Energy,[1] world energy consumption will double in 30 – 40 years and triple by the end of the century. However, as shown in Figure 1.1, even in the year 2013, the dominant world energy sources are still oil, coal and natural gas.[2] These traditional energy sources are non-sustainable and environmental unfriendly in terms of the carbon cycle. It has been predicted that the incremental improvements in existing energy networks cannot supply the world energy demand in a sustainable way.[1] Therefore, there is a strong demand for the development of renewable energy technologies.

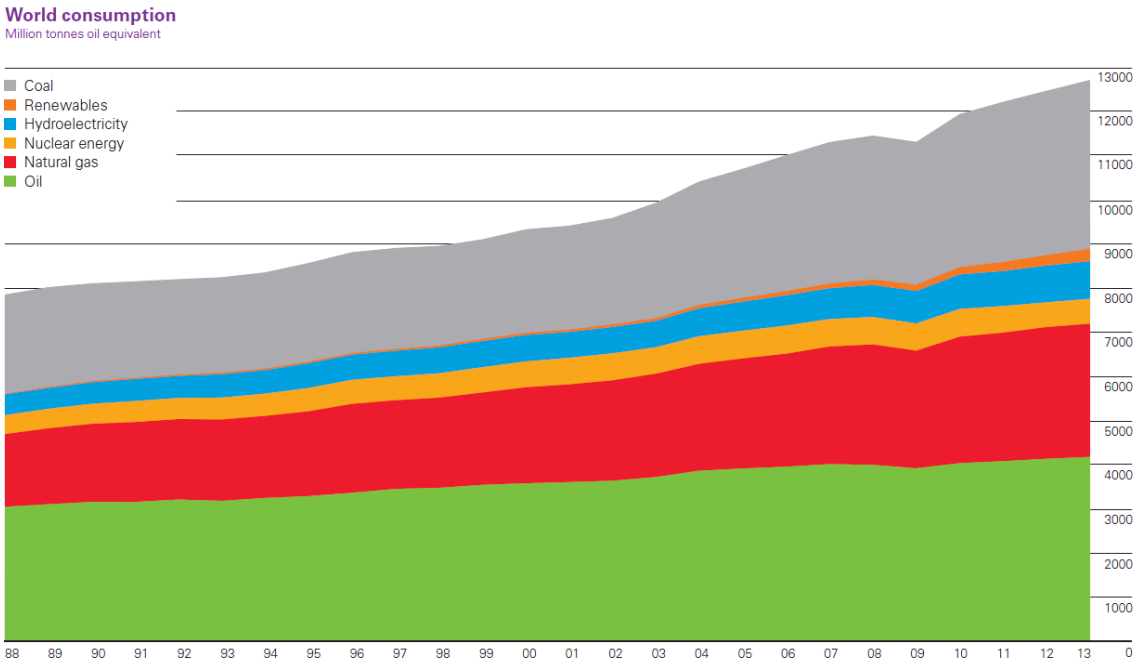

Figure 1.1 World energy consumption between 1988 – 2013. The unit for the consumption is million tons oil equivalent. Adapted from Ref. 1.

Solar energy is the largest carbon-neutral energy source up to date.[1] The energy from the sun that strikes the Earth in an hour is comparable to the total energy consumption worldwide in a year.[1] Based on calculations, a coverage area of just ~161 km^2 by flat-plate solar cells with

efficiency of 10% would be provide enough energy to supply the annual energy consumption in United States.[3]

The most mature photovoltaic technology nowadays is based on crystalline semiconductors such as Si and GaAs. Although these inorganic photovoltaics (PVs) provide decent solar cell efficiencies, their high cost processing has made them less economically competitive than other alternative energy technologies.[4]

To evaluate the efficacy of a given technology, one can analyze the energy pay-back time (EPBT),[4] which describes how quickly the technology gains back the energy invested in its making. EPBT takes account of factors such as the cost at which certain energy conversion efficiency is reached, the time required for the fabrication of the devices or facilities and the energy and materials consumed during the fabrication process. Therefore, EPBT is a useful measure to compare technologies that have different forms in terms of producing renewable energies. It has been reported by Espinosa *et al.*[4] that among various renewable energy technologies, organic photovoltaics (OPVs), even at laboratory scales, demonstrate an EPBT that beats all other PV technologies (Table 1.1). The EPBT for OPVs can be as low as 0.2 years,[4] which vastly outperforms technologies involving other energy sources such as biomass combustion.

Table 1.1 A comparison on different renewable energy technologies. GWP stands for global warming potential. Adapted from Krebs, F. C. *et al.*[5]

Energy source/Technology	Location	EPBT [years]	Embedded energy [MJ per kW h_{el}]	GWP [kg CO_2 per kW h_{el}]
Wind	Global average	0.39	0.066	0.027
PV technologies				
Mono and poly Si	US-Global average	1.65–4.14	11.9	0.032–0.36
Amorphous Si	US-Global average	1.13	2.55	0.011–0.226
CdTe	European average	0.73–1.61	9.22	0.025
OPV[a)]	Denmark/Europe	0.2–4	44.50	0.01–0.06
Hydropower	Germany-Canada	0.5	0.14	0.013–0.04
Geothermal	Germany	0.54	0.54	0.041
Biomass	China	5–10	–	0.045
Natural gas	Australia	–	12.91	0.751

[a)] Note that these LCA values are given for the production of the modules and not for the whole installatation, which is the object of this study.

The most important reason for the extremely short EPBT for OPVs that the OPV cells can be fabricated using the roll-to-roll printing technology.[6] This fast and cheap way to make OPV devices enables the potential for large-area fabrication of OPVs. Indeed, Krebs *et al.* have demonstrated a solar park based on OPVs with a scale of 100 m using roll-to-roll printing.[5] Among different PV technologies, only OPVs can be roll-to-roll printed because the key components of OPVs are based on flexible organic materials. This also offers OPVs the advantage of being light weight.

To date, the most successful OPVs are based on conjugated polymers and functionalized fullerenes.[7] The power conversion efficiency for solar cells based on these materials has kept increasing over the past decade, with the most recent reported efficiencies as high as 10.8%.[7] To understand what determines the solar cell performance, we need to understand how OPVs work.

1.2 Working Principles of OPVs

Figure 1.2 shows the general OPV device structure and the light-to-current conversion steps.

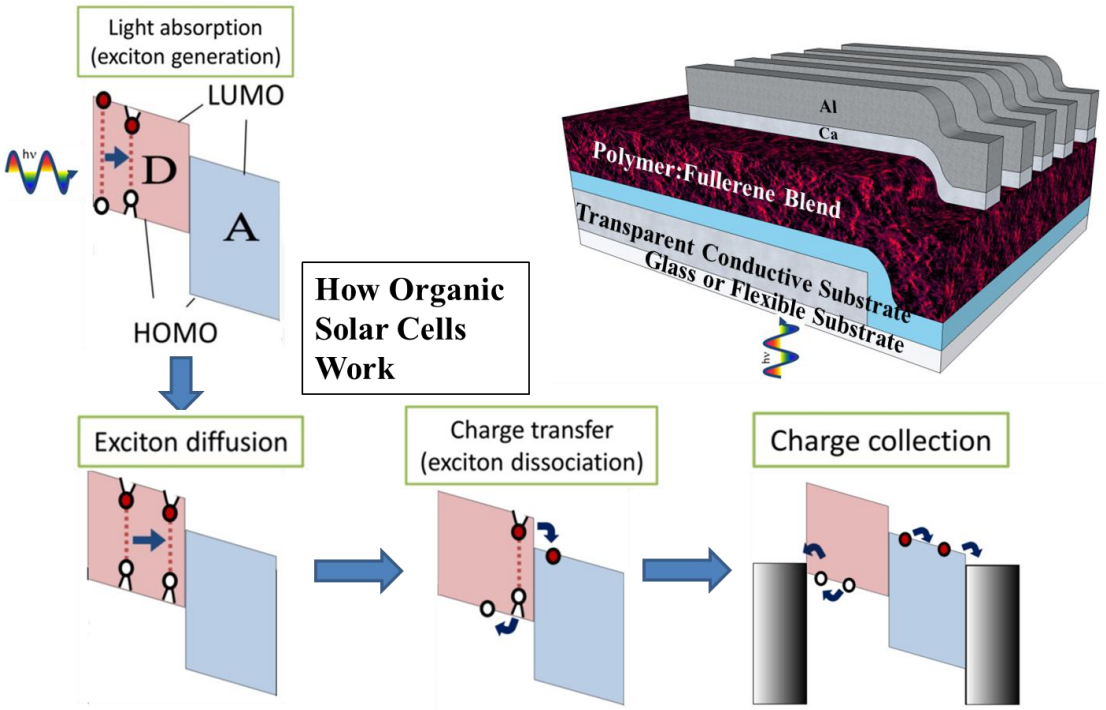

Figure 1.2 An typical structure for polymer:fullerene based solar cells (Top right) and a scheme illustrating the four-step light-to-current conversion process.

A typical OPV device usually consists of a "sandwich" structure where the polymer:fullerene active layer is placed between the top and bottom electrodes. To improve the device performance, an electron-transporting layer is often applied between the active layer and the cathode; similarly, a hole-transporting layer is applied between the active layer and the anode.

Conjugated polymer semiconductors are widely employed as the main electron donors in OPVs due to their excellent light absorbing ability; they have extremely high absorption coefficients (~10^4 – 10^5 cm^{-1}).[8] The chemical structures of a few widely used conjugated polymers are shown in Figure 1.3.

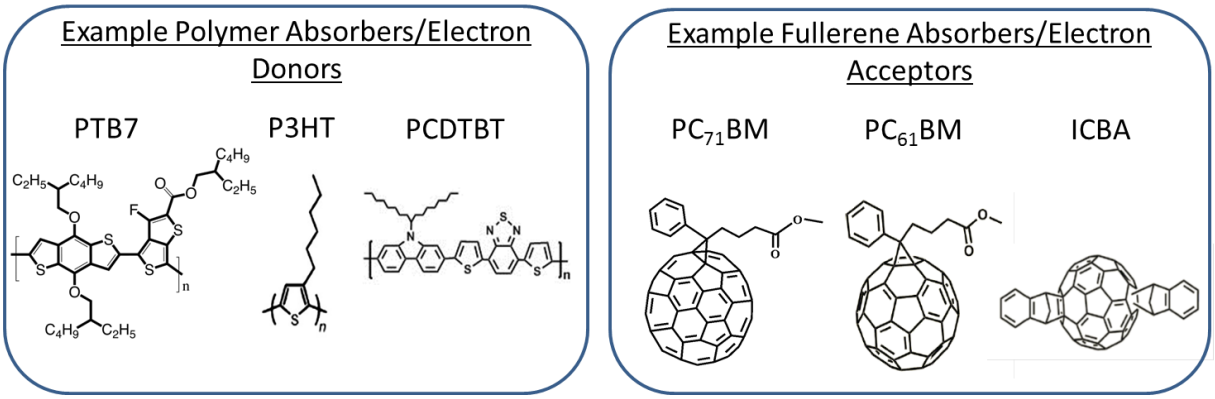

Figure 1.3 Chemical structures of three widely used conjugated polymers (left) and fullerene derivatives (right) in OPVs.

Upon light absorption by the polymer, electrons can be excited from the polymer's highest occupied molecular orbital (HOMO) to its lowest unoccupied molecular orbital (LUMO). This leaves a positively charged hole in the HOMO of the polymer. The electronic structure of the polymer works to minimize the energy of this excitation by distorting the backbone, changing the bonding scheme so as to localize the excitation.[9] The result of the polymer's tendency to localize the excitation is the formation of the "exciton", which is a Coulombically-bound electron-hole pair. All of this comprises the light absorption step shown in Figure 1.2.

The photogenerated exciton can diffuse between nearby polymer chains through Förster resonant energy transfer.[11] An exciton on the polymer has a finite lifetime, typically on the order of a few hundred picoseconds,[12] before the electron recombines with the hole. This lifetime corresponds to a diffusion length for the exciton of ~10 nm.[12] If the exciton, within its lifetime, reaches the interface formed between the polymer and fullerene, the electron can be transferred from the polymer LUMO to the lower fullerene LUMO. The minimum energy difference between the LUMO levels required for efficient exciton splitting is still under debate,[13,14] but the generally accepted value is ~0.3 – 1 eV.[15–17] Once the electron is transferred to the LUMO of the

fullerene, a free hole is left behind in the polymer HOMO. Thus, the exciton splits into an electron in the fullerene phase and a hole in the polymer phase; these charges, with their accompanying distortion of the molecules on which they reside are called polarons. It is worth mentioning that although the polymer contributes to most of the light absorption, the fullerene derivative also can absorb photons (usually in lower wavelength regions than polymers), which also can generate polarons via an uphill hole transfer from the fullerene HOMO to the polymer HOMO at the polymer/fullerene interface. These are the exciton diffusion and charge transfer steps in Figure 1.2. Three typical OPV fullerene derivative structures are given in Figure 1.3.

The final step in the operation of an excitonic solar cell is charge collection. The positively charged polarons (*p*-polarons) in the polymer phase and the negatively charged polarons (*n*-polarons) in the fullerene phase also have finite lifetime. The lifetime for a *p*-polaron, for example, is typically around a few hundred nanoseconds. Since polarons are charged species, they are affected by electric fields. The maximum distance a polaron can travel depends on the average polaron lifetime, the material's polaron mobility and the total electric field. A maximum distance of ~300 nm is typical for a *p*-polaron in the conjugated polymer P3HT.[18]

Through light absorption, exciton diffusion, exciton dissociation and charge collection, the initially-harvested photons are converted to electrical current. One of the most important parameters during this process that places strict requirements on the structure of the polymer:fullerene active layer is the ~10-nm exciton diffusion length. This diffusion length, along with the requirement that the exciton has to find a polymer/fullerene interface to generate free carriers, give rise to the need for an intimate mixing of the two components, or so-called bulk-heterojunciton (BHJ).[19,20] In an ideal BHJ, the polymer and fullerene form a bicontinuous interpenetrating network for efficient exciton harvest as well as charge transport. To achieve a

BHJ structure, it is typical to simply mix the polymer and fullerene together in a solution, spin-coat the solution onto the substrate, and then (as needed to improve device performance) apply various post-treatment methods (e.g. thermal annealing) to the polymer:fullerene film.

Based on the above discussion, to optimize the performance of an OPV device, one needs to focus on two major issues. First, how can one optimize the morphology of the BHJ? Are there other fabrication techniques one can employ to tune the morphology of the BHJ in a more controllable fashion? Second, how can one design new materials with better properties? Are there systematic ways to build molecules with better energy levels and higher mobilities? Intertwined with these two issues is the exact role that each of the materials and their BHJ morphology in the physics underlying solar cell operation. As summarized below and discussed in detail in Chapters 2 – 5, I have been working to help address all of these issues.

1.3 Study the Polymer-Fullerene BHJ Morphology Formed through a Novel Technique: Sequential Processing (SqP)

Although most polymer/fullerene-based solar cells are cast from a blend of the components in solution, it is also possible to sequentially process the polymer and fullerene layers from quasi-orthogonal solvents (Figure 1.4).

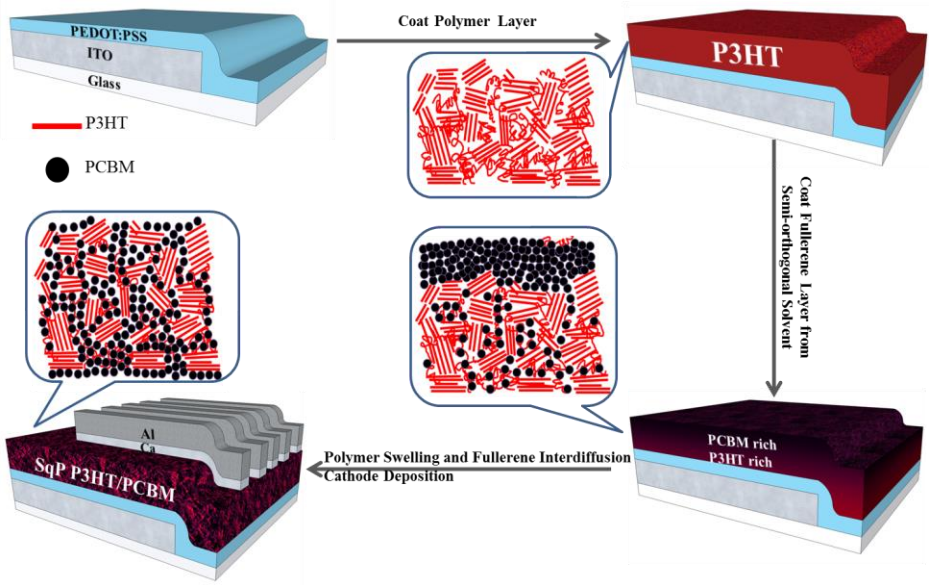

Figure 1.4 The basic steps for fabricating a P3HT:PCBM based SqP device. Instead of simply blending the polymer and fullerene derivative in one solution, we prepare the polymer layer first by spin-coating the polymer solution onto the substrate. Then a solution containing the fullerene derivatives in a quasi-orthogonal solvent is spin-coated onto the polymer underlayer. If needed, the film can be subsequently thermally annealed prior to cathode deposition to complete the device.

Sequential processing (SqP) not only produces photovoltaic devices with efficiencies comparable to the more traditional bulk heterojunction (BHJ) solar cells produced by blend casting (BC), but also offers the advantage that the polymer and fullerene layers can be optimized separately. However, the morphology formed by the polymer and fullerene in a SqP device has not been fully understood, largely because SqP requires the two components to mix during deposition, whereas the traditional BC method requires de-mixing of the polymer and fullerene during casting to form the best BHJ morphology. In Chapter 2, we explore the morphology produced when sequentially processing polymer/fullerene solar cells and compare it

that obtained by BC. We find that increasing the polymer regioregularity leads to opposite effects on the performance of SqP and BC BHJ solar cells. We start by constructing a series of SqP and BC solar cells using different types of poly(3-hexylthiophene) (P3HT) that vary in regioregulary and polysdispersity combined with [6,6]-phenyl-C_{61}-butyric-acid-methyl-ester (PCBM). We use grazing incidence wide-angle X-ray scattering to demonstrate how changes in the P3HT and PCBM crystallinity upon thermal annealing of SqP and BC BHJ films depends strongly on polymer regioregularity. For SqP devices, low regioregularity P3HT films that possess more amorphous regions allow for more PCBM crystallite growth and thus show better photovoltaic device efficiency. On the other hand, highly regioregular P3HT leads to a more favorable morphology and better device efficiency for BC BHJ films. Comparing the photovoltaic performance and structural characterization indicates that the mechanisms controlling morphology in the active layers are fundamentally different for BHJs formed via SqP and BC. Most importantly, we find that nanoscale morphology in both SqP and BC BHJs can be systematically controlled by tuning the amorphous fraction of polymer in the active layer.

1.4 Synthesis Novel Fullerene Derivatives for Efficient OPVs

As mentioned above, designing new materials is one of the most popular and effective routes for increasing solar cell efficiency. Increasing the open-circuit voltage, and thus the efficiency of organic solar cells requires the *n*-type acceptors to have a higher LUMO energy level than the classic fullerene derivative PCBM. To date, most fullerene derivatives synthesized for this purpose either fail to achieve the high photocurrent that PCBM affords or show poor compatibility with the low bandgap conjugated polymers used in high-efficiency organic solar cells. In Chapter 3, we report the facile synthesis of novel 1,4-dibenzyl fullerene bisadducts and their application as electron acceptors in conjugated polymer-based solar cells. Compared to

PCBM, the best fullerene 1,4-bisadducts show a ~20% enhancement in power conversion efficiency when used with the classic semi-crystalline polymer P3HT. When used in combination with a higher-performance low bandgap polymer, PTB7, this same bisadduct both increases the device open-circuit voltage and maintains the high photocurrent provided by PCBM. We examine 11 new 1,4-fullerene bisadducts and show that the photovoltaic device performance is very strongly influenced by both the number and position of the substituent groups on the benzyl rings connected to the fullerene: in fact, moving a single methoxy substituent by one position on the benzyl rings can change the device efficiency by a factor of 2.

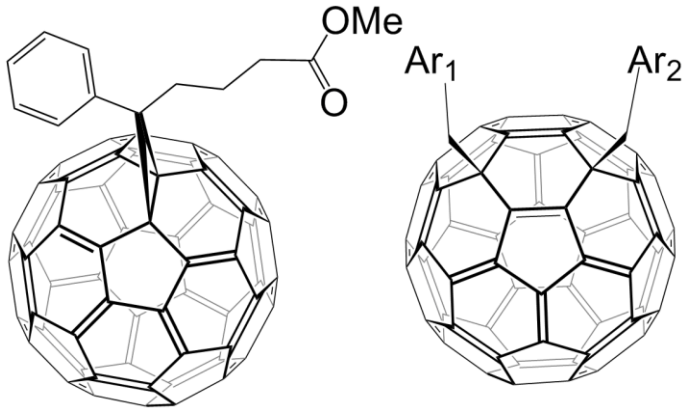

Figure 1.5 Chemical structure of the 1,2-fullerene bisadduct (PCBM) on the left and the 1,4-fullerene bisadduct used in Chapter 3 on the right.

1.5 Using 1,4-fullerene Bisadducts to Study the Vertical Phase Segregation in BHJ Solar Cells

Although the power conversion efficiency of polymer:fullerene BHJ solar cells has kept increasing in recent years, there is still much to be understood concerning the device operating principles. In addition to the phase separation between the polymer and fullerene in the bulk of the active layer, vertical phase segregation (VPS), the distribution of the polymer and fullerene

molecular composition in the vertical direction of the photovoltaic device, also can strongly affect device efficiency. It is generally difficult to separate the effects of VPS from a generally poor bulk morphology, which explains why there are few systematic studies of how VPS affect solar cell device physics. In Chapter 4, we employ two novel 1,4-dibenzyl [60] fullerene bisadducts synthesized by our group and used them as the acceptors in BHJ solar cells in combination with two different donor polymers, P3HT and PTB7. With different combinations of the two fullerene bisadducts, PCBM, and the two polymers, we have five different polymer:fullerene combinations to explore in BHJ photovoltaic devices. The fullerene bisadducts have significantly different surface energies compared to PCBM. This leads to an opposite VPS in active layers made with P3HT:bisadduct compared to P3HT:PCBM. More importantly, photocurrent spectral response measurements and diode ideality factor analysis indicates that the two fullerene bisadducts have a large variation in their bulk recombination properties. Using grazing incidence wide angle X-ray scattering (GIWAXS), we can determine that the recombination differences are caused by their different active layer morphologies. In particular, one of these two bisadducts showed bulk recombination that is similar to PCBM, while the other bisadduct is markedly different. This allows us to extract the effects of VPS by comparing with two systems that have the same bulk properties. We then performed a series of device physics studies, including transient photovoltage (TPV), transient photocurrent (TPC), and charge extraction by linear increasing voltage (CELIV), and found that different VPSs with different fullerenes cause large variations in surface recombination in the device. This in turn has a dramatic effect on both carrier lifetime and carrier density. Taken together, the results allow us to use surface energy analysis to select the best device structure for a given polymer:fullerene pair.

1.6 Apparent Fullerene Layer Doping Caused by Evaporation of Metal Electrodes

One of the consequences of the vertical phase segregation we observed during the fabrication of SqP solar cells is the apparent doping of the fullerene layer caused by the evaporation of metal electrodes. In particularly, we were able to extract dark carriers from as-cast P3HT:PCBM SqP devices using the charge extraction by linear increasing voltage (CELIV) technique. We then performed the same experiment on different polymer (or non-polymer)/fullerene systems and found a correlation between the thickness of the PCBM layer and the amount of doping. Through careful analysis of the devices' geometric capacitance, we found surprisingly that metal atoms (and in most cases, metal clusters) penetrate through the fullerenes on the top of the active layer, and that the amount of this metal penetration was directly related to the amount of doping. We are able to actually see the metal interpenetration using cross sectional transmission electron microscopy, a phenomenon that has been overlooked in two decades of OPV research and which has important implications for device performance.

1.7 References

(1) U.S. Department of Energy. *Report on Basic Research Needs for Solar Energy Utilization*; 2005.

(2) BP. *BP Statistical Review of World Energy June 2014 About This Review*; 2014; p. bp.com/statisticalreview.

(3) Turner, J. A. A Realizable Renewable Energy Future. *Science (80-.).* **1999**, *285*, 687–689.

(4) Espinosa, N.; Hösel, M.; Angmo, D.; Krebs, F. C. Solar Cells with One-Day Energy Payback for the Factories of the Future. *Energy Environ. Sci.* **2012**, *5*, 5117–5132.

(5) Krebs, F. C.; Espinosa, N.; Hösel, M.; Søndergaard, R. R.; Jørgensen, M. 25th Anniversary Article: Rise to Power - OPV-Based Solar Parks. *Adv. Mater.* **2014**, *26*, 29–39.

(6) Søndergaard, R. R.; Hösel, M.; Krebs, F. C. Roll-to-Roll Fabrication of Large Area Functional Organic Materials. *J. Polym. Sci. Part B Polym. Phys.* **2013**, *51*, 16–34.

(7) Liu, Y.; Zhao, J.; Li, Z.; Mu, C.; Ma, W.; Hu, H.; Jiang, K.; Lin, H.; Ade, H.; Yan, H. Aggregation and Morphology Control Enables Multiple Cases of High-Efficiency Polymer Solar Cells. *Nat. Commun.* **2014**, *5*, 5293.

(8) Günes, S.; Neugebauer, H.; Sariciftci, N. S. Conjugated Polymer-Based Organic Solar Cells. *Chem. Rev.* **2007**, *107*, 1324–1338.

(9) Friend, R. H.; Bradley, D. D. C.; Townsend, P. D. Photo-Excitation in Conjugated Polymers. *J. Phys. D. Appl. Phys.* **1987**, *20*, 1367–1384.

(10) Shen, Y.; Gupta, M. Investigation of Electrical Characteristics of P3HT: PCBM Organic Solar Cells. In *Photovoltaic Specialists Conference (PVSC), 2012 38th IEEE*; 2012; pp. 2770–2774.

(11) Barford, W. *Electronic and Optical Properties of Conjugated Polymers*; 2005.

(12) Piris, J.; Dykstra, T. E.; Bakulin, A. A.; Loosdrecht, P. H. M. Van; Knulst, W.; Trinh, M. T.; Schins, J. M.; Siebbeles, L. D. A. Photogeneration and Ultrafast Dynamics of Excitons and Charges in P3HT/PCBM Blends. *J. Phys. Chem. C* **2009**, *113*, 14500–14506.

(13) Bakulin, A. A.; Rao, A.; Pavelyev, V. G.; van Loosdrecht, P. H. M.; Pshenichnikov, M. S.; Niedzialek, D.; Cornil, J.; Beljonne, D.; Friend, R. H. The Role of Driving Energy and Delocalized States for Charge Separation in Organic Semiconductors. *Science* **2012**, *335*, 1340–1344.

(14) Shoaee, S.; Subramaniyan, S.; Xin, H.; Keiderling, C.; Tuladhar, P. S.; Jamieson, F.; Jenekhe, S. A.; Durrant, J. R. Charge Photogeneration for a Series of Thiazolo-Thiazole Donor Polymers Blended with the Fullerene Electron Acceptors PCBM and ICBA. *Adv. Funct. Mater.* **2013**, *23*, 3286–3298.

(15) Faist, M. A.; Shoaee, S.; Tuladhar, S.; Dibb, G. F. A.; Foster, S.; Gong, W.; Kirchartz, T.; Bradley, D. D. C.; Durrant, J. R.; Nelson, J. Understanding the Reduced Efficiencies of Organic Solar Cells Employing Fullerene Multiadducts as Acceptors. *Adv. Energy Mater.* **2013**, *3*, 744–752.

(16) Brabec, C. J.; Winder, C.; Sariciftci, N. S.; Hummelen, J. C.; Dhanabalan, A.; van Hal, P. A.; Janssen, R. A. J. A Low-Bandgap Semiconducting Polymer for Photovoltaic Devices and Infrared Emitting Diodes. *Adv. Funct. Mater.* **2002**, *12*, 709–712.

(17) Li, W.; Roelofs, W. S. C.; Wienk, M. M.; Janssen, R. A. J. Enhancing the Photocurrent in Diketopyrrolopyrrole-Based Polymer Solar Cells via Energy Level Control. *J. Am. Chem. Soc.* **2012**, *134*, 13787–13795.

(18) Schilinsky, P.; Waldauf, C.; Hauch, J.; Brabec, C. J. Simulation of Light Intensity Dependent Current Characteristics of Polymer Solar Cells. *J. Appl. Phys.* **2004**, *95*, 2816.

(19) Yu, G.; Gao, J.; Hummelen, J. C.; Wudl, F.; Heeger, A. J. Polymer Photovoltaic Cells: Enhanced Efficiencies via a Network of Internal Donor-Acceptor Heterojunctions. *Science (80-.).* **1995**, *270*, 1789–1791.

(20) Heeger, A. J. 25th Anniversary Article: Bulk Heterojunction Solar Cells: Understanding the Mechanism of Operation. *Adv. Mater.* **2014**, *26*, 10–27.

Chapter 2 Crystallinity Effects in Sequentially-processed and Blend-cast Bulk-heterojunction Polymer/Fullerene Photovoltaics

2.1 Background

In recent years, dramatic progress has been made in the field of organic photovoltaics (OPVs),[1,2] resulting in power conversion efficiencies (PCEs) of polymer/fullerene devices surpassing 10%.[3–6] This achievement is based mostly on traditional blend-cast (BC) bulk heterojunctions (BHJs),[7] in which an electron-donating polymer and electron-accepting fullerene are mixed together in a solution that is used to cast the active layer of the organic solar cell. The resulting film is then typically thermally or solvent annealed to promote phase separation of the polymer and fullerene, resulting in a conductive network for both electrons and holes as well as intermixed regions where a majority of charge separation occurs.[8–17] The morphology of BC BHJ films is dictated by multiple factors, including the donor/acceptor miscibility, the propensity of one or both materials to crystallize,[16,18–21] the relative solubilities of the two materials in the casting solution, the drying kinetics of the film, the presence of any solvent additives,[22–26] etc. Because the nm-scale morphology depends on so many of the details of how the film is cast, the device performance of BC BHJ solar cells is hypersensitive to the processing kinetics of the active layer.[7] Thus, for any new set of OPV materials, an Edisonian approach involving the fabrication of hundreds of BC devices is needed to find the processing conditions that lead to the optimal morphology and best device performance.

2.2 Introduction

An alternative approach to preparing polymer/fullerene active layers for photovoltaic applications has been to sequentially process the polymer and fullerene components in separate steps by depositing the materials from orthogonal solvents.[27] This sequential processing (SqP) technique has been studied by several groups in both polymer-fullerene[28–36] and small molecule-fullerene systems.[37] It is well established that even though the fullerene is deposited on top of the polymer layer, the resultant film still has a significant amount of fullerene dispersed through the polymer layer,[38] particularly after thermal annealing.[39–41] Not only are the PCEs of devices fabricated via SqP comparable to or better than the more traditional BC devices,[36,37,42–48] but the SqP method also provides several distinct advantages that could make it the preferred route for large-scale fabrication of polymer-based photovoltaics. First, films produced via SqP have a more reproducible morphology because SqP does not rely on kinetic control of the nm-scale structure, resulting in devices that behave more consistently (*cf*. Figure 2.1, below).[27,42,49] Second, since the two materials are deposited separately, one can optimize or otherwise deliberately alter the donor material (e.g., by chemical doping) either before[50–52] or after[53] it has been processed, without unwanted chemistry occurring with the electron-accepting material. Third, sequentially-processed films are guaranteed to have a fullerene network that is connected to the top of the film, avoiding issues with undesirable vertical phase separation that necessitate the use of an inverted device geometry. Finally, many solubility issues can be bypassed since one can separately choose optimal solvents for the donor and acceptor materials.[37,54] Thus, the SqP technique potentially opens the photovoltaic field to a variety of donor and acceptor materials that once were not usable due to compatibility issues between solvents and materials.

Although it is clear that the BHJ morphology of films produced via SqP is generally similar to that of BC films in that the fullerene is dispersed throughout the polymer, a variety of experiments have suggested that the details of the nm-scale distribution of the polymer and fullerene differ between the two processing techniques. For example, ultrafast spectroscopic studies have shown that the dynamics of exciton quenching and polaron production are different in optically-matched sequentially-processed and BC films made from the workhorse materials poly(3-hexylthiophene) (P3HT) and [6,6]-phenyl-C_{61}-butyric-acid-methyl-ester (PCBM).[55] Moreover, nominally matched sequentially-procssed and BC photovoltaic devices show different behaviors upon thermal annealing.[42,48,49,56] Thus, one of the most important issues concerning solar cells fabricated via SqP is precisely how the nm-scale morphology is different from that in BC films, and what factors control the extent and distribution of fullerene interpenetration into the polymer underlayer.

In this paper, we work to build an understanding of the fullerene distribution in P3HT/PCBM BHJ solar cells produced via both SqP and blend-casting. Our approach is to take advantage of a series of P3HTs with a narrow molecular weight distribution and precisely controlled regioregularity that allow us to explore how changing specific attributes of the polymer leads to differences in both the BHJ architecture and in the PV performance of sequentially-procssed and BC devices. It is well known that polymer regioregularity and polydispersity index (PDI) can have dramatic effects on the photovoltaic performance of BC BHJs,[57–63] and here we extend these studies to sequentially-processed devices, focusing in particular on how regioregularity affects the morphology and device performance of thermally annealed P3HT/PCBM active layers. In agreement with previous suggestions, we first find that PCBM deposited by sequential processing preferentially penetrates into the amorphous regions

of the P3HT underlayer, leaving the crystalline regions of the polymer essentially intact.[40,56] We then show that too much polymer crystallinity is actually unfavorable for SqP photovoltaic devices because too little fullerene can penetrate around the crystallites, leading to over-phase separation of the polymer and fullerene. In contrast, BC devices show the opposite behavior: highly regioregular (and thus more crystalline) P3HT provides better efficiencies than BC devices made from lower regioregularity P3HTs. We thus conclude that sequentially-processed and BC BHJ devices require different materials properties to achieve formation of their ideal active layer morphologies.

2.3 Experimental

The key feature underpinning this work is the successful synthesis of P3HT with well-defined regioregularity and extremely narrow PDI.[64] In what is described below, we compare the behavior of three different batches of P3HT: commercial P3HT purchased from Rieke Metal Inc. (BASF Sepiolid^{TM} P100), which we denote as LR P3HT, and two in-house batches synthesized with 98% regioregularity and average molecular weights of about 16 kDa (PDI = 1.18) and 37 kDa (PDI = 1.19), denoted as HR P3HTs, where LR and HR stand for low regioregularity and high regioregularity, respectively. The full characteristics of the three batches we focus on here are summarized in Table 2.1. Additional details about polymer batch information and our in-house batch purification procedures, as well as a high regioregularity 50 kDa in-house-synthesized batch, can be found in the supporting information (SI).

Table 2.1 Characteristics of P3HT used in this work.

	M_n	Regioregularity	PDI	Mobility (SCLC)

	(kDa)			(cm^2 V^{-1} s^{-1})
Low RR (LR) P3HT	~50-60	~94%	~2.20	1.6×10^{-5}
16k High RR (HR) P3HT	15.9	98%	1.18	3.4×10^{-5}
37k High RR (HR) P3HT	36.9	98%	1.19	1.3×10^{-5}

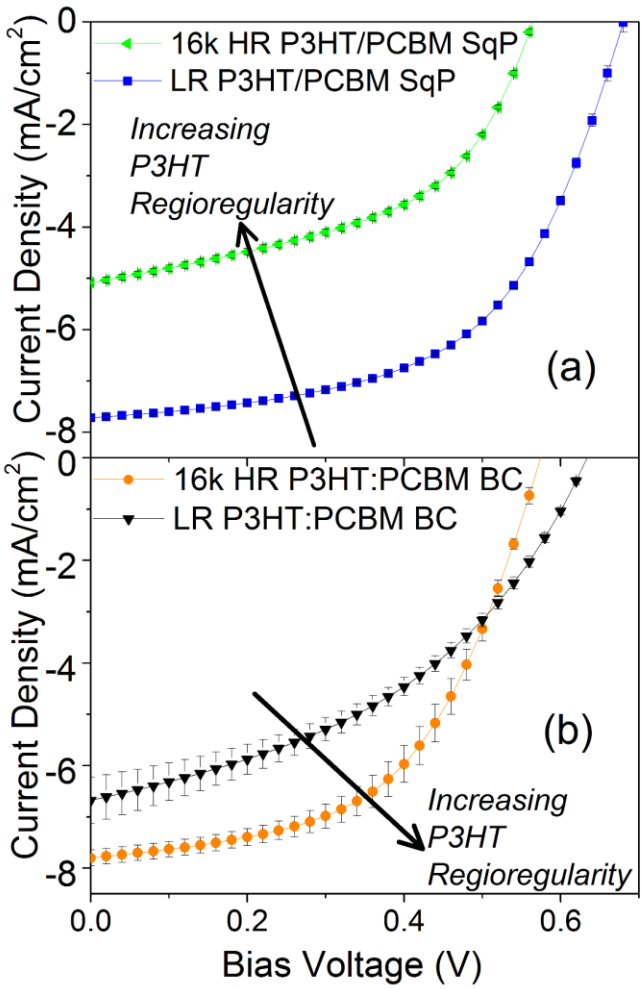

Figure 2.1 Current density versus applied bias for (a) ITO/poly(ethylene-dioxythiophene):poly(styrenesulfonic acid)(PEDOT:PSS)/P3HT/PCBM/Ca/Al sequentially-processed solar cells and (b) ITO/PEDOT:PSS/P3HT:PCBM/Ca/Al BC-BHJ solar cells under AM-1.5 illumination. The SqP active layer was made by spinning 5 mg/mL PCBM solution onto a 110 nm P3HT underlayer (see SI). All of the SqP and BC films were thermally annealed at 150 ℃ for 20 min prior to deposition of the cathode. The error bars show 1 standard deviation in measurements over at least 12 independent devices. Although error bars can be clearly seen in panel (b), they are comparable to or smaller than the symbols used to plot the data in panel (a), indicating that SqP devices are more reproducible than BC devices.

For measurements of the optical properties and for structural characterization of our BHJ films, we prepared a series of sequentially-processed active layers by first spinning a ~110-nm thick layer of P3HT from *o*-dichlorobenzene, and then we subsequently deposited PCBM layers from either 5%, 10% or 15% wt/wt dichloromethane solutions on top by spin-coating, leading to P3HT/PCBM films with a total thickness in the range of 155 to 185 nm. We then prepared BC active layers (~175 nm thick) by spinning a composite P3HT:PCBM (1:0.9 weight ratio) solution from *o*-dichlorobenzene at 1000 rpm for 60 s. Identical active layers were used to fabricate photovoltaic devices with Ca/Al evaporated on top as the cathode.

We note that no slow drying of solvent or solvent vapor treatments were performed on either the sequentially-processed or BC devices, even though such treatments are necessary to optimize the PCE for the P3HT/PCBM materials combination. Instead, we chose our spin-coating parameters to provide us with completely dry films after spinning. We made this choice to eliminate drying kinetics, which can cause marked variations in the performance of BC devices.[42,65] In this way, we were able to maintain our focus on how polymer properties such as regioregularity and molecular weight control variations in morphology and device performance. The detailed procedures of our film and device fabrication and characterization also can be found in the SI.

2.4 Results and discussions

In this section, we begin by discussing the hole mobility of the three polymer batches we investigate in this work (Table 2.1). Although we find that polymer regioregularity and molecular weight do slightly affect hole transport, the differences we observe are subtle, suggesting that BHJ morphology is a much larger factor in determining device performance than the raw hole mobility of the bare polymer. We then use these different polymer batches to

fabricate SqP and BC solar cells, and demonstrate that polymer regioregularity has the opposite effect for the two different processing techniques in terms of photovoltaic device efficiency. This result can be understood through a series of morphological studies, including thin film absorption, fluorescence quenching and grazing incidence X-ray scattering measurements, which allow us to directly explore the structural changes that occur upon thermal annealing and to define the optimal conditions needed to create ideal morphologies for BC and SqP solar cells.

2.4.1 The Device Physics of BC and SqP Solar Cells Made from Different P3HTs

2.4.1.1 Hole Mobility of Different P3HTs:

Many groups have examined how the mobilities of P3HT films are controlled by different polymer properties, such as the regioregularity and/or molecular weight.[58,59,66–70] The generally accepted trend is that increasing regioregularity and increasing molecular weight lead to higher charge carrier mobilities,[68] although most such measurements are made on field-effect transistors (FETs).[71] Since the direction of charge transport for photovoltaic devices is perpendicular to that in FETs, we chose to examine the carrier mobilities in our P3HT batches in sandwich-structure devices so that our measurements would be directly relevant for the performance of these materials in solar cells.

We fabricated diodes from each batch of P3HT using an architecture of ITO/PEDOT:PSS/P3HT/Au to ensure that the majority carriers in the device are holes. We then fit the corresponding dark *J*-*V* curves using the space-charge limited current (SCLC) model, yielding the mobilities listed in Table 2.1 (details of the device fabrication, diode performance and SCLC fitting procedure are given in the SI). The 16k HR P3HT shows the highest hole mobility, a bit over twice that of the LR P3HT, which has a molecular weight of roughly 50 kDa.

Surprisingly, the 37k HR P3HT shows the lowest mobility, even though it has the same regioregularity as the 16k HR batch but a higher molecular weight. These results indicate that P3HT hole mobility has a complex dependence on both regioregularity and molecular weight. We note, however, that the hole mobilities for all three P3HT batches all fall within a factor of 2.6. This suggests that when these different P3HTs are employed in photovoltaic devices, all else being equal, differences in hole mobility are not likely to explain any significant difference in device performance. This allows us to use these batches to understand how differences in regioregularity and molecular weight result in morphology differences that affect solar cell performance, and how these differences depend on the processing route chosen to make the BHJ active layer.

2.4.1.2 Comparing the Performance of SqP and BC Devices with Controlled P3HT Regioregularity and Fullerene Composition:

To determine the effect of polymer regioregularity/crystallinity on the performance of the solar cells with different active-layer processing methods, we constructed working photovoltaic devices with both SqP and BC active layers from both the 16k HR P3HT and LR P3HT batches. Figure 2.1 demonstrates the *J–V* characteristics of the devices under AM 1.5 solar illumination; the data plotted are the average *J–V* curves from at least twelve separate devices, and the error bars (which in some cases are smaller than the symbols used to plot the data) are ±1 standard deviation. The full *J–V* characteristics for all the devices we studied are detailed in Table 2.2. The data show clearly that even though SqP devices require one more spin-coating step than BC devices, SqP devices can be fabricated far more reproducibly. This is because SqP avoids the kinetic sensitivity of the BHJ morphology that is inherent with BC processing.[42]

The most interesting result from Figure 2.1 is the fact that the two P3HT batches show opposite performance trends, depending on the processing method used to make the devices. The SqP solar cells made with LR P3HT show *J*–*V* characteristics similar to those published previously,[27] with average open circuit voltage V_{oc} = 0.68 V, short circuit current J_{sc} = 7.2 mA cm^{-2}, fill factor *FF* = 56% and PCE = 2.9%. The HR P3HT batch, however, makes poorer SqP devices with J_{sc} values of only ~5.1 mA cm^{-2}, and PCE of only ~1.4%. In contrast, the HR P3HT:PCBM BC devices have a significantly higher J_{sc} and ~40% higher PCE compared to the BC devices fabricated with LR P3HT. Thus, the way polymer regioregularity/crystallinity affects device performance is not a simple material property, but instead depends on the route via which the active BHJ layer is processed.

To understand why changing the polymer regioregularity leads to opposite changes in performance for SqP and BC devices, we performed a series of control experiments to verify that the performance changes we observed did not result from changes in the polymer molecular weight or the polymer:fullerene composition of the active layer. Figure 2.2 and Table 2.2 summarize the *J*–*V* characteristics of SqP solar cells made from the 16k HR P3HT (green triangles) and LR P3HT (blue squares), as well as the 37k HR P3HT (violet squares). The in-house synthesized 37k HR P3HT batch has the same high regioregularity and low PDI as the 16k HR P3HT, but a molecular weight closer to that of the commercial LR P3HT. The V_{oc} and *FF* of the 37k HR batch are similar to the 16k HR P3HT, but the overall PCE is higher, mainly due to increased J_{sc}. However, even though increasing the molecular weight improves the device performance, we see that the LR P3HT still shows superior performance for devices fabricated by SqP. Thus, for SqP devices, the overall performance is governed more by the degree of P3HT regioregularity instead of the polymer molecular weight.

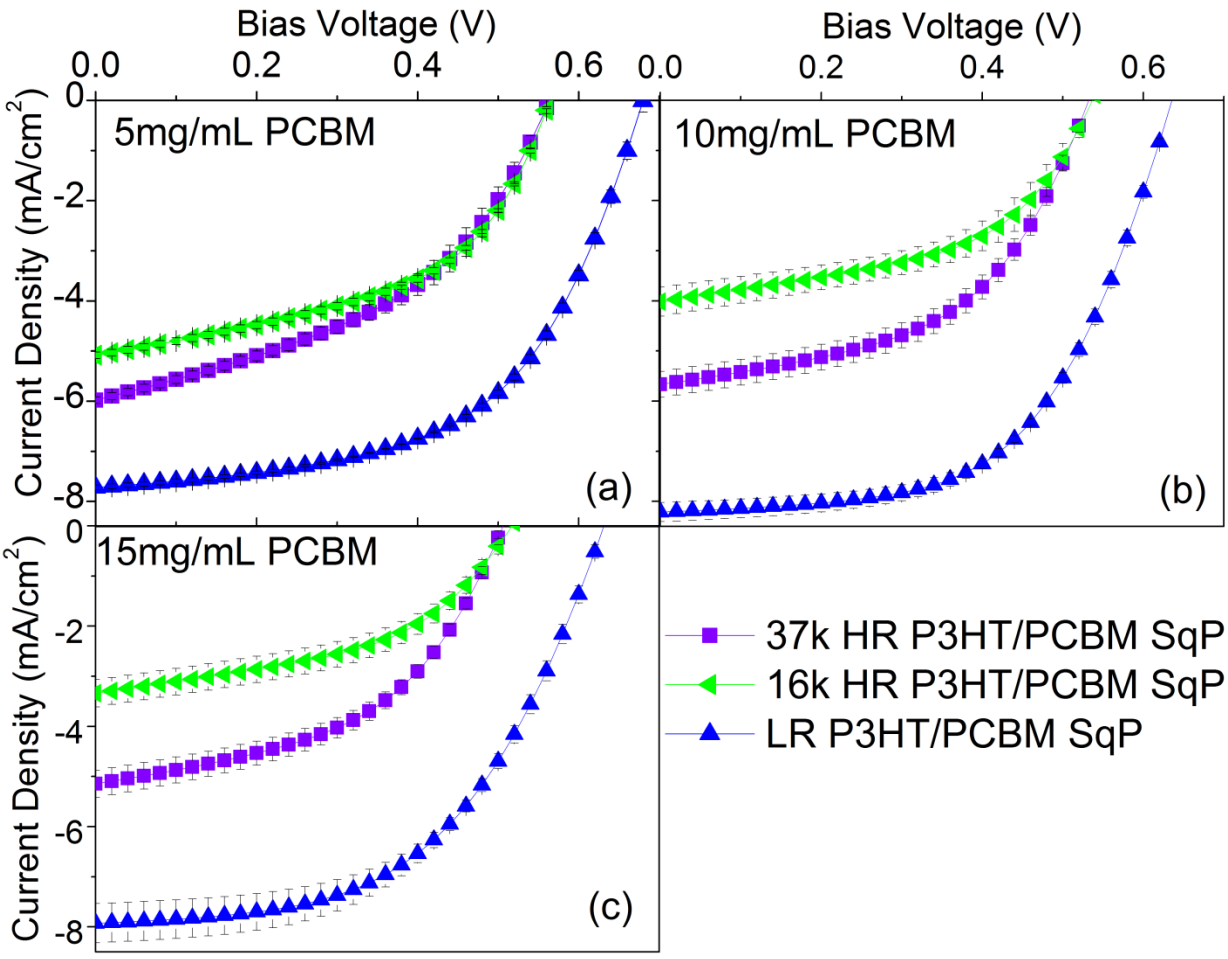

Figure 2.2 Effect of molecular weight, regioregularity and film composition on the *J–V* characteristics of P3HT/PCBM devices made via SqP. LR P3HT (blue up-triangles) and two HR P3HTs with different molecular weights, e.g. 37k Da (violet squares) and 16 kDa (green left triangles) are used as underlayer. All P3HT underlayers were kept at ~110 nm. Three different concentrations of PCBM (5 mg/mL, 10 mg/mL and 15 mg/mL) were spun on top of the P3HT underlayers from DCM and the corresponding *J–V* curves are shown in panels (a), (b) and (c), respectively. The total thicknesses of the active layers are 155 nm, 169 nm and 185 nm with increasing PCBM solution concentratio, respectively. All samples were annealed at 150 °C for

20 min before deposition of the Ca/Al cathode. The error bars show 1 standard deviation for measurements over at least 12 independent devices.

In addition to polymer regioregularity, the performance of OPVs also depends sensitively on the overall polymer:fullerene composition,[43,72] a factor that is directly controlled using the ratio of polymer to fullerene in the casting solution in BC processing. In SqP, by contrast, the composition is indirectly controlled by the relative solution concentrations and spin speeds used to deposit each component of the active layer. Figure 2.2 thus illustrates the change in SqP solar cell performance with different polymer:fullerene compositions. In these experiments, we fixed the thickness of the P3HT underlayer and increased the concentration of the PCBM solution spun on top. We find that with increasing fullerene loading in SqP active layer, the LR P3HT-based devices show only slight variations in J_{sc}, with an optimal polymer/fullerene composition obtained when the PCBM overlayer is spun from a 10 mg/mL solution.[27] In contrast, the performance of the SqP devices based on HR P3HT continually decreases with increased PCBM loading. Thus, not only does increased P3HT regioregularity lead to poorer SqP device performance, the results also imply that the introduction of extra fullerene cannot be accommodated in pre-formed high-RR P3HT underlayers.

We also have performed identical experiments exploring the changes in device performance for different batches of P3HT with different fullerene compositions for BC devices. Since similar studies have been published previously the literature,[72–74] our results are shown in the SI. We find, in agreement with the literature, that increased P3HT regioregularity is beneficial to BC device performance. Surprisingly, however, we find that for BC devices made from the 16k HR P3HT, the optimal P3HT:PCBM weight ratio is 1:1.3, significantly higher than the 1:0.9 optimal ratio typically seen in the literature (with lower regioregular, commercially-available P3HT).

Thus, for the HR-P3HT, the trend in fullerene loading for optimal BC devices also goes in the opposite direction as that for SqP devices.

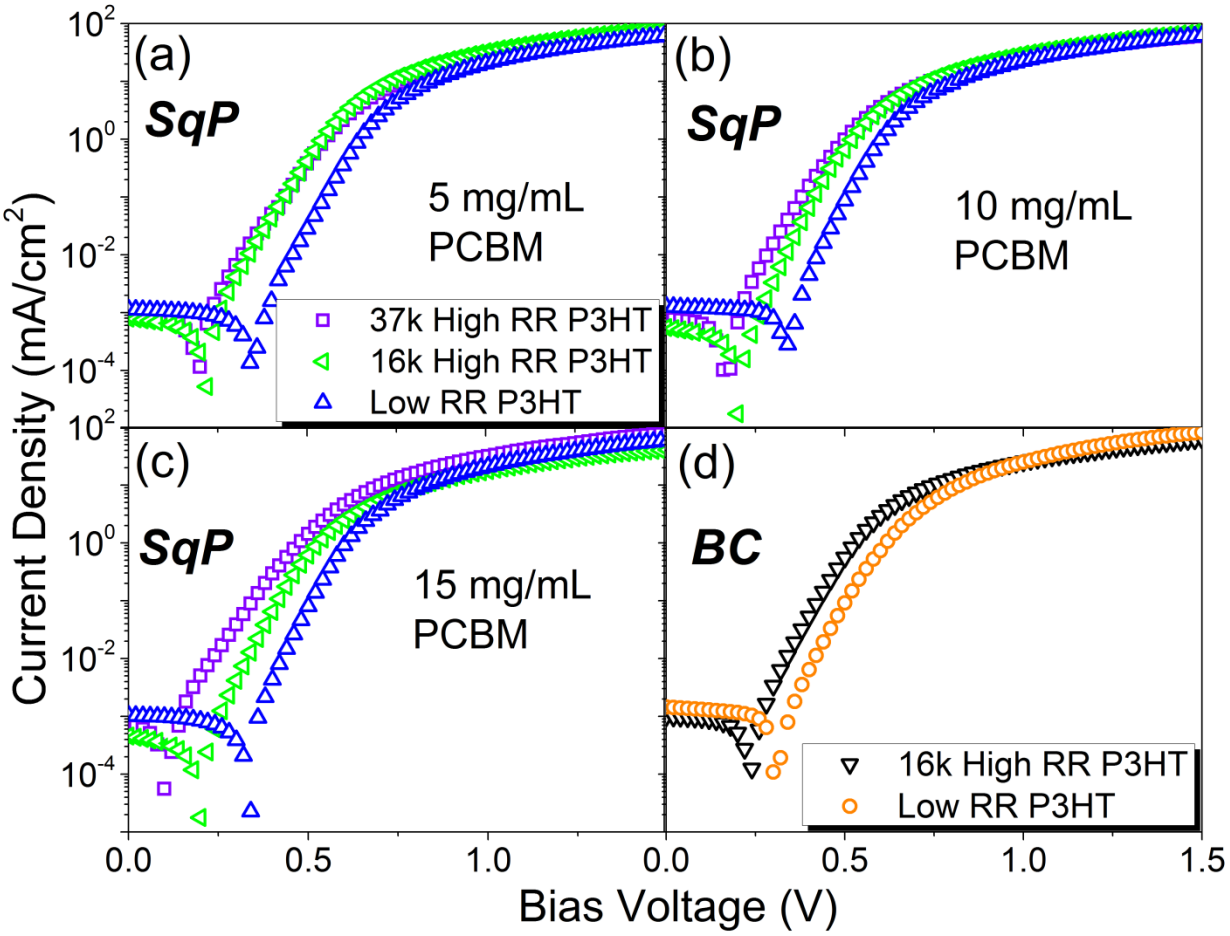

Figure 2.3 Dark *J-V* characteristics of the same SqP devices in Figure 2.2 and the same BC devices in Figure 2.1.

Table 2.2 Summary of Device Parameters

	V_{oc} (V)	J_{sc} (mA/cm^2)	*FF*	*PCE* (%)	n_{ideal} (Dark *J-V*)	R_{seires} (Ω-cm^2)	R_{shunt} (×10^5 Ω-cm^2)
37k HR P3HT/PCBM(5mg/mL) SqP	0.56 ±0.01	5.98 ±0.06	0.44 ±0.02	1.48 ±0.07	1.62 ±0.03	11.2 ±2.2	13.0 ±0.3
16k HR P3HT/PCBM(5mg/mL) SqP	0.56 ±0.01	5.08 ±0.06	0.50 ±0.01	1.43 ±0.02	1.62 ±0.03	8.8 ±0.7	7.8 ±0.0
LR	0.68	7.72	0.56	2.92	1.43	10.6	20.8

P3HT/PCBM(5mg/mL) SqP	±0.01	±0.04	±0.01	±0.02	±0.02	±0.3	±0.4
37k HR P3HT/PCBM(10mg/mL) SqP	0.53 ±0.01	5.67 ±0.26	0.51 ±0.01	1.52 ±0.09	1.88 ±0.03	12.3 ±2.2	12.6 ±0.0
16k HR P3HT/PCBM(10mg/mL) SqP	0.54 ±0.01	4.02 ±0.29	0.50 ±0.03	1.09 ±0.10	1.64 ±0.04	10.7 ±2.1	8.7 ±0.0
LR P3HT/PCBM(10mg/mL) SqP	0.64 ±0.01	8.21 ±0.19	0.57 ±0.01	2.97 ±0.03	1.40 ±0.04	10.9 ±2.1	14.8 ±0.2
37k HR P3HT/PCBM(15mg/mL) SqP	0.51 ±0.01	5.15 ±0.27	0.48 ±0.02	1.26 ±0.12	2.09 ±0.05	9.1 ±1.9	9.5 ±0.0
16k HR P3HT/PCBM(15mg/mL) SqP	0.515 ±0.01	3.34 ±0.27	0.47 ±0.02	0.82 ±0.08	1.64 ±0.05	18.3 ±1.9	10.0 ±0.0
LR P3HT/PCBM(15mg/mL) SqP	0.636 ±0.01	7.93 ±0.39	0.52 ±0.02	2.63 ±0.06	1.43 ±0.05	10.8 ±2.0	82.2 ±21
16k HR P3HT:PCBM BC	0.58 ±0.01	7.80 ±0.15	0.53 ±0.03	2.39 ±0.14	1.51 ±0.02	11.2 ±1.5	22.6 ±0.0
LR P3HT:PCBM BC	0.64 ±0.01	6.68 ±0.45	0.42 ±0.01	1.79 ±0.07	1.65 ±0.07	6.9 ±1.4	7.4 ±0.1

2.4.1.3 The Effects of Polymer Regioregularity on BC and SqP Device Physics:

To begin our exploration of why polymer regioregularity has opposite effects on solar cells fabricated via BC and SqP, we measured the dark *J–V* curves of the SqP and BC solar cells discussed above; the results are summarized in Figure 2.3 and Table 2.2.

Perhaps the most interesting parameter to consider for purposes of this study is the dark ideality factor. Typically the dark ideality factor falls into the range between 1 and 2, although numbers outside this range have been reported mainly due to resistivity effects.[75,76] Within the range of 1 and 2, a larger ideality factor is considered as a strong indication of increased trap-assisted recombination in the device, whereas lower ideality factors are more reflective of bimolecular recombination.[77–79] We derived the ideality factors for our SqP and BC devices in Table 2.2 from the slope of the linear regions in Figure 2.3; we find that the ideality factors mirror the trends in device performance. For SqP devices with a given fullerene concentration, the ideality factors for devices based on LR P3HT are consistently lower than those fabricated with HR P3HTs. For BC devices, the opposite is true: the HR P3HT-based devices exhibit lower

ideality factors than the LR P3HT-based devices. This implies that the polymer/fullerene interfacial trap distribution is quite different for the different BHJ morphologies formed through the two different processing techniques.

Based on the data presented above and the structural data presented below, we offer the following picture for the changes in device physics with polymer regioregularity. Low P3HT regioregularity typically leads to more amorphous regions in BHJ films made from the traditional blend-casting method. Since there are fewer crystalline polymer regions and more structural disorder, there is a greater degree of trap-assisted recombination. In contrast, increasing the polymer regioregularity in SqP devices causes the ideality factor to increase no matter what fullerene loading is used. This suggests that pre-existing P3HT underlayers can support only a certain amount of PCBM, an amount presumably limited by the fraction of the polymer that lies within amorphous regions. Thus, increasing the polymer regioregularity decreases the available space for fullerene intercalation, so that increased regioregularity leads to poorer device performance. If one tries to compensate for this by increasing the fullerene concentration in SqP devices, large-scale phase separation of the fullerene from the highly crystalline polymer network occurs (see SI), leading to an increase in the fraction of structural traps and thus trap-assisted recombination, as seen with the increased ideality factor.

Finally, we note that the devices made with different batches of P3HT also have slightly different V_{oc}'s. The trend that V_{oc} is lower in both SqP and BC devices with HR P3HT correlates with the concomitant red-shift of the absorption spectrum, described further below. This red-shift results from the fact that the highest occupied molecular orbital (HOMO) increases slightly in energy with increasing regioregularity of P3HT because of enhanced delocalization.[80,81] It is also known that increasing the amount of trap-assisted recombination can result in decreased V_{oc},

particularly for devices with carrier mobilities similar to those used here.[82] Since we indeed find that HR P3HT shows more trap-assisted recombination in the SqP devices but less in BC devices, this can help us explain the fact that the V_{oc} decrease observed in BC devices (0.06 V) is smaller than that seen in SqP devices (>0.1 V): the recombination effect goes in the same direction as the HOMO level effect in determining V_{oc} for the SqP devices while the two effects partially compensate in BC devices.

2.4.2 Understanding How P3HT Crystallinity Affects the BHJ Architecture for SqP and BC OPVs:

Now that we have shown that polymer regioregularity causes opposite effects in SqP and BC photovoltaic device performance, we turn in this section to study how regioregularity affects the active layer morphology in both SqP and BC films. To this end, we perform thin-film absorption, fluorescence quenching, and grazing incidence wide-angle X-ray scattering (GIWAXS) to examine differences in the active layer morphologies formed via SqP and BC.

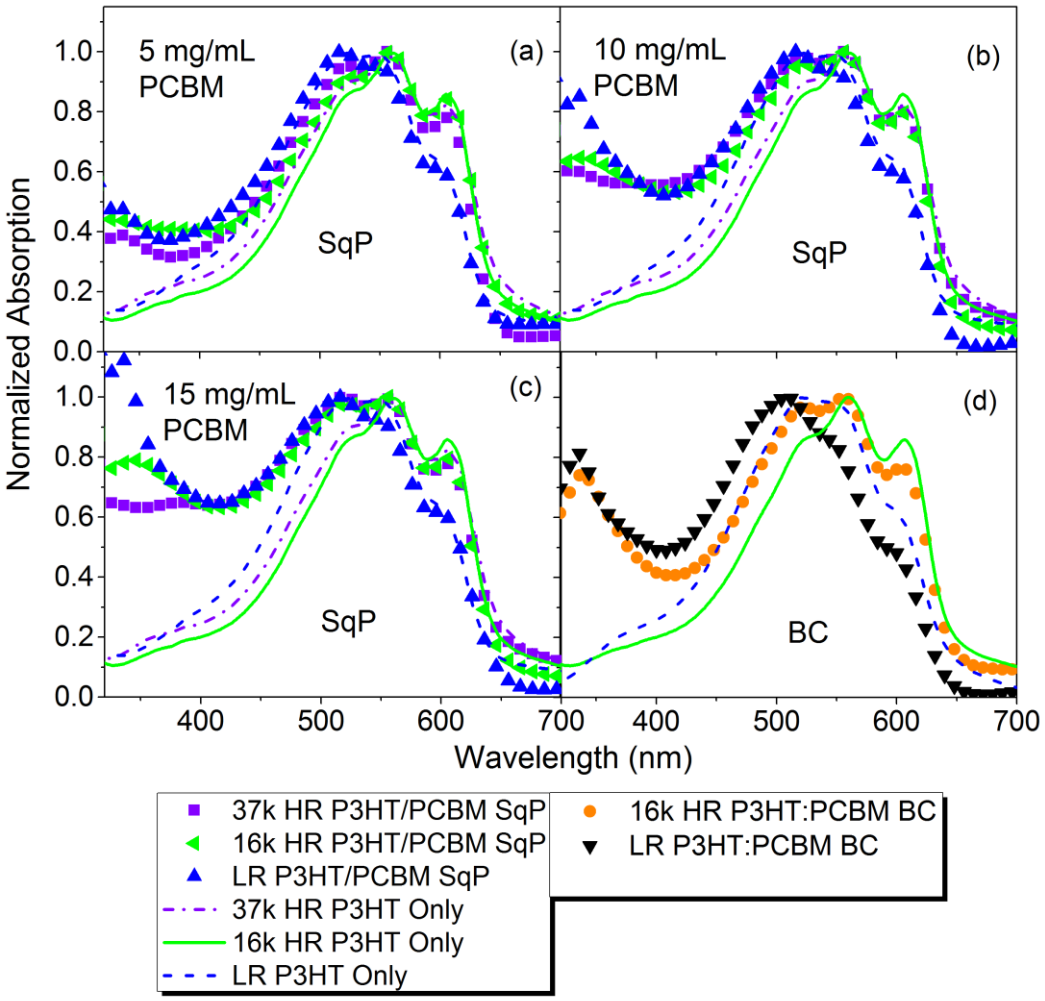

Figure 2.4 UV-visible absorption spectra of thin films made from different batches of pure P3HT (solid dashed and dash-dotted lines) and SqP P3HT/PCBM films (symbols) made from the same P3HTs with (a) 5 mg/mL PCBM, (b) 10 mg/mL PCBM and (c) 15 mg/mL PCBM spun on top; and (d) BC P3HT:PCBM films made from the same P3HTs. The pure P3HT films were 110 nm thick in all cases. All films were thermally annealed at 150 ℃ for 20 minutes and the spectra in both panels are normalized to the highest polymer optical density (i.e. highest OD red of 490 nm) for ease of comparison.

2.4.2.1 UV-Vis and PL of SqP and BC Active Layers with Different P3HT Regioregularities:

Figure 2.4 shows the UV-Visible absorption spectra of pure P3HT films from each of the different polymer batches as well as spectra for all of the SqP and BC active layers discussed above. The spectra of the pure LR P3HT (dashed curve) is shifted to the blue by about 13 nm compared to the HR P3HT (solid and dash-dotted curve), and the relative intensity of the vibronic peaks is also different. Both Spano[83,84] and others[85–87] have shown that the ratio of the intensity of the 0-0 peak ($A_{0\text{-}0}$) to the 0-1 peak ($A_{0\text{-}1}$) is directly related to the intermolecular coupling and thus the crystallinity of P3HT. For our polymer batches, we observe higher $A_{0\text{-}0}/A_{0\text{-}1}$ ratios for the 37k and 16k HR P3HT than for the LR P3HT, indicating higher crystallinity in the HR P3HT films. The slight decrease of $A_{0\text{-}0}/A_{0\text{-}1}$ for the 37k HR P3HT sample compared to the 16k sample indicates the crystallinity of the polymers is slightly affected by their molecular weights. Despite this, the data suggest the polymer regioregularity is the most important factor in determining the film crystallinity.

The symbols in Figure 2.4(a)-(c) show the absorption spectra of the same P3HT films after sequential deposition of a PCBM overlayer and subsequent thermal annealing at 150 ℃ for 20 minutes. We find that for all three P3HT batches, the SqP film absorption is nearly identical to that of the pure polymer, indicating that the fullerene incorporated into the film through sequential processing induces little disruption to the crystalline polymer domains.

The band seen near 340 nm in the BHJ films in Figure 2.4 arises primarily from the absorption of PCBM, although there is some residual absorption of P3HT at this wavelength. Since the pure P3HT absorption at 340 nm is nearly identical for all three polymer batches, we can use the 340-nm peak intensity to roughly evaluate the PCBM content in each of the SqP

films (but see Ref. 42). For SqP films with the PCBM overlayer cast from a 5 mg/mL solution, the fullerene content of the films is quite similar, suggesting that any of the underlayer films can accommodate the relatively modest amount of fullerene provided by the dilute solution. For SqP active layers produced using more concentrated PCBM solutions, however, the HR P3HT samples show much weaker fullerene absorption than LR P3HT sample. This confirms that higher crystallinity polymers are less able to incorporate fullerene during SqP; if there are fewer amorphous regions into which PCBM can penetrate into the bulk of the film, more of the fullerene is likely to simply spin off during deposition of the over-layer. In the SI, we show optical micrographs of these films whose absorption spectra are shown Figure 2.4; the films made from HR P3HT batches with high PCBM concentrations spun on top show fullerene aggregates/crystals at the μm-length scale, consistent with the idea that sequentially-processed high crystallinity films cannot accommodate significant fullerene loadings.

Unlike the sequentially-processed films, whose absorption spectra do not change upon the addition of fullerene, the vibronic features in the absorption spectra of P3HT:PCBM BC films (Figure 2.4(d)) are strongly altered by the presence of fullerene. For the LR P3HT flim, the vibronic peaks have a dramatcially decreased intensity relative to the pristine P3HT, even after 20 minutes of thermal annealing at 150 ℃. This suggests for LR P3HT, the presence of fullerene hinders the crystallization of P3HT during both the spin-coating and thermal annealing processes. In the case of the HR P3HT:PCBM BC films, although the $A_{0\text{-}1}/A_{0\text{-}0}$ ratio does not remain constant as observed in the seqentially processed films, it does not decrease as strongly as in the LR P3HT:PCBM BC-BHJ films. Thus, this data suggests that even in BC films, the inherent crystallinity of HR P3HT can be better retained than that of LR P3HT.

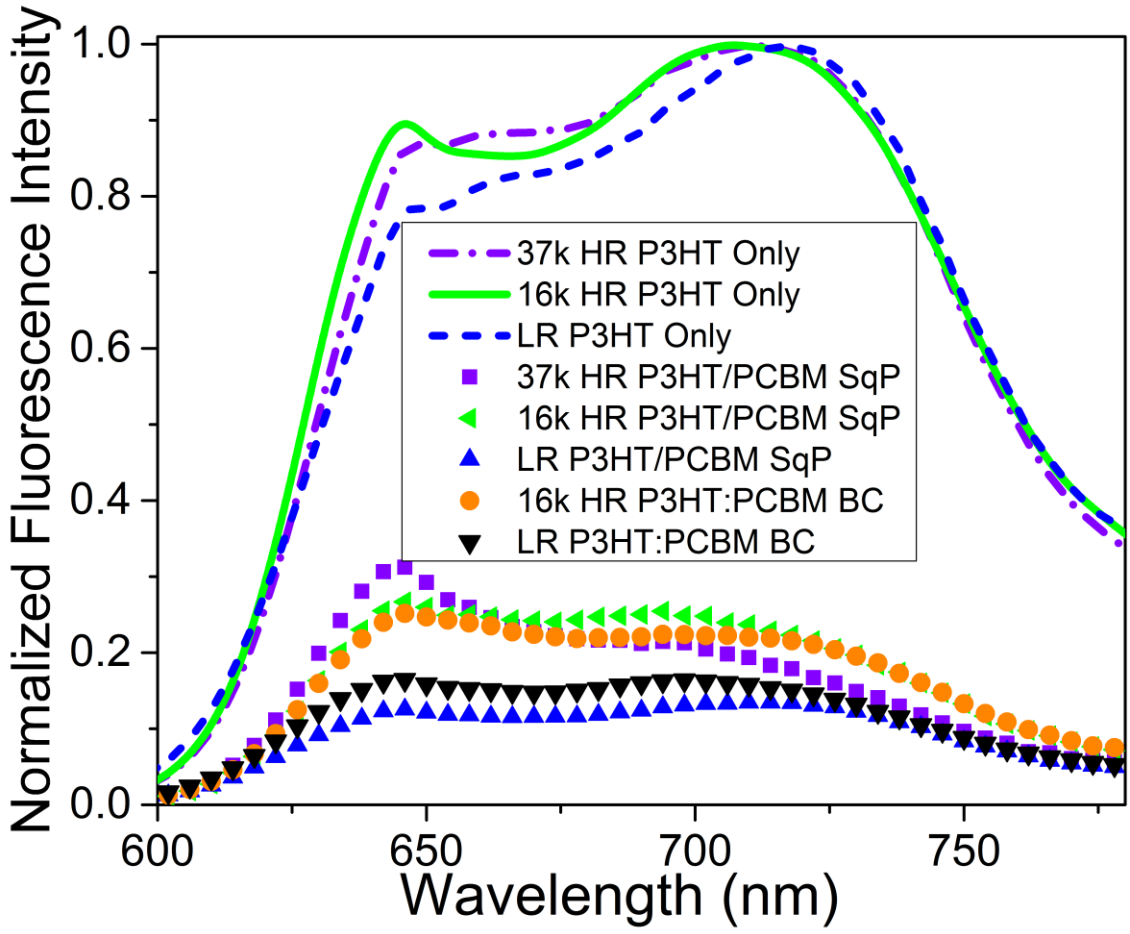

Figure 2.5 Photoluminescence (PL) spectra of thin films made from: pure P3HTs (same as Figure 2.4a), SqP P3HT/PCBM films (same as Figure 2.4a) and P3HT:PCBM BC films (same as Figure 2.4d). The measured PL intensities were divided by each film's optical density at 530 nm, the excitation wavelength used in this experiment. and then normalized to the highest PL value (that of the pure 16k HR P3HT film) to best illustrate the extent of PL quenching in the different samples.

In addition to UV-Visible spectroscopy, we also performed a series of photoluminescence (PL) quenching experiments of SqP and BC P3HT:PCBM films made from the different polymer batches, the results of which are shown in Figure 2.5. The PL spectra of the pure P3HT polymer

films are similar, with only slight differences in the relative height of the 0-0 peak near 650 nm that reflect the changes in intermolecular coupling with the degree of polymer crystallinity,[83] in agreement with the UV-Visible data in Figure 2.4. Overall, the trends observed in BC and SqP films are very similar. HR samples show less PL quenching in all cases compared to LR samples, a result that indicates that the equilibrium (i.e. post-annealing) extent of polymer-fullerene mixing at the molecular scales is driven primarily by polymer regioregularity and not by the processing method. This result is particularly interesting in light of the facts that HR material produces the best BC devices while LR material gives SqP devices with the highest efficiency. The results thus emphasize how the same level of atomic-scale mixing must be accompanied by very different nanoscale architecture using the two different processing methods. For a separation-based process like BC, strong separation appears to drive the formation of an optimized nanoscale architecture. By contrast, for a mixing-based process like SqP, a strong driving force for mixing is needed to create that same ideal architecture.

2.4.2.2 The Morphology of SqP and BC Films with Different Batches of P3HT Measured by X-Ray Diffraction:

To directly investigate how changes in the P3HT regioregularity affect the polymer and fullerene crystallinity for the different processing routes used to make BHJs, we performed a series of two-dimensional (2-D) grazing incidence wide-angle X-ray scattering (GIWAXS) measurements. For these experiments, we used all the same processing methods described above, but instead spun the active layer materials onto silicon substrates. Our GIWAXS measurements were performed at the Stanford Synchrotron Radiation Light Source on beamline 11-3 using a wavelength of 0.9742 Å. We should note that the absolute diffraction intensities cannot be compared between SqP and BC data sets because of different beam intensities during

separate experimental runs; the relative intensities for a single processing method, however, can be meaningfully compared within each set. Below, we show only radially-integrated scattering data; the full 2-D GIWAXS diffraction patterns are given in the SI. The results from our GIWAXS measurement are summarized in Figure 2.6 and Table 2.3.

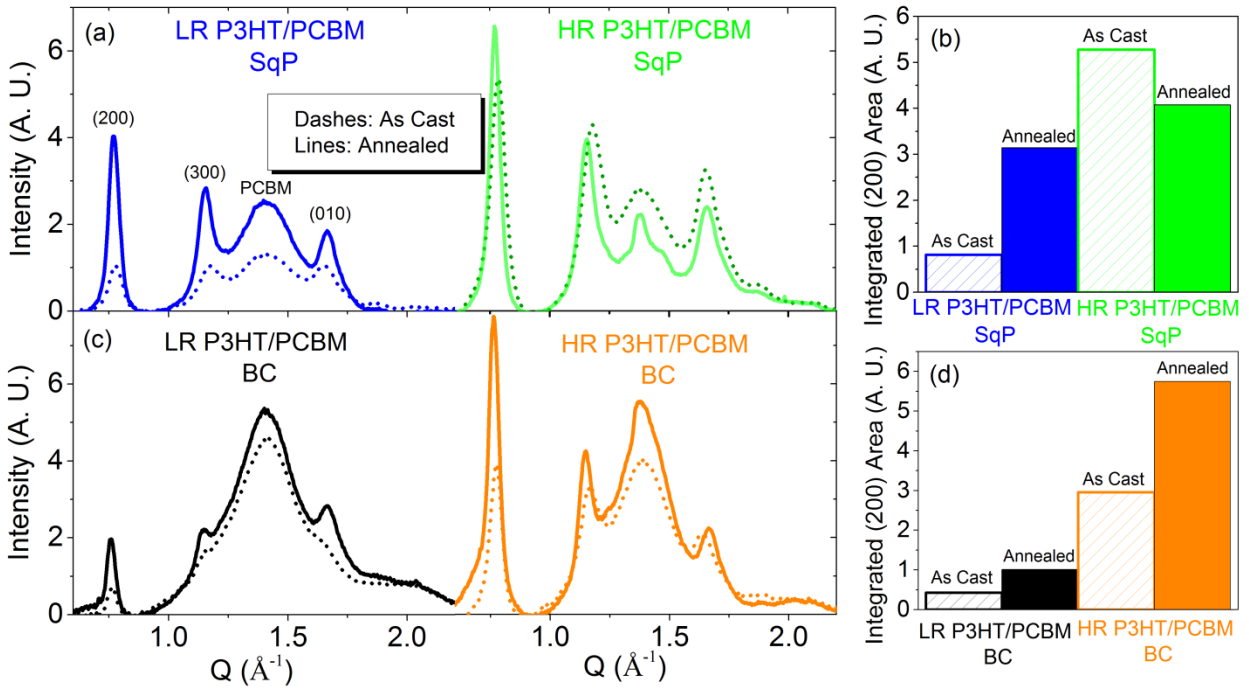

Figure 2.6 (a) Radially-integrated 2-D GIWAXS intensities for P3HT/PCBM sequentially processed active layers cast on a silicon substrate for LR and HR P3HT. In each case, the P3HT film thickness was 110 nm, and the PCBM over-layer was spun from a 5mg/mL solution. (b) Integrated peak area for the (200) polymer peak for SqP. (c) Integrated GIWAXS intensity for P3HT/PCBM BC films. (d) Integrated peak area for the (200) polymer peak for BC-BHJ films. Dashed lines indicate as-cast films and solid lines are after 20 min of thermal annealing at 150 ℃ for both (a) and (c).

Table 2.3 Summary of Parameters from GIWAXS

	(200) Peak Position ($Å^{-1}$)	(200) Peak Area (A. U.)	(200) FWHM[a] (A. U.)	(010) Peak Position ($Å^{-1}$)	(010) Peak Area (A. U.)	(010) FWHM[a] ($Å^{-1}$)
LR P3HT/PCBM SqP As Cast	0.778	8.1	6.6	1.657	10.9	10.7
LR P3HT/PCBM SqP Annealed	0.770	31.4	5.6	1.664	13.5	7.7
16k HR P3HT/PCBM SqP As Cast	0.787	52.8	6.9	1.655	35.4	10.0
16k HR P3HT/PCBM SqP Annealed	0.770	40.8	5.1	1.662	23.3	8.9
LR P3HT:PCBM BC As Cast	0.766	4.3	4.6	1.627	15.7	14.9
LR P3HT:PCBM BC Annealed	0.759	10.1	3.9	1.663	29.8	12.0
16k HR P3HT:PCBM BC As Cast	0.776	29.6	5.5	1.634	20.1	11.6
16k HR P3HT:PCBM BC Annealed	0.761	57.4	5.1	1.663	15.0	8.1

[a] *The full width at half maximum (FWHM) is inversely proportional to the coherence length, which is an estimate of the length over which the ordered crystalline packing is maintained.*

2.4.2.2.1 The Polymer Diffraction in SqP Samples:

We begin our discussion by examining the P3HT (200) peaks, located between 0.77 – 0.79 $Å^{-1}$, which arise from P3HT lamellar interchain stacking. The (200) peak is mostly distributed in the out-of-plane direction due to the dominant "edge-on" orientation of the P3HT chains relative to the substrate (see SI). For the as-cast SqP films (dashed curves), the integrated (200) peak area of the 16k HR P3HT is more than six times higher than that of the LR P3HT. The peak

center of the HR P3HT is also positioned at higher *Q* than that of LR P3HT, which indicates more compact lamellar stacking for the HR P3HT. We note that in polymeric systems, the broadening of x-ray scattering peaks results from disorder in the polymer domains, rather than from the finite size of crystallites as seen in crystalline materials.[16,88,89] Thus, the FWHM or coherence lengths reported here are those derived from the Scherrer equation, even though the size of the crystalline polymer domains are likely smaller. In Table 2.3, the two P3HT batches show similar FWHM for the (200) peaks. From this data, we conclude that a larger fraction of the as-cast HR P3HT-based SqP samples is crystalline, but the crystallites in both films have similar coherence lengths. The HR samples also show closer packing than the LR P3HT-based samples, a fact that likely arises from increased ordering of the hexyl tails in the HR films.

The literature suggests that thermal annealing of SqP films serves the dual roles of facilitating fullerene diffusion into the polymer underlayer and helping to further crystalize amorphous polymer domains.[41,90] Indeed, the solid curves in Figure 2.6(a) show that for both batches of P3HT, annealing causes the (200) peaks to become sharper, indicating the formation of more ordered P3HT domains with larger structural coherence lengths. The change in the intensity of the (200) peak area upon thermal annealing, however, is quite different for the different SqP P3HT batches. For the LR P3HT, annealing increases the peak area by over a factor of three, a result similar to previous studies on BC devices. Surprisingly, the peak area for the HR P3HT actually decreases upon thermal annealing, indicating that annealing this particular polymer/fullerene blend makes the film *less* crystalline. Further investigation reveals that unlike the LR P3HT, where annealing causes essentially no shift of the (200) peak, the HR P3HT (200) peak center also shifts slightly towards lower *Q*, indicating the *d*-spacing between the lamellar

planes becomes larger after annealing. This likely results from small amount of PCBM diffusing into the P3HT crystallites.

We next turn to investigate the trends of the (010) peak, which corresponds to the polymer π-π stacking direction and is therefore important for charge delocalization and transport. We find that the same general trends with polymer regioregularity and thermal annealing observed for the (200) peak also hold in the (010) direction for our SqP films. For the LR P3HT, however, the increase in (010) peak area upon annealing is less dramatic than that observed for the (200) peak, but the decrease in (010) peak width upon annealing is greater. These data thus indicate that in the (010) direction, thermal annealing predominantly affects on the crystalline coherence length, likely from improvements in π-π stacking upon annealing. For the HR SqP P3HT samples, we saw that the diffraction peaks decrease in intensity upon thermal annealing, and that the decrease of the (010) peak area is slightly greater than the decrease seen in the (200) direction. Overall, the change in both peak with and peak area are qualitatively similar for the (010) and (200) peaks, suggesting that for SqP samples made with HR P3HT, diffusion of PCBM into the film reduces the extent of crystallinity in a fairly isotropic manner, likely by creating amorphous polymer regions where the fullerene can reside. This is in contrast to the LR samples, where annealing of paracrystalline disorder and fullerene diffusion are coupled in a more complex manner.

Clearly, the most significant difference between the two batches of SqP P3HT films is the total amount of amorphous polymer. We believe that a certain amorphous fraction is necessary for the PCBM to penetrate into sequentially processed films. Even though the HR P3HT starts out highly crystalline with few amorphous regions, the thermally induced mixing that drives PCBM into the polymer underlayer actually disrupts the P3HT network by creating additional

amorphous regions upon incorporation. This produces the surprising result of a polymer/fullerene sample that becomes less crystalline upon annealing.

2.4.2.2.2 The Polymer Diffraction in BC Samples:

In as-cast BC films, the BHJ is formed with the presence of both the polymer and the fullerene, leading to a different morphology than the case of SqP. Based on shifts in diffraction peaks, we find that there is more PCBM intercalation into the BC P3HT network in both the (200) and (010) directions for as-cast BC films relative to SqP films. After thermal annealing, a large amount of the PCBM in BC films is pushed out of the π-π interlayers, as evidenced by a sizable shift towards high *Q* for the (010) π-stacking peak. This (010) shift upon annealing does not occur with the SqP films. But perhaps more importantly, thermal annealing causes the crystallinity of both the HR and LR P3HT batches to increase when the film is prepared via BC. This provides one reason why the BC devices made from HR P3HT show superior performance compared to those made via SqP.

Another factor that could contribute to the change in device performance with regioregularity is the shape of the polymer crystallites. The widths of the (200) and (010) peaks indicate that the length of the HR P3HT crystallites are shorter than those of the LR P3HT in the (200) direction but longer in the (010) direction. Since the charge carrier transport in the π-π direction is important to the mobility of holes in OPV devices,[88] one might expect hole extraction in HR P3HT active layers to be more efficient than that in LR P3HT samples. Since the hole mobility in P3HT:PCBM blend films is typically lower than the electron mobility,[91] the HR P3HT provides a better mobility-matched active layer and therefore a device with higher fill factor[92] than the LR P3HT BC device, as seen in Figure 2.1.

2.4.2.2.3: The Fullerene Diffraction in SqP and BC Samples:

In addition to the changes in the crystallinity of the different batches of P3HT, Figure 2.6 also shows that thermal annealing leads to changes in the crystallinity of the PCBM. For example, the PCBM diffraction (at $q \sim 1.4$ Å^{-1}) in the LR P3HT SqP film shows a significant increase in intensity upon thermal annealing, but the peak remains broad. This is consistent with the formation of many small PCBM crystallites upon thermally annealing SqP LR P3HT films. In contrast, thermal annealing dramatically sharpens the PCBM peaks in the SqP films made with HR P3HT. This indicates that in highly crystalline P3HT, there are too few amorphous regions in which the PCBM can mix with the polymer, so that annealing forces the fullerenes to crystallize into a fewer, but significantly larger domains that are not consistent with an ideal BHJ architecture. These large domains may be accompanied by isolated fullerenes at grain boundaries, but those isolate fullerenes do not diffract and do not create effective conductive paths for photogenerated electrons. This hypothesis is supported by optical images, shown in the SI, which reveal that after thermal annealing, there is optically-visible phase separation of the PCBM in the HR P3HT film.

All of these results make sense in the context of two ideas: first, that PCBM is miscible and mobile only in the amorphous regions of P3HT films,[40,42,89,93–96] and second, that P3HT only fully crystallizes in the absence of PCBM. The LR P3HT clearly possesses more amorphous regions as-cast, so in SqP films, there is ample opportunity for thermal annealing to cause PCBM to diffuse into the polymer underlayer and form semicrystalline aggregates, as well as for some of the previously amorphous P3HT regions to crystallize. In highly crystalline as-cast polymers, on the other hand, there are almost no suitable amorphous spaces available for PCBM incorporation in SqP devices, so the polymer must partially disorder to make room for fullerene

incorporation. Even with this disordering, the majority of the fullerene is still forced to aggregate into large, highly crystalline domains because it cannot mix into the already-crystalline regions of the polymer. In the case of BC films, the high propensity of the polymer to crystallize is important to help drive the phase separation of the polymer and the fullerene. In low regioregularity polymers, the P3HT cannot phase separate as easily, so an ideal interpenetrating BHJ network cannot be formed.

2.5 Experimental Details and Additional Morphological Characterization

2.5.1 Detailed Parameters for the Different Batches of P3HT Used in This Work

Table 2.4 Characteristics of P3HT used in this work[a]

	M_n (kDa)	Regioregularity	PDI
LR P3HT[b]	~50-60	~94%	~2.20
16k HR P3HT[c]	15.9	98%	1.18
37k HR P3HT[c]	36.9	98%	1.19
50k HR P3HT[c]	50.1	96%	1.48

[a]*The notations "HR or LR" and "High RR or Low RR" are used interchangeably throughout this SI. They both stand for "high regioregularity" or "low regioregularity", respectively*

[b]*The LR P3HT was purchased from Rieke Metal Inc., consisted of the following material: BASF Sepiolid ™ P100 (rr~94% via NMR, molecular weight 50 – 60 kDa via GPC and polydispersity index of ~2.2). The material was used as received without further purification*

.[c]The in-house P3HT batches was purified by successive Soxhlet extractions with MeOH, hexanes, and chloroform which has been shown to reduce the level of impurities in the polymer to undetectable levels.[97]

2.5.2 Experimental Details

2.5.2.1 Photovoltaic Device and Active Layer Fabrication Procedures:

We fabricated sequentially-processed (SqP) P3HT/PCBM solar cells by starting with prepatterned tin-doped indium oxide (ITO; TFD Inc.) coated substrates and cleaning them by successive sonication in detergent solution, deionized water, acetone and isopropanol for 8 min each. After drying with blowing argon gas, we treated the ITO substrates with an air plasma (200 mTorr, 15 min). A thin layer of PEDOT:PSS was then spin-coated onto the clean substrates in air at 5000 rpm for 60 s, and the PEDOT:PSS-covered substrate was then baked at 140 ℃ for 20 min in a nitrogen atmosphere. P3HT solutions were prepared by dissolving 20 mg/mL of each batch of P3HT in *o*-dichlorobenzene (ODCB). The solutions were stirred at 60 ℃ for at least two hours prior to being cooled to room temperature and spun onto the PEDOT:PSS-covered substrates at spin speeds ranging from 1000 to 1200 rpm for 60 s for LR P3HT and 16k HR P3HT, and from 1400 to 1500 rpm for 60 s for 37k HR P3HT. After spin-coating, the P3HT films were dried under active vacuum for at least 20 min prior to subsequent use. PCBM solutions were prepared by dissolving PCBM powder (Nano-C) in dichloromethane (DCM) at concentrations of 5 mg/mL, 10 mg/mL or 15 mg/mL and stirring at room temperature for at least 30 minutes. These solutions were then spin-cast on top of the P3HT layer from the previous step at 4000 rpm for 10 s. Film thicknesses were measured after the deposition of each successive layer with a Dektak 150 Stylus Surface Profiler. The P3HT film thickness was kept to ~110 nm

for each batch by adjusting the spin speed, as stated above, to account for the different solution viscosities: The 37k HR P3HT solution had a higher viscosity than the other P3HT solutions, whose viscosities were similar to each other. For thermally annealed samples, the films were heated to 150 ℃ for 20 min on a hot plate under an argon atmosphere. Cathode deposition consisted of ~40 nm of Ca evaporated at rates below 1 Å/s followed by 70 nm of Al at ~2 Å/s. The resulting device active areas were 6.51 mm^{98}.

The *J-V* curves were measured in an argon atmosphere using a Keithley 2400 source meter. A xenon arc lamp and an AM-1.5 filter were used as the excitation source, with the intensity calibrated to match 1 sun.

For blend-cast (BC) bulk heterojunction (BHJ) devices, except for the active layer fabrication procedure, all the subsequent steps were identical to those for the SqP devices. All of our blend solutions had polymer concentrations of 20 mg/mL in ODCB. Depending on the experiment, both 1:0.9 and 1:1.3 polymer:fullerene weight ratios were used. The solutions were stirred at 60 ℃ overnight on a hot plate in a nitrogen atmosphere. The active layers of our BC devices were prepared by spin-coating the blend solutions in the speed range of 1000 to 1200 rpm for 60 s for 16k HR P3HT:PCBM and LR P3HT:PCBM blends, and at 1200 rpm for 60 s for 50k HR P3HT:PCBM blend to account for the higher viscosity of this solution. The resulting films all had a similar thickness of about 175 nm.

The films for all other measurements (GIWAXS, UV-Vis and PL quenching, as in Figures 2.4-2.6) were prepared using the identical procedures to those described above but without deposition of a top electrode.

2.5.2.2 UV-Visible Absorption and Photoluminescence (PL) Quenching Measurement

The UV-Visible absorption spectra shown in Figure 2.4 were collected using a Lambda 25 UV/Vis Spectrophotometer. The steady-state PL measurements shown in Figure 2.5 were performed with a FluoroMax-3 (J-Y Horiba) fluorimeter. The PL spectra for all samples were collected in air at 22.5 ° with respect to the excitation beam with the sample positioned at 45 ° with respect to the excitation axis. The slit widths and integration times were kept constant during all of our measurements. All of the PL spectra displayed were normalized by the optical density at our chosen excitation wavelength of 530 nm. The spectra were further corrected for the known wavelength variation of the detector and monochromator responses. To better emphasize the PL quenching of the SqP samples, the spectra of the pure P3HTs in Figure 2.5 and Figure 2.17 were normalized to their highest PL values.

2.5.2.3 2-D Grazing Incidence Wide Angle X-ray Scattering (GIWAXS)

The image in Figure 2.7 shows the full 2-D diffractogram that corresponds to the integrated GIWAXS data shown in Figure 2.6(a) (blue). Although we only show the pattern for thermally-annealed LR P3HT/PCBM SqP, we note that all the P3HTs we studied have similar features. The (100), (200), and (300) peaks correspond to the interchain lamellar packing, and primarily occur in the out-of-plane direction. The (010) peak, corresponding to the π-π stacking, is seen only in the in-plane direction. Combined, these features indicate a predominantly edge-on stacking of the P3HT. The fullerene scattering is seen as an isotropic amorphous ring, located between the polymer (300) and the (010) peaks.

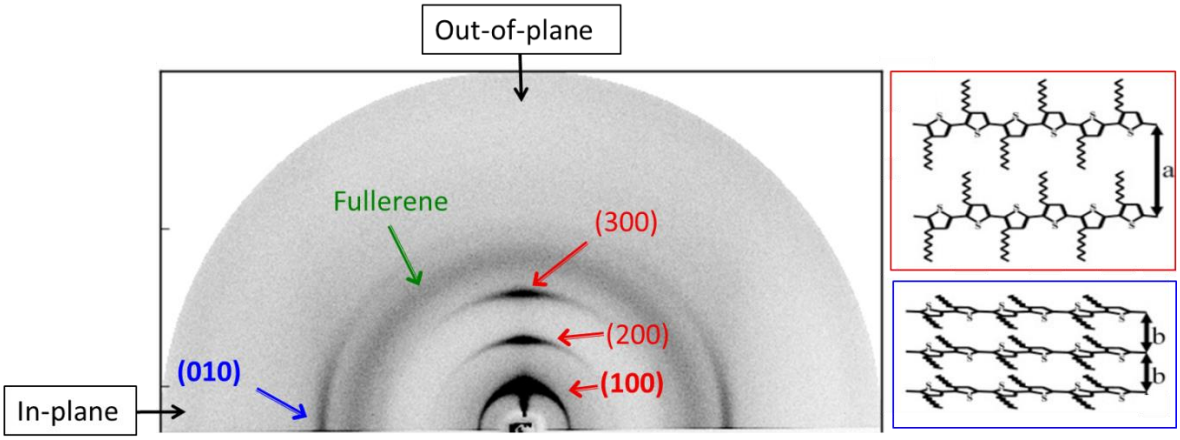

Figure 2.7 2-D GIWAXS of a thermally-annealed LR P3HT/PCBM SqP active layer (left) and corresponding P3HT packing structures (right). The (100), (200), and (300) peaks correspond to the distance *a* and the (010) peak corresponds to the distance *b*.

2.5.3 Injected Current Characteristics of Pure P3HT Diodes

For P3HT-only diodes, whose *J-V* characteristics are shown in Figure 2.8, all the fabrication procedures were the same as the SqP photovoltaic device fabrication except that there was no PCBM deposited on top of the P3HT layer and the top electrode is 70 nm of gold, evaporated at less than 1 Å/s. The final device configuration was thus ITO/PEDOT:PSS/P3HT/Au. The thicknesses of the polymer layers for the three P3HT batches were slightly different. The thicknesses for 37k HR P3HT, 16k HR P3HT and LR P3HT films were 137 nm, 107 nm and 112 nm, respectively. As shown below in equation (1), the thickness was included in our mobility calculation, so the variation in thickness did not affect our conclusions concerning the hole mobility. For these devices, the choice of the high-work function Au electrode on top ensures that only holes are injected into the device; the *J-V* characteristics of these devices shown in Figure 2.8 were measured in the dark.

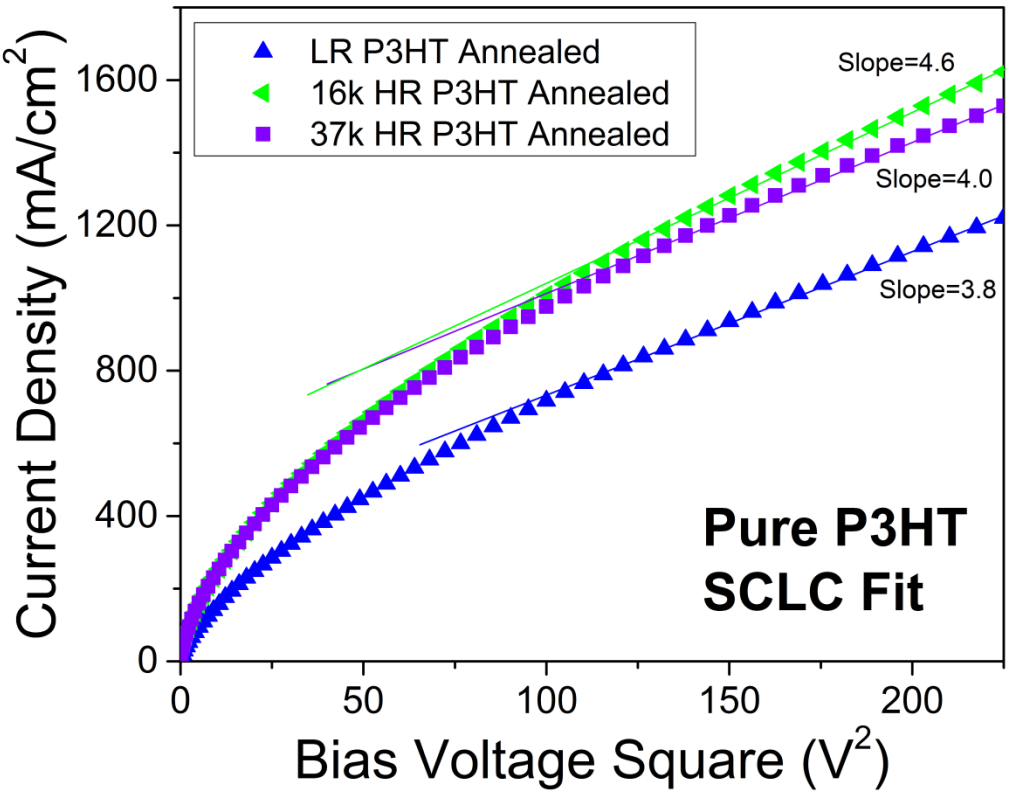

Figure 2.8 Current density vs. applied voltage square and the space charge limited current (SCLC) model fits in the high bias region for ITO/PEDOT:PSS/P3HT/Au hole only diodes. The thickness of the LR P3HT (blue upward triangle), 16k HR P3HT (green left triangle), and 37k HR P3HT (purple square) polymers were 112 nm, 137 nm and 107 nm, respectively.

To calculate the hole mobility in each batch of P3HT from the data in Figure 2.8, the space-charge limited current (SCLC) model was used:[98,99]

$$J = \frac{9}{8}\varepsilon_0\varepsilon_r\mu_p\frac{V^2}{L^3} \quad (1)$$

where ε_0 is vacuum permittivity, ε_r is the dielectric constant of P3HT, which was assumed to be 3 in our analysis, μ_p is the hole mobility, V is the voltage and L is the P3HT thickness. We fit our dark J vs. V^2 data to Eq. 1 in the high bias region to a least-squares line, and the slope

yielded the desired mobility. In this way, we calculated the hole mobility of each batch of P3HT, giving the results displayed in Table 2.1.

We also found (from an SCLC measurement using Al aluminum as the top electrode instead of Au) that the mobility of 16k HR P3HT was ~2.2 times that of LR P3HT and the mobility of the 50k HR P3HT was almost the same as the LR P3HT, similar to what we showed above. The fact that all the batches of P3HT gave SCLC hole mobilities over such a limited range reinforces our conclusions that the dramatic variation in device performance seen with different P3HTs is due to the active-medium morphology, not the intrinsic properties of the polymers.

2.5.4 SqP Solar Cells with Different P3HT/PCBM Compositions

We took optical images of the (thermally annealed) SqP films that provided the *J-V* curves in Figure 2.2; these images, shown in Figure 2.9, were focused on an area of the film between the electrodes. The different background colors seen in each image are the result of variations in the transmitted light power, and do not accurately reflect the bulk color of the samples. Across each row in Figure 2.9 horizontally are images of films with identical P3HT underlayers and a PCBM overlayer spun from solutions where the concentration increases from left to right. Each column of Figure 2.9 compares SqP films with different P3HT underlayers but an identically-cast PCBM overlayer. Figure 2.9 (a)-(c) show that for SqP films made with 16k HR P3HT, which is highly crystalline and has few amorphous regions, large-scale phase separation of PCBM occurs on optical length scales, particularly when high PCBM concentrations are used. Figure 2.9 (d)-(f) show a similar trend for SqP films made with 37k HR P3HT, except for that there appears to be relatively less PCBM phase separation in the film with the lowest PCBM concentration (Figure 2.9(d)). Figure 2.9 (g)-(i) shows that for the LR P3HT-based SqP films, there is almost no phase

separation on optical length scales except for a few large PCBM aggregates seen in Figure 2.9(i) for the highest PCBM concentration.

The fact that Figure 2.9(a) (16k HR P3HT batch) shows more phase separation than Figure 2.9(g) (LR P3HT batch) is consistent with the sharper PCBM GIWAXS peak seen in Figure 2.6 (green dashed curve), the poorer fluorescence quenching (Figure 2.5) and the smaller J_{sc} for photovoltaic devices (Figure 2.1) made using the 16k HR P3HT batch.

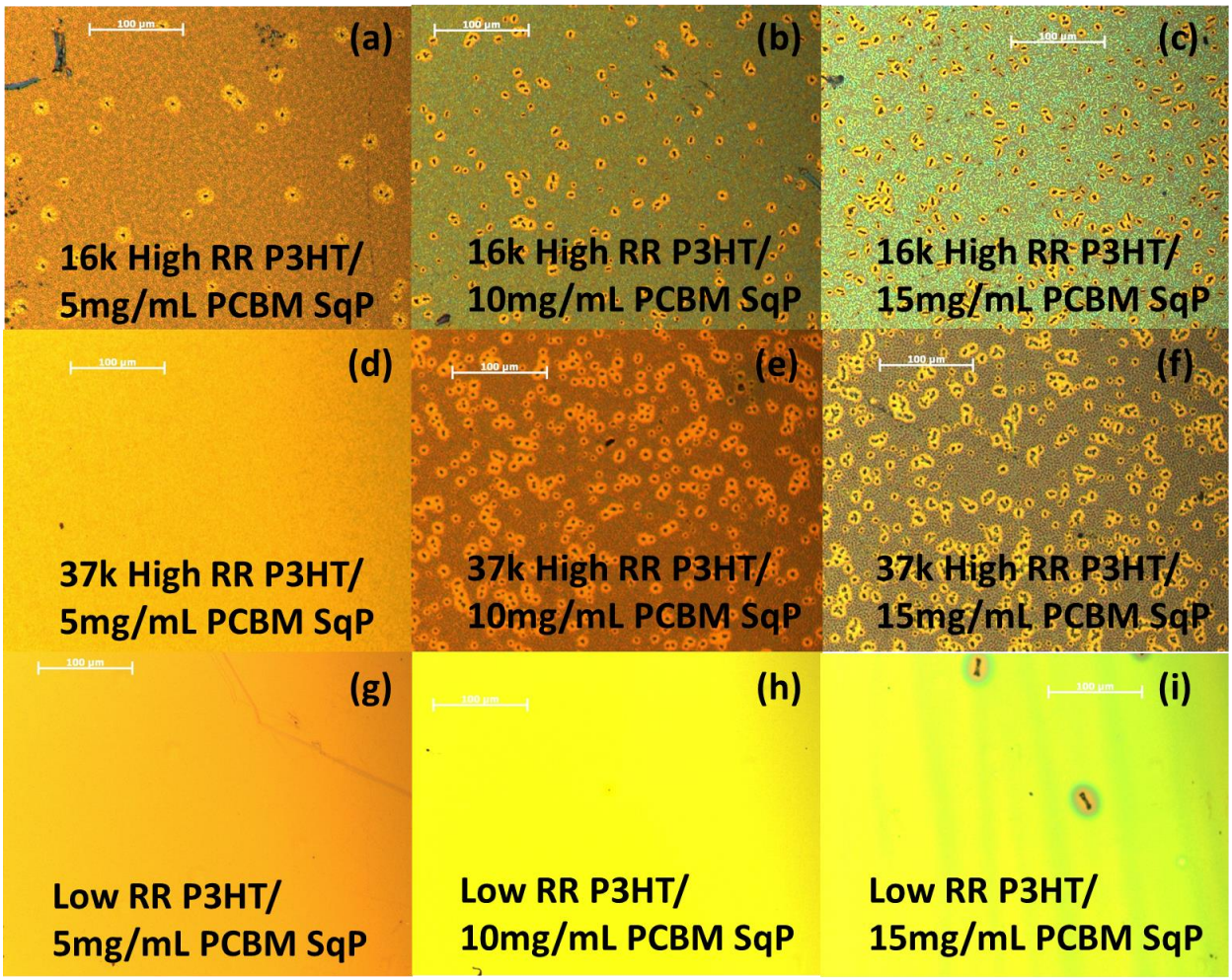

Figure 2.9 Optical microscopy images of thermally annealed films with three batches of P3HTs and three different PCBM concentrations spun on top of each batch of them. The scale bar is 100 μm.

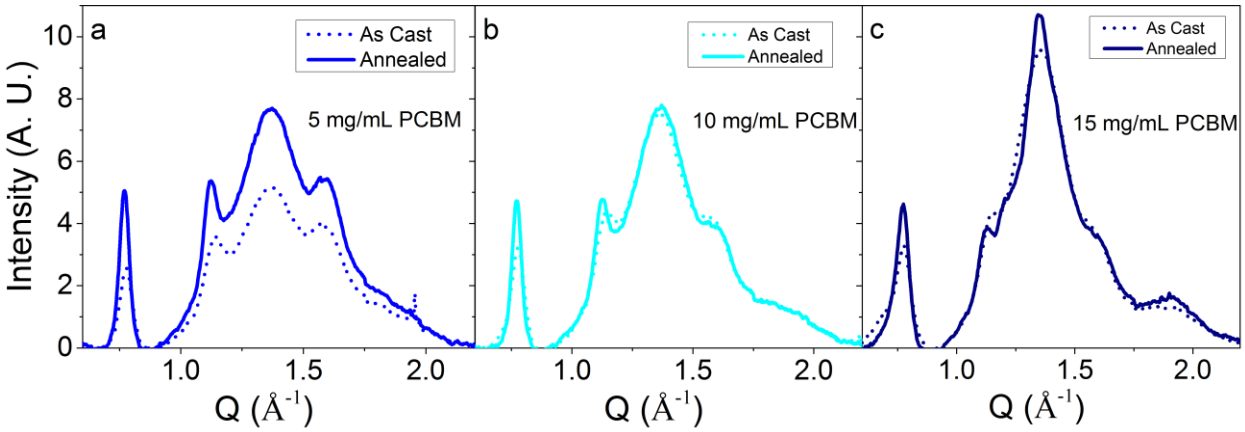

Figure 2.10 Integrated GIWAXS intensity for LR P3HT/PCBM SqP films with (a) 5 mg/mL PCBM, (b) 10 mg/mL PCBM and (c) 15 mg/mL PCBM spun on top of the P3HT underlayers. Dashed lines indicate as-cast films and solid lines are for films annealed at 150 ℃ for 20 min.

We also performed GIWAXS measurements on the LR P3HT-based SqP films with three different PCBM concentrations spun on top. The result shown in Figure 2.10 (a)-(c) corresponds to the PCBM concentrations of 5 mg/mL, 10 mg/mL and 15 mg/mL, respectively. The sharper fullerene peak in Figure 2.10(c) is consistent with the observation of PCBM aggregates in the optical microscopy and with the low fill factor for all three PCBM concentrations for the solar cell made with LR P3HT.

2.5.5 Performance Properties of As-Cast SqP Solar Cells

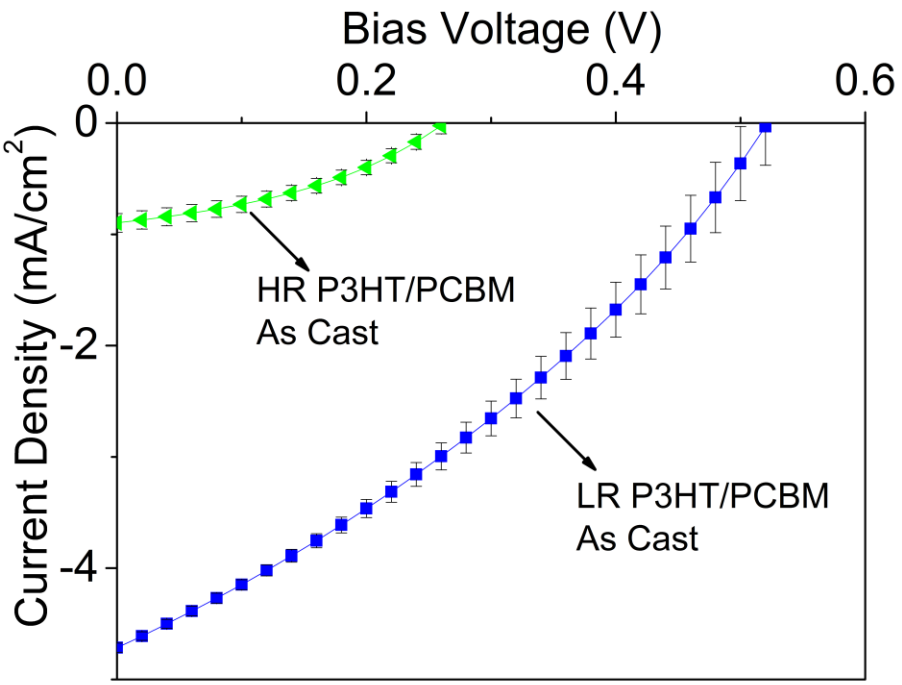

Figure 2.11 *J-V* characteristics of the as-cast P3HT/PCBM devices corresponding to the annealed device *J-V* curves used in Figure 2.1. The error bars show 1 standard deviation in measurements over at least 12 independent devices.

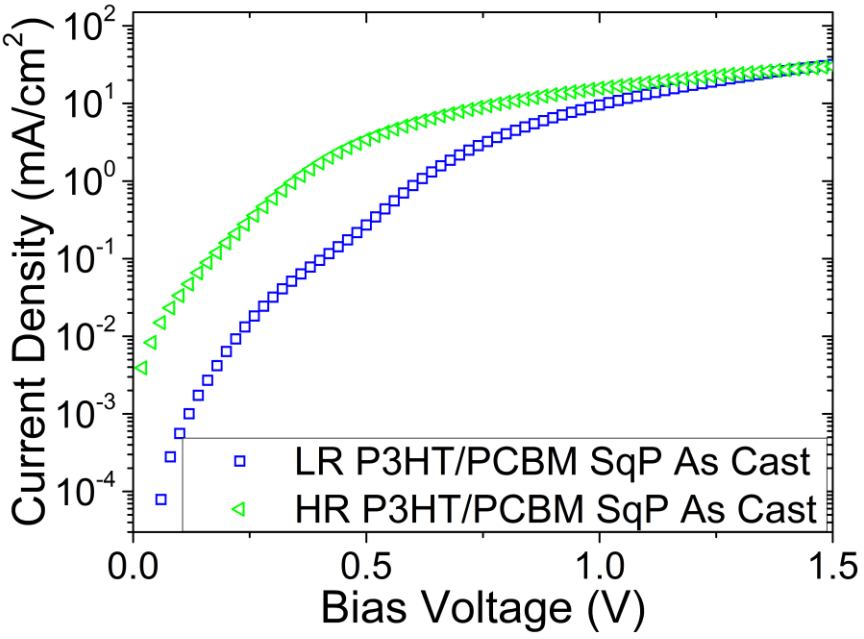

Figure 2.12 Dark *J-V* curves of the as-cast SqP P3HT/PCBM devices shown in Figure 2.11.

Table 2.5 Solar cell parameters summary for the devices in Figure 2.11 and 2.12

	V_{oc} (V)	J_{sc} (mA/cm^2)	*FF*	*PCE* (%)	n_{ideal} (Dark J-V)	R_{seires} (Ω-cm^2)	R_{shunt} (×10^5 Ω-cm^2)
16k HR P3HT/PCBM SqP As Cast	0.27 ±0.01	0.90 ±0.08	0.38 ±0.01	0.09 ±0.01	1.80 ±0.19	23.7 ±2.4	0.1 ±0.0
LR P3HT/PCBM SqP As Cast	0.52 ±0.02	4.71 ±0.04	0.33 ±0.01	0.80 ±0.05	2.12 ±0.07	16.7 ±4.9	4.8 ±0.8

2.5.6 Performance and Properties of BC BHJ Solar Cells with 50k HR P3HT

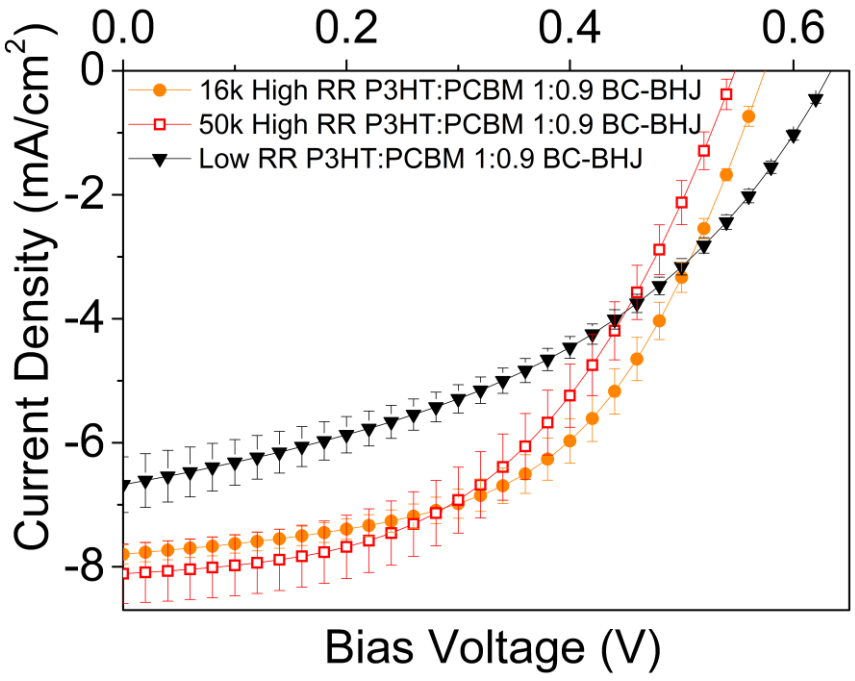

Figure 2.13 *J-V* characteristics of P3HT:PCBM 1:0.9 BC-BHJ with three batches of P3HTs. The device performance increase from LR P3HT to HR P3HT is observed in both 16k and 50k HR P3HT batches. The similarity of the molecular weights between 50k HR P3HT and LR

P3HT supports the conclusion that the increase of device performance in the BC-BHJ devices is mainly due to the increase of polymer regioregularity.

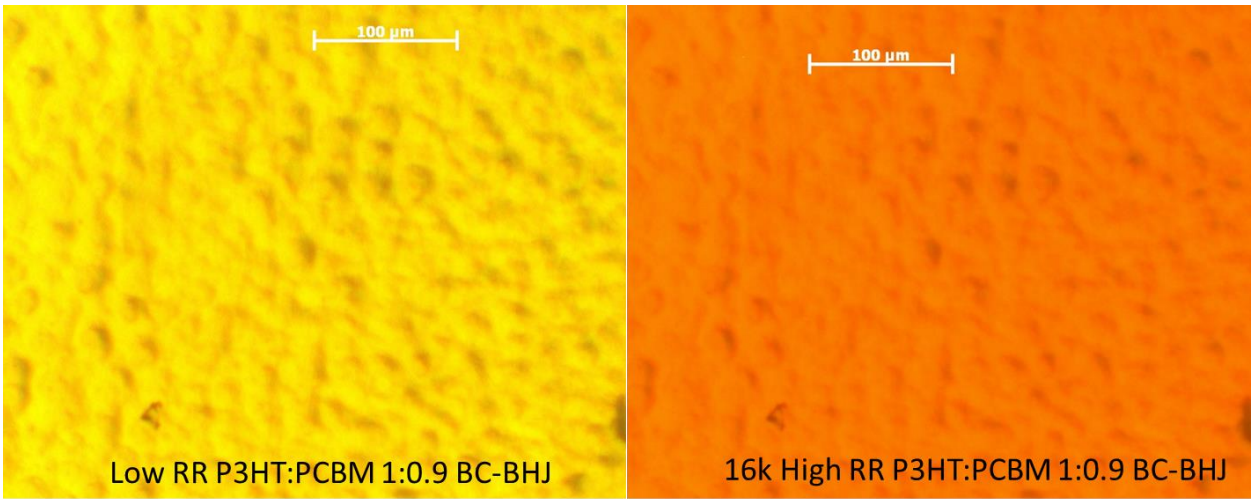

Figure 2.14 Optical microscopy images of P3HT:PCBM 1:0.9 BC-BHJ with LR P3HT (left) and 16k HR P3HT (Right). No significant phase separation is observed at this length scale for both films.

2.5.7 Composition Effect in BC-BHJ Solar Cells

For BC BHJ solar cells, in addition to polymer regioregularity, we also investigated the effect of varying the P3HT:PCBM composition on device performance. Figure 2.15 and Table 2.6, compares the *J*-*V* curves for BC devices made with the same polymer batches used above but with different P3HT:PCBM ratios. For the LR P3HT, the best device performance was obtained with a P3HT:PCBM ratio of 1:0.9, which was inside the optimal P3HT:PCBM ratio range for common commercially-available P3HT[100]. Increasing the PCBM loading to a P3HT:PCBM ratio of 1:1.3 causes a drop in both J_{sc} and V_{oc}.[101] For our in-house synthesized HR P3HT, however, we found that a P3HT:PCBM ratio of 1:1.3 yields both higher *FF*, J_{sc} and PCE

than a 1:0.9 ratio. The observation that extra fullerene can be supported by the HR P3HT in BC devices indicates that the P3HT lamella formed in BC films must differ from that of SqP films.

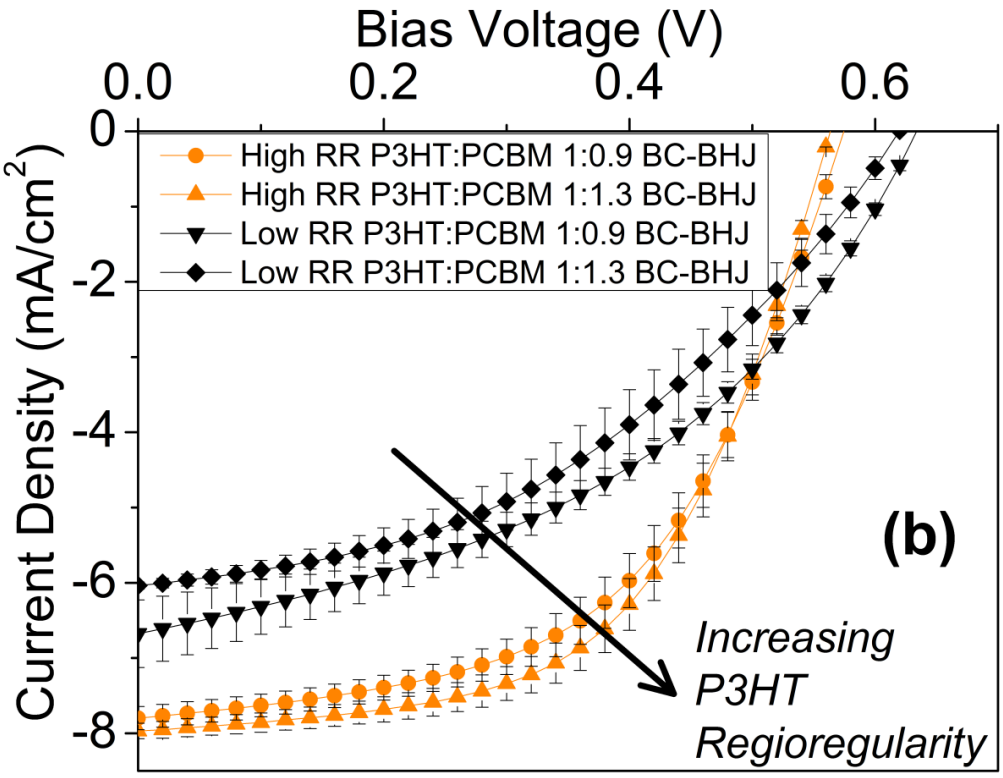

Figure 2.15 *J-V* characteristics of BC-BHJ solar cells made from 16k HR P3HT (orange) and LR P3HT (black) with two polymer:fullerene weight ratios.

Table 2.6 Solar Cell Parameters Summary for the Devices in Figure 2.15

	V_{oc} (V)	J_{sc} (mA/cm^2)	*FF*	*PCE* (%)
Low RR P3HT:PCBM 1:0.9 BC-BHJ	0.64±0.01	6.68±0.45	0.42±0.01	1.79±0.07
Low RR P3HT:PCBM 1:1.3 BC-BHJ	0.62±0.01	6.04±0.05	0.42±0.04	1.58±0.17
High RR P3HT:PCBM 1:0.9 BC-BHJ	0.58±0.01	7.80±0.15	0.53±0.03	2.39±0.14

High RR P3HT:PCBM 1:1.3 BC-BHJ	0.56±0.01	7.97±0.10	0.56±0.02	2.52±0.13

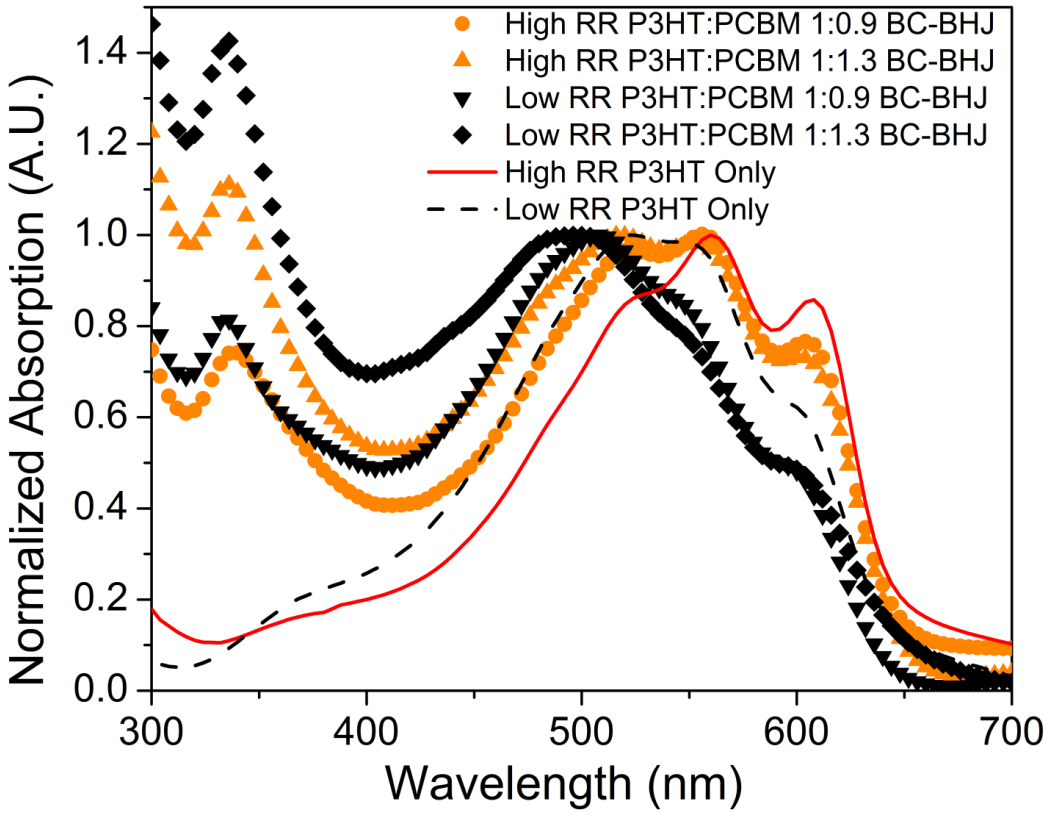

Figure 2.16 UV-Visible absorption spectra of thin BC-BHJ P3HT:PCBM films made from the same P3HTs as in Figure 2.15. All of the BC-BHJ films were thermally annealed at 150 ℃ for 20 minutes. The spectra were normalized to their highest polymer optical densities (OD) for ease of comparison.

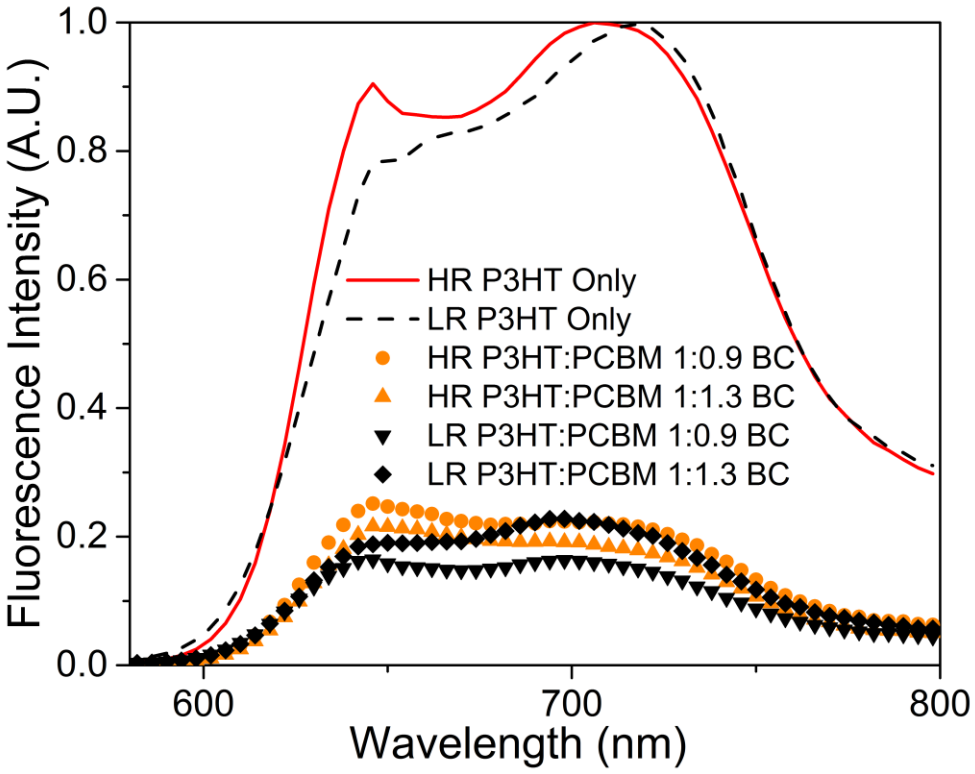

Figure 2.17 PL spectra of thin films made from: pure P3HTs (same as those in Figure 2.16) and P3HT:PCBM BC-BHJ films (same as those in Figure 2.16). The measured PL intensities were all divided by their optical densities at 530 nm, the excitation wavelength used in this experiment, and further normalized to the highest value of the pure HR P3HT film to best illustrate the extent of PL quenching in different samples.

To help understand the differences in BC device performance with different polymer:fullerene compositions, we compare the PL quenching of the BC films made from our different polymer batches in Figure 2.17. We find that a 1:1.3 BC HR P3HT:PCBM active layer has slightly better PL quenching than a 1:0.9 HR P3HT:PCBM BC film, with quenching ratios of 83% and 81%, respectively. The opposite is true for LR P3HT, with the 1:0.9 LR P3HT:PCBM BC film having 83% PL quenching while the same film with a 1:1.3 composition has only 80%

quenching. This again indicates that more crystalline P3HT requires additional fullerene to form a more ideal morphology in BC films.

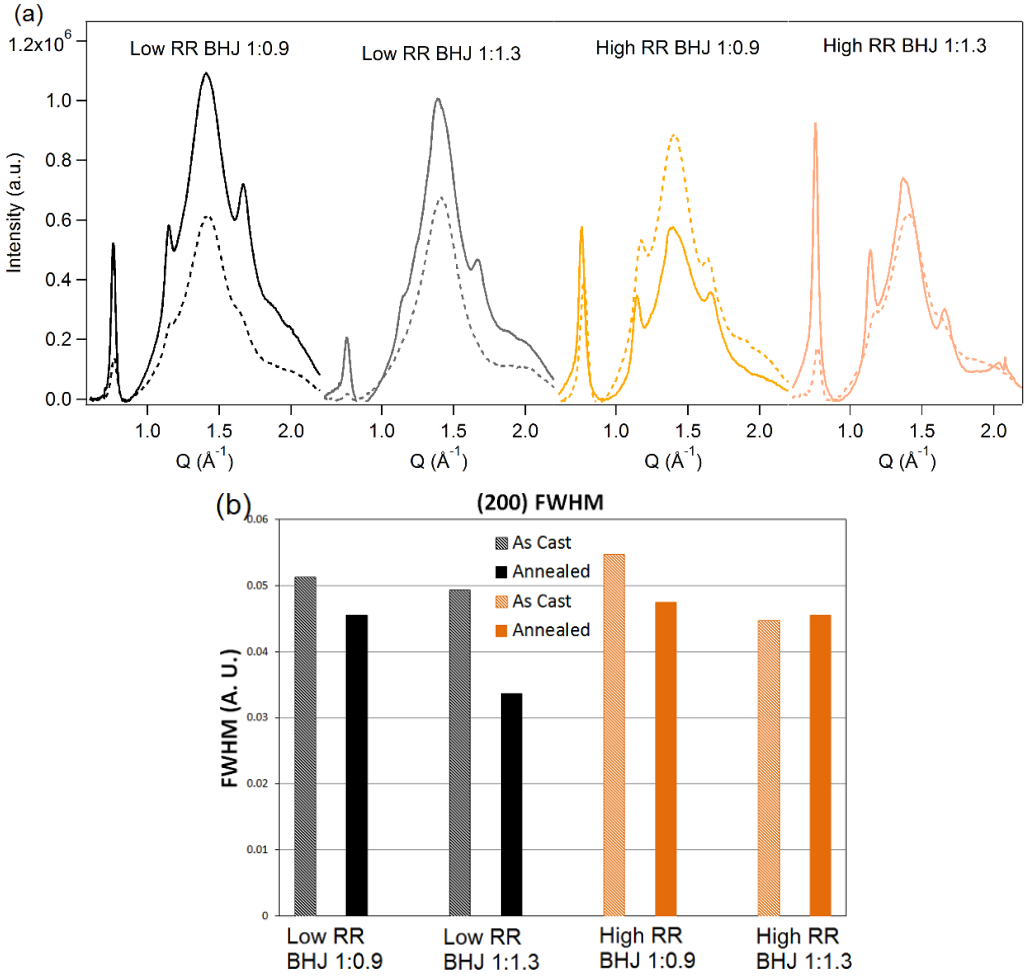

Figure 2.18 (a) Integrated GIWAXS intensity for P3HT:PCBM BC-BHJ films. Dashed lines indicate as-cast films and solid lines are after 20 min of thermal annealing at 150 ℃. (b) Full width at the half maximum (FWHM) for the polymer (200) peaks.

We also investigated the morphology of BC films by GIWAXS measurements, and obtained the results shown in Figure 2.18. When the P3HT/PCBM ratio is compared between BC BHJs, an interesting trend is observed. For the LR P3HT, increasing the fullerene ratio from 1:0.9 to 1:1.3 causes a decrease in overall crystallinity, and this crystallinity decrease does not recover

even after annealing. This is expected since PCBM incorporation into the P3HT prevents crystallization, creating an overall more amorphous polymer:fullerene network, which is slightly detrimental to the device performance. On the other hand, the opposite trend is seen for the HR P3HT. In this case, the higher 1:1.3 composition ratio still starts out more amorphous as-cast than the 1:0.9 composition, but becomes more crystalline than that of the 1:0.9 mixture upon thermal annealing. This also matches the observed increase in device performance for the 1:1.3 BC film over the 1:0.9 BC film. We believe that upon thermal annealing, the high regioregularity enables this polymer to form a larger number of small crystallites instead of increasing the size of the as-cast crystallites. A comparison of the peak width between the samples shows that indeed, the 1:1.3 HR BC crystallites do not grow in size as much as in other samples, allowing for high crystallinity even in the presence of a large amount of fullerene.

In our BC films, annealing also changes the fullerene crystallinity. In LR P3HT films, the fullerene peak increases upon annealing, indicating the formation of some fullerene crystallites. In the HR P3HT:PCBM 1:0.9 BC-BHJ, the fullerene crystallinity decreases upon annealing, which means that some of the fullerene crystallites are broken up to help form a more mixed network. On the other hand, the PCBM crystallinity remains relatively unchanged in the case of the 1:1.3 BC active layer since the phase separation is mainly being driven by the high propensity of the P3HT to crystallize.

2.6 Conclusions

In summary, we have found that the effects of changing polymer regioregularity and thus crystallinity on active layer morphology and the photovoltaic device performance differ dramatically based on how the active layer is formed. PCBM disperses only into the amorphous regions after sequential processing onto P3HT films, so that controlling the amount of the

amorphous phase has a direct impact on the subsequent device performance. SqP of P3HT with too high a polymer regioregularity results in highly crystalline films into which fullerenes cannot easily incorporate even after thermal annealing, leading to unfavorably large scale polymer/fullerene phase separation. SqP films made from P3HT with lower regioregularity possess more amorphous regions, which leads to a better polymer/fullerene network and thus more efficient solar cells. The effect of polymer crystallinity is reversed, however, if the active layer is fabricated through the traditional blend-cast method. The presence of PCBM in the mixed solution prevents P3HT from forming a highly crystalline network. Therefore, more highly regioregular P3HT is favorable because of its stronger propensity to crystallize.

This work has revealed a fundamental mechanism difference for the formation of BHJ active layer morphology between SqP and BC. All of the structural and device performance data show that SqP and BC do not produce films with the same polymer/fullerene morphology, and that different materials parameters affect the film morphology in different ways for the two processing methods. This suggests that the two processing techniques are complementary, and that the appropriate choice of which processing method to use to achieve high efficiency solar cells depends on the details of the particular batch of polymer and fullerene being used.

2.7 References

(1) Deibel, C.; Dyakonov, V. Polymer–Fullerene Bulk Heterojunction Solar Cells. *Rep. Prog. Phys* **2010**, *73*, 096401.

(2) Helgesen, M.; Søndergaard, R.; Krebs, F. C. Advanced Materials and Processes for Polymer Solar Cell Devices. *J. Mater. Chem.* **2010**, *20*, 36.

(3) He, Z.; Zhong, C.; Su, S.; Xu, M.; Wu, H.; Cao, Y. Enhanced Power-Conversion Efficiency in Polymer Solar Cells Using an Inverted Device Structure. *Nat. Photonics* **2012**, *6*, 591–595.

(4) Li, G.; Zhu, R.; Yang, Y. Polymer Solar Cells. *Nat. Photonics* **2012**, *6*, 153–161.

(5) You, J.; Chen, C.-C.; Hong, Z.; Yoshimura, K.; Ohya, K.; Xu, R.; Ye, S.; Gao, J.; Li, G.; Yang, Y. 10.2% Power Conversion Efficiency Polymer Tandem Solar Cells Consisting of Two Identical Sub-Cells. *Adv. Mater.* **2013**, *25*, 3973–3978.

(6) You, J.; Dou, L.; Yoshimura, K.; Kato, T.; Ohya, K.; Moriarty, T.; Emery, K.; Chen, C.-C.; Gao, J.; Li, G.; et al. A Polymer Tandem Solar Cell with 10.6% Power Conversion Efficiency. *Nat. Commun.* **2013**, *4*, 1446.

(7) Yu, G.; Gao, J.; Hummelen, J. C.; Wudl, F.; Heeger, A. J. Polymer Photovoltaic Cells: Enhanced Efficiencies via a Network of Internal Donor-Acceptor Heterojunctions. *Science (80-.).* **1995**, *270*, 1789–1791.

(8) Kim, Y.; Choulis, S. A.; Nelson, J.; Bradley, D. D. C.; Cook, S.; Durrant, J. R. Device Annealing Effect in Organic Solar Cells with Blends of Regioregular poly(3-Hexylthiophene) and Soluble Fullerene. *Appl. Phys. Lett.* **2005**, *86*, 63502.

(9) Ayzner, A. L.; Wanger, D. D.; Tassone, C. J.; Tolbert, S. H.; Schwartz, B. J. Room to Improve Conjugated Polymer-Based Solar Cells: Understanding How Thermal Annealing Affects the Fullerene Component of a Bulk Heterojunction Photovoltaic Device. *J. Phys. Chem. C* **2008**, *112*, 18711–18716.

(10) Collins, B. A.; Gann, E.; Guignard, L.; He, X.; McNeill, C. R.; Ade, H. Molecular Miscibility of Polymer−Fullerene Blends. *J. Phys. Chem. Lett.* **2010**, *1*, 3160–3166.

(11) Chen, D.; Nakahara, A.; Wei, D.; Nordlund, D.; Russell, T. P. P3HT/PCBM Bulk Heterojunction Organic Photovoltaics: Correlating Efficiency and Morphology. *Nano Lett.* **2011**, *11*, 561–567.

(12) Parnell, A. J.; Cadby, A. J.; Mykhaylyk, O. O.; Dunbar, A. D. F.; Hopkinson, P. E.; Donald, A. M.; Jones, R. A. L. Nanoscale Phase Separation of P3HT PCBM Thick Films As Measured by Small-Angle X-Ray Scattering. *Macromolecules* **2011**, *44*, 6503–6508.

(13) Bartelt, J. A.; Beiley, Z. M.; Hoke, E. T.; Mateker, W. R.; Douglas, J. D.; Collins, B. A.; Tumbleston, J. R.; Graham, K. R.; Amassian, A.; Ade, H.; et al. The Importance of Fullerene Percolation in the Mixed Regions of Polymer-Fullerene Bulk Heterojunction Solar Cells. *Adv. Energy Mater.* **2013**, *3*, 364–374.

(14) Shoaee, S.; Subramaniyan, S.; Xin, H.; Keiderling, C.; Tuladhar, P. S.; Jamieson, F.; Jenekhe, S. A.; Durrant, J. R. Charge Photogeneration for a Series of Thiazolo-Thiazole Donor Polymers Blended with the Fullerene Electron Acceptors PCBM and ICBA. *Adv. Funct. Mater.* **2013**, *23*, 3286–3298.

(15) Li, G.; Shrotriya, V.; Huang, J.; Yao, Y.; Moriarty, T.; Emery, K.; Yang, Y. High-Efficiency Solution Processable Polymer Photovoltaic Cells by Self-Organization of Polymer Blends. *Nat Mater* **2005**, *4*, 864–868.

(16) Verploegen, E.; Mondal, R.; Bettinger, C. J.; Sok, S.; Toney, M. F.; Bao, Z. Effects of Thermal Annealing Upon the Morphology of Polymer-Fullerene Blends. *Adv. Funct. Mater.* **2010**, *20*, 3519–3529.

(17) Westacott, P.; Tumbleston, J. R.; Shoaee, S.; Fearn, S.; Bannock, J. H.; Gilchrist, J. B.; Heutz, S.; DeMello, J.; Heeney, M.; Ade, H.; et al. On the Role of Intermixed Phases in Organic Photovoltaic Blends. *Energy Environ. Sci.* **2013**, *6*, 2756–2764.

(18) Gomez, E. D.; Barteau, K. P.; Wang, H.; Toney, M. F.; Loo, Y.-L. Correlating the Scattered Intensities of P3HT and PCBM to the Current Densities of Polymer Solar Cells. *Chem. Commun. (Camb).* **2011**, *47*, 436–438.

(19) Guo, J.; Ohkita, H.; Benten, H.; Ito, S. Charge Generation and Recombination Dynamics in Poly (3-Hexylthiophene)/fullerene Blend Films with Different Regioregularities and Morphologies. *J. Am. Chem. Soc.* **2010**, *132*, 6154–6164.

(20) Cates, N. C.; Gysel, R.; Beiley, Z.; Miller, C. E.; Toney, M. F.; Heeney, M.; McCulloch, I.; McGehee, M. D. Tuning the Properties of Polymer Bulk Heterojunction Solar Cells by Adjusting Fullerene Size to Control Intercalation. *Nano Lett.* **2009**, *9*, 4153–4157.

(21) Watts, B.; Belcher, W. J.; Thomsen, L.; Ade, H.; Dastoor, P. C. A Quantitative Study of PCBM Diffusion during Annealing of P3HT:PCBM Blend Films. *Macromolecules* **2009**, *42*, 8392–8397.

(22) Peet, J.; Soci, C.; Coffin, R. C.; Nguyen, T. Q.; Mikhailovsky, A.; Moses, D.; Bazan, G. C. Method for Increasing the Photoconductive Response in Conjugated Polymer/fullerene Composites. *Appl. Phys. Lett.* **2006**, *89*, 252103–252105.

(23) Peet, J.; Kim, J.; Coates, N.; Ma, W. L.; Moses, D.; Heeger, A. J.; Bazan, G. C. Efficiency Enhancement in Low-Bandgap Polymer Solar Cells by Processing with Alkane Dithiols. *Nat. Mater.* **2007**, *6*, 497–500.

(24) Lee, J. K.; Ma, W. L.; Brabec, C. J.; Yuen, J.; Moon, J. S.; Kim, J. Y.; Lee, K.; Bazan, G. C.; Heeger, A. J. Processing Additives for Improved Efficiency from Bulk Heterojunction Solar Cells. *J. Am. Chem. Soc.* **2008**, *130*, 3619–3623.

(25) Chang, L.; Jacobs, I. E.; Augustine, M. P.; Moulé, A. J. Correlating Dilute Solvent Interactions to Morphology and OPV Device Performance. *Org. Electron.* **2013**, *14*, 2431–2443.

(26) Chen, W.; Xu, T.; He, F.; Wang, W.; Wang, C.; Strzalka, J.; Liu, Y.; Wen, J.; Miller, D. J.; Chen, J.; et al. Hierarchical Nanomorphologies Promote Exciton Dissociation in Polymer/fullerene Bulk Heterojunction Solar Cells. *Nano Lett.* **2011**, *11*, 3707–3713.

(27) Ayzner, A. L.; Tassone, C. J.; Tolbert, S. H.; Schwartz, B. J. Reappraising the Need for Bulk Heterojunctions in Polymer− Fullerene Photovoltaics: The Role of Carrier Transport in All-Solution-Processed P3HT/PCBM Bilayer Solar. *J. Phys. Chem. C* **2009**, *113*, 20050–20060.

(28) Chen, D.; Liu, F.; Wang, C.; Nakahara, A.; Russell, T. P. Bulk Heterojunction Photovoltaic Active Layers via Bilayer. *Nano Lett.* **2011**, *11*, 2071–2078.

(29) Gevaerts, V. S.; Koster, L. J. A.; Wienk, M. M.; Janssen, R. A. J. Discriminating between Bilayer and Bulk Heterojunction Polymer:Fullerene Solar Cells Using the External Quantum Efficiency. *ACS Appl. Mater. Interfaces* **2011**, *3*, 3252–3255.

(30) Moon, J. S.; Takacs, C. J.; Sun, Y.; Heeger, A. J. Spontaneous Formation of Bulk Heterojunction Nanostructures: Multiple Routes to Equivalent Morphologies. *Nano Lett.* **2011**, *11*, 1036–1039.

(31) Cho, S.-M.; Bae, J.-H.; Jang, E.; Kim, M.-H.; Lee, C.; Lee, S.-D. Solvent Effect of the Fibrillar Morphology on the Power Conversion Efficiency of a Polymer Photovoltaic Cell in a Diffusive Heterojunction. *Semicond. Sci. Technol.* **2012**, *27*, 125018.

(32) Gadisa, A.; Tumbleston, J. R.; Ko, D.-H.; Aryal, M.; Lopez, R.; Samulski, E. T. The Role of Solvent and Morphology on Miscibility of Methanofullerene and poly(3-Hexylthiophene). *Thin Solid Films* **2012**, *520*, 5466–5471.

(33) Thummalakunta, L. N. S. A.; Yong, C. H.; Ananthanarayanan, K.; Luther, J. P3HT Based Solution-Processed Pseudo Bi-Layer Organic Solar Cell with Enhanced Performance. *Org. Electron.* **2012**, *13*, 2008–2016.

(34) Wong, M. K.; Wong, K. Y. Investigation of the Factors Affecting the Power Conversion Efficiency of All-Solution-Processed “bilayer” P3HT:PCBM Solar Cells. *Synth. Met.* **2013**, *170*, 1–6.

(35) Li, H.; Qi, Z.; Wang, J. Layer-by-Layer Processed Polymer Solar Cells with Self-Assembled Electron Buffer Layer. *Appl. Phys. Lett.* **2013**, *102*, 213901.

(36) Yang, B.; Yuan, Y.; Huang, J. Reduced Bimolecular Charge Recombination Loss in Thermally-Annealed Bilayer Heterojunction Photovoltaic Devices with Large External Quantum Efficiency and Fill Factor. *J. Phys. Chem. C* **2014**, *118*, 5196–5202.

(37) Lin, Y.; Ma, L.; Li, Y.; Liu, Y.; Zhu, D.; Zhan, X. Small-Molecule Solar Cells with Fill Factors up to 0.75 via a Layer-by-Layer Solution Process. *Adv. Energy Mater.* **2014**, *4*, 1300626.

(38) Nardes, A. M.; Ayzner, A. L.; Hammond, S. R.; Ferguson, A. J.; Schwartz, B. J.; Kopidakis, N. Photoinduced Charge Carrier Generation and Decay in Sequentially Deposited Polymer/Fullerene Layers: Bulk Heterojunction vs Planar Interface. *J. Phys. Chem. C* **2012**, *116*, 7293–7305.

(39) Lee, K. H.; Schwenn, P. E.; Smith, A. R. G.; Cavaye, H.; Shaw, P. E.; James, M.; Krueger, K. B.; Gentle, I. R.; Meredith, P.; Burn, P. L. Morphology of All-Solution-Processed "Bilayer" Organic Solar Cells. *Adv. Mater.* **2011**, *23*, 766–770.

(40) Treat, N. D.; Brady, M. A.; Smith, G.; Toney, M. F.; Kramer, E. J.; Hawker, C. J.; Chabinyc, M. L. Interdiffusion of PCBM and P3HT Reveals Miscibility in a Photovoltaically Active Blend. *Adv. Energy Mater.* **2011**, *1*, 82–89.

(41) Lee, K. H.; Zhang, Y.; Burn, P. L.; Gentle, I. R.; James, M.; Nelson, A.; Meredith, P. Correlation of Diffusion and Performance in Sequentially Processed P3HT/PCBM

Heterojunction Films by Time-Resolved Neutron Reflectometry. *J. Mater. Chem. C* **2013**, *1*, 2593–2598.

(42) Hawks, S. A.; Aguirre, J. C.; Schelhas, L. T.; Thompson, R. J.; Huber, R. C.; Ferreira, A. S.; Zhang, G.; Herzing, A. A.; Tolbert, S. H.; Schwartz, B. J. Comparing Matched Polymer:Fullerene Solar Cells Made by Solution-Sequential Processing and Traditional Blend Casting: Nanoscale Structure and Device Performance. *J. Phys. Chem. C* **2014**, DOI:10.1021/jp504560r.

(43) Dang, M.; Hirsch, L.; Wantz, G. P3HT: PCBM, Best Seller in Polymer Photovoltaic Research. *Adv. Mater.* **2011**, *23*, 3597–3602.

(44) Yang, C.; Heeger, A. Morphology of Composites of Semiconducting Polymers Mixed with C 60. *Synth. Met.* **1996**, *83*, 85–88.

(45) Wang, D. H.; Moon, J. S.; Seifter, J.; Jo, J.; Park, J. H.; Park, O. O.; Heeger, A. J. Sequential Processing: Control of Nanomorphology in Bulk Heterojunction Solar Cells. *Nano Lett.* **2011**, *11*, 3163–3168.

(46) Li, H.; Li, Y.; Wang, J. Optimizing Performance of Layer-by-Layer Processed Polymer Solar Cells. *Appl. Phys. Lett.* **2012**, *101*, 033907.

(47) Li, H.; Wang, J. Layer-by-Layer Processed High-Performance Polymer Solar Cells. *Appl. Phys. Lett.* **2012**, *101*, 263901–263905.

(48) Cheng, P.; Hou, J.; Li, Y.; Zhan, X. Layer-by-Layer Solution-Processed Low-Bandgap Polymer-PC 61 BM Solar Cells with High Efficiency. *Adv. Energy Mater.* **2014**, DOI: 10.1002/aenm.201301349.

(49) Loiudice, A.; Rizzo, A.; Latini, G.; Nobile, C.; de Giorgi, M.; Gigli, G. Graded Vertical Phase Separation of Donor/acceptor Species for Polymer Solar Cells. *Sol. Energy Mater. Sol. Cells* **2012**, *100*, 147–152.

(50) Loiudice, A.; Rizzo, A.; Biasiucci, M.; Gigli, G. Bulk Heterojunction versus Diffused Bilayer: The Role of Device Geometry in Solution P-Doped Polymer-Based Solar Cells. *J. Phys. Chem. Lett.* **2012**, *3*, 1908–1915.

(51) Tao, C.; Aljada, M.; Shaw, P. E.; Lee, K. H.; Cavaye, H.; Balfour, M. N.; Borthwick, R. J.; James, M.; Burn, P. L.; Gentle, I. R.; et al. Controlling Hierarchy in Solution-Processed Polymer Solar Cells Based on Crosslinked P3HT. *Adv. Energy Mater.* **2013**, *3*, 105–112.

(52) Yang, H. Y.; Kang, N. S.; Hong, J.-M.; Song, Y.-W.; Kim, T. W.; Lim, J. A. Efficient Bilayer Heterojunction Polymer Solar Cells with Bumpy Donor–acceptor Interface Formed by Facile Polymer Blend. *Org. Electron.* **2012**, *13*, 2688–2695.

(53) Chen, H.; Hu, S.; Zang, H.; Hu, B.; Dadmun, M. Precise Structural Development and Its Correlation to Function in Conjugated Polymer: Fullerene Thin Films by Controlled Solvent Annealing. *Adv. Funct. Mater.* **2013**, *23*, 1701–1710.

(54) Kim, D. H.; Mei, J.; Ayzner, A. L.; Schmidt, K.; Giri, G.; Appleton, A. L.; Toney, M. F.; Bao, Z. Sequentially Solution-Processed, Nanostructured Polymer Photovoltaics Using Selective Solvents. *Energy Environ. Sci.* **2014**, *7*, 1103–1109.

(55) Ayzner, A. L.; Doan, S. C.; Tremolet de Villers, B.; Schwartz, B. J. Ultrafast Studies of Exciton Migration and Polaron Formation in Sequentially Solution-Processed Conjugated Polymer/Fullerene Quasi-Bilayer Photovoltaics. *J. Phys. Chem. Lett.* **2012**, *3*, 2281–2287.

(56) Rochester, C. W.; Mauger, S. A.; Moule, A. J. Investigating the Morphology of Polymer/Fullerene Layers Coated Using Orthogonal Solvents. *J. Phys. Chem. C* **2012**, *116*, 7287–7292.

(57) Jiang, X.; Osterbacka, R.; Korovyanko, O.; An, C. P.; Horovitz, B.; Janssen, R. A. J.; Vardeny, Z. V. Spectroscopic Studies of Photoexcitations in Regioregular and Regiorandom Polythiophene Films. *Adv. Funct. Mater.* **2002**, *12*, 587–597.

(58) Kim, Y.; Cook, S.; Tuladhar, S. M.; Choulis, S. A.; Nelson, J.; Durrant, J. R.; Bradley, D. D. C.; Giles, M.; McCulloch, I.; Ha, C.-S.; et al. A Strong Regioregularity Effect in Self-Organizing Conjugated Polymer Films and High-Efficiency Polythiophene:fullerene Solar Cells. *Nat. Mater.* **2006**, *5*, 197–203.

(59) Mauer, R.; Kastler, M.; Laquai, F. The Impact of Polymer Regioregularity on Charge Transport and Efficiency of P3HT:PCBM Photovoltaic Devices. *Adv. Funct. Mater.* **2010**, *20*, 2085–2092.

(60) Adachi, T.; Brazard, J.; Ono, R. J.; Hanson, B.; Traub, M. C.; Wu, Z.; Li, Z.; Bolinger, J. C.; Ganesan, V.; Bielawski, C. W.; et al. Regioregularity and Single Polythiophene Chain Conformation. *J. Phys. Chem. Lett.* **2011**, *2*, 1400–1404.

(61) Collins, B. A.; Tumbleston, J. R.; Ade, H. Miscibility, Crystallinity, and Phase Development in P3HT/PCBM Solar Cells: Toward an Enlightened Understanding of Device Morphology and Stability. *J. Phys. Chem. Lett.* **2011**, *2*, 3135–3145.

(62) Brown, P. J.; Thomas, D. S.; Köhler, A.; Wilson, J. S.; Kim, J.-S.; Ramsdale, C. M.; Sirringhaus, H.; Friend, R. H. Effect of Interchain Interactions on the Absorption and Emission of poly(3-Hexylthiophene). *Phys. Rev. B* **2003**, *67*, 064203–064218.

(63) Kohn, P.; Rong, Z.; Scherer, K. H.; Sepe, A.; Sommer, M.; Müller-Buschbaum, P.; Friend, R. H.; Steiner, U.; Hüttner, S. Crystallization-Induced 10-Nm Structure Formation in P3HT/PCBM Blends. *Macromolecules* **2013**, *46*, 4002–4013.

(64) Bronstein, H. A.; Luscombe, C. K. Externally Initiated Regioregular P3HT with Controlled Molecular Weight and Narrow Polydispersity. *J. Am. Chem. Soc.* **2009**, *131*, 12894–12895.

(65) Brabec, C. J.; Heeney, M.; McCulloch, I.; Nelson, J. Influence of Blend Microstructure on Bulk Heterojunction Organic Photovoltaic Performance. *Chem. Soc. Rev.* **2011**, *40*, 1185–1199.

(66) Kline, R. J.; McGehee, M. D.; Kadnikova, E. N.; Liu, J.; Fréchet, J. M. J.; Toney, M. F. Dependence of Regioregular Poly (3-Hexylthiophene) Film Morphology and Field-Effect Mobility on Molecular Weight. *Macromolecules* **2005**, *38*, 3312–3319.

(67) Zhang, R.; Li, B.; Iovu, M. C.; Jeffries-el, M.; Cooper, J.; Jia, S.; Tristram-nagle, S.; Smilgies, D. M.; Lambeth, D. N.; Mccullough, R. D.; et al. Nanostructure Dependence of Field-Effect Mobility in Regioregular poly(3-Hexylthiophene) Thin Film Field Effect Transistors. *J. Am. Chem. Soc.* **2006**, *128*, 3480–3481.

(68) Noriega, R.; Rivnay, J.; Vandewal, K.; Koch, F. P. V; Stingelin, N.; Smith, P.; Toney, M. F.; Salleo, A. A General Relationship between Disorder, Aggregation and Charge Transport in Conjugated Polymers. *Nat. Mater.* **2013**, *12*, 1038–1044.

(69) Pingel, P.; Zen, A.; Abellón, R. D.; Grozema, F. C.; Siebbeles, L. D. A.; Neher, D. Temperature-Resolved Local and Macroscopic Charge Carrier Transport in Thin P3HT Layers. *Adv. Funct. Mater.* **2010**, *20*, 2286–2295.

(70) Brinkmann, M.; Rannou, P. Molecular Weight Dependence of Chain Packing and Semicrystalline Structure in Oriented Films of Regioregular Poly(3-Hexylthiophene) Revealed by High-Resolution Transmission Electron Microscopy. *Macromolecules* **2009**, *42*, 1125–1130.

(71) Kline, R. J.; McGehee, M. D.; Kadnikova, E. N.; Liu, J.; Fréchet, J. M. J. Controlling the Field-Effect Mobility of Regioregular Polythiophene by Changing the Molecular Weight. *Adv. Mater.* **2003**, *15*, 1519–1522.

(72) Müller, C.; Ferenczi, T. a. M.; Campoy-Quiles, M.; Frost, J. M.; Bradley, D. D. C.; Smith, P.; Stingelin-Stutzmann, N.; Nelson, J. Binary Organic Photovoltaic Blends: A Simple Rationale for Optimum Compositions. *Adv. Mater.* **2008**, *20*, 3510–3515.

(73) Baek, W.-H.; Yoon, T.-S.; Lee, H. H.; Kim, Y.-S. Composition-Dependent Phase Separation of P3HT:PCBM Composites for High Performance Organic Solar Cells. *Org. Electron.* **2010**, *11*, 933–937.

(74) Van Bavel, S. S.; Bärenklau, M.; de With, G.; Hoppe, H.; Loos, J. P3HT/PCBM Bulk Heterojunction Solar Cells: Impact of Blend Composition and 3D Morphology on Device Performance. *Adv. Funct. Mater.* **2010**, *20*, 1458–1463.

(75) Kirchartz, T.; Deledalle, F.; Tuladhar, P. S.; Durrant, J. R.; Nelson, J. On the Differences between Dark and Light Ideality Factor in Polymer: Fullerene Solar Cells. *J. Phys. Chem. Lett.* **2013**, *4*, 2371–2376.

(76) Street, R. A.; Krakaris, A.; Cowan, S. R. Recombination Through Different Types of Localized States in Organic Solar Cells. *Adv. Funct. Mater.* **2012**, *22*, 4608–4619.

(77) Street, R. A.; Schoendorf, M.; Roy, A.; Lee, J. H. Interface State Recombination in Organic Solar Cells. *Phys. Rev. B* **2010**, *81*, 205307.

(78) Kirchartz, T.; Pieters, B. E.; Kirkpatrick, J.; Rau, U.; Nelson, J. Recombination via Tail States in Polythiophene:fullerene Solar Cells. *Phys. Rev. B* **2011**, *83*, 115209.

(79) Foertig, A.; Rauh, J.; Dyakonov, V.; Deibel, C. Shockley Equation Parameters of P3HT:PCBM Solar Cells Determined by Transient Techniques. *Phys. Rev. B* **2012**, *86*, 115302.

(80) Woo, C. H.; Thompson, B. C.; Kim, B. J.; Toney, M. F.; Fréchet, J. M. J. The Influence of poly(3-Hexylthiophene) Regioregularity on Fullerene-Composite Solar Cell Performance. *J. Am. Chem. Soc.* **2008**, *130*, 16324–16329.

(81) Veldman, D.; Meskers, S. C. J.; Janssen, R. A. J. The Energy of Charge-Transfer States in Electron Donor-Acceptor Blends: Insight into the Energy Losses in Organic Solar Cells. *Adv. Funct. Mater.* **2009**, *19*, 1939–1948.

(82) Tress, W.; Leo, K.; Riede, M. Optimum Mobility, Contact Properties, and Open-Circuit Voltage of Organic Solar Cells: A Drift-Diffusion Simulation Study. *Phys. Rev. B* **2012**, *85*, 155201.

(83) Clark, J.; Silva, C.; Friend, R. H.; Spano, F. C. Role of Intermolecular Coupling in the Photophysics of Disordered Organic Semiconductors: Aggregate Emission in Regioregular Polythiophene. *Phys. Rev. Lett.* **2007**, *98*, 206406.

(84) Spano, F. C. Modeling Disorder in Polymer Aggregates: The Optical Spectroscopy of Regioregular poly(3-Hexylthiophene) Thin Films. *J. Chem. Phys.* **2005**, *122*, 234701.

(85) Gierschner, J.; Mack, H.-G.; Lüer, L.; Oelkrug, D. Fluorescence and Absorption Spectra of Oligophenylenevinylenes: Vibronic Coupling, Band Shapes, and Solvatochromism. *J. Chem. Phys.* **2002**, *116*, 8596.

(86) Niles, E. T.; Roehling, J. D.; Yamagata, H.; Wise, A. J.; Spano, F. C.; Moule, A. J.; Grey, J. K. J-Aggregate Behavior in Poly-3-Hexylthiophene Nanofibers. *J. Phys. Chem. Lett.* **2012**, *3*, 259–263.

(87) Gao, Y.; Grey, J. K. Resonance Chemical Imaging of Polythiophene/fullerene Photovoltaic Thin Films: Mapping Morphology-Dependent Aggregated and Unaggregated C=C Species. *J. Am. Chem. Soc.* **2009**, *131*, 9654–9662.

(88) O'Connor, B. T.; Reid, O. G.; Zhang, X.; Kline, R. J.; Richter, L. J.; Gundlach, D. J.; DeLongchamp, D. M.; Toney, M. F.; Kopidakis, N.; Rumbles, G. Morphological Origin of Charge Transport Anisotropy in Aligned Polythiophene Thin Films. *Adv. Funct. Mater.* **2014**, DOI: 10.1002/adfm.201303351.

(89) Reid, O.; Pensack, R.; Song, Y. Charge Photogeneration in Neat Conjugated Polymers. *Chem. Mater.* **2013**, DOI: 10.1021/cm4027144.

(90) Lee, K. H.; Schwenn, P. E.; Smith, A. R. G.; Cavaye, H.; Shaw, P. E.; James, M.; Krueger, K. B.; Gentle, I. R.; Meredith, P.; Burn, P. L. Morphology of All-Solution-Processed "Bilayer" Organic Solar Cells. *Adv. Mater.* **2011**, *23*, 766–770.

(91) Abbas, M.; Tekin, N. Balanced Charge Carrier Mobilities in Bulk Heterojunction Organic Solar Cells. *Appl. Phys. Lett.* **2012**, *101*, 073302.

(92) Kumar, A.; Liao, H.-H.; Yang, Y. Hole Mobility in Optimized Organic Photovoltaic Blend Films Obtained Using Extraction Current Transients. *Org. Electron.* **2009**, *10*, 1615–1620.

(93) Yin, W.; Dadmun, M. A New Model for the Morphology of P3HT/PCBM Organic Photovoltaics from Small-Angle Neutron Scattering: Rivers and Streams. *ACS Nano* **2011**, 4756–4768.

(94) Chen, H.; Hegde, R.; Browning, J.; Dadmun, M. D. The Miscibility and Depth Profile of PCBM in P3HT: Thermodynamic Information to Improve Organic Photovoltaics. *Phys. Chem. Chem. Phys.* **2012**, *14*, 5635–5641.

(95) Kozub, D. R.; Vakhshouri, K.; Orme, L. M.; Wang, C.; Hexemer, A.; Gomez, E. D. Polymer Crystallization of Partially Miscible Polythiophene/Fullerene Mixtures Controls Morphology. *Macromolecules* **2011**, *44*, 5722–5726.

(96) Chen, W.; Nikiforov, M. P.; Darling, S. B. Morphology Characterization in Organic and Hybrid Solar Cells. *Energy Environ. Sci.* **2012**, *5*, 8045–8074.

(97) Urien, M.; Wantz, G.; Cloutet, E.; Hirsch, L.; Tardy, P.; Vignau, L.; Cramail, H.; Parneix, J.-P. Field-Effect Transistors Based on poly(3-Hexylthiophene): Effect of Impurities. *Org. Electron.* **2007**, *8*, 727–734.

(98) Goodman, A. M.; Rose, A. Double Extraction of Uniformly Generated Electron-Hole Pairs from Insulators with Noninjecting Contacts. *J. Appl. Phys.* **1971**, *42*, 2823–2830.

(99) Mihailetchi, V. D.; Wildeman, J.; Blom, P. W. M. Space-Charge Limited Photocurrent. *Phys. Rev. Lett.* **2005**, *94*, 126602.

(100) Dang, M.; Hirsch, L.; Wantz, G. P3HT: PCBM, Best Seller in Polymer Photovoltaic Research. *Adv. Mater.* **2011**, *23*, 3597–3602.

(101) Müller, C.; Ferenczi, T. a. M.; Campoy-Quiles, M.; Frost, J. M.; Bradley, D. D. C.; Smith, P.; Stingelin-Stutzmann, N.; Nelson, J. Binary Organic Photovoltaic Blends: A Simple Rationale for Optimum Compositions. *Adv. Mater.* **2008**, *20*, 3510–3515.

Chapter 3 Novel 1,4-[60]Fullerene Bisadducts for Efficient Polymer Solar Cells

3.1 Introduction

Polymer solar cells have received great attention in recent years as an alternative to silicon solar cells because of their ability to be inexpensively solution processed and because they can be light weight and flexible.[1–5] The key component of a polymer-based photovoltaic is its active layer where the *p*-type conjugated polymer and *n*-type acceptor material mix to form a bicontinuous interpenetrating network, or so-called bulk heterojunction (BHJ).[6,7] Because of their high electron affinity and electron mobility, fullerene derivatives are extensively applied as the *n*-type acceptors in BHJ solar cells.[8] The power conversion efficiency (PCE) of polymer:fullerene BHJ solar cells can be as high as 10.8%,[9] with most of the recent advances coming from the design of new polymer donors and the use of new device architectures.[10] In contrast to the rapid development of polymer donors, however, progress is lagging in the design and synthesis of novel fullerene acceptors for high-efficiency organic photovoltaics. Most of the highest performing devices[9,11] still utilize the classic fullerene derivative [6,6]-phenyl-C-61-butyric acid methyl ester (PCBM), synthesized twenty years ago,[12] or its C_{70} analogue, $PC_{71}BM$.[13]

The PCE of a solar cell is proportional to the product of the short circuit current (J_{sc}), open circuit voltage (V_{oc}) and fill factor (*FF*). Thus, one strategy for improving device efficiency is to increase the V_{oc}, which is directly related to the difference between the highest occupied molecular orbital (HOMO) energy level of the polymer electron donor and the lowest unoccupied molecular orbital (LUMO) energy level of the fullerene derivative electron acceptor.

By raising the LUMO level of the fullerene derivative it should be possible to increase V_{oc} and thus the PCE.

To this end, several research groups have synthesized fullerene derivatives where 2 or more double bonds of the fullerene cage saturated.[14-19] Although V_{oc} has been demonstrated to increase with this method, devices based on most of these new fullerenes fail to maintain high J_{sc} and/or *FF* and as a result, the overall device efficiency suffers.[18,20-22] Part of this reason that altering the chemical make-up of a fullerene derivative can have detrimental effects on overall device performance is because the size and pattern of the addends can dramatically affect the electronic coupling between adjacent fullerenes, causing a significant decrease in the local electron mobility.[22]

We note that there are a few select fullerene derivatives, such as the bisadduct of PCBM (*bis*-PCBM)[23], indene C_{60} bisadduct (ICBA)[14] and its C_{70} congeners,[24] dihydronaphthyl-based C_{60} bisadduct (NCBA)[25] and di(4-methyl-phenyl)methano-C_{60} bisadduct (DMPCBA),[26] that have shown good performance when used in devices in combination with the classic crystalline semiconducting polymer poly(3-hexylthiophene-2,5-diyl) (P3HT). However, when these fullerene derivatives are used in combination with the state-of-the-art low bandgap polymers, the performance of the solar cells is typically low, with decreased J_{sc} and *FF*.[20,21,27-29] Therefore, despite the aforementioned efforts to increase the V_{oc}, PCBM (and its C_{70} analogue) are still the most successful fullerene acceptors for high performance polymer-based photovoltaics to date.

In order to design new fullerene acceptors for high performance polymer-based solar cells, the following factors need to be considered: 1) The LUMO level of the fullerene derivative should be carefully tuned so that when paired with the polymer of choice, an ideal LUMO level offset between the fullerene donor and polymer acceptor is attained. Though still under

debate,[29,30] the generally accepted range of this offset is about 0.3 eV (depending on the materials).[21,31,32] 2) Size-suitable addends are needed to assist close contacts among fullerene balls, thereby facilitating favorable electronic coupling to facilitate charge transport within the fullerene domains.[22] 3) Good solubility in organic solvents for solution processing. In this paper, we synthesize a series of new fullerene derivatives in an effort to satisfy all three of these requirements. We find that when carefully designed, fullerenes with higher LUMOs can be prepared that produce devices with higher V_{oc}'s without significant loss of J_{sc} or *FF*.

3.2 Results and discussion

To meet the requirements listed above, we have prepared a variety of 1,4-fullerene bisadducts with two addents located at the para positions of a six-membered ring of the fullerene cage (TOC Figure).[33] These fullerene derivatives have reduced symmetry and smaller π-conjugated systems,[34-36] resulting in a higher LUMO level than the corresponding 1,2-fullerene bisadducts (which have two geminate carbons being saturated, as is the case with PCBM). The LUMO level, side chain size and solubility of 1,4-fullerene bisadducts can be finely tuned by alternating the addents.[33] The particular molecules we focus on in this report are a series of 1,4-dibenzyl fullerene bisadducts (DBCBAs, Figure 3.2) bearing electron-donating methoxy group(s) on the benzyl ring(s). We also investigate the performance of these fullerenes in polymer-based solar cells in combination with both P3HT and the low bandgap polymer PTB7.[37] The best PCE based on P3HT:{1,-(2,5-dimethoxybenzyl)-4-(2',6'-dimethoxybenzyl)[60]fullerene bisadduct (2,5,2'6'-TetramethoxyDBCBA)} (**2k**) is 4.1%, which is a >20% enhancement relative to P3HT:PCBM. Furthermore, the device based on PTB7:[2,5,2',5'-TMDBCBA] (**2g**) shows a V_{oc} of 0.83 V, with a slightly higher J_{sc} (12.3 mA/cm^2) than PTB7:PCBM and a respectable *FF* (53%), resulting in a PCE of 5.4%. Perhaps

more importantly, our results clearly show that the precise nature and degree of substitution of the methoxy group(s), even by a single position on the benzyl groups, greatly influences the V_{oc} and PCE of the photovoltaic devices.

Our ability to synthesize 1,4-C_{60} bisadducts is a direct result of the ease of alkylating the C_{60} dianion.[38-43] As shown in Figure 3.2 a, the C_{60} dianion can be generated readily in dry and degased benzonitrile when C_{60} is treated with hydroquinone and base for several hours.[44] By adding a large excess of sub- stituted benzyl bromide to the dark red solution containing the C_{60} dianion, we produced the symmetric 1,4-dibenzyl C_{60} bisadducts.

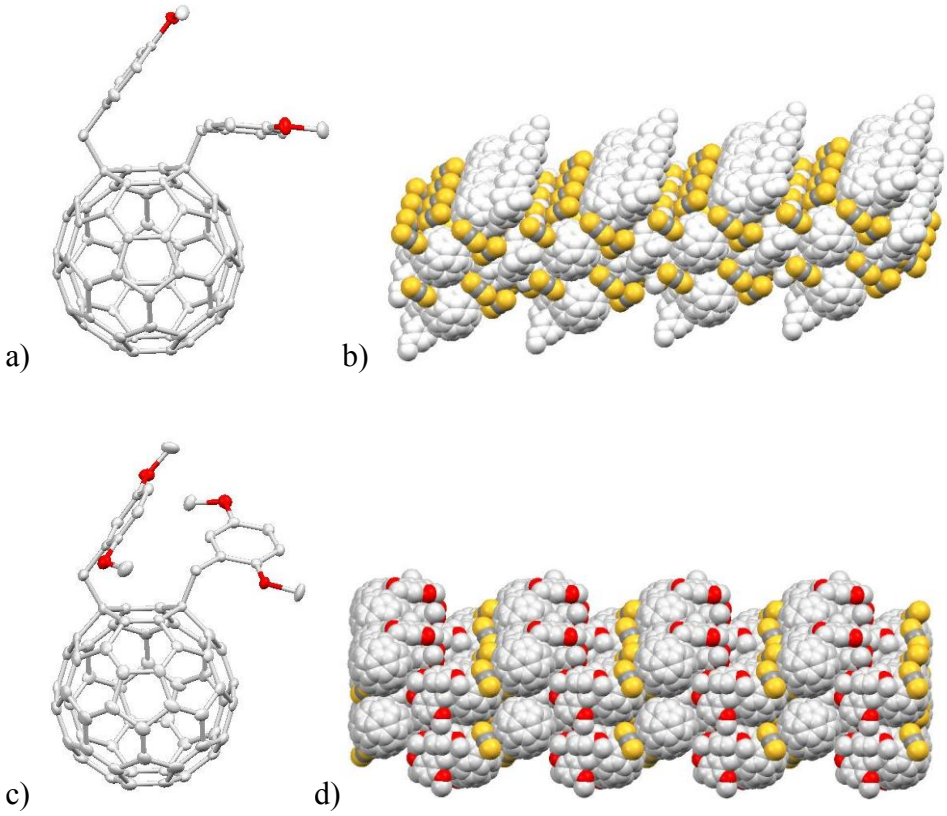

Figure 3.1 X-ray structures and packing modes of fullerene 2**c** ((a) and (b)) and fullerene 2**g** ((c) and (d)). For clarity, protons are omitted. Red: oxygen; Grey: carbon; Yellow: Sulfur.

The synthesis of the asymmetric 1,4-dibenzyl C_{60} bisadducts is more complicated, involving a two-step procedure. As shown in Figure 3.2b, C_{60} was reduced to the C_{60} dianion by proanethiolate generated *in situ* through the reaction of propanethiol and cesium carbonate in DMSO.[45] The C_{60} dianion reacted with substituted benzyl chloride to provide monoadducts with 50-60% yields. The lower reactivity of benzyl chloride relative to benzyl bromide towards S_N2, which is the last step of the reaction of C_{60} dianion, might be the reason for the different results of these two reactions.[42] The subsequent benzylation of the monoadduct then provided an asymmetrical 1,4-bisadduct bearing two different addends.

These fullerene derivatives have good solubility in common organic solvents for solar cell fabrication, such as chloroform, carbon disulfide and dichlorobenzene. The detailed synthesis of each fullerene derivative is described in the supporting information (SI). The products were characterized by mass spectrometry, ^{1}H-NMR and ^{13}C-NMR (SI). The ^{1}H-NMR spectra shows the peaks of methylene groups are split to AB quartet and four doublets for symmetrical and unsymmetrical 1,4-bisadducts, respectively, which clearly indicates a 1,4-addition pattern. Single crystals of **2c** and **2g** were obtained through slow diffusion of ethanol into a CS_2 solution. The structures of **2c** and **2g** were further confirmed by X-ray analysis (Figure 3.1). The shortest distances between the fullerene balls in the crystal structures are 3.301 Å and 3.156 Å for **2c** and **2g**, respectively.

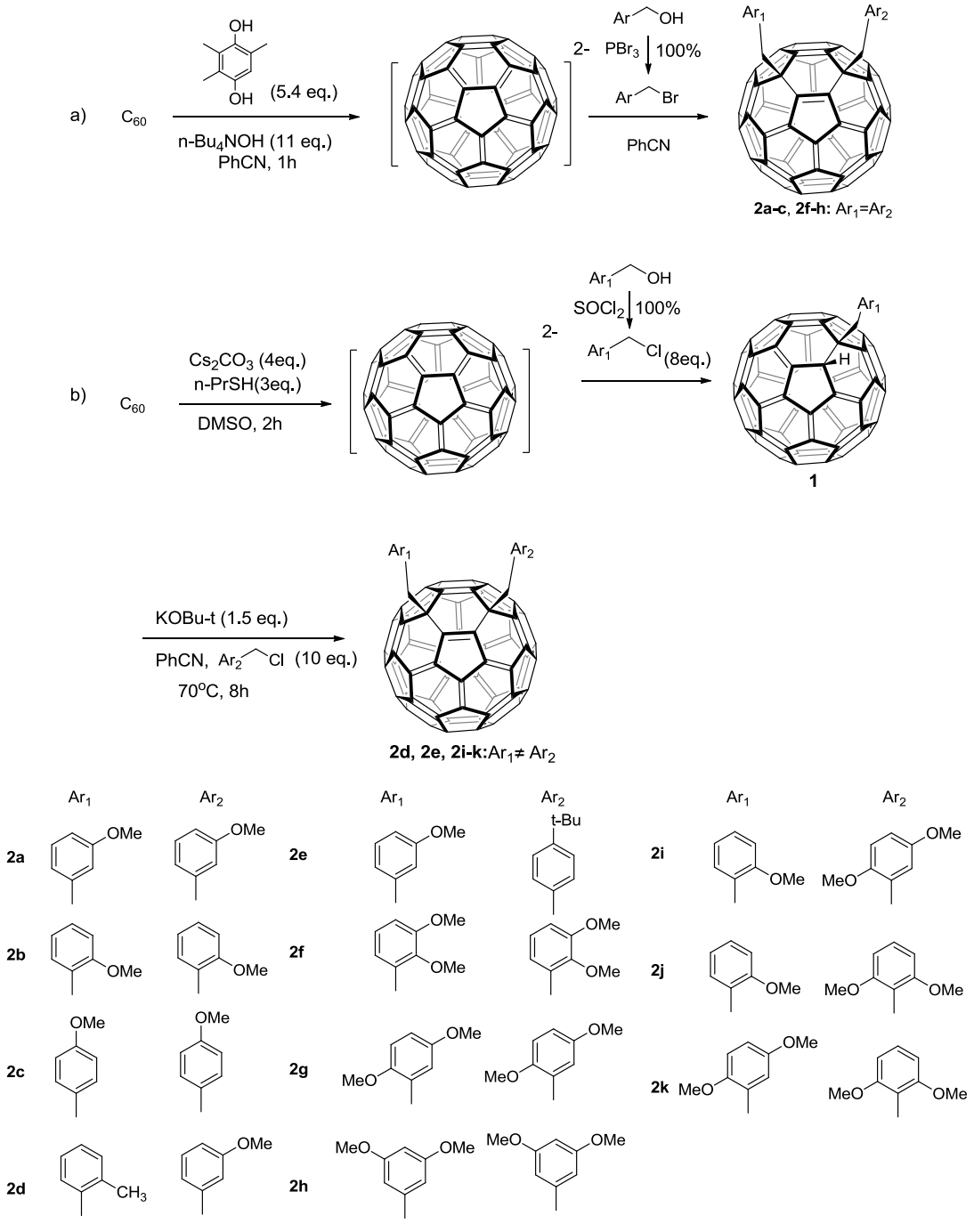

Figure 3.2 Synthesis of symmetric and asymmetric 1,4-dibenzyl [60]fullerene bisadducts.

To examine the performance of the DBCBA in solar cells, we first blended the fullerene derivatives with P3HT and fabricated photovoltaic devices with a structure of glass/ITO/poly(ethylene-dioxythiophene):poly(styrenesulfonic acid)-(PEDOT:PSS) (30

nm)/polymer:fullerene/Ca(10 nm)/Al (70 nm). All of the P3HT:fullerene-based devices (including P3HT:PCBM) had a polymer:fullerene weight ratio of 1:0.8 and an active layer thickness in the range of ~160–180 nm. Therefore the device performance comparison and conclusions we draw are based on composition- and roughly thickness-matched active layers. All active layers were thermally annealed at 150 ℃ for 20 min prior to deposition of the cathode. The details of solar cell fabrication procedures can be found in the SI. The current density (*J*) – applied bias (*V*) curves were measured for the solar cells under AM 1.5G illumination

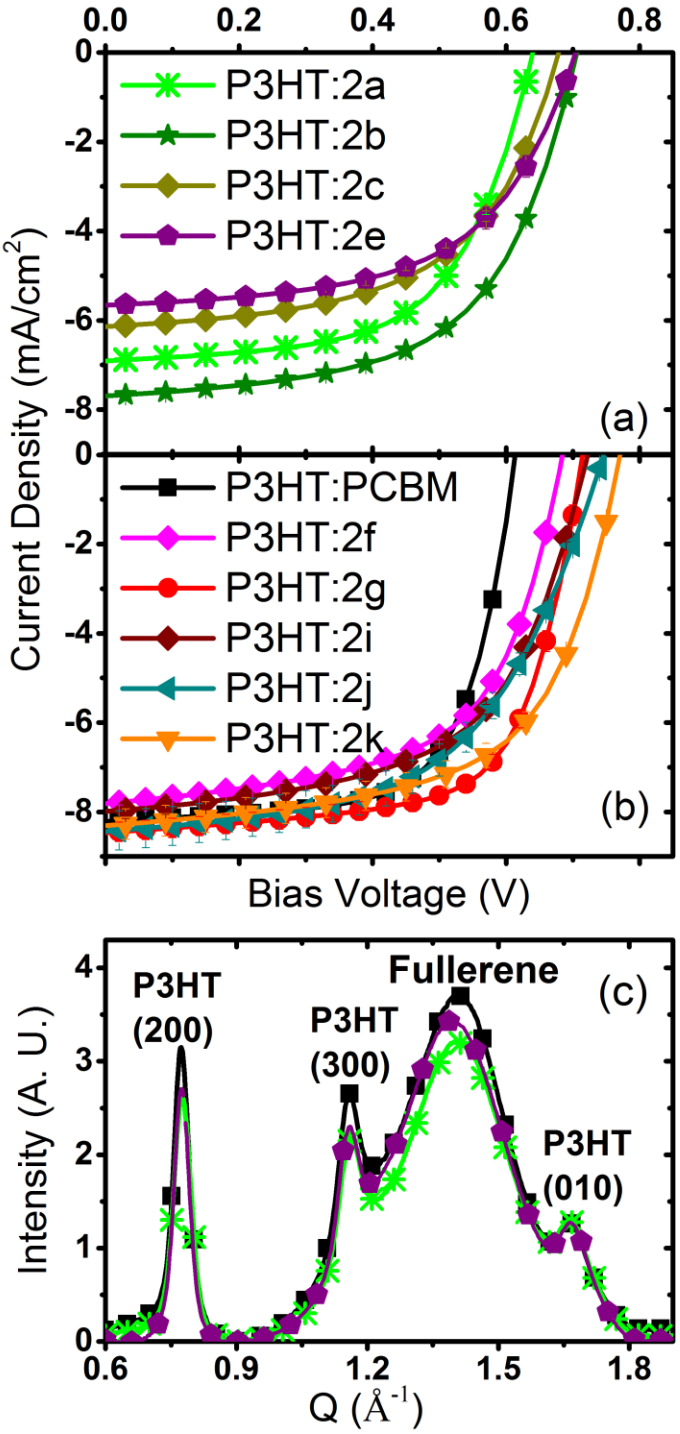

Figure 3.3 (a) and (b): Current density versus applied bias for photovoltaic devices based on P3HT:DBCBA where each of the benzyl rings in the DBCBA are substituted with one side group (a) and two methoxy groups (b). The standard P3HT:PCBM based devices is plotted in

(b) as a control. The error bars show 1 standard deviation for measurements over at least 6 independent devices. (c): Example of radially integrated 2-D GIWAXS intensities for three P3HT:fullerene active layers processed on silicon substrates.

Table 3.0-1 Summary of Photovoltaic Device Parameters

	V_{oc} (mV)	J_{sc} (mA/cm^2)	*FF* (%)	*PCE* (%)
P3HT:PCBM	613 ± 2	8.2 ± 0.2	66.6 ± 0.4	3.4 ± 0.1
P3HT:2a	640 ± 4	6.9 ± 0.2	59.4 ± 0.6	2.6 ± 0.1
P3HT:2b	716 ± 5	7.6 ± 0.3	57.6 ± 1.1	3.1 ± 0.1
P3HT:2c	679 ± 2	6.1 ± 0.2	55.4 ± 1.6	2.3 ± 0.1
P3HT:2d	667 ± 4	7.2 ± 0.1	49.2 ± 1.1	2.4 ± 0.1
P3HT:2e	704 ± 1	5.7 ± 0.3	56.1 ± 1.5	2.2 ± 0.1
P3HT:2f	680 ± 1	7.8 ± 0.1	59.7 ± 1.1	3.2 ± 0.1
P3HT:2g	715 ± 1	8.5 ± 0.2	66.3 ± 0.7	3.9 ± 0.1
P3HT:2h	588 ± 5	6.0 ± 0.1	55.4 ± 1.3	2.0 ± 0.1
P3HT:2i	720 ± 1	8.0 ± 0.2	57.5 ± 0.1	3.3 ± 0.1
P3HT:2j	740 ± 1	8.4 ± 0.5	55.0 ± 0.1	3.4 ± 0.2
P3HT:2k	771 ± 2	8.3 ± 0.3	60.1 ± 0.8	3.9 ± 0.2
PTB7:PCBM	760 ± 1	12.1 ± 0.2	64.4 ± 0.1	5.9 ± 0.3
PTB7:2g	825 ± 9	12.3 ± 0.2	53.3 ± 0.1	5.4 ± 0.1

Figure 3.3a and the upper portion of Table 1 summarize the performance of P3HT:DBCBA-based devices where the benzyl rings connected to the fullerene ball are substituent by a single side group (molecules **2a**–**2e**). We find that non-methoxy substituents on even one of the benzyl rings resulted in either lower *FF* (P3HT:**2d**) or lower J_{sc} (P3HT:**2e**) than benzyl groups with

methoxy substitution; the PCE's for devices based on non-methoxy-substituted 1,4-bisadducts were in the relatively low range of 2.2 to 2.4%. In contrast, methoxy substitution led to higher-performing devices (PCE's ranging from 2.3 to 3.1% for P3HT:**2b**) depending on the exact position at which the methoxy groups were substituted.

To understand why such subtle variations in the substitution pattern of our 1,4-bisadducts lead to such widely varying device performance, we studied the morphology of the solar cell active layers using grazing incidence wide angle X-ray scattering (GIWAXS). The experiments were performed at the Stanford Synchrotron Radiation Light Source on beamline 11−3 with a wavelength of 0.9742 Å. For these experiments, we focused on three selected polymer:fullerene systems: P3HT:PCBM, P3HT:**2a** and P3HT:**2e** (Figure 3.3c). In pure films, P3HT is an edge-on stacking polymer,[46-49] and that chain orientation is maintained upon addition of either DBCBA or PCBM (SI). However, both the characteristic fullerene diffraction observed at ~1.4 A^{-1} and the crystallinity of P3HT (as measured by the intensity of the (200) peak) are smaller when **2a** or **2e** are used in the active layer compared to when PCBM was used. This could explain the lower J_{sc} and *FF* of the photovoltaic devices based on these active layers.[49] Another notable difference is that for P3HT:**2e**, the fullerene peak is shifted towards lower Q, which corresponds to an increased spacing between fullerenes. Fullerene **2e** contains a bulky *t*-butyl group substituted on one benzyl ring, which likely hinders close packing of the fullerene molecules. Consequently, this increase in inter-fullerene spacing leads to a decreased electronic coupling between fullerenes and therefore to a decrease in carrier mobility.[22] This is also consistent with **2e** having the lowest J_{sc} among all the DCDBAs.

Figure 3.3a and the upper part of Table I also show that when the methoxy group is at the 2-position on the benzyl group, the corresponding device shows greater PCE (3.1%) compared to

the 3- position (2.6%), which in turn greater than the 4- position (2.3%). There are two potential reasons for this sensitivity to substitution position. First, the position of the methoxy group can affect the fullerene-to-fullerene contact and thus the electronic coupling and local carrier mobility. Second, the way the fullerene interacts with the polymer could be altered by the structure of the fullerene derivative, which could lead to significant variations in the resultant BHJ morphology. To investigate this, we measured the diode ideality factor, n_{ideal}, for each of our DCDBA devices by fitting their dark *J-V* curves (see SI); n_{ideal} provides a rough indicator of the charge carrier recombination mechanism.[50,51] Table S1 in the SI shows that devices with P3HT:**2b** have the most ideal (i.e. closest to bimolecular rather than trap-dominated) recombination among the **2a**-**2e** fullerene derivatives, suggesting that the variation in device performance predominantly reflects changes in the BHJ morphology.

Once we had determined that alkyl group substitution on the benzyl ring was inferior relative to methoxy group substitution for solar cell performance, we next turned to study the effect of both the number and the position of methoxy side groups. To this end, we synthesized fullerene derivatives **2f**– **2k** (Figure 3.2), and fabricated photovoltaic devices from these derivatives (whose performance parameters are summarized in the lower part of Table 1) with both P3HT and PTB7. Examples of the *J-V* curves of these devices under AM1.5G illumination are plotted in Figure 3.3b.

The most striking result of Figure 3.3b and the lower part of Table 1 is that 1,4-bisadduct fullerenes with double methoxy substituted benzyl rings lead to improved solar cell efficiency; in fact, most of the PCEs reach or surpass those of P3HT:PCBM. Both P3HT:**2g** and P3HT:**2k** show a ~20% enhancement in PCE compared to P3HT:PCBM (black squares in Figure 3.3), and P3HT:**2f**, P3HT:**2i** and P3HT:**2j** all have comparable PCEs to P3HT:PCBM devices. P3HT:**2h**

is clearly an exception, having the lowest PCE of the group, and we are currently investigating the morphology of this active layer. Compared to the monomethoxy DCDBAs **2a**–**2e**, devices using **2f**–**2k** (except for **2h**) show both higher J_{sc} as well as higher V_{oc}. The increase in V_{oc} by the second methoxy group likely results from a further increase of these fullerenes' LUMO levels. We also measured n_{ideal} values for these devices (Table S1), and found that the general trend is that devices based on **2f**–**2k** show more ideal charge carrier recombination than those based on **2a**–**2e** based ones. This indicates the nanoscale morphology of the BHJ is improved by the second methoxy group on the benzyl rings of DBCBAs, which can also contribute to the increase in both J_{sc} and V_{oc} in these devices.

Figure 3.3b and the lower part of Table 1 also reinforce the observation that the position of the methoxy group(s) has a significant effect on device performance. The dependence of V_{oc} on the methoxy position can be summarized as follows. Placing methoxy groups at the 2- or 6-positions increases V_{oc} whereas placing methoxy groups at the 3- or 5- positions lowers the V_{oc}. Furthermore, fullerenes with more methoxy groups on the 3- (or 5-) position, such as **2f** and **2g**, show lower V_{oc} than those with fewer, such as **2i**, **2j** and **2k**. When both methoxy groups are on the 3- and 5- positions, as with fullerene **2h**, the resultant device shows the lowest V_{oc}. Given this trend, we synthesized the DCDBA derivative with two methoxy groups on the 2- and 6-positions of each benzyl ring, since based on the trends discussed above this one should have even further improved device performance. Unfortunately, that fullerene was poorly soluble in the solvents needed for device fabrication, so that it could not be tested in an organic photovoltaic device.

As mentioned in the introduction, the most successful high-LUMO fullerenes studied to date (e.g., ICBA and its C_{70} analog) show poor compatibility with modern low bandgap push-pull

polymers. To see if we could break this trend with our DBCBA fullerenes, we investigated the compatibility of one of our best derivatives (**2g**) with the widely used high-performance low bandgap polymer PTB7. We employed the same device structure as described above, with the active layer consisting of PTB7 and **2g** at a polymer:fullerene weight ratio of 1:1.5 with a thickness of ~90 nm (additional fabrication details in the SI). These active layers were used as-cast without thermal annealing before cathode deposition. For comparison, we also fabricated PTB7:PCBM devices, and UV-Visible absorption shows that the 2 sets of devices were indeed thickness- and composition-matched (Fig. 3b).

The device performance results are summarized in Fig. 3a and the bottom of Table 1. The results show that **2g**, which showed the best performance when blended with P3HT, also demonstrates good compatibility with PTB7. PTB7:**2g** devices show higher V_{oc} than PTB7:PCBM devices, and a similarly high J_{sc}. The overall device efficiency of PTB7:**2g** is slightly lower than PTB7:PCBM, however, due to a slightly lower *FF*.

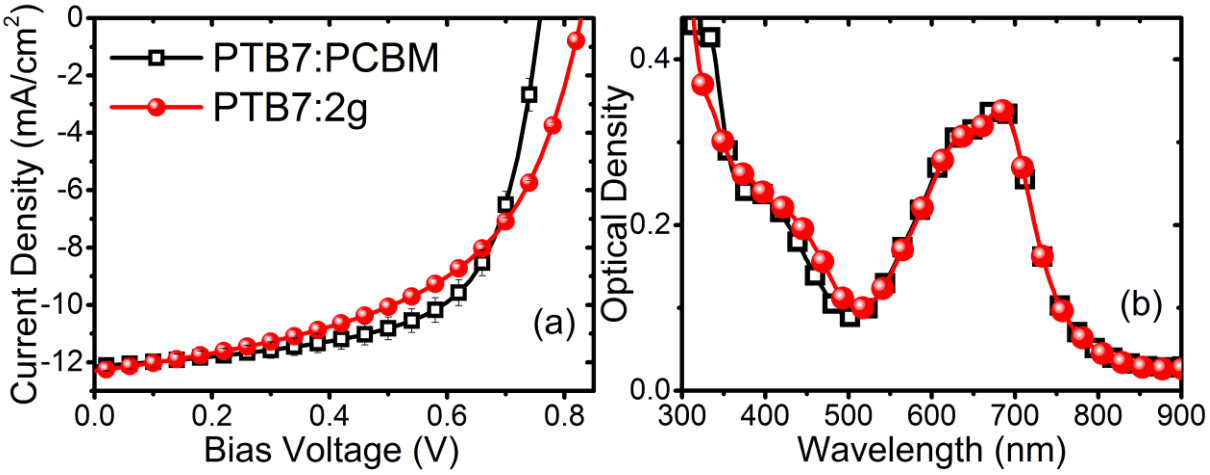

Figure 3.4 (a): Current density versus applied bias for photovoltaic devices based on PTB7:PCBM (open black square) and PTB7:**2g** (red circle). The error bars show 1 standard

deviation for measurements over at least 6 independent devices; (b): UV-visible absorption spectra for the same active layers used in (a).

In summary, we have synthesized a new series of 1,4-[60]fullerene bisadducts with higher LUMO levels than PCBM. We evaluated their performance in BHJ solar cells and comparing their morphology and performance to that of the workhorse fullerene PCBM. Our best fullerene derivatives show more than 20% enhancement in device efficiency when combined with P3HT, largely due to in improved V_{oc} in the devices due to the higher LUMO of the bis-substituted fullerenes. We found that adding methoxy groups to the benzyl rings increases the device performance and that the number and position of these groups can have a dramatic effect on the solar cell efficiency due to morphological changes. Unlike the other fullerene bisadducts, which are outperformed by PCBM when combined into BHJs with low bandgap polymers, our **2g** 1,4-bisadduct demonstrated good compatibility with one of the best performing red polymers, PTB7. We are currently working on a deeper understanding of both the device physics and active layer morphologies for these fullerene derivatives in polymer solar cells to help guide further synthesis and increase device performance. We believe that 1,4-dibenzyl fullerene bisadducts and future C_{70} versions of these molecules are promising candidates for replacing PCBM to improve the performance of conjugated polymer-based solar cells.

3.3 References

(1) Deibel, C.; Dyakonov, V. *Rep. Prog. Phys* **2010**, *73*, 096401.

(2) Jørgensen, M.; Carlé, J. E.; Søndergaard, R. R.; Lauritzen, M.; Dagnæs-Hansen, N. A.; Byskov, S. L.; Andersen, T. R.; Larsen-Olsen, T. T.; Böttiger, A. P. L.; Andreasen, B.; Fu, L.;

Zuo, L.; Liu, Y.; Bundgaard, E.; Zhan, X.; Chen, H.; Krebs, F. C. *Sol. Energy Mater. Sol. Cells* **2013**, *119*, 84.

(3) Krebs, F. C.; Espinosa, N.; Hösel, M.; Søndergaard, R. R.; Jørgensen, M. *Adv. Mater.* **2014**, *26*, 29.

(4) Søndergaard, R. R.; Hösel, M.; Krebs, F. C. *J. Polym. Sci. Part B Polym. Phys.* **2013**, *51*, 16.

(5) Scharber, M. C.; Sariciftci, N. S. *Prog. Polym. Sci.* **2013**, *38*, 1929.

(6) Yu, G.; Gao, J.; Hummelen, J. C.; Wudl, F.; Heeger, A. J. *Science (80-.).* **1995**, *270*, 1789.

(7) Heeger, A. J. *Adv. Mater.* **2014**, *26*, 10.

(8) Li, C.-Z.; Yip, H.-L.; Jen, A. K.-Y. *J. Mater. Chem.* **2012**, *22*, 4161.

(9) Liu, Y.; Zhao, J.; Li, Z.; Mu, C.; Ma, W.; Hu, H.; Jiang, K.; Lin, H.; Ade, H.; Yan, H. *Nat. Commun.* **2014**, *5*, 5293.

(10) Zhou, H.; Yang, L.; You, W. **2012**.

(11) He, Z.; Zhong, C.; Su, S.; Xu, M.; Wu, H.; Cao, Y. *Nat. Photonics* **2012**, *6*, 591.

(12) Hummelen, J. C.; Knight, B. W.; Lepeq, F.; Wudl, F.; Yao, J.; Wilkins, C. L. *J. Org. Chem.* **1995**, 532.

(13) Wienk, M. M.; Kroon, J. M.; Verhees, W. J. H.; Knol, J.; Hummelen, J. C.; van Hal, P. a; Janssen, R. A. J. *Angew. Chem. Int. Ed. Engl.* **2003**, *42*, 3371.

(14) He, Y.; Chen, H.; Hou, J.; Li, Y. *J. Am. Chem. Soc.* **2010**, 1377.

(15) He, Y.; Li, Y. *Phys. Chem. Chem. Phys.* **2011**, *13*, 1970.

(16) Meng, X.; Xu, Q.; Zhang, W.; Tan, Z.; Li, Y.; Zhang, Z.; Jiang, L.; Shu, C.; Wang, C. *ACS Appl. Mater. Interfaces* **2012**, *4*, 5966.

(17) Zhang, C.; Chen, S.; Xiao, Z.; Zuo, Q.; Ding, L. *Org. Lett.* **2012**, *14*, 1508.

(18) Kim, B.; Lee, J.; Seo, J. H.; Wudl, F.; Park, S. H.; Yang, C. *J. Mater. Chem.* **2012**, *22*, 22958.

(19) He, Y.; Shao, M.; Xiao, K.; Smith, S. C.; Hong, K. *Sol. Energy Mater. Sol. Cells* **2013**, *118*, 171.

(20) Huang, J.-H.; Hsiao, Y.-S.; Richard, E.; Chen, C.-C.; Chen, P.; Li, G.; Chu, C.-W.; Yang, Y. *Appl. Phys. Lett.* **2013**, *103*, 043304.

(21) Faist, M. A.; Shoaee, S.; Tuladhar, S.; Dibb, G. F. A.; Foster, S.; Gong, W.; Kirchartz, T.; Bradley, D. D. C.; Durrant, J. R.; Nelson, J. *Adv. Energy Mater.* **2013**, *3*, 744.

(22) Aguirre, J. C.; Arntsen, C.; Hernandez, S.; Huber, R.; Nardes, A. M.; Halim, M.; Kilbride, D.; Kopidakis, N.; Tolbert, S. H.; Schwartz, B. J.; Daniel, N. *Adv. Funct. Mater.* **2013**, *24*, 784.

(23) Lenes, M.; Wetzelaer, G.-J. A. H.; Kooistra, F. B.; Veenstra, S. C.; Hummelen, J. C.; Blom, P. W. M. *Adv. Mater.* **2008**, *20*, 2116.

(24) He, Y.; Zhao, G.; Peng, B.; Li, Y. *Adv. Funct. Mater.* **2010**, *20*, 3383.

(25) Meng, X.; Zhao, G.; Xu, Q.; Tan, Z.; Zhang, Z.; Jiang, L.; Shu, C.; Wang, C.; Li, Y. *Adv. Funct. Mater.* **2014**, *24*, 158.

(26) Cheng, Y.-J.; Liao, M.-H.; Chang, C.-Y.; Kao, W.-S.; Wu, C.-E.; Hsu, C.-S. *Chem. Mater.* **2011**, *23*, 4056.

(27) Miller, N. C.; Sweetnam, S.; Hoke, E. T.; Gysel, R.; Miller, C. E.; Bartelt, J. A.; Xie, X.; Toney, M. F.; McGehee, M. D. *Nano Lett.* **2012**, *12*, 1566.

(28) Di Nuzzo, D.; Wetzelaer, G.-J. A. H.; Bouwer, R. K. M.; Gevaerts, V. S.; Meskers, S. C. J.; Hummelen, J. C.; Blom, P. W. M.; Janssen, R. A. J. *Adv. Energy Mater.* **2013**, *3*, 85.

(29) Shoaee, S.; Subramaniyan, S.; Xin, H.; Keiderling, C.; Tuladhar, P. S.; Jamieson, F.; Jenekhe, S. A.; Durrant, J. R. *Adv. Funct. Mater.* **2013**, *23*, 3286.

(30) Bakulin, A. A.; Rao, A.; Pavelyev, V. G.; van Loosdrecht, P. H. M.; Pshenichnikov, M. S.; Niedzialek, D.; Cornil, J.; Beljonne, D.; Friend, R. H. *Science* **2012**, *335*, 1340.

(31) Brabec, C. J.; Winder, C.; Sariciftci, N. S.; Hummelen, J. C.; Dhanabalan, A.; van Hal, P. A.; Janssen, R. A. J. *Adv. Funct. Mater.* **2002**, *12*, 709.

(32) Li, W.; Roelofs, W. S. C.; Wienk, M. M.; Janssen, R. A. J. *J. Am. Chem. Soc.* **2012**, *134*, 13787.

(33) Matsuo, Y.; Oyama, H.; Soga, I.; Okamoto, T.; Tanaka, H.; Saeki, A.; Seki, S.; Nakamura, E. *Chem. Asian J.* **2013**, *8*, 121.

(34) Matsuo, Y.; Iwashita, A.; Abe, Y.; Li, C.-Z.; Matsuo, K.; Hashiguchi, M.; Nakamura, E. *J. Am. Chem. Soc.* **2008**, *130*, 15429.

(35) Matsuo, Y.; Sato, Y.; Niinomi, T.; Soga, I.; Tanaka, H.; Nakamura, E. *J. Am. Chem. Soc.* **2009**, *131*, 16048.

(36) Tanaka, H.; Abe, Y.; Matsuo, Y.; Kawai, J.; Soga, I.; Sato, Y.; Nakamura, E. *Adv. Mater.* **2012**, *24*, 3521.

(37) Liang, Y.; Xu, Z.; Xia, J.; Tsai, S.-T.; Wu, Y.; Li, G.; Ray, C.; Yu, L. *Adv. Mater.* **2010**, *22*, 1.

(38) Subramanian, R.; Kadish, K. M.; Vijayashree, M. N.; Gao, X.; Jones, M. T.; Miller, M. D.; Krause, K. L.; Suenobu, T.; Fukuzumi, S. *J. Phys. Chem.* **1996**, *100*, 16327.

(39) Allard, E.; Rivitre, L.; Delaunay, J.; Dubois, D.; Cousseau, J. *Tetrahedron Lett.* **1999**, *40*, 7223.

(40) Cheng, F.; Murata, Y.; Komatsu, K. *Org. Lett.* **2002**, *4*, 2541.

(41) Allard, E.; Delaunay, J.; Cousseau, J. *Org. Lett.* **2003**, *5*, 2239.

(42) Allard, E.; Cheng, F.; Chopin, S.; Delaunay, J.; Rondeau, D.; Cousseau, J. *New J. Chem.* **2003**, *27*, 188.

(43) Cousseau, J.; Allard, E.; Chopin, S. *Comptes Rendus Chim.* **2006**, *9*, 1051.

(44) Toganoh, M.; Suzuki, K.; Udagawa, R.; Hirai, A.; Sawamura, M.; Nakamura, E. *Org. Biomol. Chemsitry* **2003**, *1*, 2604.

(45) Subramanian, R.; Boulas, P.; Vijayashree, M. N.; D'Souza, F.; Jones, M. T.; Kadish, K. M. *J. Chem. Soc. Chem. Commun.* **1994**, 1847.

(46) Sirringhaus, H.; Brown, P. J.; Friend, R. H.; Nielsen, M. M.; Bechgaard, K.; Spiering, A. J. H. **1999**, 685.

(47) Sanyal, M.; Schmidt-Hansberg, B.; Klein, M. F. G.; Colsmann, A.; Munuera, C.; Vorobiev, A.; Lemmer, U.; Schabel, W.; Dosch, H.; Barrena, E. *Adv. Energy Mater.* **2011**, *1*, 363.

(48) Kim, Y.; Cook, S.; Tuladhar, S. M.; Choulis, S. A.; Nelson, J.; Durrant, J. R.; Bradley, D. D. C.; Giles, M.; McCulloch, I.; Ha, C.-S.; Ree, M. *Nat. Mater.* **2006**, *5*, 197.

(49) Zhang, G.; Huber, R. C.; Ferreira, A. S.; Boyd, S. D.; Luscombe, C. K.; Tolbert, S. H.; Schwartz, B. J. *J. Phys. Chem. C* **2014**, *118*, 18424.

(50) Wetzelaer, G. A. H.; Kuik, M.; Lenes, M.; Blom, P. W. M. *Appl. Phys. Lett.* **2011**, *99*, 153506.

(51) Street, R. A.; Krakaris, A.; Cowan, S. R. *Adv. Funct. Mater.* **2012**, *22*, 4608.

Chapter 4. Vertical Phase Segregation and Surface Recombination in Polymer:Fullerene BHJ Solar Cells: The Role of Surface Energy

4.1 Background

Organic photovoltaics (OPVs) have been developing rapidly for the past decade. Their low-cost processability, flexibility and light weight provide them with extremely short energy payback time compared to most other PV techniques.[1–5] The highest-efficiency OPVs consist of blends of conjugated polymers as the electron donors and functionalized fullerenes as the electron-accepting species. The polymer and fullerene derivative active layer forms a bicontinuous interpenetrating network, which is called a bulk-heterojunciton (BHJ),[6,7] and serves as the key component of OPVs. Single-junction OPVs based on such BHJ structures have demonstrated power conversion efficiencies up to 10.8%.[8]

Due to the internal disorder of the organic materials and the complexity of the intermixed network by the donor and acceptor molecules, however, the underlying physical process governing OPV device performance is still not fully understood.[7] In particular, the spatial arrangement of the polymers and fullerene derivatives, which plays a major role in defining the morphology of the OPV active layer, is one of the most important factors that determines device efficiency.[9–16] The importance of the donor-acceptor morphology not only includes intermixing or demixing of the two components, but also their vertical phase segregation (VPS), i.e., the mass distribution of the two components in the direction perpendicular to the substrate. VPS has significant impact on device performance[17–21] because carrier movement parallel to the substrate plane does not result in charge collection by the electrode.

A variety of experiments have been carried out to characterize VPS in organic photovoltaic active layers. For example, X-ray photoelectron spectroscopy[17,22] can probe the surface

properties of polymer:fullerene BHJ films by quantifying the ratio between the polymer and fullerene near the surface, providing a way to estimate the VPS inside the active layer. Measuring the contact angle[18] serves a similar purpose for estimating the polymer-to-fullerene ratio at the surface. Neutron reflectometry takes advantage of the scattering contrast between fullerene derivatives and other organic materials to directly investigate the vertical distribution of the materials in the active layer;[23–28] Dynamic secondary ion mass spectrometry is a destructive technique that allows the depth-profiling of the organic layer by removing materials using continuous focused ion beam;[13,18,29,30] Spectroscopic ellipsometry can nondestructively study the dielectric properties of the active layer and estimate the degree of VPS through fitting experimental data using mathematical representations.[31–33]

The generally accepted picture based on a combination of these measurements is that for the classic polymer-based BHJ based on P3HT and PCBM, P3HT tends to segregate towards the organic/air interface (provided the substrate consists of a high surface energy material) and that PCBM prefers to segregate towards the bottom of the active layer.[21] Indeed, most substrates used for the fabrication or characterization of OPVs, such as Si/SiO_2,[34] PEDOT:PSS-coated ITO,[21] and ZnO nanoparticles coating ITO,[20] have high surface energies, so the fact that the polymer rises to the top of most active layers is a fairly general result. Moreover, thermal annealing has been demonstrated to further enhance VPS: more PCBM molecules are driven away from the top of the active layer after thermal annealing of an as-cast film.[21] Different research groups have attributed the reason for VPS to the relative surface energies of the polymer and fullerene:[17,21,34] PCBM is a higher surface energy material than P3HT, so it prefers the higher surface energy organic/substrate interface.

The reason VPS is important to understand is that in a 'normal' sandwich-structure device geometry, the top surface of the BHJ film will be in contact with the cathode, so VPS in the P3HT:PCBM system is detrimental for charge carrier collection. This is because the electrons in the PCBM network cannot be easily collected by the cathode and the holes on the polymer cannot be conducted to the anode to generate current. Indeed, poor device performance due to unfavorable vertical phase segregation in the P3HT:PCBM device has been reported by multiple groups.[19,31,35,36] It also has been shown that VPS can lead to an "S-shaped" *J*-*V* curve for the device with an extremely poor fill factor (*FF*), thereby reducing device efficiency.[35,37]

Considering the number of literature articles that report observations regarding the effect of VPS on device performance, it is surprising how few reports have investigated the precise way in which VPS affects the device physics, such as the nature of recombination. This is because device physics experiments usually measure contributions from both the bulk of the active layer and the interface between the active layer and the electrodes. To separate the effects from the bulk and the interface, one needs to find systems where the bulk and interfacial composition can be separately controlled. This requires more than one polymer:fullerene pair, some of which must have similar contributions from the bulk while the VPS is varied, and some of which must have similar VPS with different bulk properties.

In this work, we perform exactly this type of study by combining three different fullerene derivatives with two different conjugated polymers to systematically separate the device physics contributions of VPS from the bulk. Specifically, we utilized two novel 1,4-dibenzyl fullerene bisadducts (**2g** and **2h**) synthesized by our group (basic molecular properties in Chapter 3) together with PCBM as electron acceptors and P3HT and PTB7 as electron donors. As shown in Chapter 3 and Figure 4.1 below, even though **2g** and **2h** have very similar chemical structures,

when combined with P3HT they show dramatically different solar cell performance. In particular, fullerene **2g** shows similar J_{sc} and *FF* to devices built with PCBM, but devices built with **2g** have higher PCE than PCBM because the higher LUMO energy level of **2g** leads to an increased V_{oc}.

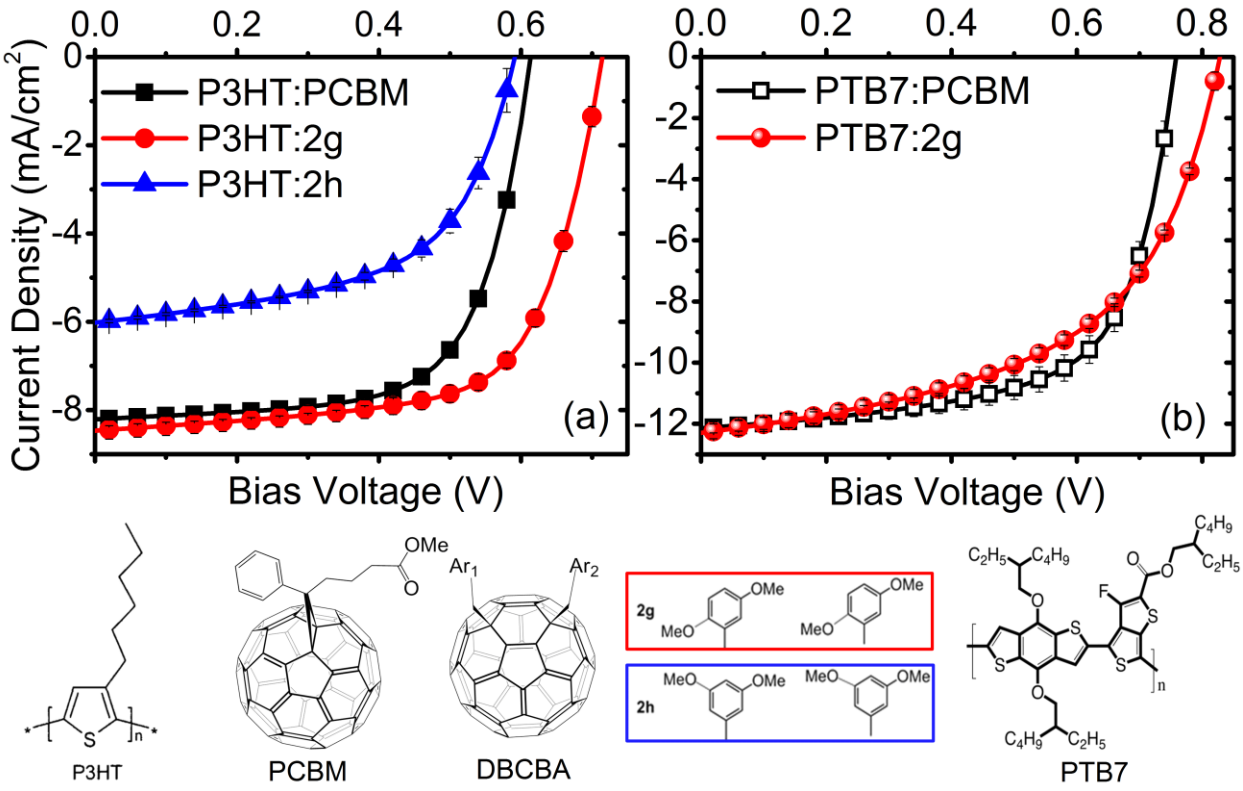

Figure 4.1 (a): *J-V* characteristics for solar cells with a structure of ITO/PEDOT:PSS/P3HT:Fullerene/Ca/Al under AM-1.5 solar illumination. All active layers were annealed at 150 ℃ for 20 min prior to the deposition of the cathode material. (b): *J-V* characteristics of PTB7:PCBM (black square) and PTB7:**2g** (red circle) photovoltaic devices under 1-sun with the same device structure as in (a). Below the *J-V* curves are the chemical structures for the polymers and fullerene derivatives used.

Our investigation begins by investigating the bulk morphology of our different polymer/fullerene pairs using grazing incidence wide angle X-ray scattering (GIWAXS), and the effects on device physics via photocurrent spectral response (PSR), transient photocurrent (TPC), transient photovoltage (TPV), and diode ideality factor analysis. We show that the main reason for the performance variation between devices with **2h** and the other fullerenes is that **2h** over phase separates from both polymers. In addition, **2h** produces a high defect state density inside the charge transfer bandgap that results in more trap-assisted recombination. In contrast, fullerene **2g** shows similar bulk device physics as devices built with PCBM. All of the analysis shows that the VPS between the devices with PCBM and the two fullerene bisadducts are different, a result of the fact that the relative surface energies of the polymer and fullerene are reversed between PCBM and either **2g** or **2h**. This allows us to demonstrate that the interface effects caused by VPS dominate bulk effects in determining charge carrier density and lifetime. Taken together, this allows us to rationally select the best device architecture for different polymer:fullerene systems by simple surface energy measurements taken prior to device fabrication.

4.2 Experimental Methods

With detailed experimental procedures provided in Section 4.5, below is the brief description of the experimental methods we used in this work.

The 1,4-dibenzyl [60] fullerene bisadducts, **2g** and **2h**, were previously synthesized and characterized by our group (see Chapter 3). PCBM, P3HT and PTB7 were commercially available materials.

Photovoltaic devices were fabricated in geometries of either ITO/PEDOT:PSS/Active Layer/Ca/Al ("normal") or ITO/ZnO nanoparticle layer/Active Layer/MoO_3/Ag ("inverted"). The P3HT:fullerene BHJ active layers were prepared by spin-coating the P3HT:fullerene (1:0.8 weight ratio) blended solutions onto the substrates to make ~180 nm thick films. The active layers were thermally annealed at 150 ℃ for 20 min prior to the deposition of any top electrode. The PTB7:fullerene active layers were prepared by spin-coating a PTB7:**2g** (1:1.5 weight ratio) or a PTB7:PCBM (1:1.34 weight ratio) blended solution onto the substrates to make ~95 nm thick films.

The active layer morphology was characterized by GIWAXS. The organic layers were prepared with the same method used for photovoltaic device fabrication, but on silicon substrates.

For all device physics characterizations, the samples analyzed were the those used in the *J-V* measurements.

The ideality factors of the photovoltaic devices were obtained with two methods: 1) fitting the dark *J-V* curve in the exponential region and 2) analyzing the open circuit voltage versus light intensity.

Electronic structures and carrier densities/lifetimes were obtained by using optoelectronic measurements including external quantum efficiency (EQE), PSR[22,38] and TPV/TPC[22,39,40]. In short, EQE and PSR spectra were obtained through the use of a lock-in amplifier, which measured the photocurrent from a chopped monochromatic beam across a resistor. A Si photodiode was used for wavelengths below 1050 nm whereas and a Ge photodiode was used for wavelengths above 1050 nm. TPV and TPC transients were measured by an oscilloscope with high and low input impedance selected, respectively. A dye-Nitrogen laser was employed as the

perturbation light to generate excess carriers while the background light was modulated with a white light LED module. The total carrier lifetimes were obtained by fitting the TPV signal to a single exponential; the excess carrier densities were obtained by using the differential capacitance method.[39]

Mobile dark carriers of the devices were studied by charge extraction with linear increasing voltage (CELIV),[41] which was performed on the devices in the dark under unbiased conditions.

The surface energies of the pure materials were obtained by measuring pairs of contact angles for each organic material using two different liquids (water and ethylene glycol(EG)) and analyzing the result (see Section 4.5.4).

4.3 Results and Discussion

4.3.1 Structural Characterization of the Polymer:Fullerene Active Layer

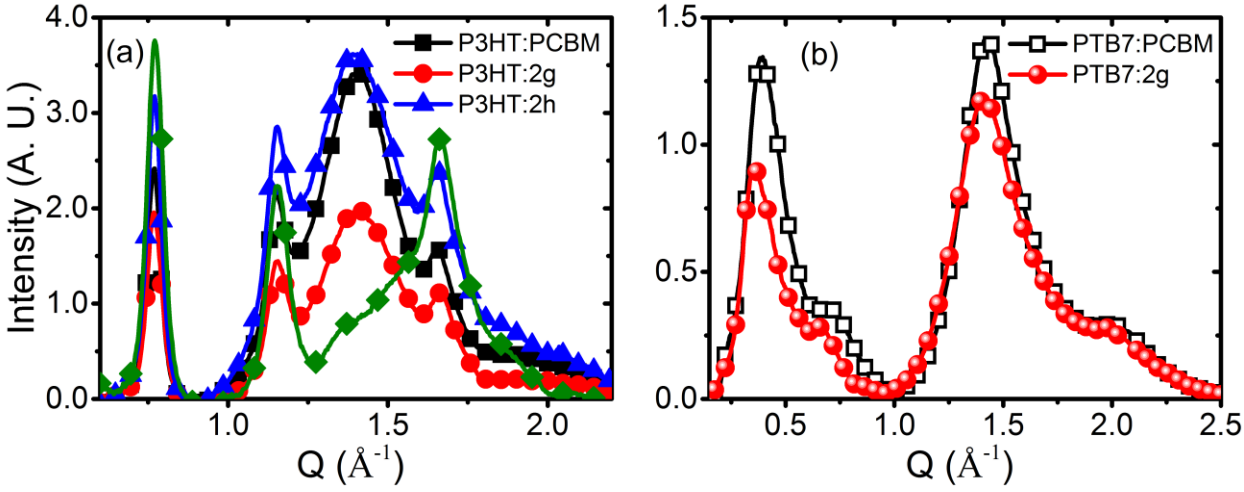

Figure 4.2 Radially integrated 2-D GIWAXS intensities for pure P3HT and three P3HT:fullerene BHJs (a) and two PTB7:fullerene BHJs (b) processed on silicon substrates. The polymer:fullerene active layers were prepared with the same method as used in device fabrication.

To understand the dramatic difference in solar cell performance between **2h** and the other fullerenes seen in Figure 5.1, we first need to investigate the bulk morphology of the active layers. As discussed in previous chapters, GIWAXS is extremely useful for determining relative crystallinities as well as the average chain orientation of the polymers. We performed GIWAXS on our polymer:fullerene BHJ samples prepared on silicon substrates at the Stanford Synchrotron Radiation Light Source on beam line 11 – 3 using a wavelength of 0.9742 Å. The active layers were prepared under the exact same conditions using the same procedures as for device fabrication. The results are plotted in Figure 4.2. We find that compared to the thickness-matched pure P3HT sample, all of the BHJ samples blended with different fullerenes show less total polymer scattering; e.g., the intensities of the P3HT (200) peak at ~ 0.77 Å and the (010) peak at ~ 1.67 Å are weaker when fullerene derivatives are present. This makes physical sense since the fullerene derivatives in the BHJs can hinder crystalline growth of the polymer.[37] Thus, relative to the pure P3HT sample, the more the scattering peak area is reduced for the BHJ sample, the more intimately mixed are polymer and fullerene in the active layer.

The P3HT:**2h** BHJ sample (blue up triangles, Figure 4.2 (a)) shows higher P3HT scattering intensity and integrated peak areas (i.e., higher overall polymer crystallinity) than the P3HT:PCBM sample (black squares), which in turn is higher than the P3HT:**2g** sample (red circles). The fullerene crystallinity/aggregation scattering band peaked at ~1.4 Å also has integrated areas that show the same trends. This indicates poor intermixing of the polymer and **2h**, suggesting that P3HT:**2h** samples are over phase separated. Indeed, photovoltaic devices based on P3HT:**2h** show both lower J_{sc}'s and *FF*'s than those based on P3HT:PCBM or P3HT:**2g**, consistent with non-ideal phase separation between the polymer and fullerene in active layers based on P3HT:**2h**.

In addition to the integrated area, the *Q* value of the scattering peak also contains useful information on the packing of the molecules.[42] The fullerene peak for P3HT:**2h** is positioned at 1.389 Å while the peaks for P3HT:PCBM and P3HT:**2g** are at 1.402 Å and 1.409 Å, respectively. This means the spacing between the **2h** fullerene derivatives is larger than the spacing between **2g** molecules or between PCBM molecules. As discussed in Chapter 3.2, the size and position of the side groups on the benzyl rings for the fullerene bisadducts have significant impact on the packing of the fullerene derivatives. Apparently, the methoxy groups on the benzyl rings of fullerene **2h**, which has a (3, 5, (3',5')) substitution pattern, hinders close packing of the fullerene molecules. Similar observations have been made previously (Chapter 3.2 Figure 3.2 (c)), where we found that a bulky *t*-butyl group substituted on the benzyl ring also shifted the fullerene scattering peak towards low *Q*. Overall, the fact that local packing of **2h** is unfavorable, in combination with the fact that **2h** over phase separates from P3HT, explains the inferior solar cell performance for P3HT:**2h** based devices.

Figure 4.2(b) shows similar results for PTB7:PCBM and PTB7:**2g** BHJ samples. The overall trend of both the polymer and fullerene crystallinity is the same as that with P3HT: both the polymer and fullerene show lower crystallinity when **2g** is used relative to when PCBM is used. However, unlike P3HT, PTB7 is not a highly crystalline polymer.[29,43] Therefore, the **2g** molecule may result in a slightly over-mixed morphology, inhibiting efficient charge transport in the PTB7 network, resulting the lower *FF* we observed in the PTB7:**2g** devices.

Overall, our GIWAXS results suggest the nanoscale morphology of P3HT:**2h** active layers is markedly different from those of P3HT:PCBM and P3HT:**2g** active layers. The over phase separation in P3HT:**2h** BHJs and the relatively poor fullerene-fullerene contact of **2h** explain the poor device performance when this fullerene is used. In the next Section, we discuss how these

factors affect the device physics, e.g., how they affect the electronic structure and change the mechanism of recombination within the device.

4.3.2 Interfacial States Measured by Photocurrent Spectral Response

Since the chemical structure of fullerene **2h** gives a different active layer BHJ morphology than standard fullerenes such as PCBM, we would like to investigate if this morphology gives a different electronic structure for the polymer:fullerene BHJs. To this end, we employed the photocurrent spectral response (PSR) technique to determine the polymer-fullerene interfacial density of states distribution. The PSR is a technique that measures the device photocurrent as a function of excitation energy.[38,44–46] This provides a sensitive way to measure the optical absorption, so long as the absorption gives rise to mobile carriers. The PSR method is useful for revealing the electronic structure at the interface between the polymer and fullerene because it can detect not only the bulk absorption from the pure materials but also the lower-energy absorptions due to band-to-band charge-transfer (CT) or even excitations due to the localized states within the CT bandgap.

Figure 4.3 shows the PSR spectra we obtained for the photovoltaic devices whose *J*-*V* characteristics are shown in Figure 4.1.

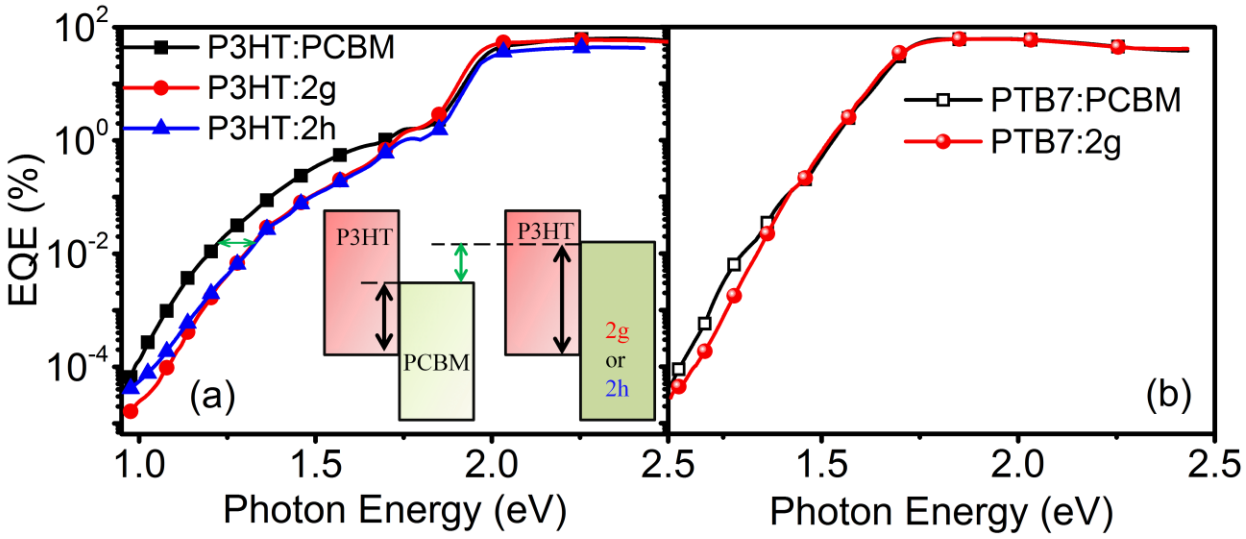

Figure 4.3 PSR spectra for the same P3HT:fullerene (a) and PTB7:fullerene (b) photovoltaic devices used in Figure 4.1. The horizontal difference (green arrow) between the spectra of devices with PCBM and **2g** (or **2h**) in the photon energy range of ~1.3 – 1.6 eV in (a) or ~1.2 – 1.4 eV in (b) is mainly ascribed as the LUMO level difference between PCBM and **2g** (or **2h**). The sub-gap EQE (<~1.3 eV) contains information on the interfacial transitions involving localized states within the CT bandgap. The device with **2h** clearly shows more localized density of states than those with **2g** or PCBM.

The PSR spectra can be typically divided into three main regions. Using the data in Figure 4.3(a) as an example, these regions include: (1) photons with energies higher than ~1.7 eV which mainly excite the bulk and cause absorption of individual materials. This region is the typically reported external quantum efficiency (EQE) spectrum that contributes to most of the photocurrent. The low spectral response for P3HT:**2h** device in this region agrees with the low J_{sc} from the *J*–*V* measurement; (2) photons with an energy between ~1.3 eV (depending on the bandgap of the materials) to ~1.7 eV, which measure the CT band-to-band excitation from the polymer HOMO to the fullerene LUMO. The increased LUMO energy of **2g** and **2h** relative to

PCBM causes a horizontal shift of the PSR spectra towards higher photon energies,[46] as shown by the green arrows in Figure 4.3(a); (3) photons with energies lower than the CT band-to-band transition energy, which probe transitions involving localized states within the CT bandgap. The lower the photon energy, the deeper the localized states within the bandgap.[45]

Our results clearly show that devices based on P3HT:**2h** contain more deep states than devices based on P3HT:PCBM or P3HT:**2g**. These deep states clearly are traps for charge carriers and therefore can function as recombination centers. Since the CT band-to-band absorption of P3HT:**2h** (blue up triangles) and P3HT:**2g** (red circles) overlap, the main difference in the subgap electronic structure between them is the increased density of deep trap states for P3HT:**2h**. These trap states will give rise to more Shockley-Read-Hall (SRH) type recombination,[47–49] which also can be reflected in an increase in the dark diode ideality factor,[45] as discussed in details in the next section. The higher density of traps with **2h** is also consistent with the poor photovoltaic performance of devices based on this material.

We also obtained PSR spectra for PTB7:fullerene devices, as shown in Figure 4.3(b). The spectral responses of the two devices start to separate around 1.45 eV due to the LUMO level difference between the fullerenes. The response in the low photon energy region for both systems decay with a similar slope and show no clear signs of deep state traps for either fullerene.

4.3.3 Ideality Factor and Bulk Recombination

The diode ideality factor (n_{ideal}) reflects the dominant recombination mechanism of a photovoltaic device.[44,50–53] For conjugated polymer-based solar cells, n_{ideal} typically ranges from 1 to 2. Diode theory tells us that $n_{ideal} = 1$ corresponds to the ideal band-to-band recombination.

Larger values of n_{ideal} are consistent with localized state/trap-assisted recombination.[50] Based on the PSR spectra in the previous Section, we would expect higher n_{ideal} values for devices made with **2h** than those with **2g** or PCBM.

We measured n_{ideal} for our devices using two different methods. First we fit the exponential region of the dark *J*–*V* curve and obtained n_{ideal} using the maximum-slope differential method (Figure 4.4(a) and (b)).[54] Second, we measured V_{oc} as a function of illumination intensity (Figure 4.4(c) and (d)). This allowed us to calculate n_{ideal} at each light intensity using the linear dependence of the photocurrent density on light intensity:

$$n_{\mathrm{ideal,light}} = \frac{qV_{\mathrm{oc}}}{kT} / \{\ln\left(\frac{J_{\mathrm{ph}}}{J_{\mathrm{s}}} + 1\right)\} \quad (1)$$

where q is the elementary charge, k is the Boltzmann's constant, T is temperature, J_{ph} is the photocurrent density, J_s is the saturation current.[54]

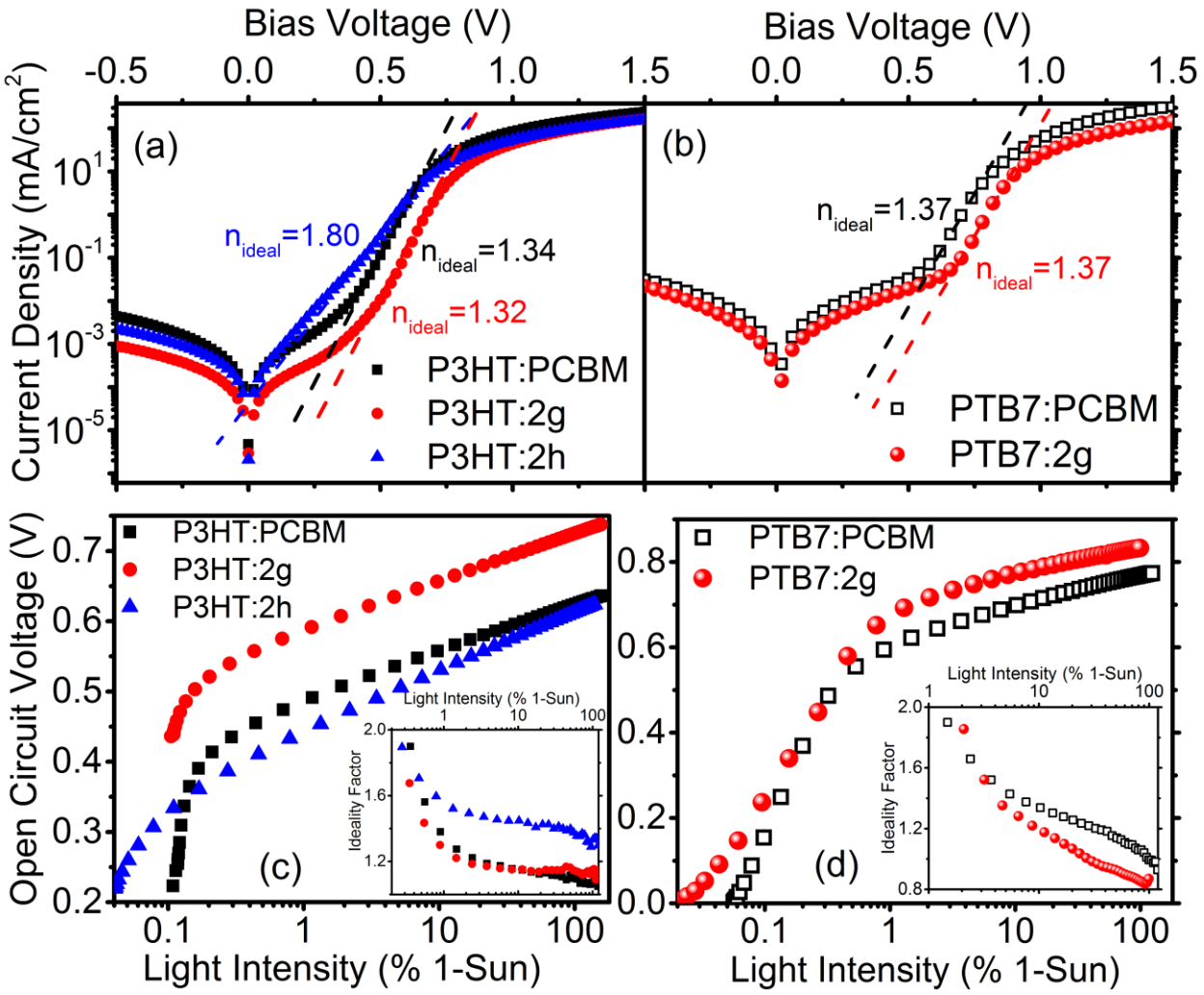

Figure 4.4 (a) and (b): Dark *J-V* curves for the same devices used in Figure 4.1. The dashed lines show the fitting region used to obtain the dark ideality factors. (c) and (d): The measured V_{oc} as a function of illumination intensity for the same devices. The insets show the corresponding differential ideality factors calculated using Eq. (1).

The solid lines in Figure 4.4(a) and (b) show the fits to the exponential regions of the dark *J-V* curve for each device. The n_{ideal} values shown next to the lines indeed confirm what we predicted from the PSR measurements. P3HT:**2h** shows the highest ideality factor, n_{ideal} = 1.80, indicating that the dominant recombination mechanism for P3HT:**2h** devices is trap-assisted, or

SRH type. The ideality factor of the P3HT:**2g** and P3HT:PCBM devices are much lower, with values of n_{ideal} = 1.32 and 1.34, respectively. This means there is more band-to-band recombination in these devices. Similarly, when PTB7 was used, the ideality factor for devices with **2g** and PCBM are indistinguishable with a value of n_{ideal} = 1.37. The data is again consistent with the PSR data, which showed that PTB7 devices with **2g** and PCBM had comparable localized state density distributions.

The trend of the $n_{ideal,light}$ values we obtained from measuring V_{oc} as a function of light intensity is the same as that obtained from the dark *J*–*V* curve fitting. The $n_{ideal,light}$ values we determined at a light intensity of 10% of 1-Sun were 1.45, 1.15 and 1.14 for P3HT:**2h**, P3HT:**2g** and P3HT:PCBM based devices, respectively. At that same intensity, the $n_{ideal,light}$ values for PTB7:**2g** and PTB7:PCBM are 1.19 and 1.34, respectively. The discrepancy between n_{ideal} and $n_{ideal,light}$ is mainly due to the fact that the dark ideality factor is affected by series resistance at low light intensities and shunt resistance at high light intensities.[50] Since the light ideality factor $n_{ideal,light}$ is obtained at open circuit, series resistance effects at high light intensities are eliminated. This makes light ideality factors easier to interpret and more representative of the underlying recombination mechanism at the typical intensities of solar cell operation.[50]

Despite these differences, both methods of measuring the ideality factor lead to the same conclusions. In P3HT:**2h** BHJ devices, the high density of states within the CT bandgap make bulk recombination trap-dominated. On the other hand, the ideality factors for devices with PCBM and **2g** are both similarly low, indicating more ideal band-to-band bulk recombination. Given the similar ideality factors and the similar J_{sc}'s and *FF*'s in their *J*–*V* curves, it is clear that the P3HT:**2g** and P3HT:PCBM systems provide two polymer:fullerene BHJs with distinct materials which have similar device physics in the bulk. Since our goal is to study the effect of

vertical phase segregation (VPS) on device physics, our next task is to investigate to see whether or not the surface properties of these BHJs are different, and if so, to relate such differences to VPS in the active layers.

4.4.4 Vertical Phase Segregation and Surface Recombination

Our analysis of the V_{oc} as a function of light intensity experiment showed a particularly interesting feature: at high light intensities, $n_{ideal,light}$ for both the PTB7:PCBM and PTB7:**2g** BHJs dropped below unity. Moreover, for the P3HT-based devices, even though $n_{ideal,light}$ stayed above 1 at all intensities, the trend in the data makes clear sign that the light ideality factor would drop below 1 if we had continued to increase the illumination intensity. The observation of less than unity ideality factors has previously been described by Kirchartz *et al.*,[50] who attributed such below unity values to surface recombination. The argument is that once V_{oc} reaches the device's built-in voltage, it cannot increase further even if the light intensity is further increased because the device has lost its selectivity for charge carriers at this voltage. However, the charge carrier concentration will still increase as the light intensity increases. Consequently, the charge carriers will be extracted by the nearest electrode as there is no internal electric field to drive the carriers toward either the cathode or anode depending on the sign of the charge. Thus, based on Eq. (1), the light ideality factor calculated at sufficiently high light intensities can show values below 1.[50] These concepts are illustrated by the cartoon shown in Figure 4.5.

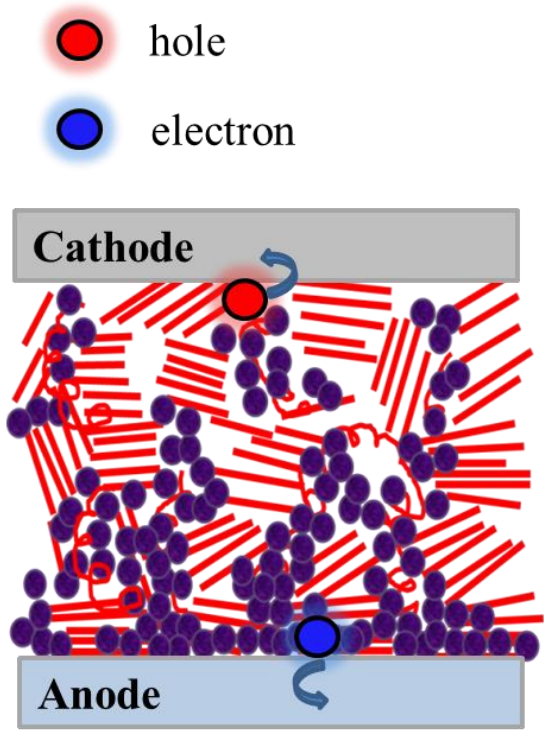

Figure 4.5 A cartoon illustrating the idea of surface recombination. The red solid lines represent the polymer and the purple circles represent the fullerene derivatives.

For the devices studied in the previous sections, $n_{ideal,light}$ decreased in P3HT:PCBM devices at high light intensities (inset of Figure 4.4(c)) but remained roughly constant in P3HT:**2g** devices at all light intensities. This indicates that in BHJ devices with P3HT as the donor, the use of PCBM as the acceptor leads to more surface recombination than the use of **2g**. This analysis is less clear for the devices made from P3HT:**2h**, as it is not straightforward to gain clues on surface recombination the light ideality factor due to the fact that the trap-assisted recombination dominates, making $n_{ideal,light}$ high even at high light intensities. When PTB7 is used as polymer donor, devices with both PCBM and **2g** show clear signatures of surface

recombination (inset of Figure 4.4(d)). Since surface recombination involves charge carriers being collected by the "incorrect" electrode, more surface recombination means that more such carriers being generated near the "incorrect" electrode. To make this happen, the VPS of the active layer with more surface recombination must be such that more fullerene derivatives are near the anode and/or more polymers are near the cathode; after all, if there were only polymer located near the cathode or fullerene near the anode, it would be impossible for carriers to be collected by the 'wrong' electrode. Thus, a rough model for VPS for the different polymer:fullerene combinations based on the light ideality factor analysis can be summarized as follows. When used in combination with P3HT, PCBM tends to segregate towards the bottom of the active layer (near the anode). Bisadduct **2g**, on the other hand, has a light ideality factor that becomes flat at higher light intensities, suggesting that it does not have a strong preference for the anode interface and therefore does not promote surface recombination. When used in combination with PTB7, in contrast, both PCBM and **2g** segregate towards the bottom of the active layer.

4.4.5 The Role of Surface Recombination in Charge Carrier Density and Lifetime

Given that we know that surface recombination is operative in all of our PV devices, it is logical to ask how surface recombination compares with bulk recombination in determining the overall recombination device recombination kinetics. For example, for fullerene derivatives **2g** and PCBM, which have similar bulk recombination in their devices when combined with P3HT, would differences in surface recombination give rise to any significant differences in carrier density or carrier lifetime? To answer this question, we employed transient photovoltage (TPV) and transient photocurrent (TPC) techniques.

TPV and TPC techniques have been widely applied in OPVs to study the excess charge carrier densities and their decay dynamics in working photovoltaic devices under standard operating conditions with regard to bias voltage and illumination intensity.[22,39,52,53,55–59] In TPV measurements, the cell is held at V_{oc} under continuous illumination and then a weak, perturbative ns-duration laser pulse is applied to the device. The excess charge carriers generated by the laser pulse will decay with time only through recombination. Fitting the decay of the transient photovoltage produced by these excess carriers provides a measurement of the total carrier lifetime, $\tau(n)$. TPC is used in conjunction with TPV to obtain the excess charge carrier density in the device. In TPC measurements, the same weak perturbative laser pulse is applied to the device at the same background illumination intensity as used in TPV, but this time the device is operated under short circuit conditions. By analyzing the current transients generated by the excess carriers using the differential capacitance method, we were able to calculate the average excess charge carrier densities n.[22,39]

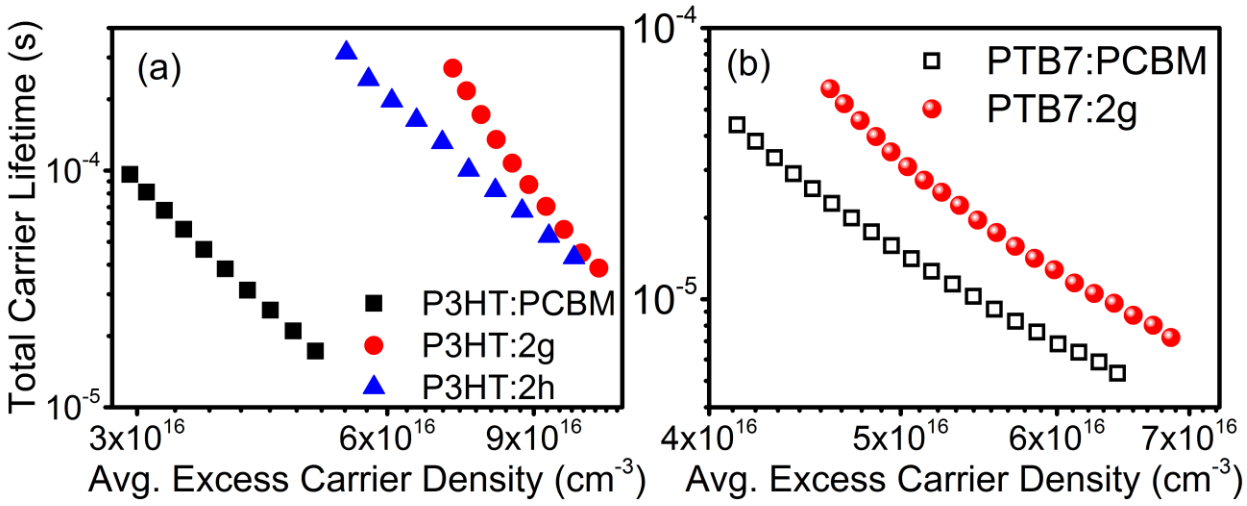

Figure 4.6 Total carrier lifetime versus average excess carrier density for the same P3HT:fullerene (a) and PTB7:fullerene (b) devices used in Figure 4.1. The total carrier lifetime

and average excess charge carrier density are obtained from TPV and TPC measurements, respectively. Each data set represents the average of at least two devices.

The results from TPV/TPC measurements on the same devices used above are plotted in Figure 4.6. Each of the polymer:fullerene BHJ devices demonstrate a power-law-like behavior with $\tau(n) \sim n^{-\lambda}$ with $\lambda > 1$, indicating the existence of trap-assisted recombination.[39,53] The order of the power law (λ) varies slightly between different material systems.[53] More importantly, however, is that Figure 4.6(a) shows that the absolute total carrier lifetime for P3HT:fullerene samples at the same carrier density varies by over an order of magnitude: devices with the fullerene bisadducts **2g** and **2h** show carrier lifetimes more than an order of magnitude greater than those with PCBM as acceptors. Or, expressed another way, the carrier densities at the same lifetime for devices with **2g** or **2h** are ~3 times higher than those with PCBM.

These differences in recombination kinetics are surprising, particularly given that the bulk recombination in these devices is described by a similar ideality factor, as discussed above. This suggests that the differences in recombination kinetics are almost entirely the result of surface recombination, so that active layers with similar bulk morphologies have significantly different VPS. For P3HT:PCBM BHJ devices, unfavorable VPS that places P3HT near the cathode and PCBM near the anode causes more surface recombination, which decreases both the average carrier density and carrier lifetime. In P3HT:**2g** devices, the VPS is reversed with respect to the P3HT:PCBM, leading to favorable VPS that causes the carriers generated in the active layer to recombine more through the internal BHJ polymer:fullerene interface rather than through the organic/electrode interfaces. The large difference in kinetics we observe between **2g** and PCBM thus indicate that the effect of the surface recombination can overwhelm that of the bulk recombination in determining the overall device recombination properties. This is highlighted

by the behavior of the P3HT:**2h** device, whose carrier density and lifetime were comparable to P3HT**:2g** device, even though these two derivatives have vastly different amounts of bulk recombination.

For PTB7, the recombination properties between devices made with PCBM and **2g** do not differ the way they do in P3HT-based devices, though the PTB7 device with **2g** still shows higher carrier lifetimes. Since the $n_{ideal,light}$ vs. light intensity data indicates both PTB7:PCBM and PTB7:**2g** devices have strong surface recombination, the relatively small difference between their carrier lifetimes is perhaps not unexpected.

The observation of huge variations in the carrier lifetimes at the same carrier density also has also been reported by other groups. Credgington *et al.*[53] reported devices with carrier lifetime varied over orders of magnitude when different polymer donors were applied in combination of PCBM or its C_{70} analog. Ryan *et al.*[58] reported a study of recombination in a squaraine donor/C_{60} acceptor bilayer system. They found by increasing the squaraine layer thickness, they could reduce the number of surface recombination sites between C_{60} and the anode, which led to enhanced carrier densities and increased in carrier lifetimes at the same carrier density. All of this work is in agreement with our results that surface recombination can dramatically alter carrier recombination properties.

4.4.6 Using the VPS Model to Explain Device Physics: Dark Carriers Measured by CELIV

In the previous section, we argued that differences in VPS could explain the different device recombination properties of polymer:PCBM and polymer**:2g** active layers. Our TPV/TPC results suggested that P3HT:2h and P3HT:**2g** have a similar degree active layer VPS, and that the VPS was reversed with P3HT:PCBM. To further investigate this conclusion, we employed the

charge extraction by linear increasing voltage (CELIV) technique.[57] We have previously reported that when a cathode metal such as Ca was evaporated onto the active layer, the device with fullerene derivative molecules segregated towards the top of the active layer showed carriers that could be extracted in a CELIV experiment in the dark.[22] Chapter 5 provides more details and a deeper investigation into this effect. Here, we take advantage of the conclusion that extracted dark carriers correspond to an active layer that has VPS enriched in fullerene at the top. The idea is that when a linear voltage ramp is applied to a PV device in the dark at voltages where carriers are not injected, the device behaves as a capacitor and the resulting current transient is constant in time. If excess carriers are presented in the sample, these carriers are swept out when the voltage ramp is applied, leading to a 'bump' in the current transient whose integral is proportional to the number of excess carriers.

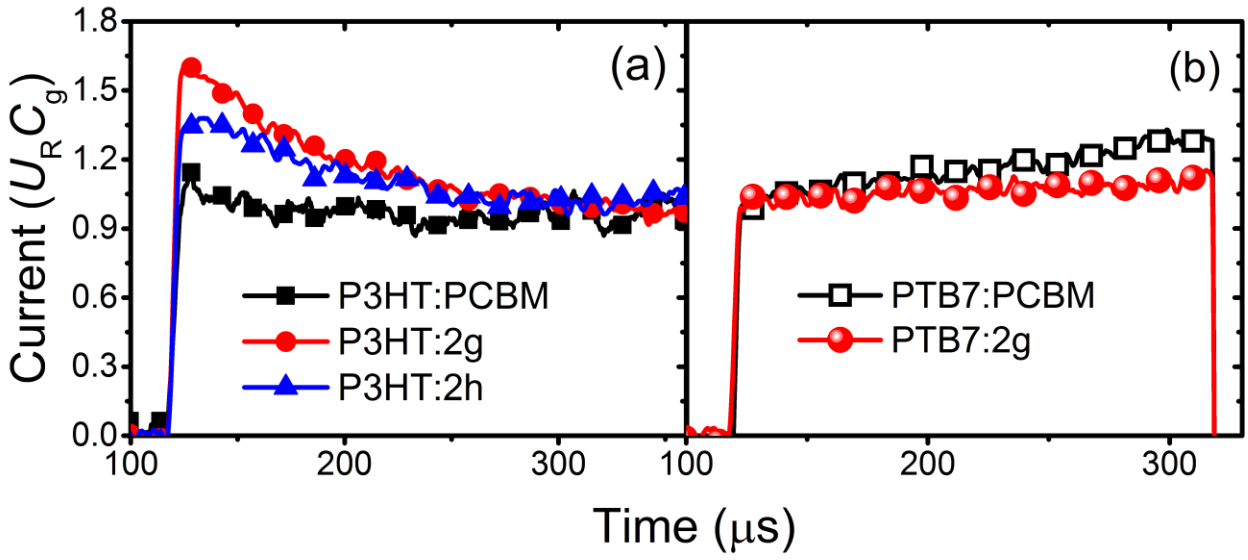

Figure 4.7 Dark CELIV current transients on diodes with P3HT:fullerene (a) and PTB7:fullerene (b). All curves were divided by the product of their geometric capacitance (C_g) and CELIV ramp rate (U_R).

Figure 4.7 shows the dark CELIV data taken on the same devices studied in this work. In Figure 4.7(a), the noticeable bumps in the CELIV transients are signatures of dark carriers present in the devices.[22] For P3HT:**2g** and P3HT:**2h** devices, the number of dark carriers is much greater than the negligable amount of dark carriers seen in the P3HT:PCBM device, indicating that the top surface of the active layer is predominantly composed **of 2g** or **2h**, while devices made with PCBM have primarily P3HT at the top interface. We observed no dark carriers in our PTB7:fullerene devices, suggesting that no significant amount of fullerene is present at the top of the active layer. All of these results are consistent with our general picture of VPS in these systems.

4.4.6 Using Vertical Phase Separation to Understand the Difference Between V_{oc} and E_{ct}

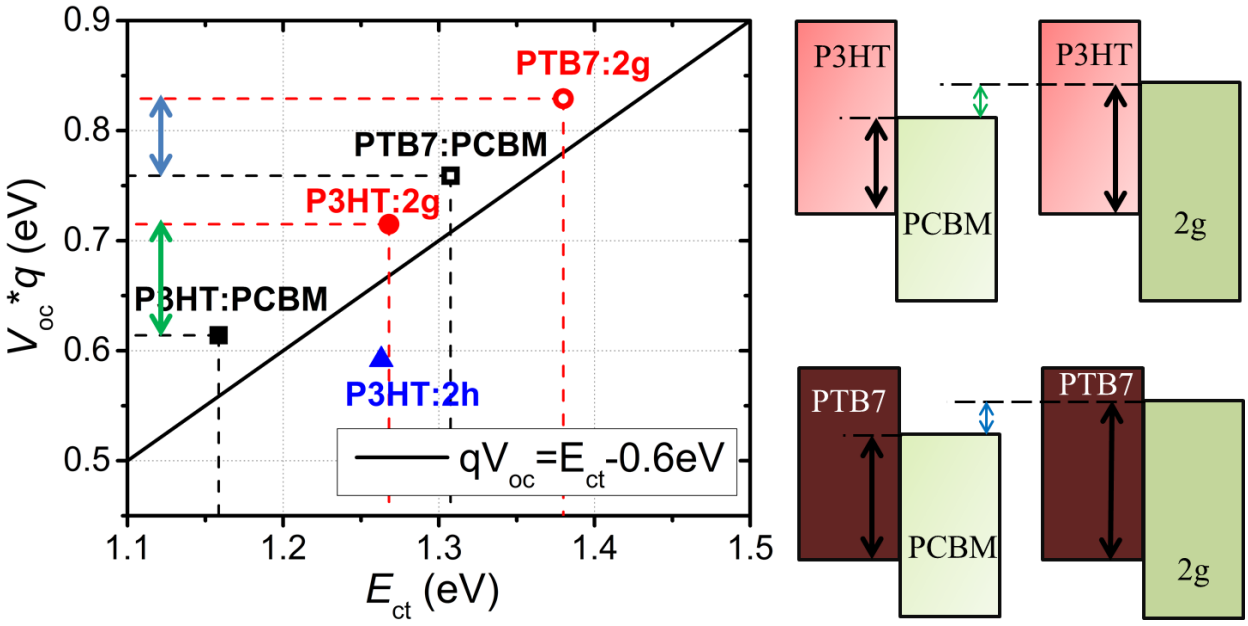

Figure 4.8 Plot of V_{oc}*q versus charge transfer state energy for the five polymer:fullerene BHJ systems. The solid line in the left plot represents the typical difference between V_{oc} and E_{ct} for OPVs, which is about 0.6 eV. All of our devices are above the line except for the P3HT:2h device due to its non-ideal bulk recombination. The arrows in the left plot show the difference

between the V_{oc} when different fullerenes are used and the arrows in the band diagrams on the right side show the LUMO difference between the fullerene derivatives.

The VPS that causes surface recombination also affects the open circuit voltage of polymer solar cells. In Figure 4.8 we plot the V_{oc} of the devices obtained from the *J*–*V* measurements of Figure 4.1 versus the CT bandgap obtained by fitting the PSR spectra (section 4.3.2) using the model by Vandewal, K. R. *et al*.[60–62] The solid line indicates the typical energy loss between the CT state energy and the measured V_{oc} (multiplied by the elementary charge) for OPVs.[63] All of the data points for the devices we made, except for P3HT:**2h**, are above the solid line; the difference between qV_{oc} and E_{ct} for these devices is in the range of 0.5 – 0.6 eV, indicating that the energy loss due to recombination in these devices is above the OPV average. For the P3HT:**2h** devices, the E_{ct} is similar to P3HT:**2g**, as expected since the LUMO level of these two fullerene bisadducts does not differ significantly (see Chapter 3). However, since trap-assisted recombination is dominant in the bulk of the P3HT:**2h** BHJ device, the data point in Figure 4.8 is far below the solid line. This again suggests that the V_{oc} of the P3HT:**2h** device is governed primarily by the poor morphology of its active layer.

Further examination of Figure 4.8 shows a variation in the V_{oc} differences between polymer:PCBM and polymer:**2g** devices when the two different polymers were used. The V_{oc} difference between devices with P3HT:PCBM and P3HT:**2g** is ~101 mV, but this difference becomes only ~70 mV when PTB7 is used. The V_{oc} of an OPV device depends on the energy gap between acceptor LUMO and donor HOMO, E_{ct}, and the nature of the carrier recombination in the cell.[53] The right side in Figure 4.8 shows an energy level diagram illustrating that even when the polymer energy levels are different, differences in E_{ct} with different fullerenes should stay constant, equal to the LUMO level differences between the fullerenes. However, our PSR

data shows that the difference in E_{ct} with different fullerenes is not constant when different polymers are used: E_{ct} (P3HT:PCBM) – E_{ct} (P3HT:2g) = ~109 meV, and E_{ct} (PTB7:PCBM) – E_{ct} (PTB7:2g) = ~ 73 meV. This change in the E_{ct} difference is roughly equal to the change in V_{oc} difference, which says that the CT bandgap energy change is the main contribution to the variation in V_{oc}.

If the change in V_{oc} does arise from a change in CT energy, this suggests that the energy level of either the polymer HOMO or the fullerene LUMO is changed in at least one of the polymer:fullerene systems. We attribute this to the change in the LUMO of **2g** when used in combination with P3HT in 'normal' structure PV devices for the following reason: as we show in the following section (4.4.8), we made 'inverted' devices we found that the variation in V_{oc} difference between devices with different polymers no longer exists: i.e., the V_{oc} difference for devices with **2g** and PCBM is independent of the polymer was used. The main change between the normal vs. inverted structure was a decrease of V_{oc} for P3HT:**2g** inverted device, which gave V_{oc} (P3HT:2g) – V_{oc} (P3HT:PCBM) ≈ V_{oc} (PTB7:2g) – V_{oc} (PTB7:PCBM). The V_{oc}'s for the other inverted devices were almost identical to the normal structure. Thus, the change had to come from a shift in the **2g** LUMO level in the P3HT:2g BHJ 'normal' device.

4.4.7 Understanding Vertical Phase Segregation by Measuring Surface Energies via Contact Angle

Overall, many experimental results can be explained by the idea that VPS is different for different fullerene derivatives in different polymers. In this section, we investigate the fundamental molecular properties that cause VPS to differ so dramatically.

Surface energy is the excess energy at the surface of a material compared to the bulk. In the OPV community, the surface energy of organic materials has been considered the reason behind VPS in BHJ solar cells.[17,20,21,34] If we consider a device with a structure of Electrode A/Polymer:Fullerene/Electrode B, where the surface energy of electrode A is larger than that of electrode B, then the organic material with the lower surface energy prefers to segregate towards B while that with the higher surface energy prefers to segregate towards A. Most substrates used in fabricating OPV devices consist of high surface energy materials, so the organic material with the higher surface energy usually spontaneously segregates towards the bottom of the film.

In addition to the surface energies of the electrodes, different processing also can enhance or hinder VPS. For example, thermal annealing can enhance the natural VPS that occurs due to electrode surface energies,[19] whereas the use of solvent additives can alter the direction of VPS.[64] There also are claims that surface energies are important for determining the bulk morphology of polymer/fullerene BHJs: in other words, that the degree of phase separation is related to the difference in surface energies between the two materials.[65]

To evaluate the surface energies of the polymers and fullerene derivatives used in this study, we performed contact angle measurements on thin films of each pure organic material. We used two different liquids, water and ethylene glycol (EG), to obtain pairs of contact angles for each material and then calculated the surface energy of each pure material via:

$$\cos\theta = 2\sqrt{\frac{\gamma_{sv}}{\gamma_{lv}}} - 1 \qquad (2)$$

where θ is the contact angle, γ_{sv} is the solid/vapor surface energy, γ_{lv} is the liquid/vapor surface energy.[66] The images used to measure the contact angle with water for P3HT, PTB7, PCBM, **2g** and **2h**, are shown in Figure 4.9. The surface energies determined from the contact angles for both water and EG, determined via Eq. 2 using literature values for γ_{lv},[67] are summarized in

Table 4.1. The small discrepancies between the surface energies obtained using different solvents is mainly due to the difference in polarity of different liquids, as has been discussed elsewhere.[66] For our purposes, however, only on the relative surface energies of the polymers and fullerenes are important for understanding VPS, and indeed the ordering of the surface energies for the five different materials stays the same between different liquids.

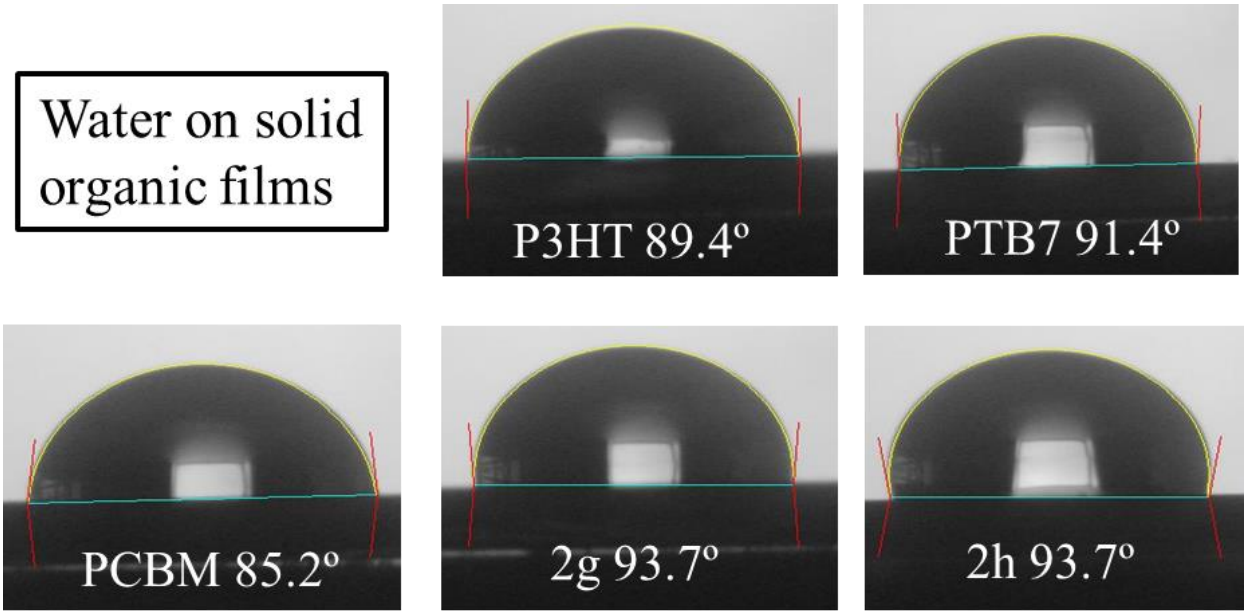

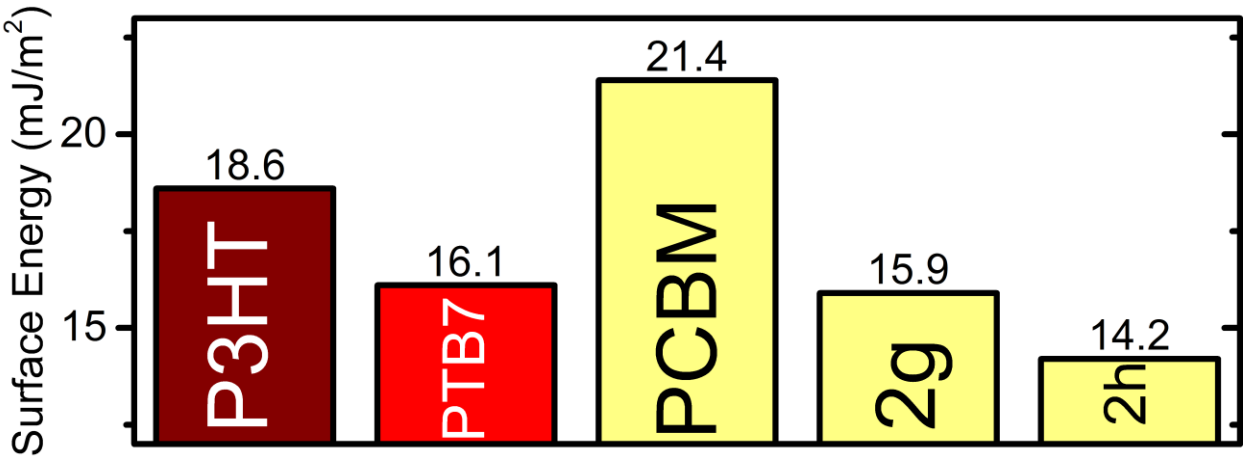

Figure 4.9 Top: Contact angle images taken on liquid water/thin films (<100 nm) consisted of pure organic material. Bottom: Bar graphs for the calculated surface energies for pure polymers or fullerene derivatives from water contact angle measurements.

Table 4.1 Summary of measured contact angles and the calculated surface energies

Organic Layer	*Contact Angle Water* (degree)	*Contact Angle EG* (degree)	*Surface Energy Water* (mN/m)	*Surface Energy EG* (mN/m)
P3HT	89.4	63.5	18.6	25.0
PTB7	93.4	66.0	16.1	23.9
PCBM	85.2	54.5	21.4	28.7
2g	93.7	65.4	15.9	23.9
2h	96.6	69.7	14.2	21.6

For either liquid, the surface energies we obtained have the following order: **2h** < **2g** ≈ PTB7 < P3HT < PCBM. This result is important for understanding VPS when fabricating active layers from blends of these materials. First, the 1,4-dibenzyl fullerene bisadducts **2g** and **2h** have much lower surface energy than PCBM. In fact, their surface energies are even lower than that of P3HT. This implies that both **2g** and **2h** will prefer to reside near the top interface of the active layer. In contrast, PCBM will tend to segregate towards the bottom of the active since its surface energy is higher than that of the polymer. For PTB7:**2g** BHJs, the polymer and fullerene are expected to form a well-mixed active layer with little VPS due to the fact that **2g** and PTB7 have almost identical surface energies. The results in Table 4.1, taken together, allow us to build an expectation for the VPS in each of our polymer/fullerene combinations that is summarized in Figure 4.10. The surface energy analysis provides us with the fundamental reason for explaining

the observed the changes in the device physics such as the TPV/TPC results and the excess carriers measured by CELIV.

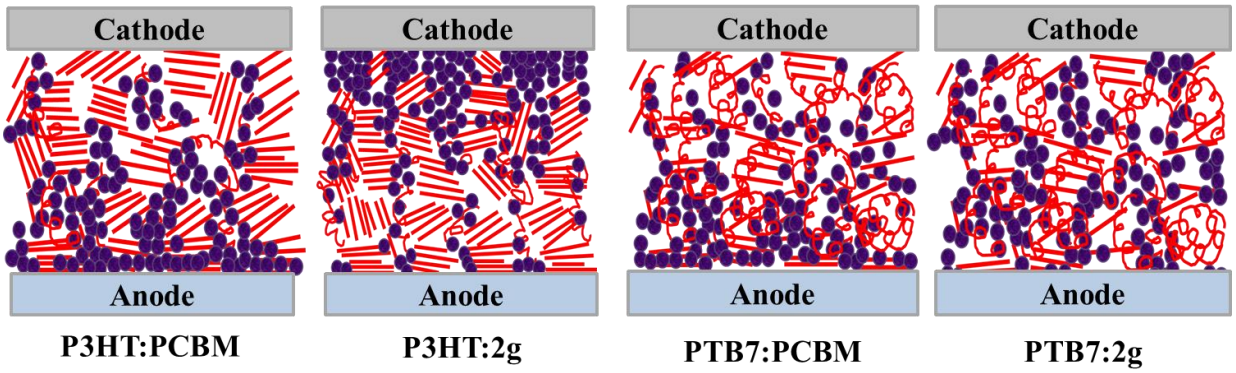

Figure 4.10 Cartoons illustrating different vertical phase segregation in different polymer:fullerene systems, based on the relative surface energies of the different polymers and fullerenes summarized in Table 4.1.

4.4.8 Using Surface Energies to Understand the Operation of Normal vs. Inverted Device

As mentioned in the Introduction, several methods have been developed to try to control VPS during or after the formation of the active layer to improve device performance.[19,28,64,68,69] If VPS is unfavorable, however, the most common way to improve device performance is to invert the structure of the solar cell by making the anode on the top and cathode on the bottom, so that the originally unfavorable VPS becomes favorable in the inverted device structure. The inverted structure also provides more favorable light management in most polymer/fullerene solar cells, leading to improved J_{sc}'s.[70,71]

Based on the relative surface energies in Table 4.1/Figure 4.10, we can predict which device structure should be optimal for a given a polymer:fullerene combination. For example, we

would predict the inverted structure is better for P3HT:PCBM than the normal structure since PCBM molecules tend to segregate towards the bottom; in contrast, inverted devices would be predicted to be less ideal for P3HT:**2g** since the relative surface energies are opposite those of P3HT:PCBM. Similarly, for PTB7:PCBM, the inverted structure should be a better choice, while for PTB7:**2g**, since there is no obvious preference for VPS, inverted and normal device geometries should give comparable performance.

To verify these predictions, we fabricated inverted devices with a structure of ITO/ZnO/Polymer:Fullerene/MoO_3/Ag for all of the materials combinations studied above. The inverted device *J–V* curves are plotted in Figure 4.11, together with the results of the normal device shown in Figure 4.1 for ease of comparison; the results confirm what we predicted from the surface energy measurements.

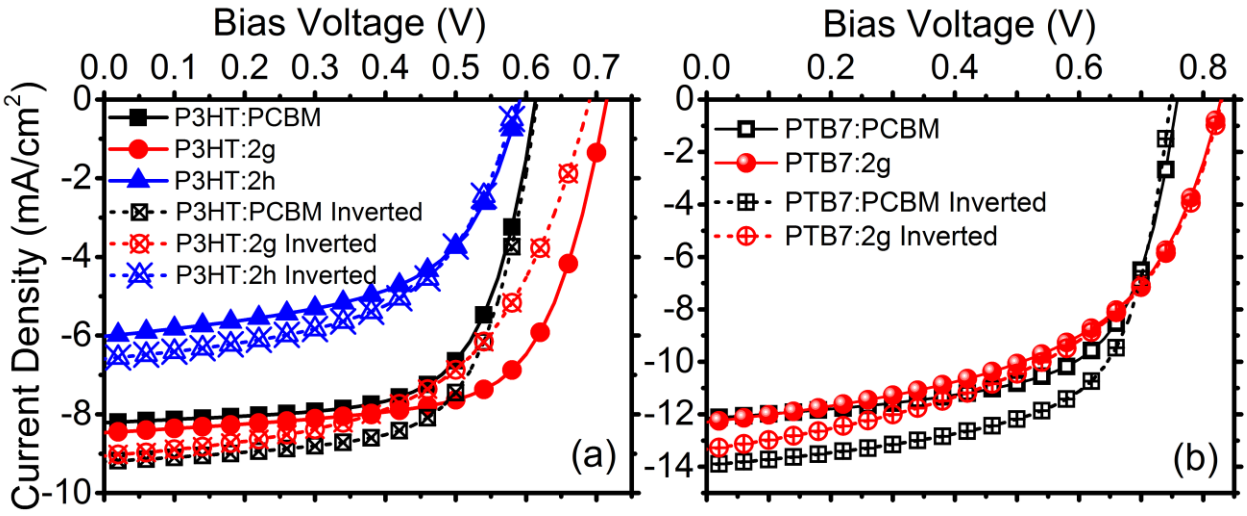

Figure 4.11 "Normal" versus "Inverted" devices using the same polymer:fullerene active layers where (a) is P3HT:fullerene and (b) is PTB7:fullerene. The "normal" devices' *J-V* curves are reprinted results from Figure 4.1 for ease of comparison. The "normal" device has a structure of ITO/PEDOT:PSS/Polymer:Fullerene/Ca/Al while the "inverted" device has a structure of

ITO/ZnO/Polymer:Fullerene/MoO_3/Ag. The error bars are omitted in the figure for clarity but the standard deviations are included in Table 4.2.

Table 4.2 Summary of photovoltaic device parameters[a]

	V_{oc} (mV)	J_{sc} (mA/cm^2)	*FF* (%)	*PCE* (%)
P3HT:PCBM	613 ± 2	8.2 ± 0.2	66.6 ± 0.4	3.4 ± 0.1
P3HT:2g	715 ± 1	8.5 ± 0.2	66.3 ± 0.7	3.9 ± 0.1
P3HT:2h	588 ± 5	6.0 ± 0.1	55.4 ± 1.3	2.0 ± 0.1
P3HT:PCBM inverted	616 ± 4	9.2 ± 0.1	65.8 ± 0.6	3.7 ± 0.1
P3HT:2g inverted	691 ± 6	9.1 ± 0.2	54.2 ± 1.6	3.4 ± 0.2
P3HT:2h inverted	588 ± 3	6.7 ± 0.1	54.8 ± 0.7	2.1 ± 0.1
PTB7:PCBM	760 ± 1	12.1 ± 0.2	64.4 ± 0.1	5.9 ± 0.2
PTB7:2g	825 ± 9	12.3 ± 0.2	53.3 ± 0.1	5.4 ± 0.1
PTB7:PCBM inverted	747 ± 3	13.9 ± 0.7	64.4 ± 1.8	6.7 ± 0.3
PTB7:2g inverted	830 ± 4	13.3 ± 0.2	50.0 ± 0.8	5.5 ± 0.1

[a] The "normal" device parameters are reprinted results from Table 3.1 in Chapter 3.2. The standard deviation is based on measurements over at least three independent devices.

For the P3HT:PCBM-based devices, the inverted structure provides the better PCE of 3.7% compared to only 3.4% for the normal device structure. When **2g** is used as acceptor with P3HT, the inverted device shows an efficiency of 3.4%, comparable to that of PCBM, yet the normal structure device has a significantly higher efficiency (3.9%) due to improvements in both the V_{oc} and *FF*. Most of the improvement of the J_{sc} for the inverted polymer:fullerene combinations is likely due to the light management, but some may also result from more favorable VPS. The poor device performance of P3HT:**2h** is governed by its overly phase separated active layer morphology and unfavorable bulk recombination, so the structure of the device contributes little to the efficiency.

For PTB7-based devices, the trend with device structure also confirms our predications based on surface energies. With PCBM, the inverted devices (PCE=6.7%) show a particularly large increase in PCE compared to the normal structure (PCE=5.9%), most likely due to the fact that PTB7 and PCBM have the largest surface energy difference of the materials studied in this work. When PTB7 is used in combination with **2g**, however, there is no clear performance trend between the normal (PCE=5.4%) and inverted structures (PCE=5.5%), consistent with the comparable surface energies of these two materials.

4.4 Conclusions

In conclusion, we have employed two novel fullerene bisadducts together with PCBM and two polymers, P3HT and PTB7, to build a system of five different polymer:fullerene combinations that allows us to separate the effects of the bulk BHJ morphology from that of the interface caused by vertical phase segregation on device performance and device physics. We found that the bulk recombination is the dominant factor for determining the overall device efficiency. Devices with the largest degree of phase separation showed the highest trap-state density. This led to a dominant trap-assisted recombination in the bulk and inferior device performance. For devices with similar bulk recombination, surface recombination, determined primarily by VPS, plays the most important role in device physics, including determining the charge carrier density and lifetime. We found that surface recombination could make the light ideality factors go below unity. We found that the surface energies of the fullerene bisadducts studied in this work were comparable to or lower than those of the polymers used, which were in turn lower than that of PCBM. This resulted in a reversal of the vertical phase segregation between devices with PCBM and those with the fullerene bisadducts. By comparing the surface energy of the pure materials, we were able to successfully predict the trend in device

performance when changing the device structure from normal to inverted. Thus, our work shows that simple contact angle measurements can offer deep insights in how to select the best device structure for a given material system.

4.5 Experimental Details

4.5.1 Device Fabrication

We fabricated polymer:fullerene BHJ solar cells by starting with cleaning pre-patterned tin-doped indium oxide (ITO; TFD Inc.) coated substrates with four successive sonication steps: detergent solution, deionized water, acetone and isopropanol for approximately 10 min each. The ITO substrates were treated with an air plasma (200 mTorr, 15 min) after drying in vacuum for at least 30 min. We then deposited a thin layer of PEDOT:PSS by spin-coating the solution in air at 5000 rpm for 20 s. The PEDOT:PSS-covered substrates were then baked at 150 ℃ for 20 min in air.

The P3HT:fullerene blend solutions were prepared by dissolving P3HT and the fullerene derivatives with a weight ratio of 1:0.8 in *o*-dichlorobenzene. The concentration with respect to P3HT was 20 mg/mL. The solutions were stirred at 60 ℃ overnight before being cooled to room temperature and spun onto the PEDOT:PSS-covered substrates at a spin speed of 1160 rpm for 20 s. The active layers were still wet when the samples were taken off from the spin-coater. After about 2 min in the nitrogen glovebox, the active layers were dry. All of the films were then thermally annealed at 150 ℃ for 20 min on a hot plate under an argon atmosphere. Film thicknesses were measured with a Dektak 150 Stylus Surface Profiler.

The PTB7:fullerene solutions were prepared by dissolving PTB7 and the fullerene derivatives in a mixture of 95% chlorobenzene/5% diiodooctane with a polymer:fullerene weight ratio of 1:1.5 for the fullerene bisadducts and 1:1.34 for PCBM (the change in weight ratio accounts for molecular weight differences to ensure that the blends were equimolar). The solutions were stirred at 55 ℃ on a hot plate overnight prior to being spun at 1000 rpm for 60 s onto the PEDOT:PSS-covered substrates. The films were then transferred to the antechamber of the glovebox and held under vacuum for ~1 hr. Then pure methanol was spun onto the films at a speed of 2500 rpm for 40 s. No further treatments were performed after this step before the deposition of the metal cathode.

For normal geometry devices, cathode deposition consisted of ~10 nm of Ca evaporated at a rate of ~0.5 Å/s followed by evaporation of 70 nm of Al at ~1 Å/s. The active areas of the resulting cells were 7.2 mm^2. For inverted geometry devices, the active layers were fabricated with the same methods. The cathode was a thin layer formed by spin-coating a ZnO nanoparticle solution, prepared following literature procedures,[72,73] at 4000 rpm for 20 s. The anode layer consisted of 15 nm of MoO_3 evaporated at a rate of ~ 0.5 Å/s followed by 70 nm of Ag evaporated at a rate of 1 Å/s. For the P3HT:fullerene devices, thermal annealing was performed before the deposition of MoO_3/Ag.

The *J*-*V* measurements were performed in an argon atmosphere using a Keithley 2400 source meter. We used a xenon arc lamp and an AM-1.5 filter as the excitation source, with the intensity calibrated to match 1 sun. For the inverted geometry devices, we performed a UV lamp treatment for at least 5 min before *J*–*V* testing.[74]

4.5.2 GIWAXS

2-D GIWAXS experiments were performed at the Stanford Synchrotron Radiation Lightsource on beamline 11-3 using a wavelength of 0.9742 Å. Figure 4.2 in the main text corresponds to the radially integrated pattern of the data from the full 2-D diffractogram. Each data curve in Figure 4.2 is the average of at least three different samples prepared under the same conditions. The 2-D images were collected on a plate with the detector 400 mm away from the center of the measured sample. The beam spot had a width of ~150 μm. A helium chamber was used to reduce the noise. The software package WxDiff was used to analyze the GIWAXS data.

4.5.3 Optoelectronic Measurements and CELIV

EQE, PSR, TPV/TPC and dark CELIV measurements were taken using the approach detailed in previous publications by our group.[22]

4.5.4 Contact Angle and Surface Energy Analysis

The surface energy analysis based on Eq. 2 in the main text comes from combining three well known relations:[66]

Young Equation: $$\gamma_{sv} - \gamma_{sl} = \gamma_{lv}\cos\theta \quad (3)$$

Dupre Equation: $$\gamma_{sl} = \gamma_{lv} + \gamma_{sv} - \mathrm{W}_{sl} \quad (4)$$

Fowkes Equation: $$W_{sl} = 2\sqrt{\gamma_{lv} \times \gamma_{sv}} \quad (5)$$

which lead directly to Eq. 2 upon substitution.

4.6 References

(1) Deibel, C.; Dyakonov, V. Polymer–Fullerene Bulk Heterojunction Solar Cells. *Rep. Prog. Phys* **2010**, *73*, 096401.

(2) Jørgensen, M.; Carlé, J. E.; Søndergaard, R. R.; Lauritzen, M.; Dagnæs-Hansen, N. A.; Byskov, S. L.; Andersen, T. R.; Larsen-Olsen, T. T.; Böttiger, A. P. L.; Andreasen, B.; et al. The State of Organic Solar cells—A Meta Analysis. *Sol. Energy Mater. Sol. Cells* **2013**, *119*, 84–93.

(3) Søndergaard, R. R.; Hösel, M.; Krebs, F. C. Roll-to-Roll Fabrication of Large Area Functional Organic Materials. *J. Polym. Sci. Part B Polym. Phys.* **2013**, *51*, 16–34.

(4) Scharber, M. C.; Sariciftci, N. S. Efficiency of Bulk-Heterojunction Organic Solar Cells. *Prog. Polym. Sci.* **2013**, *38*, 1929–1940.

(5) Krebs, F. C.; Espinosa, N.; Hösel, M.; Søndergaard, R. R.; Jørgensen, M. 25th Anniversary Article: Rise to Power - OPV-Based Solar Parks. *Adv. Mater.* **2014**, *26*, 29–39.

(6) Yu, G.; Gao, J.; Hummelen, J. C.; Wudl, F.; Heeger, A. J. Polymer Photovoltaic Cells: Enhanced Efficiencies via a Network of Internal Donor-Acceptor Heterojunctions. *Science (80-.).* **1995**, *270*, 1789–1791.

(7) Heeger, A. J. 25th Anniversary Article: Bulk Heterojunction Solar Cells: Understanding the Mechanism of Operation. *Adv. Mater.* **2014**, *26*, 10–27.

(8) Liu, Y.; Zhao, J.; Li, Z.; Mu, C.; Ma, W.; Hu, H.; Jiang, K.; Lin, H.; Ade, H.; Yan, H. Aggregation and Morphology Control Enables Multiple Cases of High-Efficiency Polymer Solar Cells. *Nat. Commun.* **2014**, *5*, 5293.

(9) Kim, Y.; Choulis, S. A.; Nelson, J.; Bradley, D. D. C.; Cook, S.; Durrant, J. R. Device Annealing Effect in Organic Solar Cells with Blends of Regioregular poly(3-Hexylthiophene) and Soluble Fullerene. *Appl. Phys. Lett.* **2005**, *86*, 63502.

(10) Ayzner, A. L.; Wanger, D. D.; Tassone, C. J.; Tolbert, S. H.; Schwartz, B. J. Room to Improve Conjugated Polymer-Based Solar Cells: Understanding How Thermal Annealing Affects the Fullerene Component of a Bulk Heterojunction Photovoltaic Device. *J. Phys. Chem. C* **2008**, *112*, 18711–18716.

(11) Collins, B. A.; Tumbleston, J. R.; Ade, H. Miscibility, Crystallinity, and Phase Development in P3HT/PCBM Solar Cells: Toward an Enlightened Understanding of Device Morphology and Stability. *J. Phys. Chem. Lett.* **2011**, *2*, 3135–3145.

(12) Parnell, A. J.; Cadby, A. J.; Mykhaylyk, O. O.; Dunbar, A. D. F.; Hopkinson, P. E.; Donald, A. M.; Jones, R. A. L. Nanoscale Phase Separation of P3HT PCBM Thick Films As Measured by Small-Angle X-Ray Scattering. *Macromolecules* **2011**, *44*, 6503–6508.

(13) Chen, D.; Nakahara, A.; Wei, D.; Nordlund, D.; Russell, T. P. P3HT/PCBM Bulk Heterojunction Organic Photovoltaics: Correlating Efficiency and Morphology. *Nano Lett.* **2011**, *11*, 561–567.

(14) Shoaee, S.; Subramaniyan, S.; Xin, H.; Keiderling, C.; Tuladhar, P. S.; Jamieson, F.; Jenekhe, S. A.; Durrant, J. R. Charge Photogeneration for a Series of Thiazolo-Thiazole Donor Polymers Blended with the Fullerene Electron Acceptors PCBM and ICBA. *Adv. Funct. Mater.* **2013**, *23*, 3286–3298.

(15) Westacott, P.; Tumbleston, J. R.; Shoaee, S.; Fearn, S.; Bannock, J. H.; Gilchrist, J. B.; Heutz, S.; DeMello, J.; Heeney, M.; Ade, H.; et al. On the Role of Intermixed Phases in Organic Photovoltaic Blends. *Energy Environ. Sci.* **2013**, *6*, 2756–2764.

(16) Zhang, G.; Huber, R. C.; Ferreira, A. S.; Boyd, S. D.; Luscombe, C. K.; Tolbert, S. H.; Schwartz, B. J. Crystallinity Effects in Sequentially Processed and Blend-Cast Bulk-Heterojunction Polymer/Fullerene Photovoltaics. *J. Phys. Chem. C* **2014**, *118*, 18424–18435.

(17) Orimo, A.; Masuda, K.; Honda, S.; Benten, H.; Ito, S.; Ohkita, H.; Tsuji, H. Surface Segregation at the Aluminum Interface of poly(3-Hexylthiophene)/fullerene Solar Cells. *Appl. Phys. Lett.* **2010**, *96*, 43305.

(18) Lu, H.; Akgun, B.; Russell, T. P. Morphological Characterization of a Low-Bandgap Crystalline Polymer:PCBM Bulk Heterojunction Solar Cells. *Adv. Energy Mater.* **2011**, *1*, 870–878.

(19) Xu, Z.; Chen, L.-M.; Yang, G.; Huang, C.-H.; Hou, J.; Wu, Y.; Li, G.; Hsu, C.-S.; Yang, Y. Vertical Phase Separation in Poly(3-Hexylthiophene): Fullerene Derivative Blends and Its Advantage for Inverted Structure Solar Cells. *Adv. Funct. Mater.* **2009**, *19*, 1227–1234.

(20) Ibrahem, M. A.; Wei, H.-Y.; Tsai, M.-H.; Ho, K.-C.; Shyue, J.-J.; Chu, C. W. Solution-Processed Zinc Oxide Nanoparticles as Interlayer Materials for Inverted Organic Solar Cells. *Sol. Energy Mater. Sol. Cells* **2013**, *108*, 156–163.

(21) Mauger, S. A.; Chang, L.; Friedrich, S.; Rochester, C. W.; Huang, D. M.; Wang, P.; Moulé, A. J. Self-Assembly of Selective Interfaces in Organic Photovoltaics. *Adv. Funct. Mater.* **2013**, *23*, 1935–1946.

(22) Hawks, S. A.; Aguirre, J. C.; Schelhas, L. T.; Thompson, R. J.; Huber, R. C.; Ferreira, A. S.; Zhang, G.; Herzing, A. A.; Tolbert, S. H.; Schwartz, B. J. Comparing Matched Polymer:Fullerene Solar Cells Made by Solution-Sequential Processing and Traditional Blend Casting: Nanoscale Structure and Device Performance. *J. Phys. Chem. C* **2014**, *118*, 17413–17425.

(23) Kiel, J. W.; Kirby, B. J.; Majkrzak, C. F.; Maranville, B. B.; Mackay, M. E. Nanoparticle Concentration Profile in Polymer-Based Solar Cells. *Soft Matter* **2010**, *6*, 641.

(24) Parnell, A. J.; Dunbar, A. D. F.; Pearson, A. J.; Staniec, P. a; Dennison, A. J. C.; Hamamatsu, H.; Skoda, M. W. A.; Lidzey, D. G.; Jones, R. A. L. Depletion of PCBM at the Cathode Interface in P3HT/PCBM Thin Films as Quantified via Neutron Reflectivity Measurements. *Adv. Mater.* **2010**, *22*, 2444–2447.

(25) Kirschner, S. B.; Smith, N. P.; Wepasnick, K. a.; Katz, H. E.; Kirby, B. J.; Borchers, J. a.; Reich, D. H. X-Ray and Neutron Reflectivity and Electronic Properties of PCBM-Poly(bromo)styrene Blends and Bilayers with poly(3-Hexylthiophene). *J. Mater. Chem.* **2012**, *22*, 4364.

(26) Lee, K. H.; Zhang, Y.; Burn, P. L.; Gentle, I. R.; James, M.; Nelson, A.; Meredith, P. Correlation of Diffusion and Performance in Sequentially Processed P3HT/PCBM Heterojunction Films by Time-Resolved Neutron Reflectometry. *J. Mater. Chem. C* **2013**, *1*, 2593–2598.

(27) Chen, H.; Hegde, R.; Browning, J.; Dadmun, M. D. The Miscibility and Depth Profile of PCBM in P3HT: Thermodynamic Information to Improve Organic Photovoltaics. *Phys. Chem. Chem. Phys.* **2012**, *14*, 5635–5641.

(28) Chen, H.; Hu, S.; Zang, H.; Hu, B.; Dadmun, M. Precise Structural Development and Its Correlation to Function in Conjugated Polymer: Fullerene Thin Films by Controlled Solvent Annealing. *Adv. Funct. Mater.* **2013**, *23*, 1701–1710.

(29) Liu, F.; Zhao, W.; Tumbleston, J. R.; Wang, C.; Gu, Y.; Wang, D.; Briseno, A. L.; Ade, H.; Russell, T. P. Understanding the Morphology of PTB7:PCBM Blends in Organic Photovoltaics. *Adv. Energy Mater.* **2014**, *4*, 1301377.

(30) Welch, G. C.; Perez, L. A.; Hoven, C. V.; Zhang, Y.; Dang, X.-D.; Sharenko, A.; Toney, M. F.; Kramer, E. J.; Nguyen, T.-Q.; Bazan, G. C. A Modular Molecular Framework for Utility in Small-Molecule Solution-Processed Organic Photovoltaic Devices. *J. Mater. Chem.* **2011**, *21*, 12700.

(31) Campoy-Quiles, M.; Ferenczi, T.; Agostinelli, T.; Etchegoin, P. G.; Kim, Y.; Anthopoulos, T. D.; Stavrinou, P. N.; Bradley, D. D. C.; Nelson, J. Morphology Evolution via Self-Organization and Lateral and Vertical Diffusion in Polymer:fullerene Solar Cell Blends. *Nat. Mater.* **2008**, *7*, 158–164.

(32) Campoy-Quiles, M.; Alonso, M. I.; Bradley, D. D. C.; Richter, L. J. Advanced Ellipsometric Characterization of Conjugated Polymer Films. *Adv. Funct. Mater.* **2014**, *24*, 2116–2134.

(33) Madsen, M. V.; Sylvester-Hvid, K. O.; Dastmalchi, B.; Hingerl, K.; Norrman, K.; Tromholt, T.; Manceau, M.; Angmo, D.; Krebs, F. C. Ellipsometry as a Nondestructive Depth Profiling Tool for Roll-to-Roll Manufactured Flexible Solar Cells. *J. Phys. Chem. C* **2011**, *115*, 10817–10822.

(34) Germack, D. S.; Chan, C. K.; Hamadani, B. H.; Richter, L. J.; Fischer, D. A.; Gundlach, D. J.; DeLongchamp, D. M. Substrate-Dependent Interface Composition and Charge Transport in Films for Organic Photovoltaics. *Appl. Phys. Lett.* **2009**, *94*, 233303.

(35) Tremolet de Villers, B.; Tassone, C. J.; Tolbert, S. H.; Schwartz, B. J. Improving the Reproducibility of P3HT:PCBM Solar Cells by Controlling the PCBM/Cathode Interface. *J. Phys. Chem. C* **2009**, *113*, 18978–18982.

(36) Li, G.; Chu, C.-W.; Shrotriya, V.; Huang, J.; Yang, Y. Efficient Inverted Polymer Solar Cells. *Appl. Phys. Lett.* **2006**, *88*, 253503.

(37) Finck, B. Y.; Schwartz, B. J. Understanding the Origin of the S-Curve in Conjugated Polymer/fullerene Photovoltaics from Drift-Diffusion Simulations. *Appl. Phys. Lett.* **2013**, *103*, 53304–53306.

(38) Street, R. A.; Song, K. W.; Northrup, J. E.; Cowan, S. Photoconductivity Measurements of the Electronic Structure of Organic Solar Cells. *Phys. Rev. B* **2011**, *83*, 165207.

(39) Shuttle, C. G.; Maurano, a.; Hamilton, R.; O'Regan, B.; de Mello, J. C.; Durrant, J. R. Charge Extraction Analysis of Charge Carrier Densities in a Polythiophene/fullerene Solar Cell: Analysis of the Origin of the Device Dark Current. *Appl. Phys. Lett.* **2008**, *93*, 183501.

(40) Maurano, A.; Hamilton, R.; Shuttle, C. G.; Ballantyne, A. M.; Nelson, J.; O'Regan, B.; Zhang, W.; McCulloch, I.; Azimi, H.; Morana, M.; et al. Recombination Dynamics as a Key Determinant of Open Circuit Voltage in Organic Bulk Heterojunction Solar Cells: A Comparison of Four Different Donor Polymers. *Adv. Mater.* **2010**, *22*, 4987–4992.

(41) Juska, G.; Arlauskas, K.; Viliunas, M.; Kocka, J. Extraction Current Transients : New Method of Study of Charge Transport in Microcrystalline Silicon. *Phys. Rev. Lett.* **2000**, *84*, 4946–4949.

(42) Kim, Y.; Cook, S.; Tuladhar, S. M.; Choulis, S. A.; Nelson, J.; Durrant, J. R.; Bradley, D. D. C.; Giles, M.; McCulloch, I.; Ha, C.-S.; et al. A Strong Regioregularity Effect in Self-Organizing Conjugated Polymer Films and High-Efficiency Polythiophene:fullerene Solar Cells. *Nat. Mater.* **2006**, *5*, 197–203.

(43) Collins, B. A.; Li, Z.; Tumbleston, J. R.; Gann, E.; McNeill, C. R.; Ade, H. Absolute Measurement of Domain Composition and Nanoscale Size Distribution Explains Performance in PTB7:PC71BM Solar Cells. *Adv. Energy Mater.* **2013**, *3*, 65–74.

(44) Street, R. A.; Schoendorf, M.; Roy, A.; Lee, J. H. Interface State Recombination in Organic Solar Cells. *Phys. Rev. B* **2010**, *81*, 205307.

(45) Street, R. A.; Krakaris, A.; Cowan, S. R. Recombination Through Different Types of Localized States in Organic Solar Cells. *Adv. Funct. Mater.* **2012**, *22*, 4608–4619.

(46) Street, R. A.; Davies, D.; Khlyabich, P. P.; Burkhart, B.; Thompson, B. C. Origin of the Tunable Open-Circuit Voltage in Ternary Blend Bulk Heterojunction Organic Solar Cells. *J. Am. Chem. Soc.* **2013**, *135*, 986–989.

(47) Shockley, W.; Jr, W. R. Statistics of the Recombinations of Holes and Electrons. *Phys. Rev.* **1952**, *87*, 835–842.

(48) Cowan, S. R.; Roy, A.; Heeger, A. J. Recombination in Polymer-Fullerene Bulk Heterojunction Solar Cells. *Phys. Rev. B* **2010**, *82*, 245207.

(49) Tzabari, L.; Tessler, N. Shockley–Read–Hall Recombination in P3HT:PCBM Solar Cells as Observed under Ultralow Light Intensities. *J. Appl. Phys.* **2011**, *109*, 064501.

(50) Kirchartz, T.; Deledalle, F.; Tuladhar, P. S.; Durrant, J. R.; Nelson, J. On the Differences between Dark and Light Ideality Factor in Polymer: Fullerene Solar Cells. *J. Phys. Chem. Lett.* **2013**, *4*, 2371–2376.

(51) Kirchartz, T.; Pieters, B. E.; Kirkpatrick, J.; Rau, U.; Nelson, J. Recombination via Tail States in Polythiophene:fullerene Solar Cells. *Phys. Rev. B* **2011**, *83*, 115209.

(52) Foertig, A.; Rauh, J.; Dyakonov, V.; Deibel, C. Shockley Equation Parameters of P3HT:PCBM Solar Cells Determined by Transient Techniques. *Phys. Rev. B* **2012**, *86*, 115302.

(53) Credgington, D.; Durrant, J. R. Insights from Transient Optoelectronic Analyses on the Open-Circuit Voltage of Organic Solar Cells. *J. Phys. Chem. Lett.* **2012**, *3*, 1465–1478.

(54) Wetzelaer, G. A. H.; Kuik, M.; Lenes, M.; Blom, P. W. M. Origin of the Dark-Current Ideality Factor in Polymer:fullerene Bulk Heterojunction Solar Cells. *Appl. Phys. Lett.* **2011**, *99*, 153506.

(55) Shuttle, C. G.; O'Regan, B.; Ballantyne, A. M.; Nelson, J.; Bradley, D. D. C.; de Mello, J.; Durrant, J. R. Experimental Determination of the Rate Law for Charge Carrier Decay in a Polythiophene: Fullerene Solar Cell. *Appl. Phys. Lett.* **2008**, *92*, 93311–93313.

(56) Ballantyne, A. M.; Ferenczi, T. a. M.; Campoy-Quiles, M.; Clarke, T. M.; Maurano, A.; Wong, K. H.; Zhang, W.; Stingelin-Stutzmann, N.; Kim, J.-S.; Bradley, D. D. C.; et al. Understanding the Influence of Morphology on Poly(3-hexylselenothiophene):PCBM Solar Cells. *Macromolecules* **2010**, *43*, 1169–1174.

(57) Maurano, A.; Shuttle, C. G.; Hamilton, R.; Ballantyne, A. M.; Nelson, J.; Zhang, W.; Heeney, M.; Durrant, J. R. Transient Optoelectronic Analysis of Charge Carrier Losses in a Selenophene/Fullerene Blend Solar Cell. *J. Phys. Chem. C* **2011**, *115*, 5947–5957.

(58) Ryan, J. W.; Kirchartz, T.; Viterisi, A.; Nelson, J.; Palomares, E. Understanding the Effect of Donor Layer Thickness and a MoO3 Hole Transport Layer on the Open-Circuit Voltage in Squaraine/C60 Bilayer Solar Cells. *J. Phys. Chem. C* **2013**, *117*, 19866–19874.

(59) Dibb, G. F. a.; Kirchartz, T.; Credgington, D.; Durrant, J. R.; Nelson, J. Analysis of the Relationship between Linearity of Corrected Photocurrent and the Order of Recombination in Organic Solar Cells. *J. Phys. Chem. Lett.* **2011**, *2*, 2407–2411.

(60) Vandewal, K.; Tvingstedt, K.; Gadisa, A.; Inganäs, O.; Manca, J. V. Relating the Open-Circuit Voltage to Interface Molecular Properties of Donor:acceptor Bulk Heterojunction Solar Cells. *Phys. Rev. B* **2010**, *81*, 125204.

(61) Graham, K. R.; Erwin, P.; Nordlund, D.; Vandewal, K.; Li, R.; Ngongang Ndjawa, G. O.; Hoke, E. T.; Salleo, A.; Thompson, M. E.; McGehee, M. D.; et al. Re-Evaluating the Role of Sterics and Electronic Coupling in Determining the Open-Circuit Voltage of Organic Solar Cells. *Adv. Mater.* **2013**, *25*, 6076–6082.

(62) Vandewal, K.; Oosterbaan, W. D.; Bertho, S.; Vrindts, V.; Gadisa, A.; Lutsen, L.; Vanderzande, D.; Manca, J. V. Varying Polymer Crystallinity in Nanofiber poly(3-Alkylthiophene): PCBM Solar Cells: Influence on Charge-Transfer State Energy and Open-Circuit Voltage. *Appl. Phys. Lett.* **2009**, *95*, 123303.

(63) Graham, K.; Amassian, A.; Erwin, P.; Thompson, M.; Nordlund, D.; Vandewal, K.; Hoke, E.; Salleo, A.; Mcgehee, M.; Lee, R.; et al. Charge-Transfer State Energy Determines Open-Circuit Voltage in Organic Photovoltaics. *SPIE Newsroom* **2013**, DOI: 10.1117/2.1201309.005006.

(64) Kong, J.; Hwang, I.-W.; Lee, K. Top-down Approach for Nanophase Reconstruction in Bulk Heterojunction Solar Cells. *Adv. Mater.* **2014**, *26*, 6275–6283.

(65) Huang, J.-H.; Hsiao, Y.-S.; Richard, E.; Chen, C.-C.; Chen, P.; Li, G.; Chu, C.-W.; Yang, Y. The Investigation of Donor-Acceptor Compatibility in Bulk-Heterojunction Polymer Systems. *Appl. Phys. Lett.* **2013**, *103*, 043304.

(66) Carré, A. Polar Interactions at Liquid/polymer Interfaces. *J. Adhes. Sci. Technol.* **2007**, *21*, 961–981.

(67) Janssen, D.; De Palma, R.; Verlaak, S.; Heremans, P.; Dehaen, W. Static Solvent Contact Angle Measurements, Surface Free Energy and Wettability Determination of Various Self-Assembled Monolayers on Silicon Dioxide. *Thin Solid Films* **2006**, *515*, 1433–1438.

(68) Zhao, Y.; Xie, Z.; Qu, Y.; Geng, Y.; Wang, L. Solvent-Vapor Treatment Induced Performance Enhancement of poly(3-Hexylthiophene):methanofullerene Bulk-Heterojunction Photovoltaic Cells. *Appl. Phys. Lett.* **2007**, *90*, 43503–43504.

(69) Chambon, S.; Derue, L.; Lahaye, M.; Pavageau, B.; Hirsch, L.; Wantz, G. MoO3 Thickness, Thermal Annealing and Solvent Annealing Effects on Inverted and Direct Polymer Photovoltaic Solar Cells. *Materials (Basel).* **2012**, *5*, 2521–2536.

(70) Hadipour, A.; Cheyns, D.; Heremans, P.; Rand, B. P. Electrode Considerations for the Optical Enhancement of Organic Bulk Heterojunction Solar Cells. *Adv. Energy Mater.* **2011**, *1*, 930–935.

(71) Yip, H.-L.; Jen, A. K. Y. Recent Advances in Solution-Processed Interfacial Materials for Efficient and Stable Polymer Solar Cells. *Energy Environ. Sci.* **2012**, *5*, 5994–6011.

(72) Beek, W. J. E.; Wienk, M. M.; Kemerink, M.; Yang, X.; Janssen, R. A. J. Hybrid Zinc Oxide Conjugated Polymer Bulk Heterojunction Solar Cells. *J. Phys. Chem. B* **2005**, *109*, 9505–9516.

(73) Sun, B.; Sirringhaus, H. Solution-Processed Zinc Oxide Field-Effect Transistors Based on Self-Assembly of Colloidal Nanorods. *Nano Lett.* **2005**, *5*, 2408–2413.

(74) Kuwabara, T.; Tamai, C.; Omura, Y.; Yamaguchi, T.; Taima, T.; Takahashi, K. Effect of UV Light Irradiation on Photovoltaic Characteristics of Inverted Polymer Solar Cells Containing Sol–gel Zinc Oxide Electron Collection Layer. *Org. Electron.* **2013**, *14*, 649–656.

Chapter 5 Investigation of the Dark Carriers in Fullerene Based Diodes Measured by CELIV: the Role of Metal Penetration into the Fullerene-layer Induced by Metal Evaporation

5.1 Introduction

In Chapter 4, we discussed the effect of vertical phase segregation (VPS) on photovoltaic device performance and device physics. One of the consequences of certain types of VPS was the presence of dark carriers inside the device that could be observed by charge extraction by the linear increasing voltage (CELIV) technique (Chapter 4, section 4.4.5). We found that the presence of dark carriers was related to the degree of fullerene segregation towards the top metal electrode in polymer:fullerene bulk-heterojunction (BHJ)[1,2] devices. A similar observation has been made previously by our group[3] when examining sequentially processed (SqP) P3HT/PCBM solar cells: we found a significant number of dark carriers in as-cast SqP devices, which are known to have a quasi-bilayer structure with a P3HT-rich layer on the bottom and a PCBM-rich layer on the top.[3–5] However, when we changed this vertical phase segregation by thermal annealing, which helps to better intermix the PCBM and P3HT[6] and reduce the amount of PCBM on the top of the active layer,[4] no significant dark carriers were observed by CELIV.[3] All of these results suggest a correlation between the VPS in the active layer and the existence of the dark carriers.

What is interesting about this observation is that most organic semiconductors that are used in photovoltaic devices are intrinsically undoped.[7,8] The dark carriers that we observe in some of our devices clearly must have something to do with the presence of VPS and the evaporated metal electrode, and could possibly result from: 1) doping of one of the organic materials by either hole transfer from the anode or electron transfer from the cathode to the active medium; or

2) extraction of intrinsic carriers that would normally be trapped but are somehow freed by the way the electrode interacts with the VPS of the active layer. In this Chapter, we will discuss experiments aimed at understanding the origin of these dark carriers. Our focus is on determining the relationship between VPS, device structure, metal evaporation and the presence of dark carriers measured by CELIV.

What we will show below is that the key phenomenon is extensive penetration of the evaporated metal cathode into any fullerenes that reside at the top surface of the film. Our results indicate that the metal penetrates through any fullerenes at the top of the film until they reach the polymer underneath.[9–12] Others have also came to a similar conclusion regarding metal penetration into organic semiconductor active layers, concluding that metal infiltration was the origin of the non-ohmic shunt behavior typically observed in these devices.[13] We attribute the presence of dark carriers to the interaction between the penetrated metal and the fullerene enriched layer.

Our evidence for metal penetration and the resultant fullerene layer doping stems from three general observations: first, diodes based on pure PCBM/metal always show a very low shunt resistance unless a blocking layer (e.g., LiF, conjugated polymer, or MoO_3) is introduced at the anode side of the device. Second, the device geometric capacitance (C_g) is not consistent with the actual organic layer thickness when doping is observed, indicating that metal has penetrated far enough into the film to create an effectively thinner device. The number of dark carriers we can extract from a device correlates well with the difference between the capacitive thickness and measured device thickness. Finally, we have direct evidence from cross-sectional TEM that metal indeed penetrates through any fullerene overlayers and is not stopped until it reaches a region of the active layer whose composition is predominantly non-fullerene. .

5.2 Results and Discussion

5.2.1 Studying Doping with the CELIV Technique

In order to quantify the number of dark carriers present in our organic semiconductor devices, we used the CELIV technique in the dark under unbiased conditions.[14–16] CELIV is ideal for these experiments because it directly measures equilibrium carriers inside a functional device.[17,18] This is not the case for other methods, which either measure chemical interactions that may or may not result in free carriers,[19–21] or assess the presence of equilibrium free carriers in a non-device environment.[22] We note that the standard Mott-Schottky (M-S) analysis for determining the doping density and built-in voltage for inorganic semiconductor devices is generally not reliable for thin-film organic semiconductor devices because the doping density and thickness are usually too low for the depletion approximation to be valid.[23,24]

CELIV analyzes mobile carriers in diodes by examining the current transient induced by a linearly changing voltage ramp.[25–29] This is ideal for studying doping in simple parallel-plate architectures because it trivializes the RC charging current inherent to the device circuit. Specifically, when applied to a parallel-plate capacitor, a linear voltage ramp produces a constant displacement current that can easily be distinguished from the current due to mobile carriers. The presence of a substantial amount of doping is readily identified as a bump in the CELIV current transient that is superimposed on the constant parallel-plate capacitor response (Figure 5.1a).[18]

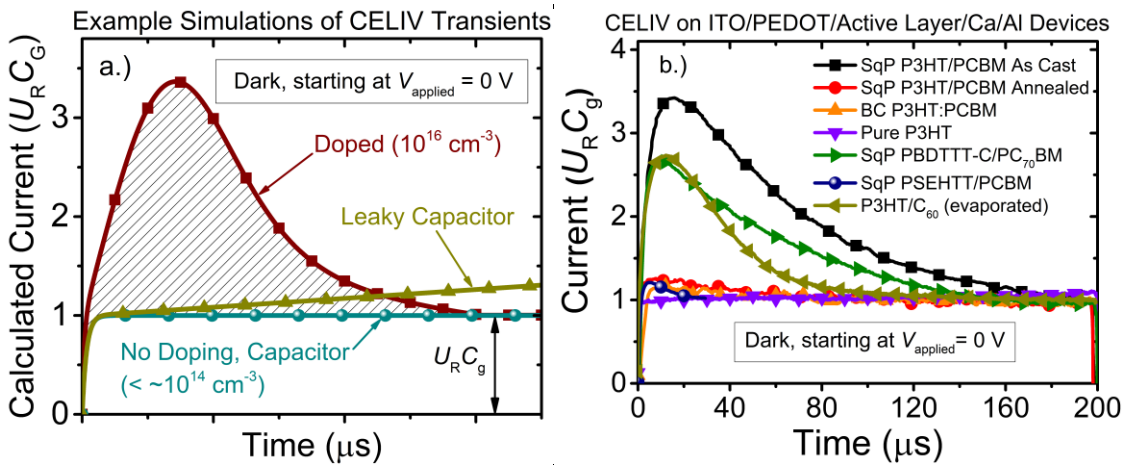

Figure 5.1 (a.) Sample simulated CELIV transients based on three commonly observed regimes. The "Doped" curve (red squares) was calculated using the Juska *et al.*[14] CELIV formalism with the addition of a finite series resistance. The "No Doping, Capacitor" curve (blue spheres) is the response of a series RC circuit to a CELIV pulse, and the "Leaky Capacitor" data (yellow triangles) corresponds to the response of a parallel RC circuit with a series resistance to the same CELIV pulse (see Section 5.4.1 for model details). All curves were divided by the product of their geometric capacitance (C_g) and the CELIV ramp rate (U_R). (b.) Experimentally measured dark CELIV current transients on diodes with different organic semiconducting materials in the configuration ITO/PEDOT:PSS/Organic Semiconductor/Ca/Al.

It is also worth noting that a leaky capacitor, to first approximation, gives a CELIV response that is the superposition of a linear Ohmic current and a capacitive charging current (Figure 5.1a and Section 5.4.1 Figure 5.9). Using example simulations, Figure 5.1a illustrates how readily doping can be identified in dark CELIV measurements by plotting the response of a classic parallel-plate capacitor with a finite series (R_s) and shunt (R_p) resistance along with a sample uniformly doped at 10^{16} cm^{-3} (26.4 nC/cm^{-2} sheet charge density for the simulated device thickness). The doped curve was calculated using the Juska *et al.*[14] model/formalism with finite

series and shunt resistances, and the capacitor curves were calculated with a simple $R_sR_pC_g$ equivalent circuit model (see Figure 5.9 for details).

Table 5.1 Measured Sheet Charge Densities for Various Organic Semiconductor Diodes[a]

Organic Semiconductor Layer[b]	Correspon-ding Figure/Section	Anode	Cathode[c]	*Sheet Charge Density* (nC/cm^{-2})	C_g (nF)
P3HT	Fig. 5.1b	PEDOT:PSS[d]	Ca/Al	No DC[e]	1.75
P3HT annealed	Fig. 5.1b	PEDOT:PSS	Ca/Al	No DC	1.63
P3HT	5.2	MoO_3	ZnO[f]	No DC	1.39[g]
P3HT	5.2	ITO	Ca/Al	No DC	1.73
PCBM	Fig. 5.2a	PEDOT:PSS	Ca/Al	Leaky	2.80
PCBM	Fig. 5.2a	MoO_3	ZnO	No DC	2.35[g]
P3HT/PCBM (5 mg/mL) SqP	Fig. 5.1b	PEDOT:PSS	Ca/Al	8.7	1.87
P3HT/PCBM (10 mg/mL) SqP[h]	Fig. 5.1b	PEDOT:PSS	Ca/Al	28.7	1.85
P3HT/PCBM (15 mg/mL) SqP	Fig. 5.1b	PEDOT:PSS	Ca/Al	35.7	1.82
P3HT/PCBM annealed 150 ºC SqP[h]	Fig. 5.1b	PEDOT:PSS	Ca/Al	1.9	1.29
P3HT/PCBM annealed 110 ºC SqP[h]	Fig. 5.1b	PEDOT:PSS	Ca/Al	6.3	1.51
P3HT/PCBM SqP	Fig. 5.1b	MoO_3	ZnO	No DC	1.53[g]
P3HT:PCBM annealed BC[h]	Fig. 5.1b	PEDOT:PSS	Ca/Al	No DC	1.25
PBDTTT-C/PC_{71}BM SqP	Fig. 5.1b	PEDOT:PSS	Ca/Al	28.8	3.68
PSEHTT/PCBM SqP	Fig. 5.1b	PEDOT:PSS	Ca/Al	1.9	3.00
PSDTTT/PCBM SqP	Fig. 5.3a	PEDOT:PSS	Ca/Al	No DC	3.11

PSDTTT/C_{60} (evaporated 55 nm)	Fig. 5.3a	PEDOT:PSS	Ca/Al	0.7	3.83
P3HT/C_{60} (evaporated 55 nm)	Fig. 5.3c	PEDOT:PSS	Ca/Al	3.6	1.48
P3HT/C_{60} (evaporated 85 nm)	Fig. 5.3c	PEDOT:PSS	Ca/Al	6.8	1.37
P3HT/C_{60} (evaporated 105 nm)	Fig. 5.2b Fig. 5.3c	PEDOT:PSS	Ca/Al	2.2	1.23
LiF/C_{60} (evaporated 105 nm)	Fig. 5.2b	ITO	Ca/Al	13.0	3.27
Highly Regioregular P3HT[i]/C_{60} (evaporated 85 nm)	5.4.4	PEDOT:PSS	Ca/Al	5.3	1.74
Regiorandom P3HT/C_{60} (evaporated 85 nm)	5.4.4	PEDOT:PSS	Ca/Al	No DC	1.86
P3HT/C_{60} (evaporated 55 nm)	-	ITO	Ag	4.6	2.51
P3HT/PCBM SqP	5.4.3	PEDOT:PSS	Ca (0.3 nm)/Al	28.0	1.87
P3HT/PCBM SqP	5.4.3	PEDOT:PSS	Ca (1.0 nm)/Al	26.0	1.45
P3HT/PCBM SqP	5.4.3	PEDOT:PSS	Ca (10 nm)/Al	28.7	2.36
P3HT/PCBM SqP	5.4.3	PEDOT:PSS	Ca (45 nm)	46.5	2.47
P3HT/PCBM SqP	Fig. 5.7	PEDOT:PSS	Al	32.8	1.78
P3HT/PCBM SqP	Fig. 5.7	PEDOT:PSS	Mg (50 nm)	34.5	2.40
P3HT/PCBM SqP	Fig. 5.7	PEDOT:PSS	Ag	Leaky	9.42
P3HT/PCBM SqP	Fig. 5.7	PEDOT:PSS	Au	31.8	2.01
P3HT/PCBM SqP	Fig. 5.7	PEDOT:PSS	Na (15 nm)/Ag	Shorted	27.8
P3HT/PCBM SqP	Fig. 5.7	PEDOT:PSS	K (15 nm)/Ag	Shorted	13.8
P3HT/ICBA SqP	5.4.2	PEDOT:PSS	Ag	Leaky	10.8
P3HT/ICBA SqP	Fig. 5.11	PEDOT:PSS	Ca (45 nm)	4.0	2.52
P3HT/ICBA SqP	Fig. 5.11	PEDOT:PSS	Al	4.9	3.11

[a] If not specified, the active layer is as-cast without any post-treatment;

[b] Obtained by multiplying the average carrier density by the device area; The average carrier density is calculated from the integrated "bump" area, e.g. (shaded area in Figure 5.1a);

[c] If not specified, the default thickness is 10 nm for Ca, 70 nm for Al and 70 nm for Ag;

[d] PEDOT:PSS is Clevios^{TM} P VP Al 4083;

[e] "No Dark Carriers (DC)" implies less than the measurement resolution of 0.3 nC/cm^{-2};

[f] Details about preparing the ZnO nanoparticle layer can be found in Chapter 4.5.1;

[g] This number includes the contribution from MoO_3 and/or the ZnO layer; Thus, it is not used to compare with the C_g's for devices with normal device structure;

[h] If not specified, the PCBM concentration is 10 mg/mL; For samples labeled with "annealed", the default condition for annealing is 150 ℃ for 20 min;

[i] Polymer regioregularity ~ 98%, polydispersity index ~1.18. Details can be found in Ref. 6.

To quantify the amount of doping, we integrate the area above the parallel-plate capacitor displacement current (shaded area in Figure 5.1a), where the displacement current is given by the product $U_R C_g$ (U_R is the CELIV ramp rate in V/s and C_g the device's geometric capacitance in F). We plot the measured current in units of the particular device's $U_R C_g$, which normalizes each measurement by the displacement current for easy comparison of the doping response. The integrated current density in Figure 5.1a is related to the average doping density in the device by the active-layer volume, the charge on an electron, and the initial space-charge distribution inside the device prior to the CELIV pulse. Thus it is not necessarily trivial to convert the shaded area in Figure 5.1a directly to a number of doped carriers. The details for this conversion will be discussed in a future publication[30] and are beyond the scope of this work. For the present case, it suffices that a larger shaded area in Figure 5.1a corresponds to more doping present within a device. Thus, the sheet-charge density values we extract, reported in units of nC/cm^{-2}, can be used to compare the relative amount of doping between devices. We chose not to normalize these sheet charge densities by the device thickness since the extracted dark carriers in our

measurements arise from metal penetration into just the fullerene-rich overlayer portion of an unknown active layer composition distribution. Finally, all values of the geometric capacitance reported herein were extracted from CELIV measurements starting at a steady-state reverse bias sufficient enough to fully deplete the device. These depleted CELIV traces were fitted to Eqns. (2-4, Section 5.4) to extract R_s, R_p, and C_g (see Figure 5.2 for example fits).

5.2.2 Investigating Fullerene Doping in Different Device Structures

In addition to the simulations, Figure 5.1b plots the measured dark CELIV current transients for various organic semiconductor diodes, demonstrating that some devices clearly show significant doping and others show purely depleted (or slightly leaky) capacitive behavior. In general, Figure 5.1b shows that many as-cast SqP polymer/PCBM active layers have significant dark carriers to extract, whereas other structures like pure PEDOT:PSS/P3HT/Ca/Al show no doping. In accordance with what we have previously reported,[3] the observation of apparent doping correlates entirely with the presence of a large number of fullerenes (e.g., PCBM) in contact with the evaporated Ca/Al metal top electrode. Although intrinsic polymer doping has been reported previously in the literature,[20,31] none of the pure polymer diodes we measured showed doping above our detection limit (~0.3 nC/cm^{-2} or < 5×10^{14} cm^{-3}) when put into diode structures without fullerene (see Table 1 and Figure 5.1b). Similarly, we also observed purely capacitive behavior (minimal to no measurable dark carriers) for traditional P3HT:PCBM blend-cast (BC) device structures where the polymer and fullerene were pre-blended in solution. When we used P3HT with the bisadduct fullerenes studied in Chapter 4, however, the reversed VPS relative to PCBM leads to a significant amount of fullerenes at the top of the active layer and thus a measurable number of dark carriers. The lack of doping has also been reported for several other blend-cast polymer:fullerene systems.[32] Other work, however, has identified doping of

unknown origin in various blend-cast polymer:fullerene systems, and this work can potentially explain the underlying reason for these previous observations.[23,33]

Taken together, Table 5.1 and Figure 5.1b indicate that the presence of CELIV-extractable dark carriers results from interaction of the fullerene with the evaporated metal electrode.[34–38] The number of extractable carriers saturates at an upper average value of ~40 nC/cm^{-2} ($10^{16\text{-}17}$ cm^{-3}) for as-cast P3HT/PCBM and PBDTTT-C/$PC_{70}BM$ quasi-bilayers, and can be considerably less for less quasi-bilayer-like device structures that do not have fullerene-rich layers in contact with the evaporated metal (e.g., SqP PSEHTT[39]/PCBM and SqP PSDTTT[40]/PCBM in Figure 5.1b). Extractable dark carriers also are present, but to a lesser degree, in conjugated polymer/C_{60} bilayers. As we will discuss further below, it is likely that part of the reason why C_{60} bilayers are doped less than PCBM is that the evaporated metal does not penetrate as effectively into the denser C_{60}. For example, Table 5.1 shows that C_g does not have an anomalously large value for C_{60} devices like in PCBM-based devices. Additionally, we find that the number of extractable dark carriers in C_{60}-based devices remains roughly constant with C_{60} overlayer thickness (Figure 5.3), which suggests that the carries are created only in a limited region around the C_{60}/metal interface.

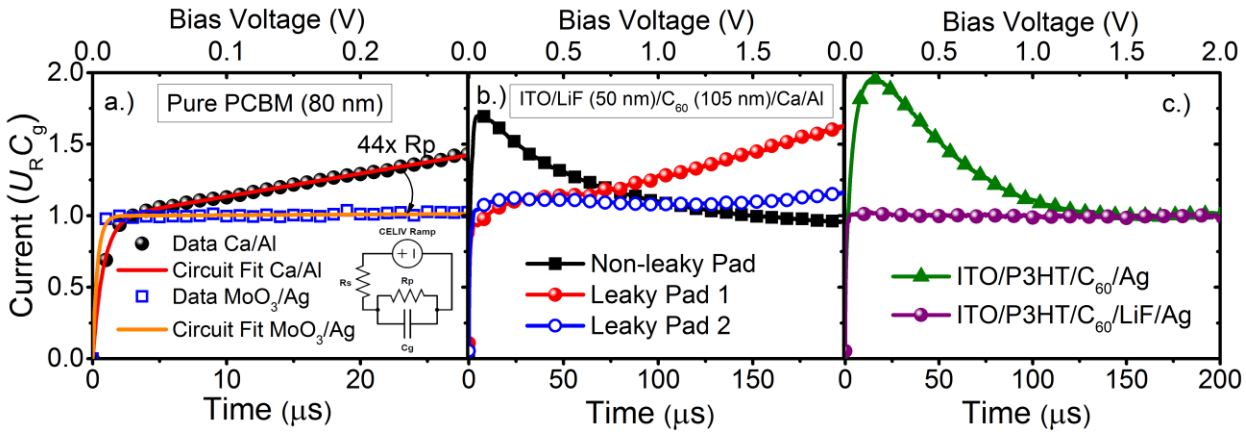

Figure 5.2 (a.) Measured (symbols) CELIV transients and fitted (lines) curves using circuit model (inset) on pure PCBM diodes with structures of ITO/PEDOT:PSS/PCBM/Ca/Al (black circle) and ITO/ZnO/PCBM/MoO_3/Ag (open blue square). The equations used for fitting are presented in Section 5.4.1. (b.) CELIV transients on diodes with a structure of ITO/LiF/C_{60}/Ca/Al. LiF (50 nm) and C_{60} (105 nm) were thermally evaporated sequentially onto ITO substrates. Both a non-leaky device and leaky devices were plotted to illustrate the effect of leakage current on CELIV transients. (c.) CELIV transients on diodes with structures of ITO/P3HT/C_{60} (105 nm)/Ag (green up triangles) and ITO/P3HT/C_{60} (105 nm)/LiF (15 nm)/Ag (purple circles).

In order to better understand the origin of extractable dark carriers, we also investigated CELIV in pure PCBM diodes. Figure 5.2a shows the dark CELIV current transients of devices with a structure ITO (150 nm)/PEDOT (30 nm)/PCBM (80 nm)/Ca (10 nm)/Al (70 nm) and ITO (150 nm)/ZnO (50 nm)/PCBM (80 nm)/MoO_3 (15 nm)/Ag (70 nm). We found that all of the PCBM devices with Ca/Al electrodes had extremely low shunt resistances, (black circles), even though the PCBM film quality was good enough to make excellent, non-leaky devices with MoO_3/Ag cathodes (Figure 5.2a, blue open squares, which have a shunt resistance 44× higher). This decrease in shunt resistance with Ca/Al as the cathode is consistent with the idea of extensive metal intercalation into the PCBM layer.

To better illustrate the effect of leakage current, Figure 5.2b shows CELIV transients for devices with identical configurations, materials, and thickness but different shunt conductances. The non-leaky ITO/LiF (50 nm)/C_{60} (105 nm)/Ca (10 nm)/Al (70 nm) device shows a significant number of dark carriers (black squares), but the devices with high shunt conductance have a dramatically different shape. What this indicates is that a strong shunt current can easily

mask/destroy the CELIV 'bump', making it difficult to identify and quantify the presence of dark carriers in such samples. One reason why the CELIV bump associated with dark carriers can disappear when there is significant leakage current is because the leaked charge can refill the depleted active layer, screening the space-charge region left behind from vacated doped carriers. We believe that this is likely the case for pure PCBM/metal devices like those exemplified in Figure 5.2a. Unless otherwise specified, though, all the dark carrier densities and related conclusions drawn throughout this work are based on diodes that possess shunt resistances large enough in the bias range of interest ($> \sim 10^5\ \Omega$) to easily and accurately quantify doping.

The fact that the devices in Figure 5.2b do not contain any polymer layer but still show significant doping (black squares) again rules out the possibility that the polymer contributes to the presence of dark carriers. It is certainly possible that the dark carriers are produced by the interaction of LiF with the fullerene derivative, particularly since there are literature reports that evaporated LiF/Al electrodes can dope C_{60}.[19] To prove that the dark carriers are indeed produced by the fullerene-layer/metal interaction, we plot in Figure 5.2c CELIV transients for diodes with structures of ITO/P3HT/C_{60}/Ag (green up triangles) and ITO/P3HT/C_{60}/LiF (15 nm)/Ag (purple circles). We find that, similar to the yellow left triangle symbols in Figure 5.1b (P3HT/C_{60}/Ca/Al), diodes with Ag as top electrode also show a significant number of dark carriers (Figure 5.2c green up triangle). However, when we evaporated an interlayer of LiF between C_{60} and Ag, no dark carriers were observed. These results demonstrate that neither P3HT nor the evaporation of LiF onto C_{60} is the reason behind the presence of extractable carriers, supporting the idea that the carriers are produced from an interaction between the fullerene and the evaporated cathode metal.

5.2.3 The Distribution of Dark Carriers: Surface or Bulk?

The dark CELIV results we obtained from as-cast P3HT:PCBM SqP films compared with annealed SqP devices (Figure 5.1b and Table 1) provide another indication where the extra carriers come from: after thermal annealing, a large fraction of the PCBM molecules on the surface of the as-cast film are brought deeper into the P3HT underlayer. This change in VPS upon annealing of SqP P3HT:PCBM films has been verified by both neutron reflectivity[4] and X-ray photoelectron spectroscopy (XPS).[3,4] The observation that more dark carriers are present in as-cast SqP diodes than annealed ones indicates that the vertical distribution of the fullerene molecules has a direct impact on doping. This suggests that the more fullerene molecules reside at the top part of the device (towards the cathode), the more extractable carriers are seen in the CELIV measurement.

This leads to the question: are the dark carriers produced only at the very top of the organic layer (i.e. at the organic/metal interface), or are carriers also made inside the bulk of any portion of the film that is predominantly fullerene in composition? To answer this surface vs. bulk question, we performed a series of experiments and simulations on devices with various active layers with different VPS compositions. The results are summarized in Figure 5.3 and Table 1.

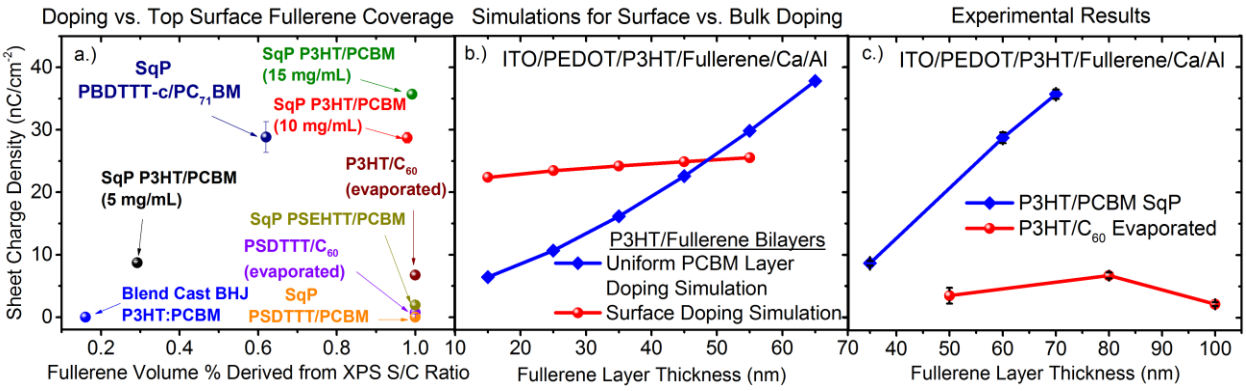

Figure 5.3 (a.) Sheet doping density versus fullerene volume fraction near the organic/cathode interface (derived from XPS analysis, see SI) for diodes made with various organic semiconductors. All devices have the structure: ITO/PEDOT:PSS/Organic Semiconductor/Ca(10 nm)/Al(70 nm); (b.) Simulation of sheet charge density versus fullerene layer thickness for diodes with a P3HT/fullerene bilayer configuration, using "A Solar Cell Capacitance Simulator" (SCAPS) simulation;[41] (c.) experimental data of measured sheet charge density versus fullerene layer thickness obtained by subtracting the P3HT layer thickness (115 nm) from the total organic layer thickness measured from profilometry. The PCBM overlayer thickness is controlled by adjusting the concentration of PCBM solution[6] while the C_{60} layer thickness controlled by the evaporation time and rate.

In Figure 5.3a, we measured the dark sheet charge densities for a number of devices with various active layers and then studied the top surface composition of these active layers using XPS. Based on the elemental ratio of sulfur/carbon obtained from XPS, we were able to calculate the volume fraction of the fullerene within the top ~10 nm of the film (see Section 5.4.5 for details). Surprisingly, there is no direct correlation between the amount of fullerene at the organic/metal interface and number of dark carriers for the corresponding diode. Instead, what we see is that for a significant number of dark carriers to be measured, the device indeed requires fullerene molecules present at the top interface. However, a high coverage of fullerene on the top surface does not guarantee a high sheet charge density: e.g., devices that all have > 95% fullerene volume fraction show orders of magnitude differences in their dark sheet charge densities.

Since there is no simple dependence of sheet charge density on the fullerene volume fraction with 10 nm of the surface, we next studied the sheet charge density versus the thickness of a

carefully controlled fullerene overlayer. First, we performed SCAPS simulations on P3HT/fullerene bilayer diodes with Ca/Al as top electrode with two different assumptions about the distribution of dark carriers: 1) we assumed that carriers were present only at the fullerene/Ca interface and 2) we also assumed that carriers were present uniformly throughout the entire fullerene overlayer. By adjusting the thickness of the fullerene overlayer while maintaining all other parameters constant, we were able to predict the relationship between sheet charge density and fullerene overlayer thickness for each of these two assumptions (Figure 5.3b). The assumption that carriers are only produced at the surface predicts an almost constant sheet charge density for all fullerene overlayer thicknesses, whereas the assumption of uniformly-distributed carriers predicts an approximately linear increase in sheet charge density with increasing fullerene layer thickness.

To determine which assumption agrees with experimental data, we constructed two series of diodes, both with structures of ITO/PEDOT:PSS/P3HT/Fullerene/Ca/Al. Similar to the simulations, we held the thicknesses of all layers constant except for the thickness of the fullerene (either PCBM or C_{60}) overlayer. The experimental results shown in Figure 5.3c are quite intriguing. The P3HT/PCBM quasi-bilayer devices whose active layers were prepared using the SqP technique show an almost linear dependence of the doping on PCBM overlayer thickness, in agreement with the assumption of uniformly distributed dark carriers. In contrast, the sheet charge density of the P3HT/C_{60} bilayer devices does not depend on C_{60} overlayer thickness, which matches the simulation results for the case where the dark carriers reside only at the interface.

As will be detailed in the following sections, all these results can be explained by metal penetration: simply speaking, the number of dark carriers depends on the amount of metal

penetration into the fullerene overlayer, which in turn depends on both the chemical identity of the fullerene and how thick the layer is. Different systems have different metal penetration depths, so different amounts of dark carriers are extracted.

5.2.4 Changes in C_g with VPS Indicate Metal Penetration

One key result that strongly supports the idea of metal penetration is the observation of how the geometric capacitance (C_g) changes when dark carriers are present. C_g can be obtained from CELIV measurements by dividing the displacement current of a depleted diode by the CELIV voltage ramp rate. For an ideal diode with clean interfaces, C_g is determined by:

$$C_g = \varepsilon_r \varepsilon_0 A / d_g \quad (1)$$

where ε_r is the permittivity of the organic material, ε_0 is the vacuum permittivity, A is the device area and d_g is the distance between the two parallel planar electrodes. The idea is to measure the exact thickness of the organic layer by profilometry or atomic force microscopy and then compare this value to the thickness calculated from C_g; we refer to these two thicknesses as the actual thickness and the d_g thickness, respectively.

When we determined the d_g thicknesses for our diodes, we found that the actual thicknesses agreed well with the d_g thicknesses for diodes with active layers consisting of pure P3HT, blend-cast P3HT:PCBM BHJs, and SqP P3HT:PCBM quasi-bilayers that were annealed at 150 ℃. However, when studying as-cast sequentially-processed P3HT/PCBM diodes, we found that the d_g thicknesses are lower than the actual thicknesses by ~30–60 nm depending on the PCBM concentration used during spin-coating. To establish a relationship between the actual thickness and the d_g thickness, we analyzed the data on a large number of samples. The results are summarized in Table 1 and Figure 5.4.

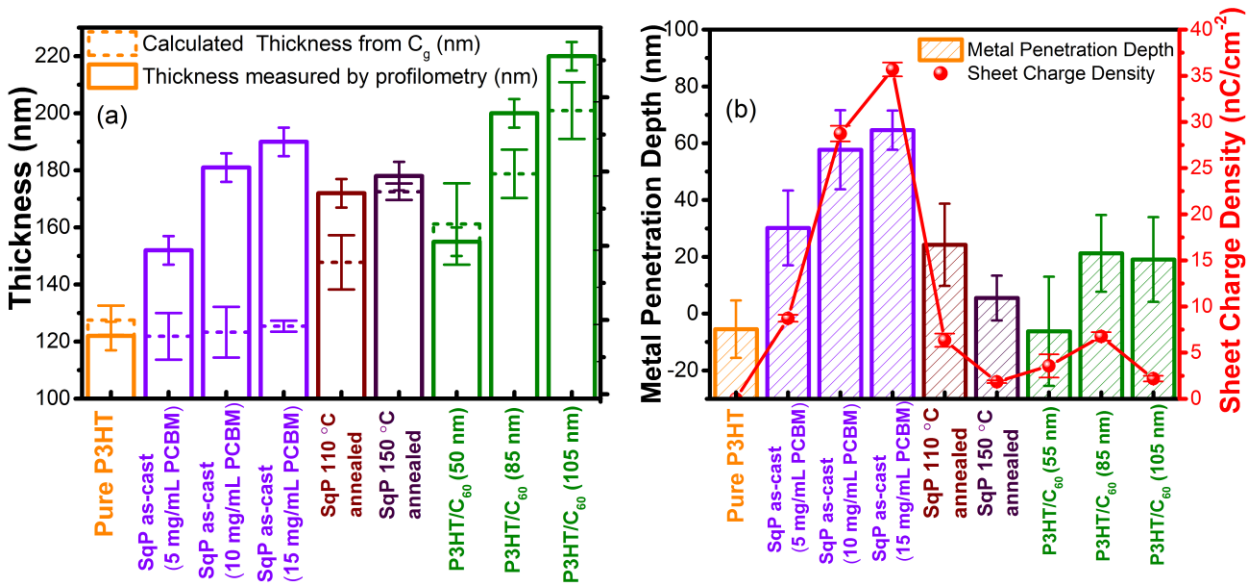

Figure 5.4 (a.) Actual organic layer thickness measured by profilometry (solid bars) and calculated thickness from C_g (dashed bars) for diodes with different organic semiconductors. (b.) Metal penetration depth (shaded bars) and sheet charge density (red circles) for the same diodes in (a.). The metal penetration depth is calculated by subtracting the d_g thickness from actual thickness. The sheet charge density is obtained from the dark CELIV measurement using the method mentioned in 5.2.1. All diodes have a structure of ITO/PEDOT:PSS/Organic Semiconductor/Ca/Al. For the annealed samples, annealing was performed prior to the evaporation of the Ca/Al electrode. The P3HT/PCBM organic layers were prepared by SqP and the P3HT/C_{60} ones by evaporation of C_{60} onto the P3HT underlayer. The error bars show 1 standard deviation over at least three separate measurements.

The left 5 bars in Fig. 5.4a show the results for pure P3HT samples as well as SqP P3HT/PCBM samples that were either as-cast or thermally annealed at different temperatures; the solid bars are the actual thicknesses measured by profilometry, and the dashed bars (which in most cases are inside the solid bars) are the calculated thicknesses from C_g. The two thicknesses

agree well for the pure P3HT samples, indicating decent accuracy of the d_g obtained using the CELIV technique. However, the three as-cast SqP P3HT/PCBM devices and the 110 ℃ annealed SqP device show much larger actual thicknesses than their d_g thicknesses. When we increased the annealing temperature to 150 ℃, we found the two thicknesses again become consistent, similar to that observed for the pure P3HT samples.

The variations in the consistency between the two measurements can be explained by different vertical phase segregation in each of these active layers. As discussed earlier, in as-cast SqP P3HT/PCBM films, most PCBM molecules stay on top of the P3HT underlayer, with only a small amount of fullerene diffused into the polymer underlayer.[4] If this as-cast layer is thermally annealed at a temperature of 150 ℃, however, both the bulk morphology and vertical distribution of the fullerene molecules is completely changed,[4] becoming similar to the traditional blend-cast BHJ, which has P3HT segregating towards the top surface due to its lower surface energy (see Chapter 4). Therefore, comparing the as-cast (Figure 5.4a middle violet bar) and the 150 ℃ annealed (Figure 5.4a purple bar) SqP devices suggests that it is the amount of enriched fullerene at the top part of the organic layer that makes the actual thickness higher than the d_g thickness.

For these devices (as-cast and annealed SqP) which have the same organic layer thickness (confirmed by profilometry), why does vertical phase segregation affect the d_g thickness? In other words, why would the effective distance between the two parallel metal plates decrease when there are a large number of fullerene molecules on top of the layer in contact with the evaporated cathode? One reasonable explanation is that the metal evaporation process causes hot metal atoms to diffuse into the fullerene-rich layer, which can increase the measured C_g by effectively making the two electrodes become closer to each other. This could be because the metal simply stays connected as it penetrates through the fullerene overlayer, or it could result

from the fact that the metal/fullerene composite has a very high dielectric constant, ε_r, which would lead to a smaller value of d_g, as seen in Eq. 1.

To investigate how deep the metal can penetrate into a fullerene overlayer, we compared the d_g's of as-cast SqP P3HT/PCBM devices with different PCBM overlayer thicknesses, shown by the three violet bars in the middle of Figure 5.4a. As expected, the actual thickness d of the active layer increases as we increase the PCBM concentration. But, the d_g thicknesses for all these as-cast SqP samples are similar to each other and roughly equal to the thickness of the pure P3HT underlayer, independent of the thickness of the PCBM overlayer. This suggests that the evaporated cathode metal, Ca/Al in this case, is able to penetrate through the entire PCBM overlayer, and does not stop until it reaches the polymer underlayer.

To further support the argument that the low d_g thickness is caused by the vertical fullerene distribution, we compared what happens when we annealed our SqP P3HT/PCBM devices at two different temperatures. Time-resolved neutron reflectivity have shown that the transition temperature for the PCBM molecules in the SqP overlayer to diffuse into the P3HT underlayer is between 110 ℃ and 120 ℃.[5] Therefore, we would expect larger difference between the actual thickness and the d_g thicknesses for devices annealed at 110 ℃ than those annealed at 150 ℃. The experimental results are shown as the two solid bars Figure 5.4a (wine colored for 110 ℃ and purple for 150 ℃) and agree with this expectation. The fact that the d_g thickness for 110 ℃ annealed sample remains between the as-cast and the 150 ℃ annealed sample fits well with the idea that d_g is primarily determined by the vertical fullerene distribution in the organic layer. The CELIV transients for these SqP P3HT/PCBM diodes can be found in the Section 5.4.2.

In addition to changing the PCBM concentration during spin-coating, another way to control the fullerene layer thickness is to simply make bilayer devices with C_{60} evaporated on top of the

polymer underlayer. In Figure 5.4a, we did the same d_g analysis for P3HT/C_{60} bilayer devices with different thickness C_{60} layers evaporated onto the P3HT layer. We find that the difference between the actual thickness and d_g thickness for these P3HT/C_{60} bilayer based diodes for these devices is smaller, in the range of ~5 – 20 nm. All three C_{60} thicknesses give larger d_g thicknesses than the pure P3HT underlayer, and the values increase monotonically with increasing amounts of evaporated C_{60}. This suggests that evaporated C_{60} layers allow less metal penetration, possibly due to the higher physical density and closer packing of C_{60} than PCBM.

5.2.5 Number of Dark Carriers Governed by Metal Penetration Depth

Now that we know metal diffusion into the fullerene layer is the reason for the inconsistency between the actual and calculated thickness from C_g, we would like to investigate the correlation between the number of extractable dark carriers and the depth of metal penetration. We define the metal penetration depth as the difference between the actual thickness and the d_g thickness. Figure 5.4b plots this metal penetration depth (shaded bars) against the number of extracted dark carriers (red circles) for the polymer/fullerene samples studied in Figure 5.4a. The result shows that the amount of doping is indeed directly correlated to the metal penetration depth. For as-cast SqP devices, Ca/Al penetrates all the way through the fullerene layer. This means that the number of dark carriers is limited by the thickness of the fullerene overlayer, so more dark carriers are measured for devices with thicker PCBM overlayers. In contrast the lower metal penetration depth for samples with evaporated C_{60} overlayers show fewer dark carriers, because the metal is confined only the surface region of the film. This same correlation holds in the two annealed diodes: more metal penetration in the 110 ℃ annealed device (~25 nm) leads to more doping than the 150 ℃ annealed case, which shows no metal penetration (<5 nm). All of these ideas are summarized in Figure 5.5.

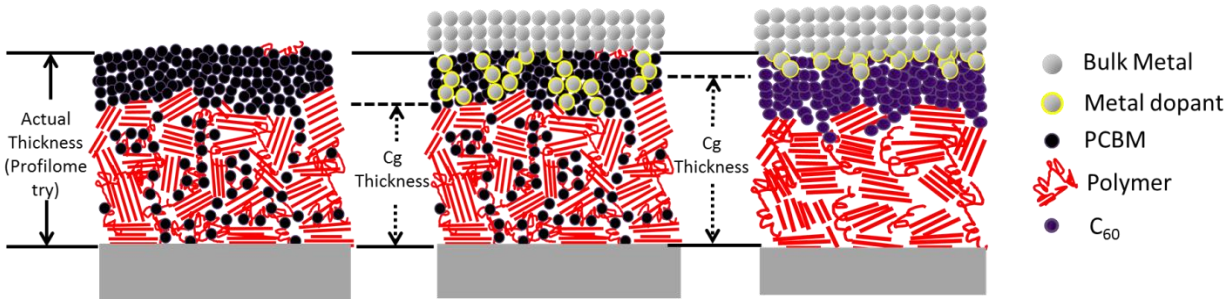

Figure 5.5 The metal penetration cartoon. Left: SqP P3HT/PCBM active layer before metal evaporation. Middle: SqP P3HT/PCBM/Evaporated Metal. Right: P3HT/C_{60} (evaporate)/Evaporated Metal.

5.2.6 Direct Evidence for Metal Penetration: Imaging the Device's Cross-section by TEM

To understand the extent of metal penetration into polymer/fullerene OPV active layers, we carried out cross sectional transmission electron microscopy (TEM). For the images shown in Fig. 5.6, the diode had a structure of ITO/PEDOT:PSS/SqP P3HT/PCBM/Au and was cut but a focused ion beam. Au was chosen as the top electrode for this experiment for three reasons: 1) Au has better stability in air than the low work function metals such as Ca; 2) Au gives better contrast in TEM; 3) SqP P3HT/PCBM/Au diodes show similar amount of dark carriers and similar metal penetration depth (Table 5.1 and Figure 5.7 in the next section) as diodes with Ca/Al electrodes.

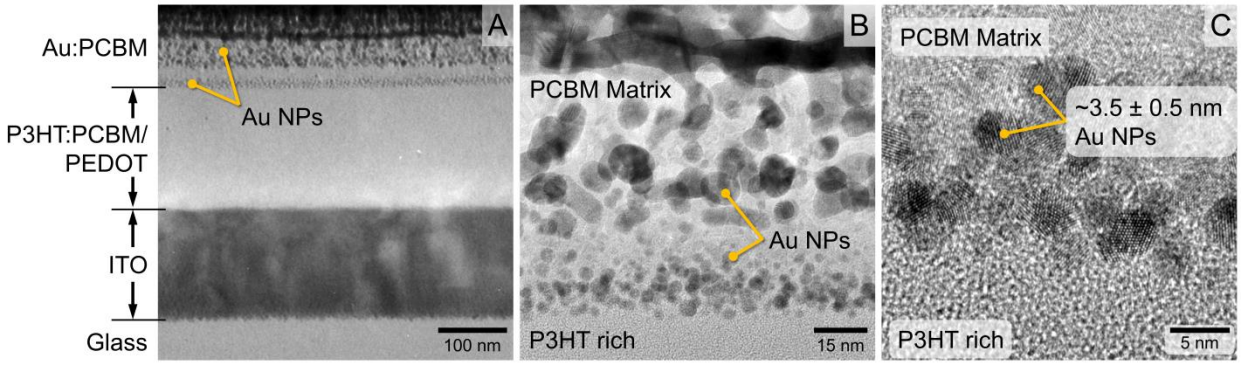

Figure 5.6 Bright field cross-sectional images of glass/ITO/PEDOT/P3HT:PCBM/PCBM:Au/Au as-cast SqP devices. A) Zoomed out image of the entire device, showing the various layers and their persistence in the in-plane direction. B) Zoomed in image of the P3HT:PCBM/PCBM:Au/Au interface, showing the remarkable nanoparticle formation resulting from thermal evaporation of Au onto a PCBM-rich layer. C) Further zoomed in image on the belt of ~3.5 nm nanoparticle at the P3HT-rich interface. The elemental composition in each portion of the image was identified by EDX analysis).

Figure 5.6(a) makes it clear that thermally evaporated Au atoms penetrate all the way through the PCBM overlayer and stop at the top of the P3HT underlayer. This result is surprising because both the materials (conjugated polymers, fullerene derivatives and metal electrodes) and the cathode deposition technique (thermal evaporation) are standard for making organic photovoltaics (OPVs), but this is the first report that evaporated metal atoms can penetrate through the tens of nm of the fullerene material.

Figure 5.6(b) shows an expanded view of the same cross sections, zoomed in on the P3HT:PCBM/PCBM:Au/Au interface. From the top to the bottom of this image are: the bottom of the bulk Au layer, a mixed PCBM:Au layer of ~40–50 nm thickness with Au nanoparticles of average size ~9 nm, a nearly pure PCBM layer (no Au or S signal from EDX) of ~15–25 nm

thickness, a thin layer of smaller-sized Au nanoparticles at the very top of the P3HT underlayer, and finally the bulk of the P3HT layer. The formation of the thin layer that is nearly depleted of Au between the PCBM:Au intermixed layer and the P3HT layer possibly forms from the fact that the P3HT surface is a favorable place for Au nanoparticles to reside, so Au atoms in this region migrate toward the P3HT surface as they cool. This is not surprising since Au is well known to interact with S,[42–47] and of course P3HT contains S in its thiophene backbone. Figure 5.6(c) shows a further zoomed in image at the P3HT/PCBM interface, revealing that the size of the Au nanoparticles at the P3HT/PCBM interface is ~3.5 nm.

5.2.7 Exploring the Possible Origin of Doping: C_g Analysis for Different Metals and Temperature Dependence of the Carrier Concentration and Mobility

Now that we know Au is able to penetrate through the fullerene, we would like to investigate how such penetration varies with different metals and how this interpenetration is correlated with the number of extracted dark carriers. To this end, we performed the same C_g analysis described above using as-cast SqP P3HT/PCBM active layers but different top metal electrodes. The results are shown in Figure 5.7.

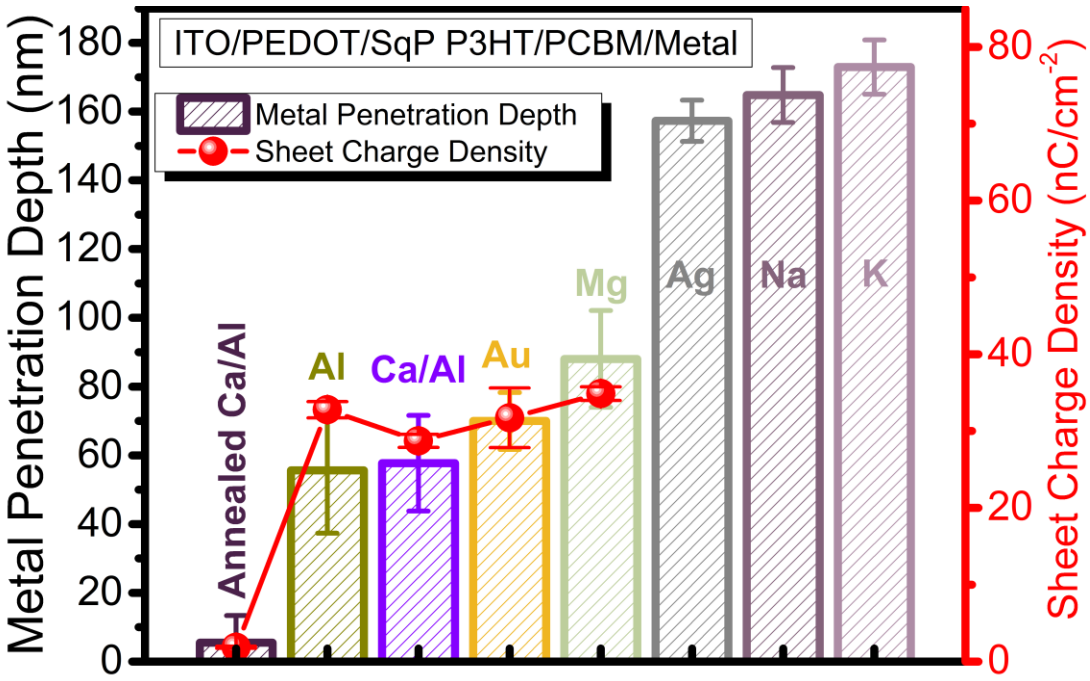

Figure 5.7 Metal penetration depth (shaded bars) and sheet charge density (red circles) for SqP ITO/PEDOT:PSS/P3HT/PCBM/Metal diodes with different top metal electrodes. The first shaded bar is the same 150 ℃ annealed SqP P3HT/PCBM sample used in Figure 5.4. The rest of the bars summarize the results for as-cast SqP P3HT/PCBM active layers prepared under the same conditions with 10 mg/mL PCBM spun on top of the P3HT underlayer. The total organic layer thickness measured by profilometry is ~180 nm for all samples. The metal penetration depths are obtained by subtracting the C_g thicknesses from the actual thicknesses.

Figure 5.7 tells us that different metals indeed penetrate into the organic layers to different depths. Similar to Au, the C_g analysis shows Al and Ca/Al are able to penetrate through the entire fullerene layer but stop at the very top of the P3HT surface. For Mg, the metal penetrates slightly deeper into the P3HT underlayer but still stops ~20–30 nm from the top of the P3HT underlayer. In contrast, Ag, Na and K are not only able to penetrate through the fullerene overlayer, but they also penetrate through almost the entire P3HT underlayer, leading to diodes

that are often shorted or nearly-shorted (Section 5.4.3); such diodes cannot show measurable dark carriers for the reasons discussed in Section 5.2.2.

For the non-leaky devices with Al, Ca/Al, Au and Mg top electrodes, the number of dark carriers extracted is about the same. This is a clear indicator that it is the amount of metal in the fullerene layer that controls the number of extracted dark carriers, but not any particular property of the metal. This is a somewhat non-intuitive result because these metals we have used have significantly different work functions and ionization energies; e.g., the work function for Au is ~5.1 eV while that for Ca is ~2.9 eV; the 1st ionization energy for Au is ~890 kJ/mol while that for Al is ~578 kJ/mol. If the dark carriers are resulted from transfer of electrons from the metal conduction band to PCBM's lowest unoccupied molecular orbital (LUMO), we would expect the amount of doping to vary markedly between different metals. Instead, all of the metals studied in this work (not including the alkali metals and Ag, which give shorted diodes) lead to similar numbers of extracted dark carriers.

Even though there are reports that C_{60} can undergo charge transfer with nearly any metal (e.g., Al, Au, Ag, Mg, W, etc),[35,37,48–51] there is yet another argument as to why the dark carriers we observe are unlikely to be the result of a metal-to-fullerene LUMO charge transfer. A simple calculation shows that number of carriers we extract corresponds to a doping of 1 part per ~10^5 PCBM molecules. Given the large difference in the diodes' actual thickness and d_g thickness and the large amount of Au presenting in the PCBM-rich layer (Figure 5.6), 1 part per 10^5 doping is far too small if the doping were a bulk metal-to-bulk fullerene electron transfer process.

To further investigate the origin of the dark carriers, we performed temperature dependent CELIV measurements on as-cast SqP ITO/P3HT/PCBM/Ca/Al diodes (same structure as in Figure 5.1b). The result is shown in Figure 5.8.

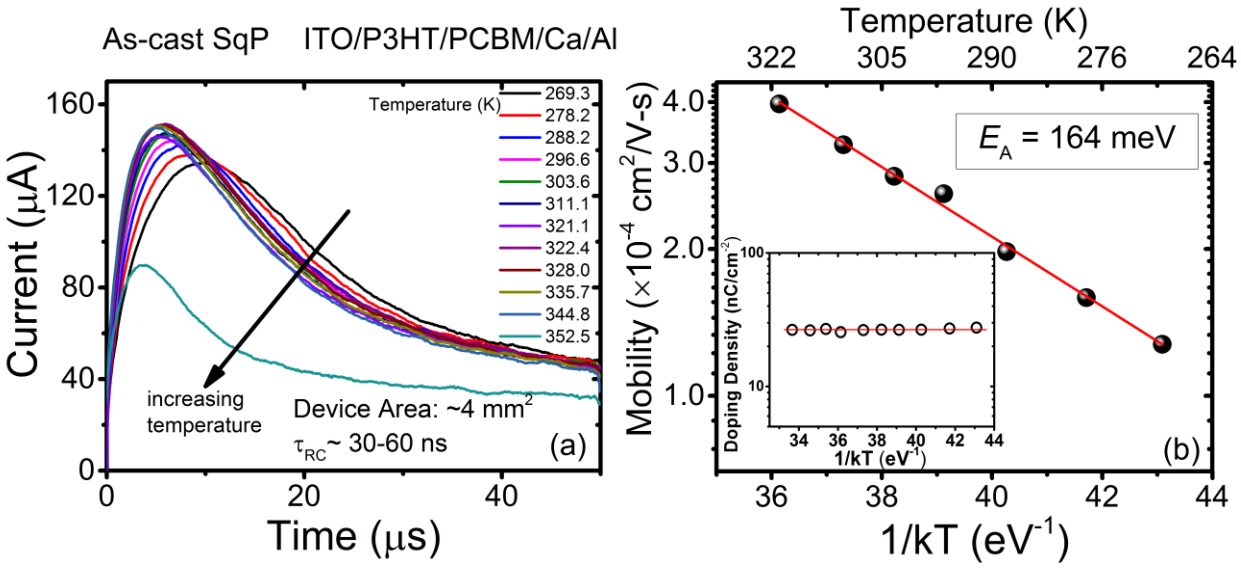

Figure 5.8 (a): CELIV transients for as-cast SqP ITO/P3HT/PCBM/Ca/Al diode at different temperatures. The device area is small enough (~4 mm^2) to ensure the transient is not RC time constant limited and that the mobility calculated is meaningful. (b): Calculated mobility of the dark carriers versus temperature. E_A is the activation energy obtained from fitting. The inset shows the sheet charge density versus temperature for the same device.

The device structure we chose for this study, ITO/P3HT/PCBM/Ca/Al, eliminates the series resistance of the PEDOT:PSS layer. We also reduced the device area to make sure the CELIV transients were not RC time-constant limited. Figure 5.8a clearly shows that the CELIV peak shifts towards earlier times with increasing temperature, indicating the mobility of the dark carriers increases with increasing temperature, the classic signature of carriers moving through an organic semiconductor. At a high enough temperatures, e.g., around 352.5 K, PCBM molecules start to migrate into the P3HT underlayer, changing the overall VPS to decrease the amount of PCBM on top of the active layer, reducing the amount of extracted dark carriers decreasing C_g.

In Figure 5.8b, we plot the mobility calculated from the CELIV transients at different temperatures shown in Figure 5.8a. We find that the carrier mobilities increase with increasing temperature, with values on the order of 10^{-4} cm^2 V^{-1} s^{-1}, similar to the electron mobility of PCBM.[52,53] Therefore, this result suggests that the organic layer is not degenerately doped and still behaves like a classic organic semiconductor even with the intermixed metal:fullerene layer. Furthermore, although the peaks for the CELIV transients shift to earlier times with increasing temperature, the integrated areas of the "bumps" do not change with temperature, meaning that the number of dark carriers does not change with temperature. This indicates that the temperature range we explored is within the saturation regime, where the charge carrier density is equal to the doping density. This density does not change with temperature due to the fact that the change in Fermi energy compensates the tendency of the doped carrier density to change with temperature, which results in a stable carrier density over a wide range of temperatures.[54]

Finally, we also investigated the presence of dark carriers in organic solar cell diodes with different fullerene derivatives. We already showed above that the number of dark carriers was quite different between the diodes with PCBM and $C_{60,}$ largely due to different degrees of metal penetration. In addition to these two fullerene derivatives, we performed the same experiments on another fullerene derivative, indene-C_{60}-bisadduct (ICBA), which is widely used in the OPV field for high-open circuit voltage solar cells.[55–57] We fabricated SqP P3HT/ICBA active layers following the same methods as for PCBM. The result in Table 1 and Figure 5.14 demonstrate that even though metal can penetrate through the entire ICBA layer, based on diodes' C_g, the number of dark carriers is much lower than from diodes with PCBM. This result suggests that the dark carriers must be intrinsic to the fullerenes: different fullerenes contain different level of defects/impurities, which become extractable once any metal penetrates into the fullerene

domains, likely due to the fact that the local dielectric constant is raised to the point where trapped carriers become free.

5.3 Conclusion

In conclusion, we have conducted a study on metal interpenetration in fullerene-based organic semiconductor solar cell diodes. The investigation reveals the unexpected phenomenon that the evaporated metals commonly used as cathodes are able to penetrate through tens of nm of fullerene material, as verified by cross sectional TEM. The interpenetrated metal disperses metal atoms and nanoparticles throughout the fullerene overlayer, and the penetration stops only at the top surface of the polymer underlayer. Moreover, the interpenetrated metal leads to a significant number of extractable dark carriers in CELIV. The dark carriers are observed only for active layers that contain a fullerene-rich or pure fullerene overlayer exposed to the evaporated cathode metal, and the number of dark carriers is directly related to the amount of metal penetration. Another consequence of metal penetration is that the geometric capacitance changes dramatically with the depth of the metal penetration, producing a large change in the devices' effective electrical thickness. This could cause a mis-interpretation of device physics experiments for measurements requiring the effective thickness as an input parameter.

The implications of these observations for device physics, optimizing device structure and even increasing the device efficiency for organic solar cells are vast. Since the evaporated cathode metals can form nanoparticles deep in the fullerene layer, one could potentially take advantage of these nanoparticles by tailoring them for increasing light absorption through plasmonic resonance.[58,59] Moreover, since the metal penetration is directly related to vertical phase segregation, one could employ different active layer fabrication techniques, such as

sequential processing or solvent-assisted slow growth, to control the degree of the interpenetration and potentially tune the size and distribution of the metal nanoparticles in the organic layer. Other effects such as increasing or decreasing surface recombination by tuning the amount of metal penetration could also be studied in future work.

5.4 CELIV Transients and Experimental Methods

5.4.1 Equivilant Circuit Modeling of Depleted Devices

We modeled depleted CELIV curves using the circuit depicted in Figure 5.9. The solution to the differential equation for the current flowing through the circuit in Figure 5.9 when applying a CELIV ramp of the form $V_{app} = U_R t$ where t is the time after the start of the ramp and U_R is the ramp rate in V/s is:

$$I = I_D \left(1 - e^{-\frac{t}{\tau}}\right) + \frac{U_R t}{R_p + R_s} \tag{2}$$

$$\tau = \frac{C_g R_p R_s}{R_p + R_s} \tag{3}$$

$$I_D = \frac{C_g U_R}{(1 + R_s)^2} \tag{4}$$

Interestingly, with finite series (R_s) and shunt (R_p) resistances, the apparent displacement current (I_D) is reduced from its classical magnitude ($C_g U_R$) by a factor of $(1 + R_s/R_p)^{-2}$, though this reduction is typically quite small since usually $R_p \gg R_s$. In previous Sections, the simulated depleted curves in Figure 5.1a along with any subsequent fitting results were obtained by using Eqns. (2-4).

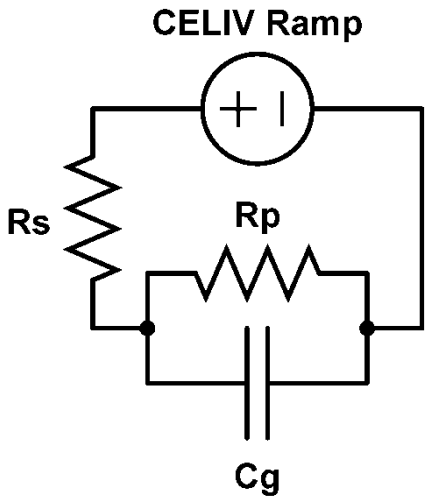

Figure 5.9 The equivalent circuit for modeling depleted (no doping) CELIV curves. The current for this circuit/voltage-ramp combination are given by Eqns. (2-4).

5.4.2 CELIV Transients for Devices with Various Organic Layers

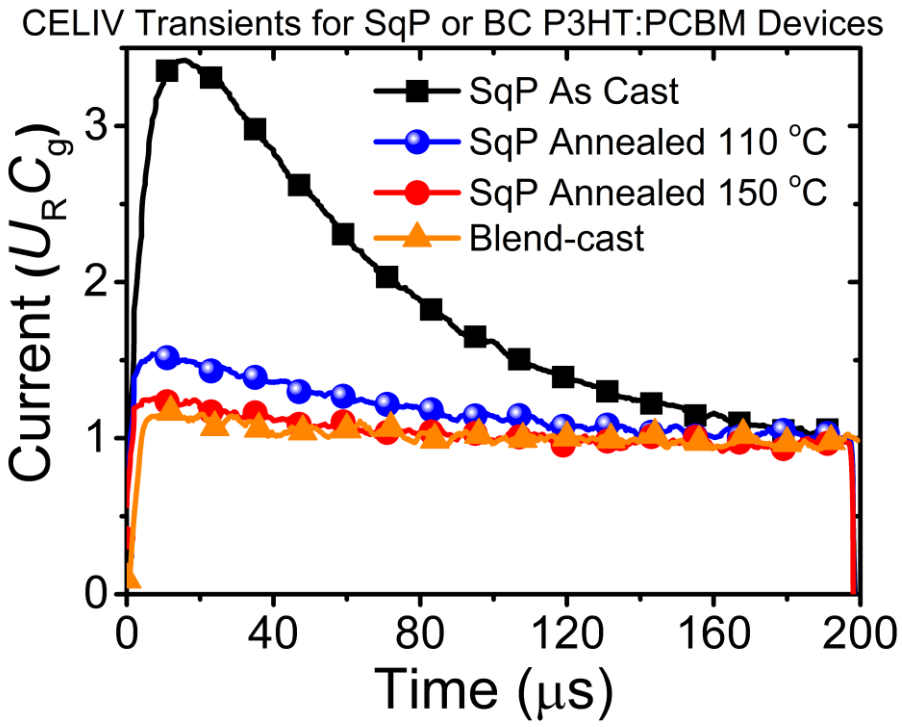

Figure 5.10 The effect of annealing on the measured CELIV transients of SqP P3HT/PCBM devices, compared with a BC device. Annealing at higher temperature causes more PCBM to mix into the P3HT underlayer, leading to less apparent doping upon metal cathode evaporation.

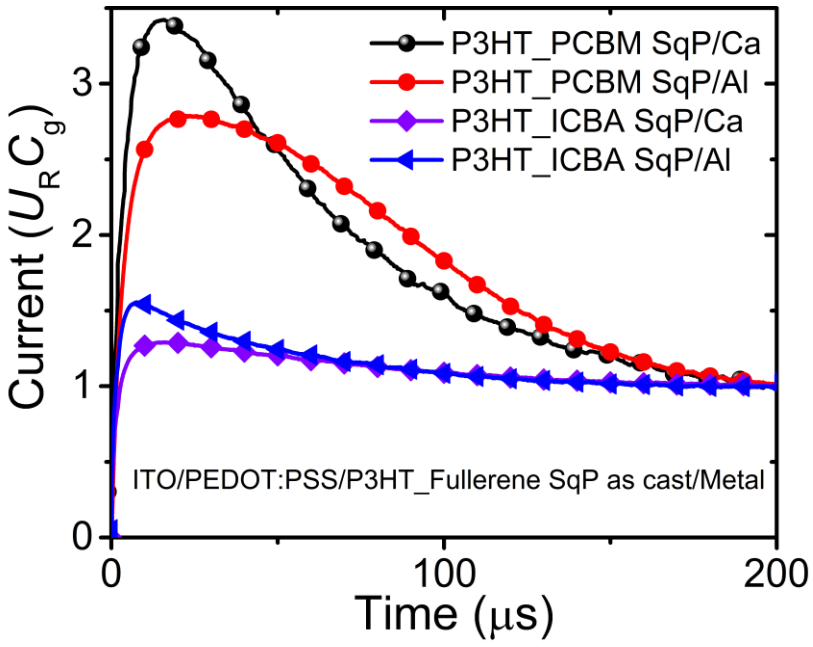

Figure 5.11 CELIV transients for as-cast SqP P3HT/PCBM and as-cast SqP P3HT/ICBA devices with different metal electrodes. The devices with ICBA show much less dark carriers. The SqP P3HT/ICBA/Ag result (Table 5.1) is not shown here due to the high leakage current.

5.4.3 Devices with Different Metal Cathodes

We have demonstrated the effect of metal penetration on device C_g in the main text. The metals that penetrate through the fullerene layer and stop at around the polymer/fullerene interface show C_g's close to the P3HT underlayer, while the metals such as K and Na can penetrate into and even through the polymer layer to make the device extremely leaky. In Figure 5.15, we show that the ability for the polymer layer to stop further metal penetration is crucial to

maintain the devices' diodic characteristics. Examples of metals that are stopped by the polymer underlayer are Ca, Mg and Al.

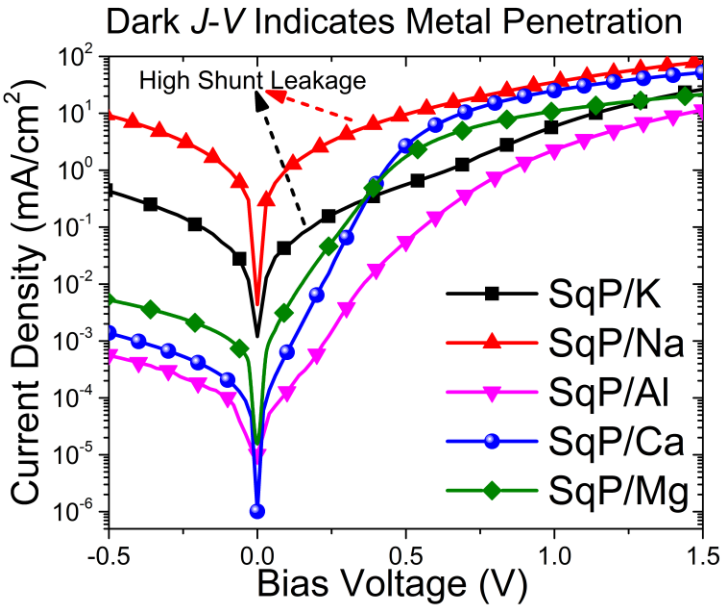

Figure 5.12 The effect of metal penetration on device dark *J-V* characteristics.

In accordance with the dark *J-V* characteristics, the CELIV transients for as-cast SqP devices with different metal electrodes can also be divided into two groups. Na and K behave like leaky capacitors (see main text Figure 5.1a), while Ca, Ma and Al show "bumps" in their CELIV transients. A non-leaky diode, ZnO/SqP/MoO_3/Ag, is plotted in the same figure for comparison.

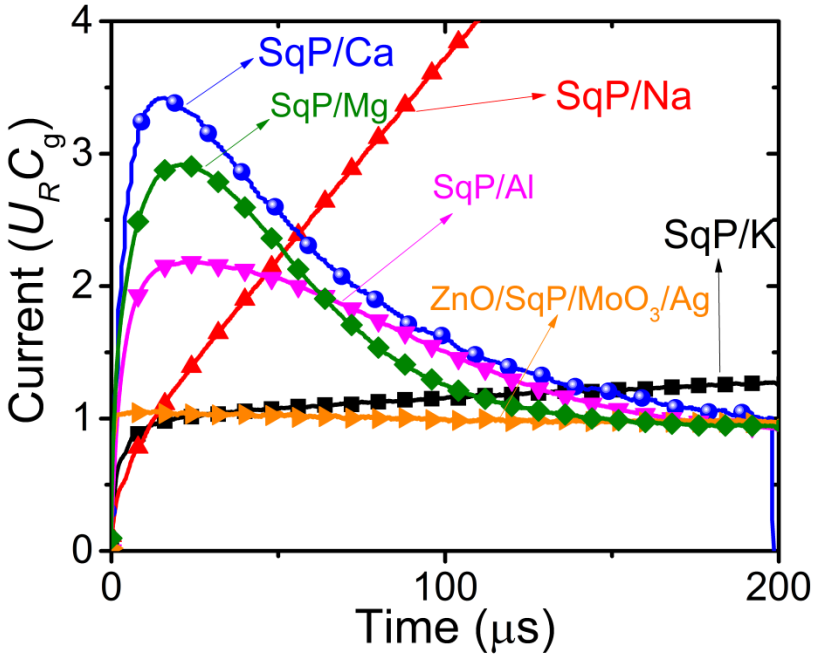

Figure 5.13 CELIV transients for as-cast P3HT/PCBM SqP devices with different metal electrodes.

It is worth mentioning that we fabricated a series of as-cast SqP P3HT/PCBM/Ca/Al diodes with different Ca layer thicknesses, from 0.3 nm to 40 nm (Table 5.1). We found the number of dark carriers did not scale with the Ca layer thickness. A 0.3 nm Ca layer was able to able to provide approximately the same amount of dark carriers as the 10 nm Ca layer. This supports our argument in the main text that the amount of carriers is most likely determined by the property of the fullerene underlayer, not the top electrode.

5.4.4 Discussion on Polymer Effect on Measured Dark Carriers

It is worth pointing out again that P3HT does not contribute to the extractable dark carriers we measured from CELIV. Though others have reported that chemical reactions between calcium and P3HT indeed take place,[9] we believe such reactions have no contribution to the dark

carriers, but might contribute to the increased C_g values we observed. The first reason is as mentioned earlier, we fabricated P3HT only diodes with structures of ITO/PEDOT:PSS/P3HT/Ca/Al, ITO/P3HT/Ca/Al or ITO/ZnO/P3HT/MoO_3/Ag and we found no dark carriers in any of these devices. Second, we fabricated P3HT/C_{60} diodes with three different P3HTs: highly regioregular P3HT,[6] Rieke P100 P3HT and regiorandom P3HT. The first two P3HTs gave dark carriers in CELIV but regiorandom P3HT did not. The reason for the absence of dark carriers in regiorandom P3HT based devices is probably similar to that for PSDTTT-based devices: due to these polymers' highly amorphous nature, the fullerene molecules intermix into the polymer network during spin-coating and become buried inside the polymer network, leading less contact of the fullerene with the evaporated metal. The fact that no dark carriers are seen in the regiorandom P3HT based device also suggests that chemical interactions between sulfur in P3HT and calcium do not contribute to the dark carriers because the same chemical reactions should occur for P3HT with any regioregularity. However, the chemical reactions between P3HT and calcium could serve as the explanation for why sulfur-based polymers top metal atoms from penetrating into the polymer layer.

5.4.5 XPS Analysis: Calculating Volume Fraction from C/S Ratio

For P3HT and PCBM samples, the volume fraction of P3HT is calculated using:

$$\frac{n_{PCBM}}{n_{P3HT}} = \frac{\frac{C}{S}(BC\ or\ SqP) - \frac{C}{S}(Pure\ P3HT)}{72}$$

$$P3HT\ weight\ \% = \frac{n_{P3HT} \times M_{P3HT}}{n_{P3HT} \times M_{P3HT} + n_{PCBM} \times M_{PCBM}} \times 100\%$$

$$P3HT\ volume\ \% = \frac{\frac{P3HT\ weight\ \%}{P3HT\ physical\ density}}{\frac{P3HT\ weight\ \%}{P3HT\ physical\ density} + \frac{PCBM\ weight\ \%}{PCBM\ physical\ density}} \times 100\%$$

$$PCBM\ volume\ \% = 1 - P3HT\ volume\ \%$$

Volume fractions for other polymer/fullerene systems are obtained similarly.

5.4.6 Device Fabrication Procedure

Glass/ITO substrates were cleaned with soap water, deionized water, acetone and isopropanol successively in a sonicator. For devices with PEDOT:PSS, the PEDOT:PSS (AI 4083) was spun onto dried glass/ITO substrates at 5000 rpm for 20 s. The substrates were then baked at 150 °C for 20 min in air. For devices with ZnO, the ZnO nanoparticle layer was prepared using the same method described in Chapter 4, section 4.5.1.

Different organic materials' solutions are prepared as followed:

Regioregular P3HT solution was prepared by dissolving P3HT (regioregular, P100, Rieke Metal Inc) in *o*-dichlorobenzene at a concentration of 20 mg/mL. The solution was heated at 60 °C on a hot plate in a nitrogen glovebox for at least 2 hr before being cooled down to room temperature and spin-coated onto the substrates at 1000 rpm for 60 s.

Regiorandom P3HT solutions were prepared the same way as for regioregular P3HT, and the spin-coating parameters were also the same.

PSDTTT solutions were prepared by dissolving PSDTTT[40] in *o*-dichlorobenzene at a concentration of 10 mg/mL. The solution was heated at ~100–120 °C for at least 2 hr before

being spin-coated onto the substrates (the solution was kept hot during spin-coating) at 1000 rpm for 60 s.

The PSEHTT[39] solutions were prepared the same way as the PSDTTT solutions and the spin-coating parameters were also the same.

The PBDTTT-C solution was prepared by dissolving PBDTTT-C (Solarmer Energy Inc.) in chlorobenzene at a concentration of 10 mg/mL. The solution was heated at 60 ^{o}C on a hot plate in a nitrogen glovebox for at least 2 hr before being cooled down to room temperature and being spin-coated onto the substrates at 1000 rpm for 60 s.

For all SqP polymer/fullerene active layers, the polymer films were brought into the antechamber of the glovebox and held under vaccum for at least 20 min before being brought back into the nitrogen glovebox.

PCBM solutions were prepared by dissolving PCBM powder (nano-C) in dichloromethane at various concentrations. The solutions were stirred on a hot plate at room temperature for ~30–60 min before being spin-coated onto the polymer underlayer at 4000 rpm for 10 s.

ICBA solutions were prepared the same way as PCBM solutions. The spin-coating parameters were also the same.

The P3HT:PCBM BC solution and its spin-coating parameters followed identical procedures to those used in Chapter 4, section 4.5.1.

Thermal annealing was performed before the deposition of any top electrode in an argon atmosphere glovebox.

For thermal evaporation, electrode materials including LiF, MoO_3, Ca, Mg, Ag, Au, K, Na and Al (when used as cathode) were all evaporated at rates below 0.3 Å/s. When Al was used as a protection layer on top of Ca, the evaporation rate was kept below 1 Å/s. All devices had an

active area of 7.2 mm^2 except for those used in the temperature-dependent CELIV studies, whose active areas were ~4 mm^2, created using a smaller evaporation mask.

5.5 References

(1) Yu, G.; Gao, J.; Hummelen, J. C.; Wudl, F.; Heeger, A. J. Polymer Photovoltaic Cells: Enhanced Efficiencies via a Network of Internal Donor-Acceptor Heterojunctions. *Science (80-.).* **1995**, *270*, 1789–1791.

(2) Heeger, A. J. 25th Anniversary Article: Bulk Heterojunction Solar Cells: Understanding the Mechanism of Operation. *Adv. Mater.* **2014**, *26*, 10–27.

(3) Hawks, S. A.; Aguirre, J. C.; Schelhas, L. T.; Thompson, R. J.; Huber, R. C.; Ferreira, A. S.; Zhang, G.; Herzing, A. A.; Tolbert, S. H.; Schwartz, B. J. Comparing Matched Polymer:Fullerene Solar Cells Made by Solution-Sequential Processing and Traditional Blend Casting: Nanoscale Structure and Device Performance. *J. Phys. Chem. C* **2014**, *118*, 17413–17425.

(4) Lee, K. H.; Schwenn, P. E.; Smith, A. R. G.; Cavaye, H.; Shaw, P. E.; James, M.; Krueger, K. B.; Gentle, I. R.; Meredith, P.; Burn, P. L. Morphology of All-Solution-Processed "Bilayer" Organic Solar Cells. *Adv. Mater.* **2011**, *23*, 766–770.

(5) Lee, K. H.; Zhang, Y.; Burn, P. L.; Gentle, I. R.; James, M.; Nelson, A.; Meredith, P. Correlation of Diffusion and Performance in Sequentially Processed P3HT/PCBM

Heterojunction Films by Time-Resolved Neutron Reflectometry. *J. Mater. Chem. C* **2013**, *1*, 2593–2598.

(6) Zhang, G.; Huber, R. C.; Ferreira, A. S.; Boyd, S. D.; Luscombe, C. K.; Tolbert, S. H.; Schwartz, B. J. Crystallinity Effects in Sequentially Processed and Blend-Cast Bulk-Heterojunction Polymer/Fullerene Photovoltaics. *J. Phys. Chem. C* **2014**, *118*, 18424–18435.

(7) Sandberg, O. J.; Nyman, M.; Österbacka, R. Direct Determination of Doping Concentration and Built-in Voltage from Extraction Current Transients. *Org. Electron.* **2014**, *15*, 3413–3420.

(8) Lüssem, B.; Riede, M.; Leo, K. Doping of Organic Semiconductors. *Phys. Status Solidi* **2013**, *210*, 9–43.

(9) Bebensee, F.; Schmid, M.; Steinrück, H.-P.; Campbell, C. T.; Gottfried, J. M. Toward Well-Defined Metal-Polymer Interfaces: Temperature-Controlled Suppression of Subsurface Diffusion and Reaction at the calcium/poly(3-Hexylthiophene) Interface. *J. Am. Chem. Soc.* **2010**, *132*, 12163–12165.

(10) Bebensee, F.; Zhu, J.; Baricuatro, J. H.; Farmer, J. a; Bai, Y.; Steinrück, H.-P.; Campbell, C. T.; Gottfried, J. M. Interface Formation between Calcium and Electron-Irradiated poly(3-Hexylthiophene). *Langmuir* **2010**, *26*, 9632–9639.

(11) Tseng, W.-H.; Chen, M.-H.; Wang, J.-Y.; Tseng, C.-T.; Lo, H.; Wang, P.-S.; Wu, C.-I. Investigations of Efficiency Improvements in poly(3-Hexylthiophene) Based Organic Solar Cells Using Calcium Cathodes. *Sol. Energy Mater. Sol. Cells* **2011**, *95*, 3424–3427.

(12) Bharathan, J. M.; Yang, Y. Polymer/metal Interfaces and the Performance of Polymer Light-Emitting Diodes. *J. Appl. Phys.* **1998**, *84*, 3207.

(13) Dongaonkar, S.; Servaites, J. D.; Ford, G. M.; Loser, S.; Moore, J.; Gelfand, R. M.; Mohseni, H.; Hillhouse, H. W.; Agrawal, R.; Ratner, M. A.; et al. Universality of Non-Ohmic Shunt Leakage in Thin-Film Solar Cells. *J. Appl. Phys.* **2010**, *108*, 124509.

(14) Juska, G.; Arlauskas, K.; Viliunas, M.; Kocka, J. Extraction Current Transients : New Method of Study of Charge Transport in Microcrystalline Silicon. *Phys. Rev. Lett.* **2000**, *84*, 4946–4949.

(15) Lorrmann, J.; Badada, B. H.; Inganäs, O.; Dyakonov, V.; Deibel, C. Charge Carrier Extraction by Linearly Increasing Voltage: Analytic Framework and Ambipolar Transients. *J. Appl. Phys.* **2010**, *108*, 113705.

(16) Bange, S.; Schubert, M.; Neher, D. Charge Mobility Determination by Current Extraction under Linear Increasing Voltages: Case of Nonequilibrium Charges and Field-Dependent Mobilities. *Phys. Rev. B* **2010**, *81*, 035209.

(17) Schafferhans, J.; Baumann, A.; Wagenpfahl, A.; Deibel, C.; Dyakonov, V. Oxygen Doping of P3HT:PCBM Blends: Influence on Trap States, Charge Carrier Mobility and Solar Cell Performance. *Org. Electron.* **2010**, *11*, 1693–1700.

(18) Armin, A.; Juska, G.; Philippa, B. W.; Burn, P. L.; Meredith, P.; White, R. D.; Pivrikas, A. Doping-Induced Screening of the Built-in-Field in Organic Solar Cells: Effect on Charge Transport and Recombination. *Adv. Energy Mater.* **2013**, *3*, 321–327.

(19) Głowacki, E. D.; Marshall, K. L.; Tang, C. W.; Sariciftci, N. S. Doping of Organic Semiconductors Induced by Lithium Fluoride/aluminum Electrodes Studied by Electron Spin Resonance and Infrared Reflection-Absorption Spectroscopy. *Appl. Phys. Lett.* **2011**, *99*, 043305.

(20) Mor, G. K.; Jones, D.; Le, T. P.; Shang, Z.; Weathers, P. J.; Woltermann, M. K. B.; Vakhshouri, K.; Williams, B. P.; Tohran, S. a.; Saito, T.; et al. Contact Doping with Sub-Monolayers of Strong Polyelectrolytes for Organic Photovoltaics. *Adv. Energy Mater.* **2014**, n/a – n/a.

(21) Garcia-Belmonte, G.; Munar, A.; Barea, E. M.; Bisquert, J.; Ugarte, I.; Pacios, R. Charge Carrier Mobility and Lifetime of Organic Bulk Heterojunctions Analyzed by Impedance Spectroscopy. *Org. Electron.* **2008**, *9*, 847–851.

(22) Mauger, S. A.; Chang, L.; Friedrich, S.; Rochester, C. W.; Huang, D. M.; Wang, P.; Moulé, A. J. Self-Assembly of Selective Interfaces in Organic Photovoltaics. *Adv. Funct. Mater.* **2013**, *23*, 1935–1946.

(23) Kirchartz, T.; Gong, W.; Hawks, S. a.; Agostinelli, T.; MacKenzie, R. C. I.; Yang, Y.; Nelson, J. Sensitivity of the Mott–Schottky Analysis in Organic Solar Cells. *J. Phys. Chem. C* **2012**, *116*, 7672–7680.

(24) Mingebach, M.; Deibel, C.; Dyakonov, V. Built-in Potential and Validity of the Mott-Schottky Analysis in Organic Bulk Heterojunction Solar Cells. *Phys. Rev. B* **2011**, *84*, 153201.

(25) Tremolet de Villers, B.; Tassone, C. J.; Tolbert, S. H.; Schwartz, B. J. Improving the Reproducibility of P3HT:PCBM Solar Cells by Controlling the PCBM/Cathode Interface. *J. Phys. Chem. C* **2009**, *113*, 18978–18982.

(26) Juška, G.; Genevičius, K.; Arlauskas, K.; Österbacka, R.; Stubb, H. Charge Transport at Low Electric Fields in Π-Conjugated Polymers. *Phys. Rev. B* **2002**, *65*, 233208.

(27) Arlauskas, K.; Viliu, M.; Genevic, K.; Jus, G.; Stubb, H. Charge Transport in Pi-Conjugated Polymers from Extraction Current Transients. *Phys. Rev. B* **2000**, *62*, 235–238.

(28) Pivrikas, A.; Ullah, M.; Singh, T. B.; Simbrunner, C.; Matt, G.; Sitter, H.; Sariciftci, N. S. Meyer–Neldel Rule for Charge Carrier Transport in Fullerene Devices: A Comparative Study. *Org. Electron.* **2011**, *12*, 161–168.

(29) Juška, G.; Nekrašas, N.; Valentinavičius, V.; Meredith, P.; Pivrikas, a. Extraction of Photogenerated Charge Carriers by Linearly Increasing Voltage in the Case of Langevin Recombination. *Phys. Rev. B* **2011**, *84*, 155202.

(30) Hawks, S. A.; Finck, B. Y.; Schwartz, B. J. Theory of Current Transients in Planar Optoelectronic Devices Using Average Charge Densities : Insights and Applications to Organic Solar Cell Characterization. *Phys. Rev. Appl.* **2014**, *Submitted*.

(31) Liang, Z.; Gregg, B. a. Compensating poly(3-Hexylthiophene) Reveals Its Doping Density and Its Strong Exciton Quenching by Free Carriers. *Adv. Mater.* **2012**, *24*, 3258–3262.

(32) Hawks, S. a.; Li, G.; Yang, Y.; Street, R. a. Band Tail Recombination in Polymer:fullerene Organic Solar Cells. *J. Appl. Phys.* **2014**, *116*, 074503.

(33) Dibb, G. F. a.; Muth, M.-A.; Kirchartz, T.; Engmann, S.; Hoppe, H.; Gobsch, G.; Thelakkat, M.; Blouin, N.; Tierney, S.; Carrasco-Orozco, M.; et al. Influence of Doping on Charge Carrier Collection in Normal and Inverted Geometry Polymer:fullerene Solar Cells. *Sci. Rep.* **2013**, *3*, 1–7.

(34) Liu, D.; Nagamori, T.; Yabusaki, M.; Yasuda, T.; Han, L.; Marumoto, K. Dramatic Enhancement of Fullerene Anion Formation in Polymer Solar Cells by Thermal Annealing: Direct Observation by Electron Spin Resonance. *Appl. Phys. Lett.* **2014**, *104*, 243903.

(35) Chikamatsu, M.; Taima, T.; Yoshida, Y.; Saito, K.; Yase, K. Mg-Doped C60 Thin Film as Improved N-Type Organic Semiconductor for a Solar Cell. *Appl. Phys. Lett.* **2004**, *84*, 127.

(36) Tseng, W.-H.; Lo, H.; Chang, J.-K.; Liu, I.-H.; Chen, M.-H.; Wu, C.-I. Metal-Induced Molecular Diffusion in [6,6]-Phenyl-C61-Butyric Acid Methyl Ester poly(3-Hexylthiophene) Based Bulk-Heterojunction Solar Cells. *Appl. Phys. Lett.* **2013**, *103*, 183506.

(37) Matz, D. L.; Ratcliff, E. L.; Meyer, J.; Kahn, A.; Pemberton, J. E. Deciphering the Metal-C60 Interface in Optoelectronic Devices: Evidence for C60 Reduction by Vapor Deposited Al. *ACS Appl. Mater. Interfaces* **2013**, *5*, 6001–6008.

(38) Rong, Z.; Rokhinson, L. STM Study of Gold-Overlayer Formation on C 60 Monolayers. *Phys. Rev. B* **1994**, *49*, 7749–7753.

(39) Subramaniyan, S.; Xin, H.; Kim, F. S.; Shoaee, S.; Durrant, J. R.; Jenekhe, S. A. Effects of Side Chains on Thiazolothiazole-Based Copolymer Semiconductors for High Performance Solar Cells. *Adv. Energy Mater.* **2011**, *1*, 854–860.

(40) Subramaniyan, S.; Xin, H.; Kim, F. S.; Jenekhe, S. A. New Thiazolothiazole Copolymer Semiconductors for Highly Efficient Solar Cells. *Macromolecules* **2011**, *44*, 6245–6248.

(41) Burgelman, M.; Nollet, P.; Degrave, S. Modelling Polycrystalline Semiconductor Solar Cells. *Thin Solid Films* **2000**, *361-362*, 527–532.

(42) Tachibana, M.; Yoshizawa, K.; Ogawa, A.; Fujimoto, H.; Hoffmann, R. Sulfur - Gold Orbital Interactions Which Determine the Structure of Alkanethiolate / Au (111) Self-Assembled Monolayer Systems. *J. Phys. Chem. B* **2002**, *106*, 12727–12736.

(43) Pensa, E.; Corte, E.; Corthey, G.; Carro, P.; Vericat, C.; Fonticelli, M. H.; Ben ́ez, G.; Rubert, A.; Salvarezza, R. C. The Chemistry of the Sulfur-Gold Interface : In Search of a Unified Model. *Acc. Chem. Res.* **2012**, *45*, 1183–1192.

(44) Gro, H.; Curioni, A.; Andreoni, W. Thiols and Disulfides on the Au (111) Surface : The Headgroup - Gold Interaction. *J. Am. Chem. Soc.* **2000**, *122*, 3839–3842.

(45) Häkkinen, H. The Gold-Sulfur Interface at the Nanoscale. *Nat. Chem.* **2012**, *4*, 443–455.

(46) Badia, A.; Demers, L.; Dickinson, L.; Morin, F. G.; Lennox, R. B.; Reven, L. Gold - Sulfur Interactions in Alkylthiol Self-Assembled Monolayers Formed on Gold Nanoparticles Studied by Solid-State NMR. *J. Am. Chem. Soc.* **1997**, *7863*, 11104–11105.

(47) Rodriguez, J. A.; Dvorak, J.; Jirsak, T.; Liu, G.; Hrbek, J.; Aray, Y.; Gonza, C. Coverage Effects and the Nature of the Metal - Sulfur Bond in S / Au (111): High-Resolution Photoemission and Density-Functional Studies. *J. Am. Chem. Soc.* **2003**, *125*, 276–285.

(48) Wenheim, G. K.; Buchanan, D. N. E. Reaction of C60 with Metals: W. *Solid State Commun.* **1993**, *88*, 97–100.

(49) Devenyi, A.; Manaila, R.; Belu-Marian, A.; Macovei, D.; Manciu, M.; Popescu, E. M.; Tanase, M.; Fratiloiu, D.; Mihai, N. D.; Barna, P. B.; et al. Nanocrystalline Gold in Au-Doped Thin C60 Films. *Thin Solid Films* **1998**, *335*, 258–265.

(50) Hou, J. G.; Wang, Y.; Xu, W.; Zhang, S. Y.; Jian, Z.; Zhang, Y. H. Synthesis and Characterization of Ag–C[sub 60] Nanostructure Film. *Appl. Phys. Lett.* **1997**, *70*, 3110.

(51) Li, X.; Tang, Y. J.; Zhao, H. W.; Zhan, W. S.; Wang, H.; Hou, J. G. Characteristic of Interface Effect in Cu–C60 Granular Films. *Appl. Phys. Lett.* **2000**, *77*, 984.

(52) Mihailetchi, B. V. D.; Duren, J. K. J. Van; Blom, P. W. M.; Hummelen, J. C.; Janssen, R. A. J.; Kroon, J. M.; Rispens, M. T.; Verhees, W. J. H.; Wienk, M. M. Electron Transport in a Methanofullerene. *Adv. Funct. Mater.* **2003**, *13*, 43–46.

(53) Von Hauff, E.; Dyakonov, V.; Parisi, J. Study of Field Effect Mobility in PCBM Films and P3HT:PCBM Blends. *Sol. Energy Mater. Sol. Cells* **2005**, *87*, 149–156.

(54) Yang, E. S. *Microelectronic Devices*; McGraw-Hill Book Company: New York, NY, 1988.

(55) He, Y.; Chen, H.; Hou, J.; Li, Y. Indene - C60 Bisadduct : A New Acceptor for High-Performance Polymer Solar Cells. *J. Am. Chem. Soc.* **2010**, 1377–1382.

(56) Meng, X.; Zhao, G.; Xu, Q.; Tan, Z.; Zhang, Z.; Jiang, L.; Shu, C.; Wang, C.; Li, Y. Effects of Fullerene Bisadduct Regioisomers on Photovoltaic Performance. *Adv. Funct. Mater.* **2014**, *24*, 158–163.

(57) Xin, H.; Subramaniyan, S.; Kwon, T.; Shoaee, S.; Durrant, J. R.; Jenekhe, S. A. Enhanced Open Circuit Voltage and E Ffi Ciency of Donor − Acceptor Copolymer Solar Cells by Using Indene-C60 Bisadduct. *Chem. Mater.* **2012**, *24*, 1995–2001.

(58) Gan, Q.; Bartoli, F. J.; Kafafi, Z. H. Plasmonic-Enhanced Organic Photovoltaics: Breaking the 10% Efficiency Barrier. *Adv. Mater.* **2013**, *25*, 2385–2396.

(59) Kasuya, A.; Itoh, Y.; Okada, T.; Osawa, M.; Takahashi, Y.; Kazuma, E.; Tatsuma, T.; Hasegawa, T. Anisotropic Light Absorption by Localized Surface Plasmon Resonance in a Thin Film of Gold Nanoparticles Studied by Visible Multiple-Angle Incidence Resolution Spectrometry. *Phys. Chem. Chem. Phys.* **2011**, *13*, 9691–9696.